Modélisation du transfert radiatif rapide pour la Prévision Numérique du Temps

Jérôme Vidot

UNIVERSITÉ DE TOULOUSE
Institut National Polytechnique

Manuscript présenté en vue de l'obtention du diplôme d'Habilitation à Diriger des Recherches

Présentée par
Jérôme VIDOT

Modélisation du transfert radiatif rapide pour la Prévision Numérique du Temps

préparée au Centre d'Études en Météorologie Satellitaire du CNRM (MÉTÉO-FRANCE ET CNRS)

soutenue le 21 janvier 2020

Jury :

Rapporteurs :	Céline CORNET	-	LOA, Univ. Lille
	Jacques PELON	-	LATMOS, Sorbonne Univ.
	Jean-François MAHFOUF	-	CNRM
Directrice :	Nadia FOURRIÉ	-	CNRM
Examinateurs :	Jean-Pierre CHABOUREAU	-	LA, Univ. de Toulouse
	Cyril CREVOISIER	-	LMD, Ecole Polytechnique

Remerciements

Table des matières

Glossaire

4A Automatized Atmospheric Absorption Atlas. 47–49

AIRS Atmospheric InfraRed Sounder. 21, 47, 51, 55
AMA Ateliers de Modélisation de l'Atmosphère. 14
AMSU Advanced Microwave Sounding Unit. 21
AMV Atmospheric Motion Vector. 21
AOS Atmospheric and Oceanic Sciences. 2
ARPEGE Action de Recherche Petite Échelle Grande Échelle. 20, 21, 45, 46, 48
ARSA Analyzed RadioSounding Archive. 48, 49
ASCAT Advanced Scatterometer. 21
ATMS Advanced Technology Microwave Sounder. 21
AVHRR Advanced Very High Resolution Radiometer. 23

BCC Black Carbon Content. 39–41
BRDF Bidirectional Reflectance Distribution Function. iv, 27, 37–39, 41
BTS Brevet de Technicien Supérieur. iii, 3

C3S Copernicus Climate Change Service. 4, 13
CADS Cloud and Aerosol Detection Software. 13
CALIOP Cloud-Aerosol LIdar with Orthogonal Polarization. 3
CALIPSO Cloud-Aerosol Lidar and Infrared Pathfinder Satellite Observation. 4
CDOP Continuous Development and Operations Phase. 18
CEMS Centre d'Études en Météorologie Satellitaire. 1, 2, 18, 22, 23, 56
CEN Centre d'Étude de la Neige. 39
CEPMMT Centre Européen pour les Prévisions Météorologiques à Moyen Terme. 19, 28, 32, 35, 36, 49, 51, 55
CESBIO Centre d'Études Spatiales de la BIOsphère. 22
CGMS Coordination Group for Meteorological Satellites. 14, 23
CIRCLE CIRrus CLoud Experiment. 4, 43
CMA China Meteorological Administration. 24
CMS Centre de Météorologie Spatiale. 3, 17
CMSS Cloud fraction Maximum Simple Stream. 37, 52, 53
CNES Centre National d'Études Spatiales. 2, 14, 22
CNRM Centre National de Recherches Météorologiques. 1, 4, 14, 15, 17, 42

CNRS Centre National de la Recherche Scientifique. 1, 17

CPAR Cloud Perimeter to Area Ratio. 57, 58

CrIS Cross-track Infrared Sounder. 20, 21, 23

CRTM Community Radiative Transfer Model. 23–25, 33

DEA Diplôme d'Études Approfondies. 2

DISORT DIScrete Ordinate Radiative Transfer. 39

DWD service météorologique de l'Allemagne. 19, 28

EECLAT Expecting Earth-Care, Learning from A-Train. 14, 55

ENM École Nationale de la Météorologie. 15

ENSSAT École Nationale Supérieure des Sciences Appliquées et de Technologie. 3

ENSTA École Nationale Supérieure de Techniques Avancées. 4, 15

EPICA European Project for Ice Coring in Antarctica. 2

EPS-SG EUMETSAT Polar System - Seconde Génération. 18, 46

ESA European Space Agency. 45

ETR Équation du Transfert Radiatif. iv, 19, 20, 27–29, 31, 35–37

EUMETSAT Organisation européenne pour l'exploitation des satellites météorologiques. 18, 22, 57

FORUM Far-infrared Outgoing Radiation Understanding and Monitoring. iv, 13, 27, 45–47

GEISA Gestion et Étude des Informations Spectroscopiques Atmosphériques. 31, 49

GMI GPM Microwave Imager. 21

GOES Geostationary Operational Environmental Satellite. 21

HIRS High Resolution Infrared Radiation Sounder. 21, 28, 47

HITRAN HIgh-resolution TRANsmission molecular absorption database. 31, 49

IASI Interféromètre Atmosphérique de Sondage Infrarouge. 3, 14, 20, 21, 23, 34, 36, 47–52

IASI-NG IASI-Nouvelle Génération. 14, 46

ICWG International Cloud Working Group. 14

IFS Integrated Forecasting System. 51

IIR Infrared Imager Radiometer. 43, 55, 56

INSU Institut National des Sciences de l'Univers. 22

IRRTM International Reference Radiative Transfer Model. 25

IRS InfraRed Sounder. 4

ISSWG IASI Sounding Science Working Group. 14

ISWG International Surface Working Group. 14

ITSC International TOVS Study conference. 24

IUT Institut Universitaire de Technologie. iii, 3

IWC Ice Water Content. 36, 42, 43, 45, 46, 51, 52, 55

JCSDA Joint Center for Satellite Data Assimilation. 24

JPL Jet Propulsion Laboratory. 51

LaMP Laboratoire de Météorologie Physique. 2, 43

LATMOS Laboratoire ATmosphères, Milieux, Observations Spatiales. 22

LBLRTM Line-By-Line Radiative Transfer Model. 48

LGGE Laboratoire de Glaciologie et Géophysique de l'Environnement. 2

LIDORT LInearized Discrete Ordinate Radiative Transfer. 50–54

LISA Laboratoire Interuniversitaire des Systèmes Atmosphériques. 22

LISE Laboratoire Interdisciplinaire des Sciences de l'Environnement. 2

LMD Laboratoire de Météorologie Dynamique. 15, 22, 47–49

LOA Laboratoire d'Optique Atmosphérique. 4, 15, 22, 50, 57

LOG Laboratoire d'Océanologie et de Géosciences. 22

LSA Land Surface Analysis. 38

LWC Liquid Water Content. 36, 42

MAIA Masque AVHRR pour les Inversions ATOVS. 23

MERIS Medium Resolution Imaging Spectrometer. 2

MMR Minimum Residual Method. 35

MODIS Moderate Resolution Imaging Spectroradiometer. 38, 39, 41, 42

MPE Multi-sensor Precipitation Estimate. 3

MRO Maximum Random Overlap. 37, 52, 53

MSG Meteosat Seconde Génération. 4, 18, 21, 38, 56

MSU Microwave Sounding Unit. 28

MT-CKD MlawerTobinCloughKneizysDavies. 32, 48, 49

MTES Ministère de la Transition Écologique et Solidaire. 1, 17

MTG Meteosat Troisième Génération. 4, 18

MWHS Micro-Wave Humidity Sounder. 21

NCEP National Centers for Environmental Prediction. 24

NEDT Noise Equivalent Differential Temperature. 34

OCO Orbiting Carbon Observatory. 2

ONERA Office National d'Études et de Recherches Aérospatiales. 22

OPAC Optical Properties of Aerosols and Clouds. 42

PNT Prévision Numérique du Temps. 15, 19, 20, 22, 23, 28, 33, 36–40, 42, 57

PNTS Programme National de Télédétection Spatiale. 14

RTSPWG Radiative Transfer and Surface Properties Working Group. 14, 24

RTTOV Radiative Transfer model for TOVS. iv, 3, 4, 13, 19, 20, 22–29, 31–56

SAF Satellite Application Facilities. 18, 38

SAF-NWP SAF for Numerical Weather Prediction. 18, 22, 28, 43, 51, 53

SATMOS Service d'Archivage et de Traitement Météorologique des Observations Satellitaires. 17

SEVIRI Spinning Enhanced Visible and InfraRed Imager. 4, 38–40, 45, 46, 56, 57

SOI Successive Order of Interaction. 25

SOS Successive Order of Scattering. 25

SRF Fonction de réponse spectrale. 31, 34

SRON Institut Néerlandais de Recherches Spatiales. 2, 13

SSA Specific Surface Area. 39–41

SSMIS Special Sensor Microwave - Imager/Sounder. 21

TIROS Télévision InfraRed Observation Satellite. 27

TOSCA Terre solide, Océan, Surfaces Continentales, Atmosphère. 22, 47

TOVS TIROS Operational Vertical Sounder. 27

. 14, 22–24

TRMM Tropical Rainfall Measuring Mission. 4

TROPOMI TROPOspheric Monitoring Instrument. 13

UBO Université de Bretagne Occidentale. 15

UK Met-Office service météorologique du Royaume-Uni. 19, 28, 35, 38, 39

UMR Unité Mixte de Recherche. 1, 17

USGS United States Geological Survey. 38, 39

UW University of Wisconsin. 2

VIIRS Visible Infrared Imaging Radiometer Suite. 23

Chapitre 1

Curriculum Vitae détaillé

1.1 Curriculum Vitae

Nom, Prénom	VIDOT, Jérôme
Date de Naissance (âge)	26 août 1976 (43 ans)
Nationalité	Française
Situation de famille	Séparé, 2 enfants
Corps	Chargé de Recherche de Classe Normale du Ministère de la Transition Écologique et Solidaire (MTES) (au 4$^{\text{ième}}$ échelon depuis le 01/10/2017) à Météo-France
Affectation	Centre d'Études en Météorologie Satellitaire (CEMS), Centre National de Recherches Météorologiques (CNRM)/Centre National de la Recherche Scientifique (CNRS), Unité Mixte de Recherche (UMR), Météo-France, Avenue de Lorraine, 22300 Lannion
Courriel	jerome.vidot@meteo.fr
Téléphone	02.96.05.67.66

Thèmes de Recherche

Météorologie satellitaire, Modélisation du transfert radiatif rapide, Paramétrisation des propriétés optiques de l'atmosphère et des surfaces du visible à l'infrarouge lointain.

Activités de Recherche

Depuis janvier 2019 CEMS	**Chargé de Recherche** Responsable adjoint du CEMS, Responsable de l'équipe Sondage
Sep. 2011 - déc. 2018 CEMS	**Chargé de Recherche** Equipe Sondage
Oct. 2010 - août 2011 CEMS	**Contractuel** Equipe Sondage
Oct. 2009 - sep. 2010 Institut Néerlandais de Recherches Spatiales (SRON), Utrecht, Pays-bas	**Scientist** Responsable scientifique : Dr Jochen Landgraf Thème de recherche : Restitution de CO en présence de nuages pour Sentinel-5p
Jan. 2008 - sep. 2009 Laboratoire de Météorologie Physique (LaMP), Clermont-Fd, France	**Post-doctorant Centre National d'Études Spatiales (CNES)** Responsables scientifiques : Dr Vincent Giraud et Dr Olivier Jourdan Thème de recherche : Prise en compte des cirrus dans la restitution du NO_2 à partir des observations de l'A-Train
Jan. 2006 - nov. 2007 Atmospheric and Oceanic Sciences (AOS), University of Wisconsin (UW)-Madison, USA	**Visiting Research Associate** Responsable scientifique : Dr Ralf Bennartz Thème de recherche : Restitution de CO_2 au-dessus des nuages pour Orbiting Carbon Observatory (OCO)
Nov. 2000 - jui. 2005 Laboratoire Interdisciplinaire des Sciences de l'Environnement (LISE), Wimereux, France	**Doctorant** Directeur de Thèse : Pr Richard Santer Sujet : Restitution des propriétés optiques des aérosols au-dessus des terres pour l'instrument Medium Resolution Imaging Spectrometer (MERIS)
Jan. 2000 - jui. 2000 Laboratoire de Glaciologie et Géophysique de l'Environnement (LGGE), Grenoble, France	**Stagiaire de Diplôme d'Études Approfondies (DEA)** Encadrant : Dr Jérôme Weiss Sujet : Impact des poussières sur la croissance des grains de glace dans un carottage d'European Project for Ice Coring in Antarctica (EPICA)
Mar. 1999 - jui. 1999 Univ. Joensuu, Finlande	**Stagiaire de Maîtrise de Physique** Encadrant : Pr Raimo Silvenoinnen Sujet : Etude de l'orientation des fibres de bois par laser

Diplômes

2005	**Université du Littoral Côte d'Opale** Thèse de doctorat *« Télédétection des aérosols au-dessus des terres émergés à l'aide des capteurs couleur de l'eau et applications »* Soutenue le 7 juillet 2005. Mention Très Honorable.
2000	**Université Blaise Pascal de Clermont-Ferrand** *DEA de Climat et Physico-Chimie de l'Atmosphère* Mention Assez Bien.
1999	**Université de Lille** *Maîtrise de Physique*
1994	**Lycée Baggio de Lille** *Baccalauréat série E*

1.2 Encadrement

1.2.1 Master 1, Licence, IUT, BTS

N.B. : le taux d'encadrement est donné en %

2018 Marie-Laure Roussel (100%, stage de Master 1 - Université Toulouse 3 / Toulouse - 4 mois), « Évaluation de la contribution solaire dans le canal à 3.9 µm de SEVIRI simulée par le modèle RTTOV »

2016 Nicolas Maury (100%, stage de Master 1 - Université Toulouse 3 / Toulouse - 4 mois), « Etude des variations interannuelles et saisonnières du cycle diurne du banc de stratocumulus marins au large de la Namibie »

2015 Pierre Brunel (100%, stage de 1ère année de BTS - Lycée Le Dantec / Lannion - 2 mois), « Outil de gestion et de recherche de documentation pour l'équipe R&D du Centre de Météorologie Spatiale (CMS) »

2015 Baptiste Hugonnet (100%, stage ingénieur de 2ème année - Télécom Bretagne / Brest - 1 mois), « Etude de l'apodisation de l'interféromètre Interféromètre Atmosphérique de Sondage Infrarouge (IASI) »

2014 Clément Monaton (100%, stage ingénieur de 1ère année - École Nationale Supérieure des Sciences Appliquées et de Technologie (ENSSAT) / Lannion - 1 mois), « Etude des produits aérosols issus du lidar Cloud-Aerosol LIdar with Orthogonal Polarization (CALIOP) »

2013 Maximilien Patou (100%, stage de Master 1 - Université de Lille - 4 mois), « Evaluation of RTTOV cirrus parameterisations with A-Train satellites in thermal infrared »

2012 Justine Rozé (50%, stage de 2ième année - IUT de Lannion - 2 mois), « Comparaison du produit de précipitation Multi-sensor Precipitation Estimate (MPE)

avec des observations spatiales Tropical Rainfall Measuring Mission (TRMM) et sol »

1.2.2 Master 2 ou équivalent

N.B. : le taux d'encadrement est donné en %

2017 Emeric Lemercier (100%, stage de 3ième année - École Nationale Supérieure de Techniques Avancées (ENSTA)-Bretagne / Brest - 6 mois), « Nouvelle méthode de correction des aérosols désertiques pour la restitution de la température des surfaces océaniques »

2011 Gwennolé Guyot (100%, stage de Master 2 - Université de Clermont-Ferrand - 6 mois),« Evaluation des nouvelles paramétrisations des cirrus dans le modèle RTTOV à l'aide de la campagne CIRus CLoud Experiment (CIRCLE)-2 et de Cloud-Aerosol Lidar and Infrared Pathfinder Satellite Observation (CALIPSO) »

1.2.3 Co-encadrement de thèse

Sept. 2014 - mars 2018 Maximilien Patou (Directeur : Pr Jerôme Riedi, Laboratoire d'Optique Atmosphérique (LOA))
Sujet : Analyse temporelle des propriétés optiques, microphysiques et macrophysiques de systèmes nuageux fortement précipitants à partir de Spinning Enhanced Visible and InfraRed Imager (SEVIRI)/Meteosat Seconde Génération (MSG).
Financement de l'Université de Lille et Météo-France. Thèse soutenue le 5 mars 2018 à Lille.

Depuis décembre 2019 Francesca Vittorioso (Directrice : Dr Nadia Fourrié, CNRM)
Sujet : Apport de l'assimilation des luminances de Meteosat Troisième Génération (MTG)/InfraRed Sounder (IRS) pour caractériser la composition chimique de l'atmosphère.
Financement de Thales Alenia Space et Météo-France.

1.2.4 Post-Doctorant

Depuis juillet 2019 Bruna Barbosa Silveira
Sujet : Simulations de transfert radiatif pour des instruments satellitaires infrarouges des années 1970 à 1990.
Financement sur projet Copernicus Copernicus Climate Change Service (C3S) 311c Lot1 "Satellite data rescue".

1.3 Production Scientifique

1.3.1 Thèse de doctorat

Vidot J., 2005 : Télédétection des aérosols au-dessus des terres émergées à l'aide des capteurs « couleur de l'eau ». Thèse de doctorat. Université du Littoral Côte d'Opale. Soutenue le 7 juillet 2005. Mention Très Honorable. Accessible sur la page internet https://tel.archives-ouvertes.fr/tel-00011216.

1.3.2 Publications soumises ou en cours de rédaction

1 **Vidot J.**, C.-Labonnote L., Matricardi M., Baran A. and Brunel P., Evaluation of the scattering approximation of RTTOV with LIDORT for hyperspectral IR cloudy radiances and jacobians, en cours de rédaction.

2 Mattioli, V., C. Accadia, C. Prigent, S. Crewell, A. Geer, P. Eriksson, S. Fox, J.R. Pardo, E.J. Mlawer, M. Cadeddu, M. Bremer, C. De Breuck, A. Smette, D. Cimini, E. Turner, M. Mech, F.S. Marzano, P. Brunel, **J. Vidot**, R. Bennartz, T. Wehr, S. Di Michele, and V. John, 0 : Atmospheric gas absorption knowledge in the sub-millimeter : Modeling, field measurements, and uncertainty quantification. Bull. Amer. Meteor. Soc., 2020, https ://doi.org/10.1175/BAMS-D-19-0074.1

1.3.3 Tableau récapitulatif des publications et communications

	Nombre total
Article dans des revues à comité de lecture (ACL)	21
Article dans des revues à comité de lecture non répertoriées (ACLN)	1
Conférence invitée dans un congrès international ou national (INV)	2
Communication avec actes dans congrès international (ACTI)	21
Communication orale sans actes dans un congrès international ou national (COM)	8
Communication par affiche dans un congrès international ou national (AFF)	18
Rapport de recherche (RR)	12

1.3.4 Articles dans des revues à comité de lecture (ACL)

N.B. : 21 publications référencées dont 10 en premier auteur (h-index de 11 selon Scopus) au 15 novembre 2019

ACL.1 Silvennoinen R., Wahl P., and **Vidot J.**, 2000 : Inspection of orientation of micro fibres in dried wood by a diffractive optical element, *Optics and Lasers in Engineering*, 33, pp. 29-38, http ://dx.doi.org/10.1016/S0143-8166(00)00025-7

ACL.2 Weiss J., **Vidot J.**, Gay M., Arnaud L. Duval. P. and Petit J. R., 2002 : Dome Concordia ice microstructure : impurities effect on grain growth, *Annals of Glaciology*, 35, pp. 552-558, http ://dx.doi.org/10.3189/172756402781816573

ACL.3 **Vidot J.**, and Santer R., 2005 : Atmospheric correction over inland waters : Applications to SeaWiFS, *International Journal of Remote Sensing*, Vol. 26, No. 17, pp. 3663-3682. http ://dx.doi.org/10.1080/01431160500034029

ACL.4 Santer R., Ramon D., **Vidot J.**, and Dilligeard E., 2007 : A surface reflectance model for aerosol remote sensing over land, *International Journal of Remote Sensing*, Vol. 28, Issue 3-4, pp. 737-760, http ://dx.doi.org/10.1080/01431160600821028

ACL.5 Pelletier B., Santer R., and **Vidot J.**, 2007 : Retrieving of particulate matter from optical measurements : A semiparametric approach, *Journal of Geophysical Research*, Vol. 112, Issue D6, Article Number : D06208. http ://dx.doi.org/10.1029/2005JD006737

ACL.6 **Vidot J.**, Ramon D., and Santer R., 2007 : Atmospheric particulate matter (PM) estimation from SeaWiFS imagery, *Remote Sensing of Environment*, Vol. 111, Issue 1, pp. 1-10, http ://dx.doi.org/10.1016/j.rse.2007.03.009

ACL.7 **Vidot J.**, Santer R., and Aznay O., 2008 : Evaluation of the MERIS aerosol optical depth over land with AERONET, *Atmospheric Chemistry and Physics*, Vol. 8, pp. 7603-7617, http ://dx.doi.org/10.5194/acp-8-7603-2008

ACL.8 **Vidot J.**, Bennartz R., O'Dell C. W., Preusker R., Lindstrot R., and Heidinger A.K., 2009 : CO2 Retrieval over Clouds from the OCO Mission : Model Simulations and Error Analysis, *Journal of Atmospheric and Oceanic Technology*, Vol. 26, pp. 1090-1104, http ://dx.doi.org/10.1175/2009JTECHA1200.1

ACL.9 Jourdan O., Mioche G., Garrett T. J., Schwarzenböck A., **Vidot J.**, Xie P., Shcherbakov V., Yang P., and Gayet J.-F., 2010 : Coupling of the microphysical and optical properties of an Artic nimbostratus cloud during the ASTAR 2004 experiment : Implications for light-scattering modelling, *Journal of Geophysical Research*, Vol. 115, D23206, http ://dx.doi.org/10.1029/2010JD014016

ACL.10 Butz A., Hasekamp O. P., Frankenberg C., **Vidot J.**, and Aben I., 2010 : CH4 retrievals from space-based solar backscatter measurements : Performance evaluation against simulated aerosol and cirrus loaded scenes, *Journal of Geophysical Research*, Vol. 115, D24302, http ://dx.doi.org/10.1029/2010JD014514

ACL.11 **Vidot J.**, Jourdan O., Kokhanosvky A.A., Szczap F., Giraud V., and Rozanov V.V., 2010 : Retrieval of tropospheric NO2 columns from satellite measurements in presence of cirrus : A theoretical sensitivity study using SCIATRAN and prospect application for the A-Train, *Journal of Quantitative Spectroscopy and Radiative Transfer*, Vol. 111, pp. 586-601, http ://dx.doi.org/10.1016/j.jqsrt.2009.10.015

ACL.12 **Vidot J.**, Landgraf J., Hasekamp O. P., Butz A., Galli A., Tol P., Aben I., 2012 : Carbon Monoxide from shortwave infrared reflectance

measurements : An algorithm concept for clear sky and partially cloudy atmospheres, *Remote Sensing of Environment*, Vol. 120, pp. 255-266, http ://dx.doi.org/10.1016/j.rse.2011.09.032

ACL.13 **Vidot J.** and Borbas E., 2014 : Land surface VIS/NIR BRDF atlas for RTTOV-11 : Model and Validation against SEVIRI Land SAF Albedo product. *Quarterly Journal of the Royal Meteorological Society*, http ://dx.doi.org/10.1002/qj.2288

ACL.14 **Vidot J.**, Baran A. J., and Brunel P. 2015 : A new ice cloud parameterization for infrared radiative transfer simulation of cloudy radiances : Evaluation and optimization with IIR observations and ice cloud profile retrieval products, *J. Geophys. Res. Atmos.*, 120, http ://dx.doi.org/10.1002/2015JD023462

ACL.15 Hoareau C., Noel V., Chepfer H., **Vidot, J.**, Chiriaco M., Bastin S., Reverdy M. and Cesana G., 2016, Remote sensing ice supersaturation inside and near cirrus clouds : a case study in the subtropics. *Atmos. Sci. Lett.*, 17 : 639-645. doi :10.1002/asl.714

ACL.16 **Vidot, J.**, Bellec B., Dumont M., and Brunel P. 2017, A daytime VIIRS RGB pseudo composite for snow detection, *Remote Sensing of Environment*, Vol. 196, pp. 134-139, https ://doi.org/10.1016/j.rse.2017.04.028

ACL.17 **Vidot, J.**, Brunel P., Dumont M., Carmagnola C., and Hocking J. 2018, The VIS/NIR Land and Snow BRDF Atlas for RTTOV : Comparison between MODIS MCD43C1 C5 and C6, *Remote Sensing*, vol. 10, 21, https ://doi.org/10.3390/rs10010021

ACL.18 Patou M., **Vidot J.**, Riedi J., Garrett T.J. and Penide G., 2018, Prediction of the onset of heavy rain using SEVIRI cloud observations, *Journal of Applied Meteorology and Climatology*, Vol. 57, pp. 2343-2361, https ://doi.org/10.1175/JAMC-D-17-0352.1

ACL.19 Aumann H.H., Chen X., Fishbein E., Geer A., Havemann S., Huang X., Liu X., Liuzzi G., DeSouza-Machado S., Manning E.M., Masiello G., Matricardi M., Moradi I., Natraj V., Serio S., Strow L., **Vidot J.**, Wilson R.C., Wu W., Yang Q., Yung Y.L., 2018, Evaluation of Radiative Transfer Models with Clouds, *Journal of Geophysical Research - Atmosphere*, Vol. 123, pp. 6142-6157, https ://doi.org/10.1029/2017JD028063

ACL.20 Saunders, R., Hocking, J., Turner, E., Rayer, P., Rundle, D., Brunel, P., **Vidot, J.**, Roquet, P., Matricardi, M., Geer, A., Bormann, N., and Lupu, C., 2018, An update on the RTTOV fast radiative transfer model (currently at version 12), *Geoscientific Model Development*, Vol. 11, pp. 2717-2737, https ://doi.org/10.5194/gmd-11-2717-2018.

ACL.21 Descheemaecker, M., Plu, M., Marécal, V., Claeyman, M., Olivier, F., Aoun, Y., Blanc, P., Wald, L., Guth, J., Sic, B., **Vidot, J.**, Piacentini, A., and Josse, B., 2019, Monitoring aerosols over Europe : an assessment of the potential benefit of assimilating the VIS04 measurements from the future MTG/FCI geo-

stationary imager, *Atmospheric Measurement Techniques*, Vol. 12, pp. 1251-1275, https ://doi.org/10.5194/amt-12-1251-2019.

1.3.5 Articles dans des revues à comité de lecture non répertoriées (ACLN)

ACLN.1 Mafhouf J.-F., Moisselin J.-M., Autonès F, et **Vidot, J.** 2017, Apport de l'observation satellitaire pour la prévision du temps. *La Météorologie*, Vol. 97, mai 2017.

1.3.6 Conférences invitées dans un congrès international ou national (INV)

INV.1 **Vidot J.** : Overview of the status of radiative transfer models for satellite data assimilation. ECMWF Seminar 2014 : Use of Satellite Observations in Numerical Weather Prediction, 8-12 septembre 2014, Reading, Angleterre.

INV.2 **Vidot J.** : Detecting cloud contamination in MTG-IRS observed spectra. ECMWF/EUMETSAT workshop on assimilation of hyper-spectral geostationnary satellite observation, 22-25 mai 2017, Reading, Angleterre.

1.3.7 Communications avec actes dans congrès international (ACTI)

ACTI.1 **Vidot J.**, and Brunel P. : Comparison of the RTTOV-12 ice cloud models for hyperspectral IR instruments using the A-Train, Proc. SPIE 10780, Multispectral, Hyperspectral, and Ultraspectral Remote Sensing Technology, Techniques and Applications VII, 1078004 (23 October 2018) *SPIE Asia-Pacific Remote Sensing*, 24-26 septembre 2018, Honolulu, Hawaii, United States, https ://doi.org/10.1117/12.2324673

ACTI.2 Patou M., Riedi J., **Vidot J.**, and Garrett T. J. : Temporal analysis of cloud parameter fileds before heavy rainfall events over France, Proceedings accessible sur le site internet de la conférence. *2015 EUMETSAT Meteorological Satellite Conference*, 21-25 septembre 2015, Toulouse, France.

ACTI.3 Bellec B., **Vidot J.**, Roquet P. and Brunel P. : A Snow RGB composite for Suomi NPP VIIRS, Proceedings accessible sur le site internet de la conférence. *2015 EUMETSAT Meteorological Satellite Conference*, 21-25 septembre 2015, Toulouse, France.

ACTI.4 **Vidot J.**, Brunel P. and Baran A. : A New Ice Cloud Parametrization in the Infrared for RTTOV-11 : Model and Comparison With other RTTOV parametrizations against A-Train observations, Proceedings accessible sur le site internet de la conférence. *2013 EUMETSAT Meteorological Satellite Conference*

and the 19th Satellite Meteorology, Oceanography and Climatology Conference of the American Meteorological Society (AMS), 16-20 septembre 2013, Vienne, Autriche.

ACTI.5 **Vidot J.**, Santer R., and Fell F., Inter comparison of satellite derived products in the SISCAL project, *Proceedings of the 2004 Envisat & ERS Symposium*, ESA SP (572), pp. 359-3 64. Envisat & ERS Symposium, 6-10 septembre 2004, Salzburg, Autriche.

ACTI.6 **Vidot J.**, Santer R., and Ramon D., Remote sensing of particle matter using MERIS, *Proceedings of the 2004 Envisat & ERS Symposium*, 6-10 September 2004, Salzburg, Austria, ESA SP (572), pp. 2055-2062. Envisat & ERS Symposium, 6-10 septembre 2004, Salzburg, Autriche.

ACTI.7 Santer R., Ramon D., **Vidot J.**, and Dilligeard E., A surface reflectance model for aerosol remote sensing over land, *Proceedings of the 2004 Envisat & ERS Symposium*, ESA SP (572), pp. 2045-2054. Envisat & ERS Symposium, 6-10 septembre 2004, Salzburg, Autriche.

ACTI.8 Ramon D., Blanchet A., Schadkowski C., Dilligeard E., Santer R., and **Vidot J.**, Integrated air quality monitoringservice using ground networks measurements and EO products, *Proceedings of the 2004 Envisat & ERSSymposium*, ESA SP (572), pp. 2091-2096. Envisat & ERS Symposium, 6-10 septembre 2004, Salzburg, Autriche.

ACTI.9 **Vidot J.** and Santer R., Atmospheric correction for inland waters, *Proceedings of SPIE, Remote Sensing of the Ocean and Sea Ice 2003*. Editor(s) : Charles R. Bostater, Jr., Rosalia Santoleri, Vol. 5233, pp. 269-281. SPIE Remote Sensing, 8-12 septembre 2003, Barcelone, Espagne.

ACTI.10 Santer R. and **Vidot J.**, Atmospheric correction over turbid waters in the SISCAL project, *Proceedings of SPIE, Remote Sensing of the Ocean and Sea Ice 2003*. Editor(s) : Charles R. Bostater, Jr., Rosalia Santoleri, Vol. 5233, pp. 25-34. SPIE Remote Sensing, 8-12 septembre 2003, Barcelone, Espagne.

ACTI.11 **Vidot J.**, Santer R. and Ramon D., Remote sensing of particle matter using SeaWiFS, *Proceedings of SPIE, Remote Sensing of Clouds and the Atmosphere VIII*. Editor(s) : Klaus Schäfer, Adolfo Comerón, Michel R. Carleer, Richard H. Picard, Vol. 5235, pp. 619-626. SPIE Remote Sensing, 8-12 septembre 2003, Barcelone, Espagne.

ACTI.12 **Vidot J.** and Santer R., SeaWiFS level 3 products over land, *Proceedings of SPIE, Remote Sensing of Cloudsand the Atmosphere VIII*. Editor(s) : Klaus Schäfer, Adolfo Comerón, Michel R. Carleer, Richard H. Picard, Vol. 5235 , pp. 357-365. SPIE Remote Sensing, 8-12 septembre 2003, Barcelone, Espagne.

ACTI.13 Bokoyé I. A., Santer R., Maitiny N. and **Vidot J.**, Evaluation of Junge power law as a tool for atmospheric correction validation, *Proceedings of SPIE, Remote Sensing of Clouds and the Atmosphere VIII*. Editor(s) : Klaus Schäfer, Adolfo Comerón, Michel R. Carleer, Richard H. Picard, Vol. 523 5, pp. 67-78. SPIE Remote Sensing, 8-12 septembre 2003, Barcelone, Espagne.

ACTI.14 Ramon D., Santer R. and **Vidot J.**, Determination of fme particulate matter from MERIS and SeaWiFS aerosol data, Proceedings of the MERIS User Workshop, ESA SP (549), pp. 233-241. MERIS User Workshop, 10-13 Novembre 2003, Frascatti, Italie.

ACTI.15 Ramon D., Santer R., Dilligeard E., Jolivet D. and **Vidot J.**, MERIS land product validation, *Proceedings of the MERIS User Workshop*, ESA SP (549), pp. 57-66. MERIS User Workshop, 10-13, Novembre 2003, F rascatti, Italie.

ACTI.16 Santer R., **Vidot J.** and Ramon D., Meris level 2 products over land validation and potential improvements, Proceedings of the IEEE International Geoscience and Remote Sensing Symposium, Volume 3, pp. 1594-1596 IEEE International Geoscience and Remote Sensing Symposium, 21 -25 juillet 2003, Toulouse, France. ‘

ACTI.17 Ramon D., Santer R. and **Vidot J.**, MERIS level 2 products over land : present status and potential improvements, *Proceedings of SPIE, Optical Remote Sensing of the Atmosphere and Clouds III*. Editor(s) : Hung-Lung Huang, Daren Lu, Yasuhiro Sasano, Vol. 4891, pp. 524-534. SPIE Remote Sensing, 2002, Hangzhou, Chine.

ACTI.18 **Vidot J.**, Borde R. and Santer R., Aerosol remote sensing over land : Comparison of two methods, *Proceedings of SPIE, Optical Remote Sensing of the Atmosphere and Clouds III*. Editor(s) : Hung-Lung Huang, Daren Lu, Yasuhiro Sasano. Vol. 4891, pp. 535-545. SPIE Remote Sensing, 2002, Hangzhou, Chine.

ACTI.19 **Vidot J.** and Santer, R., Atmospheric correction for inland waters. Application to SeaWiFS and MERIS, *Proceedings of SPIE, Ocean Remote Sensing and Applications*. Editor(s) : Robert J. Frouin, Yeli Yuan, Hiroshi Kawamura, Vol. 4892, pp. 536-545. SPIE Remote Sensing, 2002, Hangzhou, Chine.

ACTI.20 Martiny N., Santer R. and **Vidot J.**, Validation of the SeaWiFS atmospheric correction over coastal Waters, *Ocean Optics XVI*, Proceedings on CD-rom. Ocean Optics XVI, 18 - 22 Novembre 2002, Santa Fe, USA.

ACTI.21 **Vidot J.**, Santer R., Dilligeard E. and Ramon D., Atmospheric correction for coastal and inland Waters in the SISCAL project. Application to the SeaWiFS and MERIS sensors, *Ocean Optics XVI*, Proceedings on CD-rom. Ocean Optics XVI, 18 - 22 Novembre 2002, Santa Fe, USA.

1.3.8 Communications orales sans actes dans un congrès international ou national (COM)

COM.1 **Vidot J.** and Brunel P., Validation of RTTOV ice cloud and aerosol IR parameterization using the A-Train, EarthCare-EECLAT joint meeting, 29 janvier - 1er février 2018, Colmar, France.

COM.2 **Vidot J.**, E. Borbas, J. Hocking and P. Brunel, The VIS/NIR BRDF atlas for RTTOV : From MODIS C5 to C6, First International Surface Working Group (ISWG), 19-20 July 2017, Monterey, USA.

COM.3 **Vidot J.** and Brunel P., Validation of RTTOV ice cloud and aerosol IR parameterization using the A-Train, Third A-Train Symposium 2017, 16 - 22 avril 2017, Pasadena, Californie, USA.

COM.4 **Vidot J.**, P. Brunel, A. Geer, J. Hocking, C. Lupu, M. Matricardi, P. Rayer, D. Rundle, P. Roquet, R. Saunders, RTTOV : A very fast RTM for satellite data assimilation and many applications, International Radiation Symposium 2016, 16 - 22 avril 2016, Auckland, Nouvelle-Zélande.

COM.5 **Vidot J.** et C.-Labonnote, High resolution IR cloudy radiances simulations : comparison between RTTOV-11.3 and VLIDORT, 20ième International TOVS Conference Study (ITSC), 28 octobre - 3 novembre 2015, Lake Geneva, Wisconsin, USA.

COM.6 **Vidot J.** et Borbas E. : Developpement d'un atlas global de réflectance bidirectiomielle hyperspectrale des surfaces terrestres dans le visible et le proche infrarouge pour RTTOV, Ateliers de Modélisation de l 'Atmosphère 2013, 21 - 25 janvier 2013, Toulouse, France.

COM.7 **Vidot J.** and Borbas E. : Developing a visible and near infrared land surface BRDF model for RTTOV, International Radiation Symposium 2012, 6-10 août 2012, Berlin, Allemagne.

COM.8 **Vidot J.** and Borbas E. : Developing a VIS and NIR surface réflectance model for RTTOV, Third Workshop on Remote Sensing and Modelling of Surface Properties, 18-20 octobre 2011, Pékin, Chine.

1.3.9 Communications par affiche dans un congrès international ou national (AFF)

AFF.1 **Vidot J.**, P. Brunel, J. Hocking, M. Matricardi, Saunders R., RTTOV for FORUM : what is needed ?, First Workshop on the FORUM mission, 23-25 octobre 2018, Florence, Italie.

AFF.2 **Vidot J.**, L-C. Labonnote, and P. Brunel, Hyperspectral IR cloudy radiances and jacobians simulations : comparison between RTTOV-12 and LIDORT, EUMETSAT 2017 Meteorological Satellite conference, 2-6 October 2017, Rome, Italy.

AFF.3 **Vidot J.** and P. Brunel, A new RTTOV 12 profile dataset for visible to infraredatmospheric transmittance, EUMETSAT 2017 Meteorological Satellite conference, 2-6 October 2017, Rome, Italy.

AFF.4 **Vidot J.**, S. DeSouza-Machado, M. Matricardi, A. Geer, J. Hocking and P. Brunel, Hyperspectral IR cloudy radiances simulations : Comparison between

RTTOV and SARTA, AGU Fall Meeting, 12-16 December 2016, San Francisco, USA.

AFF.5 **Vidot J.** and P. Brunel, Evaluation of the RTTOV v11 aerosol model in IR with MACC and CALIPSO, EUMETSAT 2016 Meteorological Satellite conference, 26-30 September 2016, Darmstadt, Germany.

AFF.6 **Vidot J.** and N. Maury, Study of the diurnal cycle of marine stratocumulus field off the coast of Southwest Africa with SEVIRI, International Cloud Working Group (ICWG) 2016, 17-20 May 2016, Lille, France.

AFF.7 **Vidot J.**, L-C. Labonnote, A. J. Baran, P. Brunel, A new ice cloud parameterization for infrared radiaitve transfer : Comparison of two scattering schemes, International Radiation Symposium 2016, 16 - 22 avril 2016, Auckland, Nouvelle-Zélande.

AFF.8 **Vidot J.**, P. Brunel, J. Hocking, M. Matricardi, D. Rundle, P. Roquet, R. Saunders , RTTOV for hyperspectral IR sounders : Status and future developments, 4ième conférence international IASI, 11-15 April 2016, Antibes, France.

AFF.9 **Vidot J.**, RTTOV : description scientifique, Atelier de transfert radiatif dans les atmosphères terrestres pour les observations Spatiales (TRATTORIA), 23-25 mars 2015, Lille, France.

AFF.10 **Vidot J.**, RTTOV : description technique, Atelier de transfert radiatif dans les atmosphères terrestres pour les observations Spatiales (TRATTORIA), 23-25 mars 2015, Lille, France.

AFF.11 **Vidot J.**, R. Armante, P. Brunel, J. Pernin and M. Ben Sassi A comparison between RTTOV-11 and 4A/OP-2012 using IASI observations in collocation with the LMD ARSA radiosoundings database, 2014 EUMETSAT Meteorological Satellite Conference, 22-26 septembre 2014, Genève, Suisse.

AFF.12 **Vidot J.**, Brunel P. and Baran A. : A new ice cloud optical properties database in RTTOV for IASI. 3ième Conférence Internationale IASI, 4-8 février 2013, Hyères, France.

AFF.13 **Vidot J.** and Borbas E. : Land surface VIS/NIR BRDF module for RTTOV-11 : Model and Validation against SEVIRI Land SAF Albedo product, 18th International TOVS Study Conference, 21-27 mars 2012, Toulouse, France.

AFF.14 **Vidot J.**, Guyot G., Jourdan O., Sourdeval O., Brunel P., Labonnote L. and Brogniez G., Evaluation of RTTOV ice cloud parameterization by comparison with infrared measurements from IIR/CALIPSO during the CIRCLE-2 Experiment, 2011 EUMETSAT Meteorological Satellite Conference, 5-9 septembre 2011, Oslo, Norvège.

AFF.15 **Vidot J.**, Jourdan O., Kokhanovsky A., Szczap F., Cornet C., Giraud V., and Rozanov V., Retrieval of tropospheric NO2 columns from satellite measurements in presence of cirms : a theoretical sensitivity study With SCIATRAN and prospect application for the A-Train, Session AS3.15, European Geosciences Union (EGU), General Assembly 2009, 19 - 24 avril 2009 Vienne, Autriche.

AFF.16 **Vidot J.**, Giraud V., Jourdan O., Szczap F., Bennartz R., and Dubuisson P., A Cirrus correction approach for tropospheric gas inversion with the help of the CIRCLE-2 experiment, Session AS3. 16, European Geosciences Union (EGU), General Assembly 2008, 13-18 avril 2008, Vienne, Autriche.

AFF.17 **Vidot J.**, Bennartz R., O'Dell C., Preusker R., and Heidinger A., CO2 retrieval over clouds : The OCO methodology applied to SCIAMACHY, Session AS1.20, European Geosciences Union (EGU), General Assembly 2008, 13-18 avril 2008, Vienne, Autriche.

AFF.18 **Vidot J.**, Santer R., and Ramon D., Particulate matter (PM) retrieval from SeaWiFS measurements, Session IV, 12th Conference on Atmospheric Radiation / 12th Conference on Cloud Physics, American Meteorological Society (AMS), 1 0-1 4 juillet 2006, Madison, USA.

1.3.10 Rapports de recherche (RR)

RR.1 **J. Vidot**, L. C-Labonnote, and R. Saunders : Extension of RTTOV to the FORUM spectral range, FORUMreq WP 3300 ESA report, 15 pages, 2019.

RR.2 **J. Vidot**, P. Roquet, P. Brunel, V. Guidard, E. Turner, and R. Saunders : Identification of RTTOV issue for priority instruments, C3S 311c Lot1 report no 1.4.1.1, 7 pages, 2019.

RR.3 **J. Vidot**, P. Roquet, P. Brunel, V. Guidard, E. Turner, and R. Saunders : Preliminary RTTOV update with respect to v12.2, C3S 311c Lot1 report no 1.4.1.0, 17 pages, 2019.

RR.4 Saunders, R., J. Hocking, D. Rundle, P. Rayer, S. Haveman, M. Matricardi, A. Geer, C. Lupu, P. Brunel, and **J. Vidot** : RTTOV-12 Science and Validation Report, 78 pages, 2017. Accessible sur le lien `https://nwpsaf.eu/site/download/documentation/rtm/docs_rttov12/rttov12_svr.pdf`.

RR.5 **Vidot J.** and Hocking : Note on RTTOV v12 unit conversions for gases, clouds and aerosols, 5 pages, 2017. Accessible sur le lien `https://nwpsaf.eu/site/download/documentation/rtm/docs_rttov12/rttov_gas_cloud_aerosol_units.pdf`.

RR.6 **Vidot J.** : Cloud and Aerosol Detection Software (CADS) Version 2.3 Aerosol Validation, NWP-SAF report no NWPSAF-MF-TV-001, 10 pages, 2017. Accessible sur le lien `https://nwpsaf.eu/publications/tech_reports/NWPSAF-MF-TV-001_CADS_aerosol_validation.pdf`.

RR.7 Saunders, R., J. Hocking, D. Rundle, P. Rayer, M. Matricardi, A. Geer, C. Lupu, P. Brunel, and **J. Vidot**, RTTOV-11 Science and Validation Report, 2013. Accessible sur le lien `https://www.nwpsaf.eu/site/download/documentation/rtm/docs_rttov11/rttov11_svr.pdf`.

RR.8 **Vidot J.** and J. Landgraf, CO retrieval from the Shortwave-Infared spectral range in presence of clouds, Technical Note of the TROPOspheric Monitoring Instrument (TROPOMI) project, SRON, 2010.

RR.9 **Vidot J.**, Santer R., Smolskaia I. and Martiny N., Validation of pixel classification and atmospheric correction for the SISCAL processor, report of the SISCAL project, 2004.

RR.10 **Vidot J.** and Santer R., Atmospheric Correction for TM, report of the SISCAL project, 2003.

RR.11 **Vidot J.**, Santer R., Puskaric E. and Martiny N., Algorithm Theoretical Basis Document of the SISCAL processor, report of the SISCAL project, 2002.

RR.12 **Vidot J.**, Santer R., Puskaric E. and Martiny N., SISCAL prototype technical validation document, report of the SISCAL project, 2002.

1.4 Animation et administration de la Recherche

— **Membre** du groupe consultatif d'experts scientifiques pour le CNES et Eumetsat sur IASI et IASI-Nouvelle Génération (IASI-NG) (IASI Sounding Science Working Group (ISSWG)) depuis 2013.

— **Membre** du comité scientifique des 4$^{\text{ième}}$ et 5$^{\text{ième}}$ conférences internationales IASI.

— **Membre** du comité de programme de l'atelier Transfert Radiatif dans les ATmosphères Terrestres pour les ObseRvations spatIAles (TRATTORIA) 2020.

— **Co-animateur** de la session spectroscopie et transfert radiatif de la 4$^{\text{ième}}$ conférence internationale IASI (11-15 avril 2016 à Antibes).

— **Co-animateur** et rapporteur du groupe de travail sur les modèles de raie et de bande de l'atelier TRATTORIA 2015 (23-25 mars 2015 à Lille).

— **Co-animateur** de la session sur la prévision du rayonnement solaire en surface des Ateliers de Modélisation de l'Atmosphère (AMA) 2018 (13-14 février 2018 à Toulouse).

— **Co-animateur** et rapporteur du groupe de travail sur les interactions avec la communauté scientifique à l'assemblée générale du CNRM (7-8 février 2019 à Toulouse).

— **Co-animateur** du groupe transverse (G3T) sur le rayonnement du CNRM.

— **Organisateur local** de l'atelier Expecting Earth-Care, Learning from A-Train (EECLAT) 2015 (19-21 janvier à Ploumanac'h)

— **Participant** à différents groupes de travail scientifique du Coordination Group for Meteorological Satellites (CGMS) : Radiative Transfer and Surface Properties Working Group (RTSPWG), International Surface Working Group (ISWG) et International Cloud Working Group (ICWG).

— **Evaluateur** d'un projet du Programme National de Télédétection Spatiale (PNTS) en 2019.

1.5 Participation à des jurys et à des instances ou comités en lien avec l'enseignement

— En 2015-2016 : Participation au comité de thèse de Justin Rusalem. Thèse dirigée par le Pr. Hervé Herbin du LOA. Thèse suspendue en octobre 2016.

— 2016-2019 : Participation au comité de thèse et au jury de thèse d'Imane Farouk. Thèse dirigée par Nadia Fourrié et Vincent Guidard du CNRM. Thèse soutenue le 19 décembre 2018.

— Depuis 2019 : Participation au comité de thèse de Rémi Chalinel (thèse dirigée par Philippe Ricaud du CNRM) et de Yoann Tellier (thèse dirigée par Cyril Crevoisier du Laboratoire de Météorologie Dynamique (LMD)).

1.6 Enseignement et formation

— 2012-2017 : Introduction au transfert radiatif atmosphérique et à l'assimilation des observations satellites dans les modèles de PNT (3h00/an). Formation annuelle de l'École Nationale de la Météorologie (ENM) à Lannion.

— Depuis 2013 : Observation de l'atmosphère par satellite (3h45/an). Cours de Master 2 de l'Université de Bretagne Occidentale (UBO)/ENSTA à Brest.

1.7 Projets nationaux et internationaux

— Projet international SAF for Numerical Weather Prediction (SAF-NWP) : Responsable pour la contribution de Météo-France depuis 2019. Le financement global de la Continuous Development and Operations Phase (CDOP)-3 entre 2017 et 2022 est de 920 k€. Financement Organisation européenne pour l'exploitation des satellites météorologiques (EUMETSAT).

— Projet international C3S "Satellite data rescue" : Responsable pour la contribution de Météo-France. Le financement global entre 2018 et 2021 est de 168 k€. Ffinancement du Centre Européen pour les Prévisions Météorologiques à Moyen Terme (CEPMMT)

— Projet national Terre solide, Océan, Surfaces Continentales, Atmosphère (TOSCA) IASI : Participant à la tâche sur la spectroscopie et le transfert radiatif pour intercomparer RTTOV avec Automatized Atmospheric Absorption Atlas (4A)/OP. Le financement annuel est d'environ 12 k€. Financement CNES.

— Projet national TOSCA EECLAT : Responsable d'une tâche de validation de RTTOV. Le financement annuel est d'environ 3.5 k€. Ffinancement CNES.

Chapitre 2

Contexte de mes travaux de recherche

Sommaire

2.1 Contexte général

La prévision du temps, la prévision de la qualité de l'air et les projections de l'évolution climatique du système Terre-Océans-Atmosphère sont devenues des préoccupations majeures de nos sociétés contemporaines, mais pas toujours des politiques publiques ou uniquement lorsque surviennent des catastrophes naturelles. Pourtant, les impacts socio-économiques et sanitaires sont tels qu'ils en font des sujets primordiaux de recherches scientifiques. À titre d'exemple en 2018, une étude commandée par le MTES a estimé les bénéfices socio-économiques annuels de Météo-France au minimum compris entre 1 et 2.5 milliards d'euros, soit entre 2.5 et 6 fois plus que le budget de l'établissement (de Brux et al., 2018).

Pour améliorer la compréhension et la prévision de notre environnement, les observations satellitaires sont devenues un élément clé du dispositif d'observation de la Terre et le site de Lannion peut se targuer d'avoir été un des composants fondateurs de ce dispositif. En effet le 24 décembre 1963, la réception de la première image satellite en Europe fut réalisée par le CMS de Météo-France à Lannion. Depuis cette date, le CMS a acquis une reconnaissance nationale et internationale dans l'acquisition, le traitement et l'archivage des données satellitaires à vocation météorologique au travers notamment du Service d'Archivage et de Traitement Météorologique des Observations Satellitaires (SATMOS) dès 1983 et qui fait partie maintenant du pôle de données et de services pour l'atmosphère AERIS. Pour cela, le CMS s'est toujours reposé sur l'expertise scientifique et technique de sa division Recherche et Développement qui s'est rattachée depuis le 1er janvier 2019 au CNRM, UMR 3589

du CNRS. Dès lors, un nouveau centre de recherche a émergé à Lannion sous le nom de Centre d'Études en Météorologie Satellitaire (CEMS). Ce centre est réparti en trois équipes : Océans, Nuages et Sondage. Les thématiques de recherche de ces trois équipes sont intimement liées à trois grands projets scientifiques européens pour lesquels ces équipes opèrent principalement depuis une quinzaine d'années. Ces trois projets appelés Satellite Application Facilities (SAF) font parties des huit SAF financés par EUMETSAT. Ces projets ont vocation à fédérer les compétences des services météorologiques européens pour faciliter l'exploitation opérationnelle des observations des satellites météorologiques.

Il est important de noter ici que dans le domaine de la météorologie satellitaire, les programme spatiaux sont prévus sur de longues périodes avec souvent plusieurs séries de satellites de même génération. Par exemple on peut citer la série des MSG dont le premier satellite a été lancé en 2002 et le quatrième et dernier en 2015 ou la série des MetOp, avec le premier en 2006 et le troisième et dernier en 2018, le premier étant toujours opérationnel. Ainsi une stabilité et une continuité de service sont assurées pour les applications opérationnelles météorologiques. Cette continuité de service sera encore assurée jusqu'à l'horizon 2040 avec les nouveaux programmes MTG, EUMETSAT Polar System - Seconde Génération (EPS-SG) et Sentinel/Copernicus (voir Figure 2.1).

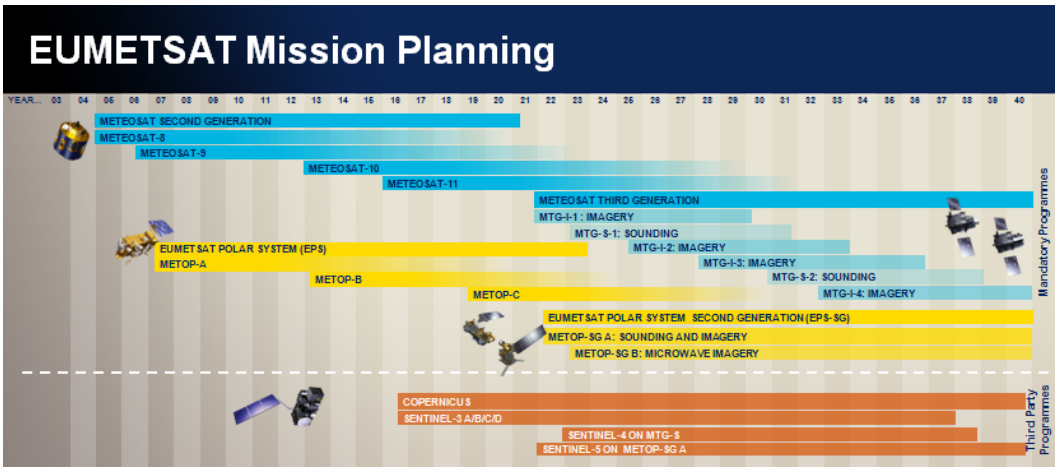

FIGURE 2.1 – Planning des programmes spatiaux d'EUMETSAT de 2006 à 2040.

Dans la même optique de continuité opérationnelle, les projets SAF sont aussi prévus sur de longues périodes. Nous sommes actuellement dans la 3$^{\text{ième}}$ phase de développement et d'exploitation opérationnelles (CDOP-3) des SAF couvrant la période 2017-2022. Le financement des CDOP-4 et CDOP-5 étant assuré jusqu'en 2032, cette stabilité et longévité des projets SAF assurent un haut niveau de garantie des perspectives scientifiques du CEMS. L'objectif prioritaire du projet SAF-NWP dans lequel je travaille principalement est de fournir aux services nationaux de prévisions météorologiques des outils numériques dédiés à l'assimilation des observations satellitaires dans leurs modèles de PNT. Parmi ces outils, le modèle de transfert radiatif

rapide RTTOV est un élément indispensable à l'assimilation et à l'interprétation des observations satellitaires (Saunders et al., 2018). Il est le fruit d'une collaboration entre le service météorologique du Royaume-Uni (UK Met-Office), le CEPMMT, le service météorologique de l'Allemagne (DWD) et Météo-France. L'application principale de RTTOV est l'assimilation des observations satellites dans les modèles de PNT mais il est aussi de plus en plus utilisé par la communauté scientifique pour faire des inversions de paramètres géophysiques ou pour des études préparatoires de futures missions spatiales. Dans le vocabulaire météorologique, le modèle de transfert radiatif est aussi une composante essentielle de l'opérateur d'observations satellitaires. Ainsi, chaque source d'observations - satellitaires ou conventionnelles (par exemple depuis le sol, aéroportées, ou obtenues par radiosondage) - assimilées dans les modèles de PNT a son propre opérateur reliant les variables mesurées aux variables des modèles. Parmi tous ces opérateurs, l'opérateur d'observations satellitaires est le plus gourmand en temps de calcul. En effet, les instruments satellitaires ne mesurent pas directement les variables géophysiques pronostiquées par les modèles de PNT telles que la température, l'humidité ou les taux de précipitations mais ils mesurent un rayonnement au sommet de l'atmosphère intégré sur toute la colonne atmosphérique depuis la surface et dans la direction d'observation du satellite. L'intégration du rayonnement dans cette atmosphère se fait donc au travers du modèle de transfert radiatif par résolution de l'ETR de manière numérique.

Pour être utilisés en environnement opérationnel, les modèles de transfert radiatif de type RTTOV ont plusieurs contraintes qu'il est important de rappeler. Tout d'abord ils doivent être en mesure de simuler de façon suffisamment précise l'importante collection d'instruments passifs couvrant principalement les domaines spectraux infrarouge et micro-ondes dédiés à l'assimilation opérationnelle des luminances mesurées au sommet de l'atmosphère. En effet, les centres de prévisions météorologiques ont fait le choix depuis plusieurs années d'assimiler les luminances au sommet de l'atmosphère plutôt que des produits géophysiques inversés (Eyre et al., 1993). L'article récent de Eyre et al. (2019) retrace précisément les différents étapes et problématiques qui ont menés à ce changement important. Les luminances sont uniquement assimilées dans les domaines infrarouge et micro-ondes car ces domaines sont sensibles aux profils verticaux de température et d'humidité de l'atmosphère contrairement aux domaines visible et proche infrarouge qui ne sont sensibles qu'au contenu intégré en vapeur d'eau. En revanche, si l'assimilation des luminances infrarouges et micro-ondes observées en ciel clair a rapidement montré un impact positif sur les prévisions (McNally et al., 1999; Bauer et al., 2003), les observations en ciel nuageux et notamment dans le domaine infrarouge ne sont toujours pas véritablement exploitées (Errico et al., 2007; Geer et al., 2018). Plusieurs raisons peuvent l'expliquer, la première est le choix des observations et la caractérisation de leurs erreurs. La deuxième concerne le contrôle de la qualité des données et leurs sélections pour éviter les redondances. La deuxième concerne la modélisation du transfert radiatif pour ces observations qui est plus complexe en présence de nuages. Dans le domaine des micro-ondes, la méthode de résolution de l'ETR du modèle RTTOV est suffisamment précise pour simuler les luminances nuageuses avec des erreurs in-

férieures à 1 K (Bauer et al., 2006). Dans le domaine infrarouge, l'utilisation d'un modèle de nuage opaque à une couche permet d'assimiler les luminances nuageuses mais pour n'en retirer de l'information qu'au-dessus des nuages (McNally, 2009; Pangaud et al., 2009).

Ensuite ces modèles doivent être stables et rapides pour les besoins en assimilation de la quantité très importante d'observations issues de ces satellites et qui est en constante augmentation. La Figure 2.2 montre ainsi le cumul d'observations satellitaires assimilées mensuellement dans le modèle global de Météo-France Action de Recherche Petite Échelle Grande Échelle (ARPEGE) depuis 2002. Ce nombre a tout récemment dépassé le milliard d'observations en novembre 2019 avec l'arrivée du troisième sondeur hyperspectral infrarouge européen IASI sur Metop-C. Une majeure partie du nombre d'observations de ces cumuls mensuels sont des luminances infrarouges et micro-ondes. Il est à noter que les évolutions importantes de ce cumul peuvent être reliées soient à l'arrivée d'un nouvel instrument (comme en 2008 avec le premier IASI sur Metop-A et en 2013 avec le sondeur hyperspectral infrarouge américain Cross-track Infrared Sounder (CrIS) et le deuxième IASI sur Metop-B) ou soient à l'augmentation du nombre d'observations assimilées dans chaque point de grille par évolution du modèle de PNT (comme en 2010 avec l'augmentation des résolutions verticale et horizontale).

D'autre part les modèles de transfert radiatif rapide doivent à la fois simuler les luminances au sommet de l'atmosphère à partir de la meilleure connaissance de l'état de l'atmosphère et de la surface (ce qu'on appelle le modèle direct) mais aussi simuler la sensibilité du modèle direct à toute variation des paramètres d'entrée sous trois formes de modèles (tangent-linéaire, adjoint ou jacobien). Les trois modèles sont des éléments indispensables à l'assimilation variationnelle de type 3D-Var ou 4D-Var (Errico, 1997).

Enfin les entrées du modèle de transfert radiatif sont forcées par les variables des modèles de PNT qui, dans la plupart des cas, ne sont pas des variables optiques nécessaires à la résolution de l'ETR. Les relations entre variables d'entrée et propriétés optiques sont obtenues généralement par l'intermédiaire de paramétrisation linéaire. La linéarité facilite la dérivation et donc le calcul analytique des jacobiens sans passer par la méthode des différences finies. La méthode des différences finies est souvent utilisée pour déduire les jacobiens lorsqu'on utilise des modèles de transfert radiatif non linéarisés.

2.2 Contexte scientifique

La modélisation du transfert radiatif dans l'atmosphère est une thématique scientifique qui couvre une multitude de champs d'applications particulièrement stimulantes dans le domaine spatial car elle concentre en elle plusieurs pans de recherche fondamentale : de la spectroscopie moléculaire aux méthodes numériques de résolution d'équations intégro-différentielles en passant par la modélisation des propriétés optiques des surfaces ou des particules atmosphériques solides (aérosols et nuages),

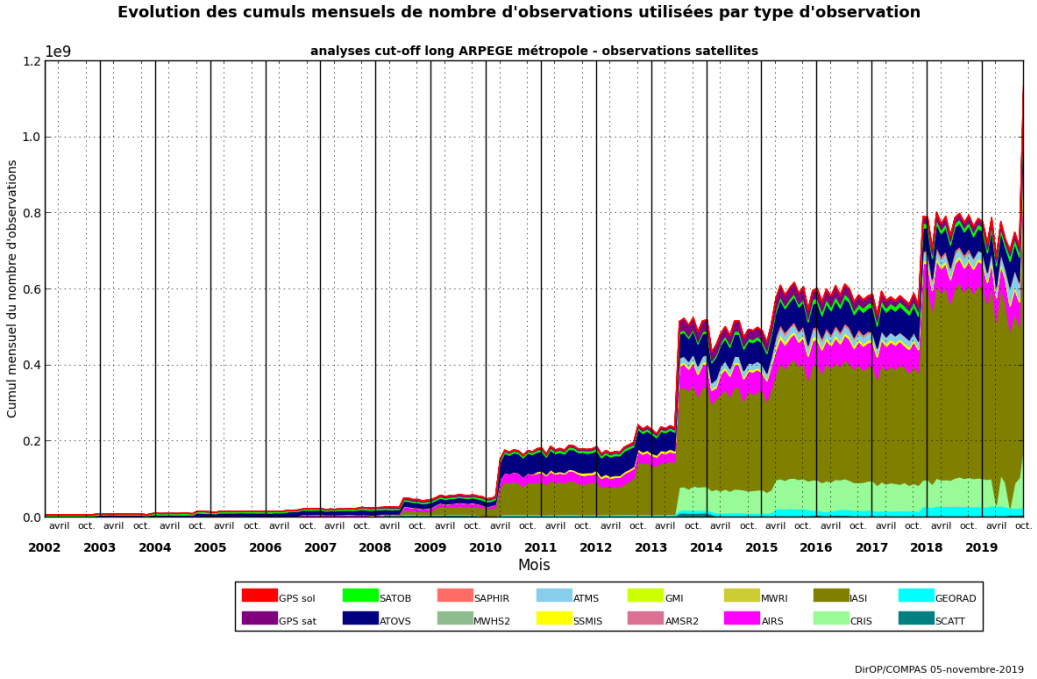

FIGURE 2.2 – Evolution des cumuls mensuels de nombre d'observations assimilées dans ARPEGE par instrument ou type de mesure. GPS sol et sat concernent les observations par radio-occultation. Les SATOB concernent les Atmospheric Motion Vector (AMV) issus des satellites géostationnaires et des satellites à orbites polaires. ATOVS concernent les radiances des instruments infrarouges High Resolution Infrared Radiation Sounder (HIRS) et micro-ondes Advanced Microwave Sounding Unit (AMSU) sur des satellites à orbites polaires. SAPHIR, Micro-Wave Humidity Sounder (MWHS)-2, Advanced Technology Microwave Sounder (ATMS), Special Sensor Microwave - Imager/Sounder (SSMIS) et GPM Microwave Imager (GMI) sont des instruments micro-ondes. Atmospheric InfraRed Sounder (AIRS), IASI et CrIS sont des instruments hyperspectraux infrarouges. GEORAD concernent les luminances mesurées par les satellites geostationnaires MSG, HIMAWARI et Geostationary Operational Environmental Satellite (GOES). SCATT sont les mesures des diffusiomètres des instruments Advanced Scatterometer (ASCAT). *NB : Plusieurs satellites et plusieurs instruments seront cités dans ce manuscrit et je fais le choix de ne pas mettre de publications scientifiques en référence de chacun d'eux. J'encourage le lecteur à aller sur le site Observing Systems Capability Analysis and Review Tool (OSCAR) de l'Organisation Météorologique Mondiale (OMM)* `https://www.wmo-sat.info/oscar/spacecapabilities` *pour y trouver une mine d'informations sur les satellites et instruments.*

particules toutes plus variées les unes que les autres. Ainsi il est impossible pour un chercheur de développer sa thématique de recherche sur tous ces aspects et dans mon cas il est plutôt de chercher à combiner les travaux fondamentaux pour en extraire

les informations pertinentes qui permettront le transfert vers des applications de météorologie opérationnelle, et ceci au travers du modèle RTTOV. Dans cette approche il est néanmoins important que certaines questions scientifiques soient considérées :

— Comment paramétrer au mieux les interactions rayonnement-particules et les propriétés optiques tout en gardant précision et efficacité ?

— Comment conserver une cohérence spectrale des propriétés optiques sur les différents domaines spectraux ?

— Comment valider ces paramétrisations de la manière la plus indépendante ?

2.2.1 Contexte National

A l'échelle française, la communauté scientifique de la modélisation du transfert radiatif pour les applications spatiales est relativement large avec des laboratoires reconnus dans leurs domaines de compétence. On peut citer notamment le LOA (domaine visible/infrarouge, aérosol/nuage, polarisation, effets 3D), le LMD (domaine proche infrarouge/infrarouge, spectroscopie), le Centre d'Études Spatiales de la BIOsphère (CESBIO) (visible, surface/vegétation), le LaMP (Nuages, effets 3D, instruments actifs), l'Office National d'Études et de Recherches Aérospatiales (ONERA) (visible à infrarouge, visée horizontale), le Laboratoire ATmosphères, Milieux, Observations Spatiales (LATMOS) (visible/ micro-ondes, instrument actif), le Laboratoire Interuniversitaire des Systèmes Atmosphériques (LISA) (ultraviolet/infrarouge, spectroscopie), le Laboratoire d'Océanologie et de Géosciences (LOG) (couleur de l'eau, polarisation), etc.. Les modèles de transfert radiatif qui résultent des équipes de recherche de ces différents laboratoires sont très bien identifiés par la communauté française. Avec l'appui du CNES et de l'Institut National des Sciences de l'Univers (INSU), cette communauté se réunit occasionnellement au travers de l'atelier TRATTORIA afin de partager et échanger sur les nouveaux développements de chacun de ces modèles ou en faisant participer des chercheurs d'autres communautés. Les recommandations qui émergent de cet atelier ont vocation à orienter les soutiens financiers du CNES, notamment au travers des projets TOSCA. Les Tables 2.1 et 2.2 résument les caractéristiques des principaux modèles de transfert radiatif discutés lors de la table ronde sur les modèles de raies et de bandes dont j'ai été le rapporteur en 2015. Il y a deux grandes catégories de modèles :

— Les modèles raie-par-raie qui permettent de simuler les caractéristiques spectrales très fines de l'absorption moléculaire avec des résolutions spectrales inférieures à 0.01 cm^{-1} (voir Table 2.1).

— Les modèles multispectraux et/ou hyperspectraux qui permettent de simuler les caractéristiques spectrales plus larges des canaux des observations satellitaires (de 0.25 cm^{-1} à plusieurs cm^{-1}) (voir Table 2.2).

Chaque modèle a des spécificités (domaines spectraux couverts, jacobien, polarisation, flux, etc.) liées à ses applications que ce soit à vocation de recherche ou opérationnelle. Dans ce paysage, l'équipe Sondage du CEMS est reconnue pour ses

compétences en modélisation du transfert radiatif rapide pour des applications opérationnelles à partir d'instruments passifs du visible à l'infrarouge.

TABLE 2.1 – Liste non exhaustive des modèles de transfert radiatif raie-par-raie identifiés lors de l'atelier TRATTORIA de 2015.

Code	domaine	sorties	Lien
LBLRTM	VIS-IR	Transmittances, Radiances, jacobiens, flux	rtweb.aer.com/**lblrtm**.html
4AOP	VIS-IR	Transmittances, Radiances, Jacobiens	http://4aop.noveltis.com/
ARAHMIS	VIS-IR	Transmittances, Radiances, Jacobiens?	LOA, disponibilité à confirmer
LARA	IR	Transmittances, Radiances, Jacobiens	
MOMO	VIS-IR	Transmittances, Radiances	disponibilité à confirmer
AMSUTRAN	MO	Transmittances, Radiances	Code hyperfréquences ?
RFM	VIS-IR	Transmittances, Radiances, jacobiens, flux	http://eodg.atm.ox.ac.uk/RFM/
KOPRA	IR	Transmittances, Radiances, Jacobiens	http://www.imk-asf.kit.edu/english/312.php

2.2.2 Contexte Européen

A l'échelle européenne, la communauté du transfert radiatif est encore plus large et si nous nous limitons aux modèles rapides à vocation opérationnelle pour la météorologie, il faut bien reconnaître que le modèle RTTOV est unique et utilisé par tous les services météorologiques nationaux européens. Ce modèle réunit une communauté scientifique autour du projet SAF-NWP financé par EUMETSAT dans lequel l'équipe Sondage du CEMS contribue fortement depuis près d'une vingtaine d'années. Les objectifs principaux du projet SAF-NWP sont de développer et de mettre à disposition des outils pour faciliter l'assimilation des observations satellitaires dans les modèles de PNT. De ce fait deux axes principaux du projet se sont construits :

— Un sur les outils de pré-traitement des observations satellitaires, c'est à dire les outils qui permettent à partir de l'acquisition locale, de passer des niveaux bruts L0 transmises aux stations sols aux niveaux L1, c'est à dire des luminances étalonnées radiométriquement et géolocalisées (L1B) et apodisées (L1C, uniquement pour les sondeurs hyperspectraux basés sur des interféromètres à Transformée de Fourier). Dans ce cadre l'équipe Sondage du CEMS

TABLE 2.2 – Liste non exhaustive des modèles de transfert radiatif multi-spectraux et/ou hyperspectraux identifiés lors de l'atelier TRATTORIA de 2015

Code	domaine	Jac.	Pol.	Hyp.	Lien
6S/V6S	VIS		X		http://6s.ltdri.org/
ARTS	VIS-IR				http://www.sat.ltu.se/arts/
CRTM	VIS-MO	X		X	http://www.star.nesdis.noaa.gov/smcd/spb/CRTM/
DISORT	UV-IR			X	ftp://climate1.gsfc.nasa.gov/wiscombe/Multiple_Scatt/
RRTM	UV-IR			X	http://rtweb.aer.com/
MATISSE	VIS-IR			X	http://matisse.onera.fr/accueil
STREAMER	VIS-IR			X	http://stratus.ssec.wisc.edu/streamer/
LIBRADTRAN	UV-IR		X		http://www.libradtran.org/
OSS	IR-MO	X		X	http://rtweb.aer.com/oss_frame.html
RTTOV	IR-MO	X		X	https://nwpsaf.eu/deliverables/rtm/
LIDORT/ VLIDORT	UV-IR	X	X	X	http://www.rtslidort.com
MODTRAN	UV-IR			X	http://modtran5.com/
ARTDECO	UV-IR		X	X	LOA/ICARE

Jac. = Jacobiens ; Pol. = Polarisation ; Hyp. = hyperfréquence ?

est aussi reconnue pour ses travaux de détection et de classification nuageuse dans l'empreinte des sondeurs hyperspectraux infrarouges (IASI ou CrIS) à partir d'imageurs à résolutions spatiales plus fines et colocalisés (Advanced Very High Resolution Radiometer (AVHRR) ou Visible Infrared Imaging Radiometer Suite (VIIRS), respectivement), dont l'algorithme est connu sous le nom de Masque AVHRR pour les Inversions ATOVS (MAIA) (Lavanant et al., 2011).

— Un sur l'outil de modélisation du transfert radiatif rapide pour simuler et assimiler les observations satellitaires dans les modèles de PNT, à savoir RTTOV.

2.2.3 Contexte International

La météorologie satellitaire opérationnelle est évidemment un sujet mondial, plusieurs pays y participent et la coordination internationale est assurée par le CGMS. Le modèle RTTOV n'est pas unique et son plus proche concurrent est le

modèle Community Radiative Transfer Model (CRTM) (Weng et al., 2005) développé aux États-Unis. CRTM tout comme RTTOV s'appuient sur un long héritage scientifique commençant au milieu des années 1970 avec les travaux de McMillin and Fleming (1976) sur la paramétrisation de la transmittance atmosphérique. Nous reviendrons sur cette paramétrisation fondatrice des modèles de transfert radiatif rapides dans le chapitre suivant. Le modèle CRTM a réellement commencé à être maintenu en 2005 grâce aux équipes du Joint Center for Satellite Data Assimilation (JCSDA) et est actuellement opérationnel au National Centers for Environmental Prediction (NCEP). Les développeurs scientifiques de CRTM et RTTOV partagent des idées, des améliorations et des développements via le groupe de travail RTSPWG dont les rencontres ont lieu tous les 18 mois lors de la conférence International TOVS Study conference (ITSC) (voir la page internet `https://groups.ssec.wisc.edu/groups/itwg/rtsp`). Il est aussi intéressant de noter que la Chine souhaite se doter de son propre modèle de transfert radiatif rapide dans les années à venir. Une réunion dans ce sens a été organisée en avril 2019 à la China Meteorological Administration (CMA) avec les équipes CRTM et RTTOV. Une des principales recommandations qui a fait suite à cette réunion est la volonté de disposer d'un modèle de transfert radiatif de référence pour valider les modèles rapides. Le nom a déjà été trouvé International Reference Radiative Transfer Model (IRRTM) et un projet de coordination est en train de se mettre en place dans lequel je participerai.

2.3 Apport de mon parcours personnel

Le contexte scientifique de mes travaux de recherche actuels est assez éloigné du contexte dans lequel j'ai poursuivi mes activités de recherche entre le doctorat et mon arrivée à Météo-France. En revanche, les observations satellites ont toujours été au centre de mes travaux de recherche. Dans cette première partie de vie scientifique, c'est la restitution de propriétés optiques ou physiques de l'atmosphère, que ce soit pour les aérosols, les nuages ou les gaz atmosphériques que j'étudiais. Lorsqu'on restitue des propriétés optiques ou physiques à partir de mesures issues d'observations satellites, on est rapidement amené à comprendre la physique du rayonnement dans l'atmosphère et à utiliser des modèles de transfert radiatif. Les modèles de transfert radiatif m'ont toujours suivi dans mes travaux de recherche, que ce soit le modèle Successive Order of Scattering (SOS) (Deuzé et al., 1989) pour les corrections atmosphériques pendant ma thèse (Vidot et al., 2008), le modèle Successive Order of Interaction (SOI) (Heidinger et al., 2006; ODell et al., 2006) pour la restitution du CO_2 au-dessus des nuages (Vidot et al., 2009) au cours de mon premier post-doctorat, le modèle SCIATRAN (Rozanov et al., 2014) pour la prise en compte des cirrus dans la restitution du N_2O (Vidot et al., 2010) sur le second post-doctorat ou le modèle LINTRAN (Schepers et al., 2014) pour la restitution du CO au-dessus des nuages (Vidot et al., 2012) pour mon troisième post-doctorat. Ainsi, la perspective scientifique de travailler sur un nouveau modèle de transfert radiatif en arrivant à

Météo-France m'a paru très intéressante et valorisatrice des compétences acquises auparavant. J'ai par la suite découvert non seulement un modèle de transfert radiatif, mais toute une équipe provenant de différents services météorologiques européens et organisée autour d'un projet qui fait de ce modèle une référence internationale pour la météorologie opérationnelle.

2.4 Positionnement de mes travaux

Pour décrire le positionnement des mes travaux dans le contexte de la météorologie satellitaire, je présenterai tout d'abord les bases théoriques de la modélisation du transfert radiatif rapide de RTTOV (Chapitre 3.2) et notamment les fondations de la rapidité du modèle RTTOV grâce à la paramétrisation de la transmittance atmosphérique et la paramétrisation de la diffusion en infrarouge. La description complète du modèle a fait l'objet d'un récent article de référence de toute l'équipe du projet RTTOV (Saunders et al., 2018). Je présenterai ensuite mes principales contributions au modèle RTTOV (Chapitre 3.3) en commençant par le modèle de réflectance des surfaces terrestres (Vidot and Borbas, 2014) puis la nouvelle paramétrisation des propriétés optiques des cristaux de glace (Vidot et al., 2015). Je présenterai aussi les travaux d'intercomparaison de modèles de transfert radiatif (Chapitre 3.4) et notamment le premier exercice international d'intercomparaison de modèles de transfert radiatif nuageux dans l'infrarouge (Aumann et al., 2018). Pour finir la synthèse de mes travaux, je présenterai les travaux que j'ai réalisés en parallèle de RTTOV (Chapitre 3.5) dans le cadre d'un co-encadrement de thèse sur l'utilisation de produits nuageux issus des satellites géostationnaires pour étudier l'évolution temporelle des systèmes nuageux fortement précipitants (Patou et al., 2018). Pour finir, je présenterai mon projet de recherche (Chapitre 4) qui s'orientera principalement vers les nouveaux instruments arrivant avec les nouvelles générations de satellites météorologiques et je conclurai ce manuscrit.

Chapitre 3

Synthèse

Sommaire

3.1 Une brève histoire de RTTOV

Pour commencer il est amusant de noter que dans le nom RTTOV se cache l'histoire de la météorologie satellitaire puisqu'il contient le nom du satellite TIROS Operational Vertical Sounder (TOVS) qui lui même contient le nom du satellite Télévision InfraRed Observation Satellite (TIROS), dont le premier TIROS-1 a été lancé le 1er avril 1960 et est considéré comme le premier satellite météorologique opérationnel (Wexler and Fritz, 1960). La génération des satellites TIROS est longtemps restée l'unique source d'observations globales de l'atmosphère et a opérée pendant plusieurs décennies (Manna, 1985).

Au début des années 1990, lorsque l'assimilation des luminances observées au sommet de l'atmosphère par l'instrument TOVS a commencé à être opérationnel dans le modèles de PNT du CEPMMT, la modélisation précise et rapide du transfert

radiatif est devenue primordiale en Europe. A cette époque, John Eyre (UK Met-Office) est revenu de l'Université du Wisconsin aux USA avec la première version d'un modèle rapide qui ne s'appelait pas encore à l'époque RTTOV. Cette version permettait de simuler les luminances en ciel clair observées dans l'infrarouge avec l'instrument HIRS et dans les micro-ondes avec l'instrument Microwave Sounding Unit (MSU) (Eyre, 1991). Quelques années plus tard, les premières versions de RTTOV ont été développés à la fois au UK Met-Office, à CEPMMT et à Météo-France. Et c'est en 1999, que trois versions de RTTOV ont été fusionnées pour n'en avoir plus qu'une de référence, la version 5 (Saunders et al., 1999). Les versions suivantes ont alors été développées dans le cadre du SAF-NWP en collaboration entre les trois services météorologiques auquel s'est rajouté récemment le DWD. Le rythme actuel est d'une version majeure fournie à la communauté scientifique tous les trois ans avec des versions mineures tous les ans. La dernière version est la version 12.3 (Saunders et al., 2018). Cette version simule actuellement plus de 100 instruments passifs couvrant les domaines spectraux du visible aux micro-ondes en passant par le proche infrarouge, l'infrarouge et l'infrarouge lointain soit de 0.4 à 100 µm et de 20 à 200 GHz.

3.2 Description théorique du modèle RTTOV

3.2.1 Formulation générale de l'ETR et fonctions sources

Afin d'écrire la formulation générale de l'ETR utilisée par le modèle RTTOV, de nombreuses hypothèses doivent être retenues. Tout d'abord, l'atmosphère terrestre est considérée comme un empilement stratifié de plusieurs couches homogènes et planes-parallèles où l'équilibre thermodynamique local s'applique (c'est à dire que les variations temporelles et spatiales en température et pression sont négligées) et où les effets 3-D (c'est-à-dire le transport horizontal des photons) et la polarisation sont ignorés. Ainsi, le gradient de luminance monochromatique dL (en $\mathrm{W/(m^2 srcm^{-1})}$) le long d'un chemin optique dans une couche atmosphérique d'épaisseur dz (en m) dans la direction donnée par les coordonnées sphériques (θ, ϕ) est donné par :

$$\mu \frac{dL(\nu;\mu,\phi)}{dz} = -k_e(\nu)L(\nu;\mu,\phi) + k_e(\nu)J(\nu;\mu,\phi) \tag{3.1}$$

où $\mu = \cos(\theta)$, $k_e(\nu)$ (en $\mathrm{m^{-1}}$) est le coefficient spectral d'extinction de la couche atmosphérique, L est la luminance monochromatique incidente et J est la fonction source. Le premier terme de la partie droite de l'équation 3.1 est négatif par convention en raison d'une atténuation du rayonnement par extinction, alors que le second terme du côté droit de l'Équation 3.1 est positif en raison d'une augmentation du rayonnement introduite par la fonction source. La fonction source peut avoir deux composantes : l'émission et la diffusion.

La composante d'émission de la fonction source J est due à l'émission thermique du Soleil et de l'environnement terrestre. La luminance énergétique émise par un objet considéré comme un corps noir est donnée par la fonction de Planck notée B qui

dépend de la température et du nombre d'onde. La Figure 3.1 représente les courbes d'émissions normalisées (c'est-à-dire que les surfaces situées sous chaque courbe sont égales) d'un corps noir ayant trois températures différentes. La première courbe à gauche représente l'émission spectrale du Soleil à une température de 6000 K, les deux autres courbes à droite représentent l'émission spectrale typique de l'environnement terrestre à 300 K pour la surface terrestre et à 250 K pour l'atmosphère.

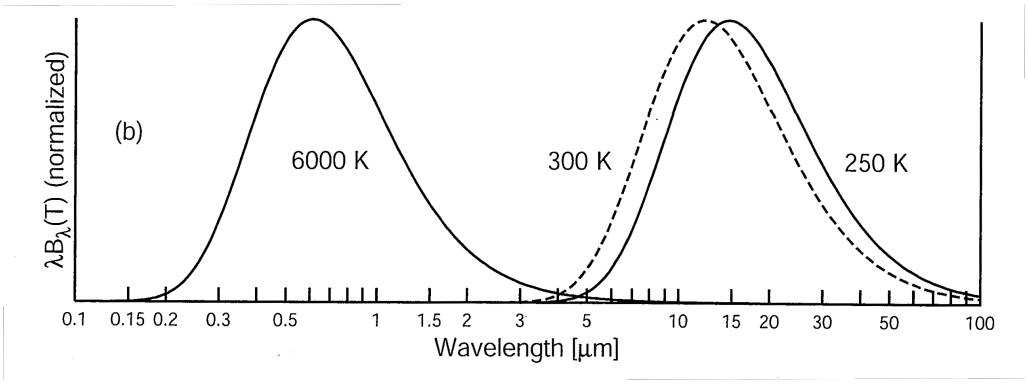

FIGURE 3.1 – Courbes normalisées d'émission spectrale de corps noirs à des températures typiques du Soleil, de la surface terrestre et de l'atmosphère (source : page 118 de Petty (2006)).

L'émission spectrale du Soleil a un maximum dans le domaine visible, tandis que les émissions spectrales de l'environnement terrestre ont des valeurs maximales dans le domaine infrarouge. La Figure 3.1 montre ainsi que pour la plupart des applications satellitaires, les fonctions sources d'émissions provenant du Soleil et de l'environnement terrestre peuvent-être traitées séparément. En revanche entre 4 et 5 µm, les deux fonctions sources se chevauchent.

La composante de diffusion de la fonction source J dépend aussi des domaines spectraux mais également de la taille des particules. Les différents régimes de diffusion sont données par le paramètre de taille x :

$$x = \frac{2\pi r}{\lambda} \tag{3.2}$$

où λ est la longueur d'onde (en m) et r la taille des particules (en m). La Figure 3.2 montre le régime de diffusion pour les différents types de particules atmosphériques et pour les différents domaines spectraux. Dans le domaine infrarouge, seule la diffusion par les molécules est négligeable tandis que dans le domaine des micro-ondes, la diffusion par les molécules et les aérosols l'est. Le traitement de la diffusion, qui peut-être résolu à l'aide des théories de Rayleigh, de Mie ou de l'optique géométrique, dépend du paramètre de taille.

3.2.2 L'équation de Schwarzschild

L'ETR dans les domaines infrarouge et micro-ondes par ciel clair (appelée équation de Schwarzschild) est obtenue en considérant une atmosphère homogène et

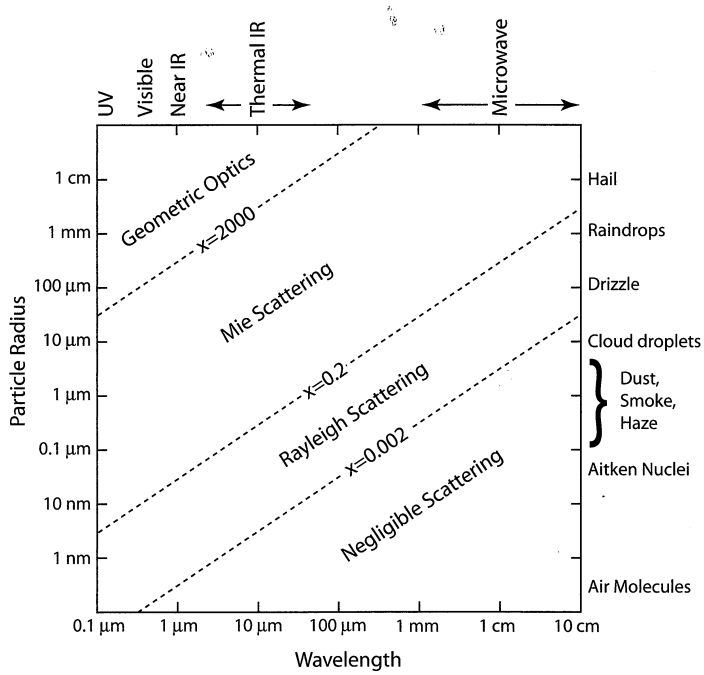

FIGURE 3.2 – Relation entre la taille des particules, la longueur d'onde du rayonnement et le comportement de diffusion des particules atmosphériques. Les lignes pointillées représentent les limites approximatives entre les régimes de diffusion en fonction du paramètre de taille (source : page 346 de Petty (2006)).

plane-parallèle sans diffusion et sans contribution solaire. Dans ce cas, l'extinction de chaque couche atmosphérique n'est représentée que par l'absorption et la fonction source J est donnée par la fonction de Planck. L'équation de Schwarzschild se déduit de l'Equation 3.1 comme :

$$\mu \frac{dL(\nu;\mu)}{dz} = -k_a(\nu)L(\nu;\mu) + k_a(\nu)B(\nu,T) \tag{3.3}$$

Où $k_a(\nu)$ est le coefficient spectral d'absorption (en m^{-1}) de la couche atmosphérique dz et $B(\nu,T)$ est la fonction de Planck de la couche atmosphérique de température T. Dans la suite du manuscrit, la dépendance spectrale sera souvent omise pour plus de clarté. L'indépendance en azimuth s'applique en raison de la caractéristique isotrope de l'émission. En considérant une surface réfléchissante spéculairement et en intégrant verticalement sur toute l'atmosphère, la luminance mesurée par un instrument infrarouge ou micro-ondes en ciel clair dans la direction d'observation μ est donnée par :

$$L(\mu) = t_{tot}(\mu)\varepsilon_{sfc}(\mu)B(T_{sfc}) + \int_{t_{tot}}^{1} B(T)dt + (1-\varepsilon_{sfc}(\mu))t_{tot}^2(\mu)\int_{t_{tot}}^{1}\frac{B(T)}{t^2}dt \tag{3.4}$$

Le premier terme de la partie droite de l'Equation 3.4 est dû à l'émission de la surface donnée par la fonction de Planck à la température de la surface T_{sfc} pondérée

par l'émissivité de la surface ε_{sfc} et atténuée par la transmittance atmosphérique totale t_{tot}. Le second terme de la partie droite de l'équation est dû aux émissions atmosphériques montantes de chaque couche atmosphérique de température T. Le troisième terme du côté droit de l'équation est dû aux émissions atmosphériques descendantes réfléchies par la surface et atténuées deux fois.

Pour simuler l'observation par satellite, il faut considérer que les canaux des instruments passifs sont polychromatiques et non monochromatiques. Ainsi idéalement il faudrait calculer l'Équation 3.4 à de nombreuses longueurs d'onde et intégrer les luminances spectrales résultantes sur la Fonction de réponse spectrale (SRF) de chaque canal des instruments. En pratique, nous intégrons les transmittances atmosphériques sur la SRF et résolvons l'ETR une fois par canal.

3.2.3 La transmittance atmosphérique

L'inconnue principale de l'Équation 3.4 est la transmittance atmosphérique t. La transmittance exprime l'atténuation par absorption moléculaire dans une couche atmosphérique. Dans la direction μ, elle est donnée par :

$$t(\mu) = \exp(-\tau_a/\mu) \tag{3.5}$$

où τ_a est l'épaisseur optique d'absorption (sans unités) de la couche atmosphérique donnée par l'intégration du coefficient d'absorption entre les altitudes p_1 et p_2, à savoir

$$\tau_a = \int_{p_1}^{p_2} k_a dp \tag{3.6}$$

Le coefficient d'absorption k_a s'écrit :

$$k_a(\nu) = \sum_{i=1}^{M} N_i \sigma_{a,i}(\nu) = \sum_{i=1}^{M} N_i [\sigma_{cont,i}(\nu) + \sum_{j=1}^{R_i} S_{ij} f_{ij}(\nu - \nu_{ij}, P, T)] \tag{3.7}$$

où N_i est la concentration en molécules atmosphériques i (en cm^{-3}), M est le nombre total d'espèces chimiques présentes dans la couche et $\sigma_{a,i}$ leurs sections efficaces d'absorption (en cm^2). La section efficace d'absorption a deux termes : un premier correspondant au continuum $\sigma_{cont,i}$ typique de certaines molécules (notamment la vapeur d'eau) et un deuxième correspondant aux raies d'absorption des molécules. Les raies d'absorption j de chaque molécule i sont données par S_{ij} qui est l'intensité de la raie d'absorption, f_{ij} qui est la forme de la raie d'absorption (simulée avec une certaine fonction comme Voigt dans le cas de RTTOV) centrée sur la position ν_{ij}. R_i est le nombre total de raies d'absorption de la molécule i. Les positions, intensités et paramètres de forme des raies d'absorptions sont fournies par des bases de données spectroscopiques comme HIgh-resolution TRANsmission molecular absorption database (HITRAN) (Gordon et al., 2017) ou Gestion et Étude des Informations Spectroscopiques Atmosphériques (GEISA) (Jacquinet-Husson et al.,

2016). Les continuums sont généralement modélisés ou paramétrés comme le modèle MlawerTobinCloughKneizysDavies (MT-CKD) (Mlawer et al., 2012) pour les molécules H_2O, O_2, N_2, O_3 et CO_2. Les transmittances atmosphériques sont calculées à l'aide de modèles raie-par-raie en supposant des profils atmosphériques de concentration pour chaque molécule considérée N_i.

3.2.4 Paramétrisation de la transmittance atmosphérique

Les calculs de transmittances atmosphériques des modèles raie-par-raie sont très précis mais doivent être réalisés à des intervalles spectraux très faibles pour reproduire les caractéristiques d'absorptions fines des molécules (généralement à $0.001\,\mathrm{cm}^{-1}$ pour les sondeurs hyperspectraux infrarouges). En contexte opérationnel, ces simulations sont beaucoup trop coûteuses en temps de calcul. Pour accélérer le calcul, McMillin and Fleming (1976) ont mis au point une méthode de paramétrisation de la transmittance atmosphérique. L'idée principale de ce modèle rapide est de réaliser un développement de Taylor de la formulation du rapport de transmittance entre 2 couches adjacentes (appelée transmittance effective). Le rapport de transmittance entre deux couches adjacentes s'écrit à partir de l'Équation 3.5 comme :

$$\ln \frac{t_l(\mu)}{t_{l-1}(\mu)} = \frac{\mu}{G} \Delta p_l \sum_{i=1}^{M} q_{l,i} \tag{3.8}$$

Où Δp_l est la différence de pression entre les niveaux l et $l-1$, q les rapports de mélange de chaque molécule i (en $\mathrm{kg\,kg}^{-1}$) et G l'accélération de la pesanteur. Eyre and Woolf (1988) proposent alors une expression pour l'Équation 3.8 sous la forme :

$$\ln \frac{t_l(\mu)}{t_{l-1}(\mu)} = \mu \sum_{m=1}^{K} c_{l,m} X_{l,m} \tag{3.9}$$

permettant ainsi de définir l'épaisseur optique d'absorption du sommet de l'atmosphère au niveau l par :

$$\tau_{a,l} = \tau_{a,l-1} + \sum_{m=1}^{K} c_{l,m} X_{l,m} \tag{3.10}$$

où c sont les coefficients, X les prédicteurs et K le nombre total de prédicteurs m. Les prédicteurs sont des fonctions de variables atmosphériques (pression, température, quantité d'absorbeur) et sécantes (cosinus inverse de l'angle zénithal). Les coefficients c sont précalculés à partir d'un ensemble de profils atmosphériques d'entrainement qui doivent représenter la variabilité naturelle de l'atmosphère terrestre. Deux approches pour les coordonnées verticales peuvent être utilisées, soit sur des niveaux de pression fixes (McMillin and Fleming, 1976), soit sur des niveaux de concentration d'absorbeur fixes (McMillin et al., 1979). Pour RTTOV, une méthode améliorée de niveaux de pression fixes est actuellement utilisée (Eyre, 1991; Saunders et al., 1999; Matricardi et al., 2004) avec un jeu de 83 profils du CEPMMT à

91 niveaux sélectionnés à partir des travaux de Chevallier et al. (2006) et interpolés à 101 niveaux. Les coefficients sont fournis à 101 niveaux avec des valeurs comprises entre 0.005 et 1100 hPa ou à 54 niveaux avec des valeurs comprises entre 0.01 et 1050 hPa (Hocking et al., 2017).

3.2.5 Sélection des prédicteurs

Le nombre de prédicteurs dépend de la molécule. Dans les modèles rapides, nous séparons les molécules atmosphériques en deux types d'absorbeurs. Certains d'entre eux sont considérés comme ayant des profils fixes dans l'atmosphère (par exemple les CFC, N_2, O_2, etc.) et d'autres sont considérés comme ayant des profils variables dans l'atmosphère (H_2O, O_3, CO_2, etc.). La Figure 3.3a montre les 83 profils de concentration en H_2O, qui comprend 80 profils (en gris) plus le profil moyen (en noir) et les deux profils enveloppes (en bleu). La Figure 3.3b montre les 83 profils d'O_3.

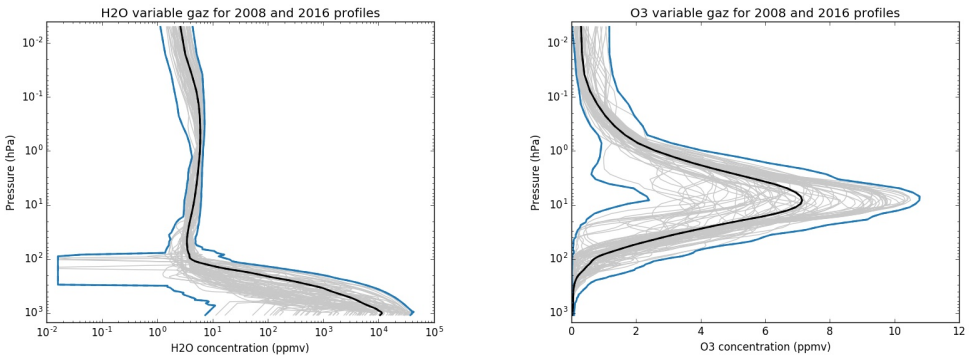

(a) Vapeur d'eau (b) Ozone

FIGURE 3.3 – Représentation verticale des 83 profils d'entraînement utilisés pour le calcul des coefficients RTTOV en vapeur d'eau (a) et ozone (b) en ppmv. Le profil tracé en noir représente le profil moyen et les profils tracés en bleu représentent les enveloppes minimales et maximales.

Les autres molécules considérées dans RTTOV ainsi que les profils sont présentées dans Saunders et al. (2017). La Figure 3.4 montre les transmittances sur toute l'atmosphère calculées avec le modèle Line-By-Line Radiative Transfer Model (LBLRTM) et pour le profil moyen des 83 profils d'entrainement pour tous les gaz confondues (C), pour la vapeur d'eau (B) et pour les autres principaux gaz absorbants (A). On voit nettement la prépondérance de la vapeur d'eau sur la transmittance totale mais aussi l'absorption par l'ozone entre 1000 et 1100 cm^{-1}.

Dans les premières versions de RTTOV, un nombre fixe de 10 prédicteurs étaient utilisés à la fois pour les gaz fixes et pour les gaz variables H_2O et O_3 (Eyre, 1991). De nos jours, il existe trois versions de prédicteurs :

— **Prédicteurs version 7** (Nommés ainsi parce qu'ils ont été implémentés dans la version 7 de RTTOV) : 10 prédicteurs sont utilisés pour les gaz fixes, 15

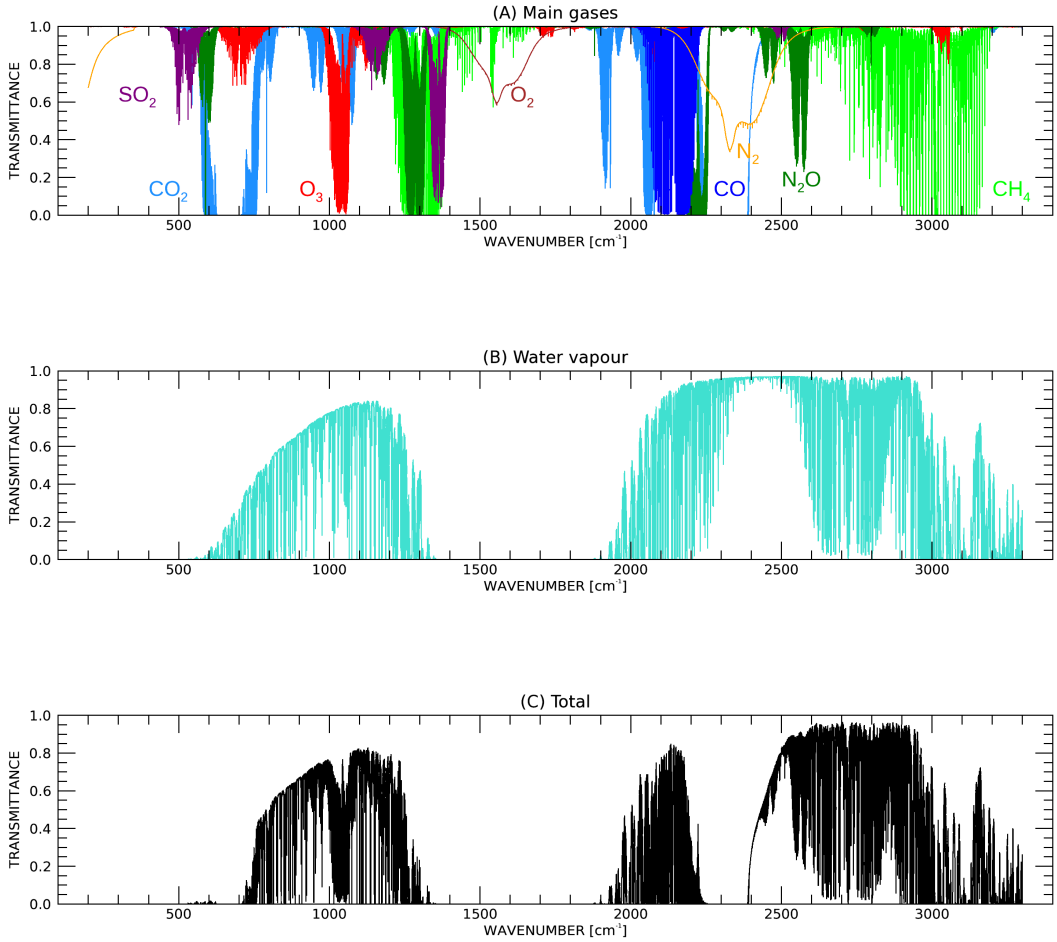

FIGURE 3.4 – (A) : Transmittance du sommet de l'atmosphère à la surface pour chacun des gaz les plus absorbants dans le domaine infrarouge calculé à partir du profil moyen des 83 profils d'entrainement et du modèle raie-par-raie LBLRTM. (B) Transmittance de la vapeur d'eau et (C) transmittance totale de tous les gaz combinés.

pour H_2O et 11 pour O_3 (Saunders et al., 1999). Ces prédicteurs sont les plus utilisés en environnement opérationnel car les espèces H_2O et O_3 sont les seules pronostiquées par les modèles de PNT.

— **Prédicteurs version 8** : Une séparation entre les raies d'absorption de H_2O (avec 12 prédicteurs) et le continuum de H_2O (avec 4 prédicteurs) a été introduite ainsi que l'ajout de CO_2 en tant que gaz variable avec 10 prédicteurs. Ces prédicteurs peuvent être utiles pour la validation des réanalyses sur plusieurs décennies avec des observations spatiales où l'augmentation de la concentration en CO_2 doit être prise en compte (Poli and Brunel, 2018). Ils sont aussi utilisés pour la même raison avec l'assimilation des luminances satellitaires dans la dernière réanalyse du CEPMMT ERA-5 avec RTTOV-11 (Hersbach and Dee, 2016).

— **Prédicteurs version 9** : Plusieurs molécules considérées comme variables ont été incluses (CH_4, CO, N_2O et plus récemment le SO_2) pour les sondeurs hyperspectraux et les prédicteurs ont été sélectionnés de manière optimale (Matricardi et al., 2004). Ces prédicteurs ne sont pas utilisés en opérationnel car les espèces chimiques ajoutées ne sont pas des variables pronostiquées par les modèles de PNT. En revanche ils sont utilisés pour des inversions de profils de gaz traces comme par exemple pour l'O_3 (Barret et al., 2011) ou le CO (De Wachter et al., 2012).

A titre de comparaison dans CRTM une sélection du nombre de prédicteurs est effectuée sur un ensemble de 18 prédicteurs (McMillin et al., 2006; Chen et al., 2010). Les épaisseurs optiques calculées à l'aide de l'Équation 3.10 sont ensuite converties en transmittance effective en combinant les gaz fixes et variables (McMillin et al., 1995). La transmittance totale est obtenue par exemple pour 2 gaz variables (H_2O et O_3) par :

$$t_l^{tot} = t_l^{fixes} \cdot \frac{t_l^{fixes+H_2O}}{t_l^{fixes}} \cdot \frac{t_l^{fixes+H_2O+O_3}}{t_l^{fixes+H_2O}} \tag{3.11}$$

Cette méthode de calcul de transmittances effectives montre ses limites lorsque l'on ajoute plusieurs gaz variables et McMillin et al. (2006) suggère une approche plus simple qui est en train d'être testée pour RTTOV. La validation de la paramétrisation des transmittances est réalisée pour chaque instrument en comparant les luminances raie-par-raie convoluées par les SRF de chaque canal d'un instrument aux luminances RTTOV. En infrarouge, les luminances sont souvent converties en températures de brillance (en K) en inversant la fonction de Planck. La Figure 3.5 montre les résultats de validation pour l'instrument IASI avec les prédicteurs version 7, 8 et 9 (tracés en bleu, rouge et vert, respectivement). Les biais moyens sont compris entre $\pm$ 0.2 K (en haut). L'intérêt d'avoir ajouté des molécules dans les prédicteurs version 9 est visible par une forte réduction des biais entre 1200 et 1400 cm^{-1} (régions à forte absorption du CH_4 et du N_2O) et entre 2000 et 2200 cm^{-1} (régions à forte absorption du CO). Les écarts en températures de brillance peuvent être comparés au bruit radiométrique de IASI qui est donné sous forme de Noise Equivalent Differential Temperature (NEDT) à 280 K. Pour cela, les valeurs d'écarts en températures de brillance sont transformées en NEDT à 280 K en suivant l'Équation (1) de Crevoisier et al. (2014). Le panneau du bas de la Figure 3.5 montre les écart-types de NEDT à 280 K des trois versions de prédicteurs ainsi que le bruit radiométrique de IASI tracé en noir. On peut voir que la précision de la paramétrisation des transmittances de RTTOV est inférieure au bruit radiométrique dans la plupart des canaux sauf en début de bande 2 vers 1200-1400 cm^{-1}.

3.2.6 l'ETR en ciel nuageux

La prise en compte des nuages dans le domaine infrarouge pour RTTOV est proposée selon deux méthodes distinctes, soit à partir de l'hypothèse d'un nuage à une couche considéré comme opaque (donc sans phénomène de diffusion dans le

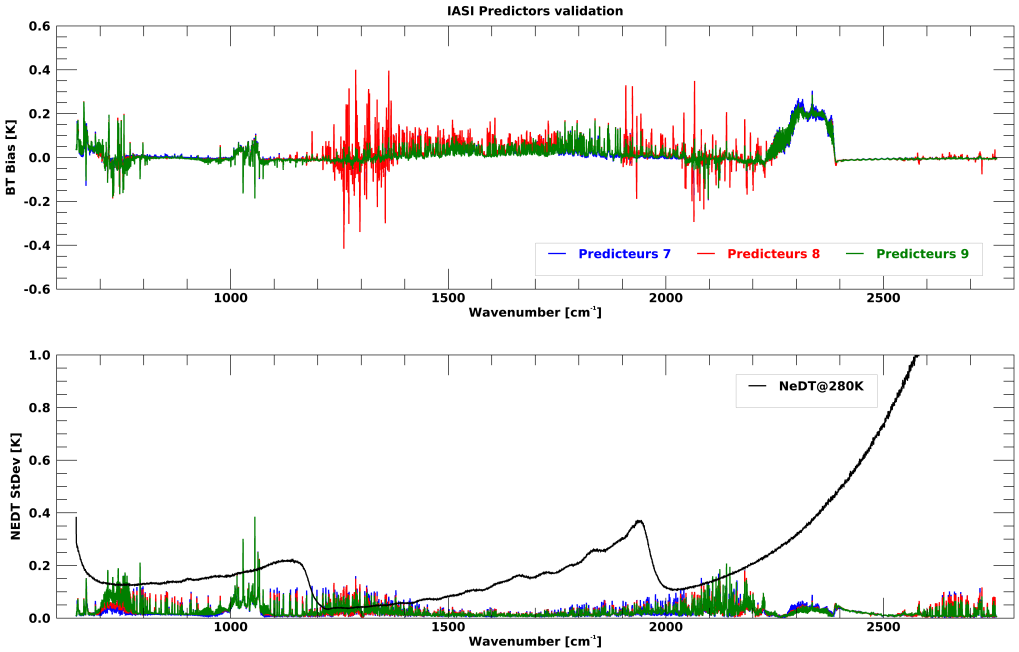

FIGURE 3.5 – Biais en température de brillance (haut) et écarts-types en NEDT à 280 K (bas) de validation des prédicteurs version 7 (en bleu), 8 (en rouge) et 9 (en vert) pour IASI sur 101 niveaux. Ces statistiques sont obtenues en comparant les simulations RTTOV à partir des 83 profils d'entraînement aux simulations raie-par-raie convoluées. Les écarts-types sont données en NEDT à 280 K pour être comparés au bruit instrumental de IASI représenté en trait noir.

nuage), soit à partir d'une paramétrisation de la diffusion dans toutes les couches nuageuses. Ces deux méthodes sont présentées ci-dessous.

3.2.6.1 L'approximation du nuage opaque

La plupart des services météorologiques qui assimilent les luminances infrarouges nuageuses avec RTTOV utilise l'approximation du nuage opaque (Eyre, 1991) qui n'implique aucune diffusion. Dans ce cas la modélisation du transfert radiatif reste très efficace pour simuler rapidement les observations. Le rayonnement simulé au sommet de l'atmosphère en présence de nuage s'écrit :

$$L(\mu) = (1 - N_e)L_{clair}(\mu) + N_e L_{nuage}(\mu) \tag{3.12}$$

où N_e est la fraction nuageuse effective (c'est à dire le produit entre la fraction nuageuse N et l'émissivité du nuage ε_{nuage}), $L_{clair}(\mu)$ est donnée par l'Équation 3.4 et $L_{nuage}(\mu)$ est la luminance nuageuse donnée par :

$$L_{nuage}(\mu) = t_{nuage}(\mu)B(T_{nuage}) + \int_{t_{nuage}}^{1} B(T)dt \tag{3.13}$$

où t_{nuage} est la transmittance du sommet de l'atmosphère au sommet de la couche nuageuse et T_{nuage} est la température au sommet du nuage. Pour simuler la radiance nuageuse il est donc nécessaire de connaître l'altitude du sommet de la couche nuageuse (ou la pression) et pour simuler la radiance totale il faut connaître la fraction nuageuse et l'émissivité du nuage. Les deux premières informations peuvent être déduites des observations en considérant que le nuage a une émissivité de 1. Plusieurs méthodes de restitution de ces informations existent : la méthode appelée "CO_2-slicing" (Chahine, 1974; Menzel et al., 1983) utilisée opérationnellement à Météo-France (Pangaud et al., 2009), la méthode Minimum Residual Method (MMR) (Eyre and Menzel, 1989) utilisée opérationnellement au CEPMMT (McNally, 2009) ou la méthode 1D-VAR (Pavelin et al., 2008) utilisée opérationnellement au UK Met-Office. Cependant, comme seules les scènes entièrement couvertes de nuages opaques sont assimilées (c'est-à-dire $N_e = 1$), cela réduit fortement le gain en nombre d'observations nuageuses assimilées (estimé entre 3 et 10 % suivant les méthodes). Il est à noter aussi que ces méthodes crées des ambiguïtés pour les nuages optiquement fins et les nuages multi-couches (Pavelin et al., 2008). Enfin, les nuages bas sont plus difficiles à détecter dans l'infrarouge en raison du faible contraste avec la température de surface.

3.2.6.2 La paramétrisation de la diffusion

Pour simuler tous les types de conditions nuageuses il est indispensable d'introduire la diffusion. La composante de diffusion dans la fonction source J de l'Équation 3.1 est donnée par :

$$J(\mu,\phi) = \frac{\omega_0}{4\pi}\int_0^{2\pi}\int_{-1}^{1} L(\mu',\phi')P(\mu,\phi;\mu',\phi')d\mu' d\phi' \tag{3.14}$$

où ω_0 est l'albédo de simple diffusion donné par le rapport entre le coefficient de diffusion sur le coefficient d'extinction (lui-même somme des coefficients d'absorption et de diffusion). La fonction de phase P donne la probabilité qu'un rayonnement arrivant de la direction (μ',ϕ') soit redirigé dans la direction (μ,ϕ). L'Équation 3.14 montre que la source de rayonnement due à la diffusion nécessite une intégration sur toutes les directions d'incidences possibles. La résolution de l'ETR dans ce cas est beaucoup plus complexe et devient beaucoup moins efficace en temps de calcul pour des applications opérationnelles. C'est ainsi qu'une paramétrisation de la diffusion dans l'infrarouge a été introduite dans la version 9 de RTTOV (Matricardi, 2005) en utilisant la méthode appelée "Chou-scaling" (Chou et al., 1999). Cette méthode est basée sur l'hypothèse que dans l'infrarouge la diffusion dans un hémisphère est isotrope et peut-être donc représentée par la fonction de Planck. Cette hypothèse est très efficace en temps de calcul puisqu'elle permet de faire une simulation de type ciel-clair tout en modifiant les épaisseurs optiques des couches atmosphériques qui contiennent des particules diffusantes. L'épaisseur optique effective d'une couche contenant ces particules diffusantes est alors écrite :

$$\tau_{eff} = \tau_a + b\tau_s \tag{3.15}$$

où τ_s est l'épaisseur optique de diffusion et b est la fraction de rétro-diffusion. La fraction de rétro-diffusion b est donnée par :

$$b = \frac{1}{2}\int_0^1 d\mu \int_{-1}^0 \overline{P(\mu,\mu')}d\mu' \tag{3.16}$$

où $\overline{P(\mu,\mu')}$ est la fonction de phase moyennée en azimuth et μ et μ' sont les cosinus des angles entre les directions de propagation. La méthode de "Chou-scaling" a déjà été utilisée pour des études préparatoires en vue d'assimiler des radiances nuageuses infrarouges dans les modèles de PNT. Par exemple, l'étude de Martinet et al. (2014b) a proposé une sélection de 144 canaux IASI sensibles aux nuages dans le prolongement des 366 canaux actuellement utilisés en assimilation au CEPMMT (Collard, 2007). Des tests de faisabilité pour ajouter les variables des nuages au vecteur d'état d'un système d'assimilation ont été étudiés par Martinet et al. (2013) et l'analyse des différences entre des observations IASI tout ciel (c'est-à-dire comprenant des cas de ciel clair et des cas de ciel nuageux) et des simulations RTTOV ont été estimées comprises entre ± 10 K par Okamoto et al. (2014). Plus récemment, Geer et al. (2019) a montré le bénéfice d'une assimilation tout ciel sur 7 canaux vapeur d'eau de IASI par rapport à une assimilation en ciel clair uniquement.

3.2.6.3 La prise en compte du recouvrement nuageux

Dans les modèles de PNT, les variables nuageuses des nuages non précipitants sont données par les profils de Ice Water Content (IWC) et de Liquid Water Content (LWC) (en $\mathrm{kg\,kg^{-1}}$). A cela s'ajoute le profil de fraction nuageuse (sans unités) déduit des fractions liquide et glace dans chaque point de grille des modèles de PNT. La prise en compte du recouvrement nuageux provenant de ces profils de fraction nuageuse pour simuler la luminance au sommet de l'atmosphère n'est pas directe et plusieurs méthodes existent. Ces méthodes sont généralement fondées sur les schémas de rayonnement large bande que l'on retrouve dans les modèles de PNT (Morcrette and Jakob, 2000). Pour RTTOV, la méthode Maximum Random Overlap (MRO) a été intégrée par Matricardi (2005). Cette méthode se révèle cependant trop consommatrice en temps de calcul car le nombre de colonnes nuageuses estimées avec la méthode MRO est encore trop important en regard du nombre de couches nuageuses des profils d'entrées. Une méthode appelée Cloud fraction Maximum Simple Stream (CMSS), qui ne prend en compte que la couche ayant le maximum de fraction nuageuse a été testée par Geer et al. (2019) mais dans son étude cette méthode engendre des erreurs systématiques comprises entre 5 et 10 K alors qu'avec la méthode MRO, les simulations sont quasiment non biaisées.

3.3 Mes contributions scientifiques au modèle RTTOV

3.3.1 Un modèle de BRDF des surfaces terrestres dans les domaines visible à proche infrarouge

Un des principaux objectifs de la version 10 de RTTOV était de permettre aux utilisateurs de simuler des instruments observant dans les domaines du visible au proche infrarouge (typiquement entre 0.4 et 2.5 µm). Les observations spatiales dans ces domaines spectraux ne sont pas assimilées dans les modèles de PNT mais d'autres applications sont possibles comme par exemple la génération de seuils en ciel clair pour les méthodes d'inversions de propriétés nuageuses (Derrien and Gléau, 2005) ou les images satellites prévues (Blackmore et al., 2014). Un des freins essentiels à l'extension du modèle RTTOV au domaine solaire était la prise en compte de la diffusion. En effet, la méthode de "Chou-Scaling" n'est pas applicable au domaine solaire car la diffusion y est très anisotropique. Ainsi deux options de RTTOV sont proposées : une option pour simuler efficacement les cas de ciel clair et une option plus lente pour simuler les cas nuageux. En ciel nuageux, la méthode de résolution de l'ETR est basée sur les ordonnées discrètes (Stamnes et al., 1988). Cette version de RTTOV appelée RTTOV_DOM ne sera pas décrite dans ce manuscript mais les détails sont dans Hocking (2015). En ciel clair, la luminance dans le domaine solaire au sommet de l'atmosphère est donnée par :

$$L_{Sol}(\mu,\mu_S,\Delta\phi) = \int_{t_{tot}}^{1} J^{\uparrow}(\mu,\mu_S,\Delta\phi)dt + r_{sfc}(\mu,\mu_S,\Delta\phi)t_{tot}^2 \int_{t_{tot}}^{1} \frac{J^{\downarrow}(\mu,\mu_S,\Delta\phi)}{t^2}dt \tag{3.17}$$

où μ_S est le cosinus de l'angle zénithal solaire, μ est le cosinus de l'angle zénithal d'observation et $\Delta\Phi$ est la différence d'angles azimuthaux entre la direction d'observation et la direction du Soleil. $J^{\uparrow}$ et $J^{\downarrow}$ sont les fonctions sources montante et descendante respectivement (voir Équation (6) de Saunders et al. (2018)) et r est la réflectance de surface. Pour garder la même philosophie que dans les autres domaines spectraux de RTTOV, il fallait introduire un modèle fournissant la réflectance des surfaces continentales sur tout le domaine visible et proche infrarouge. Dans ces domaines, les variabilités naturelles spatiales, spectrales et temporelles des réflectances des surfaces terrestres sont très importantes compte-tenu du nombre important de types de surface (végétation, forêt, sol nu, désert, etc....). De plus ces réflectances dépendent aussi très fortement des géométries d'éclairement et d'observation. Les propriétés optiques des surfaces terrestres sont représentées par un modèle de BRDF (Schaepman-Strub et al., 2006).

Afin de représenter ces différentes variabilités, j'ai introduit un modèle de BRDF basé sur la méthode du modèle d'émissivité infrarouge des surfaces terrestres de RTTOV développé par Borbas and Ruston (2010). L'idée originale de cette méthode est de combiner observations satellitaires de l'instrument Moderate Resolution Imaging Spectroradiometer (MODIS) pour décrire les variabilités spatiales et temporelles des propriétés de surface avec des mesures in-situ à haute résolution spectrale pour représenter la dépendance spectrale de ces propriétés. La BRDF des surfaces ter-

restres est basée sur le modèle semi-empirique à trois noyaux développé pour les produits opérationnels et globaux de MODIS (Lucht et al., 2000). La BRDF est calculée comme :

$$r(\mu, \mu_S, \Delta\phi) = f_{iso} + f_{vol} K_{vol}(\mu, \mu_S, \Delta\phi) + f_{geo} K_{geo}(\mu, \mu_S, \Delta\phi) \tag{3.18}$$

Le premier paramètre f_{iso} est la contribution de diffusion isotropique des surfaces, c'est à dire représentant la partie lambertienne ou spéculaire de la réflectance. Le deuxième paramètre f_{vol} est la contribution volumétrique, c'est à dire celle prenant en compte la diffusion à l'intérieur du couvert végétal. Le troisième paramètre f_{geo} est la contribution des effets d'ombrages lorsque les angles sont différents du nadir. Les fonctions K_{vol} et K_{geo} sont données dans Lucht et al. (2000). Dans les produits opérationnels de la collection 5 de MODIS (Schaaf et al., 2002) il y a 7 canaux entre 0.4 et 2.5 µm. Pour obtenir la variabilité spectrale de la BRDF, les observations spatiales ont été couplées à des mesures sol de réflectance à très haute résolution spectrale. La base de données de l'United States Geological Survey (USGS) permet d'avoir ces spectres de différents types de surface à une résolution spectrale de 0.1 µm (voir Figure 3.6). Une décomposition en composantes principales a ensuite été réalisée sur cette base de données de 126 spectres en forçant les points d'ancrage aux longueurs d'onde centrales de MODIS. Ainsi la BRDF multispectrale obtenue à partir des observations MODIS est ensuite recomposée en BRDF hyperspectrale à l'aide de l'analyse en composantes principales. Finalement, la réflectance de surface de n'importe quel canal de n'importe quel instrument est interpolée sur cette BRDF hyperspectrale. Ce modèle a été intégré à version 10 de RTTOV en 2013 (Vidot and Borbas, 2014). Une comparaison aux produits du projet SAF-Land Surface Analysis (LSA) (voir le site internet `https://landsaf.ipma.pt/en/`) d'albédo de surface des canaux visible et proche infrarouge de SEVIRI a montré des différences inférieures à 3 % lorsque les géométries de visée ou solaire sont inférieures à 65°.

Pour illustrer l'utilité de ce modèle, les Figures 3.7(a) et 3.7(c) représentent deux images en niveau de gris de réflectance à 0.6 et 0.8 µm observées par le satellite géostationnaire SEVIRI à bord de MSG le 23 avril 2010 à 10 :00 UTC. Les Figures 3.7(b) et 3.7(d) représentent les réflectances en niveau de gris simulées par RTTOV à partir de champs du modèle global de PNT du UK Met-Office à T0+10h. Visuellement, les différences de réflectances observées et simulées en ciel clair au-dessus des surfaces terrestres sur l'Afrique sont très faibles. Ceci est en partie expliqué par la proximité des canaux MODIS et des canaux SEVIRI. Il serait intéressant de simuler des images satellites prévues pour des instruments ayant des canaux éloignés de ceux de MODIS, par exemple dans les canaux à 1.38 ou à 2.25 µm. On peut noter aussi que les différences en ciel nuageux sont plus flagrantes. Les simulations RTTOV en ciel nuageux ont été réalisées avec l'option RTTOV_DOM. On peut remarquer que les systèmes nuageux très brillants sont assez bien reproduits par RTTOV même si dans certains cas (comme au-dessus de l'Afrique Centrale), les simulations ne montrent pas de systèmes nuageux car le modèle de PNT ne prévoit pas de profils nuageux dans cette zone. On voit aussi que les nuages fractionnées ne sont pas suffisamment présents dans les simulations sans doute pour la même raison. Ce type de

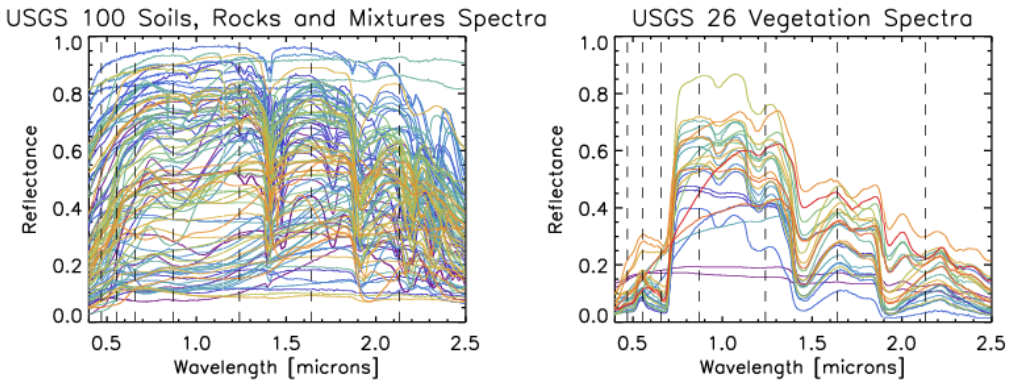

FIGURE 3.6 – Spectres de réflectance mesurés en laboratoire ou *in situ* pour 100 types de sols (à gauche) et pour 26 types de végétation (à droite) sélectionnés pour l'analyse en composante principale à partir de la base de données de l'USGS. Les lignes verticales en pointillés représentent les longueurs d'ondes centrales des canaux MODIS.

simulation est maintenant produit opérationnellement par le UK Met-Office pour fournir aux prévisionnistes des images prévues de couverture nuageuse (Blackmore et al., 2014). Ces informations peuvent être particulièrement intéressantes pour la prévision des nuages bas comme les brouillards qui sont plus difficiles à observer dans l'infrarouge. Récemment, mon modèle de BRDF a été utilisé dans le cadre d'une Observing System Simulation Experiments (OSSE) pour montrer l'apport de l'assimilation d'épaisseurs optiques des aérosols issues du canal à 444 nm sur le futur imageur Flexible Combined Imager (FCI) de MTG pour la prévision des PM_{10} (Descheemaecker et al., 2019).

Dans la version 12 de RTTOV, une extension du modèle de BRDF aux surfaces enneigées a été développée. N'ayant quasiment pas de spectres laboratoires dans les bases de données de l'USGS, j'ai entrepris une collaboration avec Marie Dumont du Centre d'Étude de la Neige (CEN) du CNRM pour qu'elle me fournisse des spectres d'albédo de neige théorique. Pour cela, Marie a utilisé le modèle de transfert radiatif DIScrete Ordinate Radiative Transfer (DISORT) (Stamnes et al., 1988) adapté au manteau neigeux pour simuler des albédos spectraux. Dans le domaine visible et proche infrarouge l'albédo spectral de la neige a de très belles signatures spectrales et la simulation de l'albédo spectral peut être réalisée à l'aide de deux paramètres : la Specific Surface Area (SSA) de la neige qui représente le rapport entre la surface et le volume des grains de neige et le Black Carbon Content (BCC) qui représente la concentration en poussières présentes dans le manteau neigeux (Carmagnola et al., 2013). La Figure 3.8 montre des simulations d'albédo de la neige à un angle solaire de 0°. On voit que les albédos spectraux sont très sensibles aux valeurs de SSA et de BCC mais surtout que les effets de l'un ou de l'autre n'agissent pas sur la même partie du spectre. Dans la partie proche infrarouge lorsque le SSA est grand la neige est formée de cristaux complexes (car la surface est plus grande comme

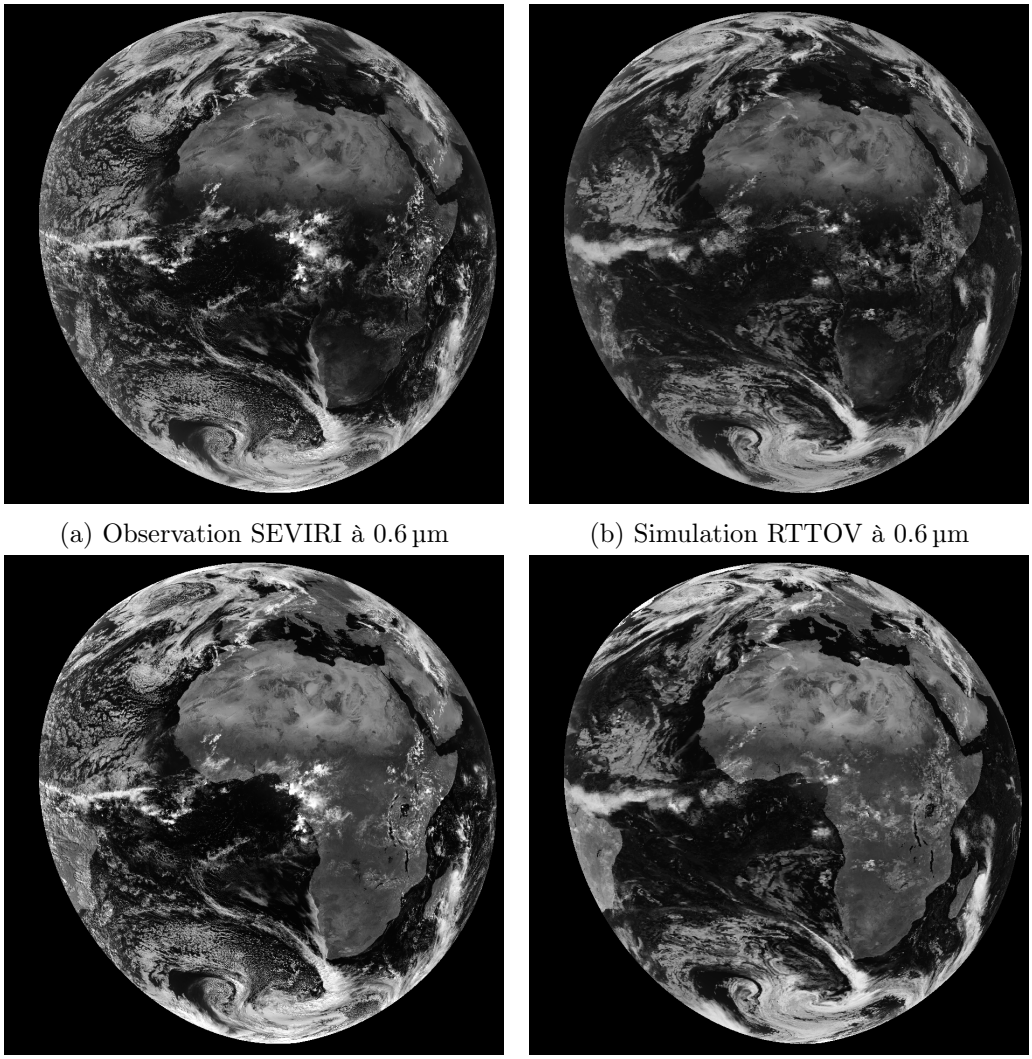

(a) Observation SEVIRI à 0.6 µm (b) Simulation RTTOV à 0.6 µm

(c) Observation SEVIRI à 0.8 µm (d) Simulation RTTOV à 0.8 µm

FIGURE 3.7 – Exemple de réflectances (en échelle de gris compris entre 0 et 0.9) observées au sommet de l'atmosphère par SEVIRI le 23 avril 2018 à 10h00 UTC dans le canal à 0.6 µm (a) et le canal à 0.8 µm (c) et respectivement simulées en (b) et (d) par RTTOV à l'aide des entrées du modèle global de PNT du Met-Office à T0+10h.

pour de la neige fraîche) avec un fort albédo et deux pics à 1.8 et 2.25 µm alors que lorsque le SSA est petit, les cristaux sont quasi sphériques comme pour de la neige fondue, avec pour effet de diminuer l'albédo. Dans le domaine visible, c'est la quantité de poussière qui modifie l'albédo. Plus la concentration en BCC augmente et plus l'albédo diminue. Il est donc important de faire varier ces deux paramètres pour avoir une base de données la plus représentative possible de la variabilité des albédos spectraux de la neige.

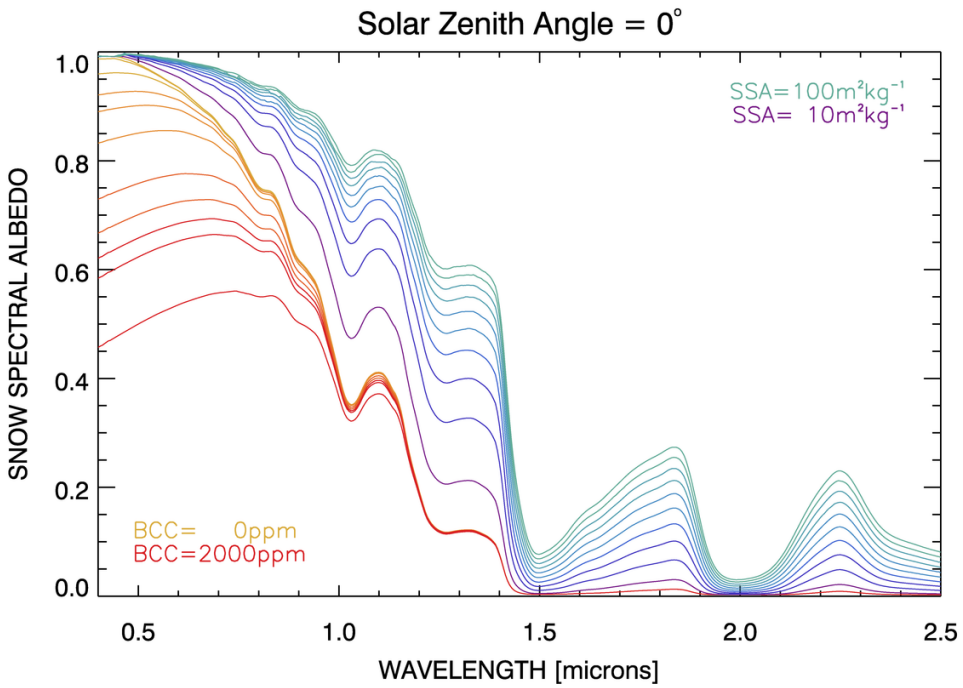

FIGURE 3.8 – Albedos spectraux de la neige entre 0.4 et 2.5 µm simulés pour un angle solaire de 0°. Les courbes bleues sont simulées avec différentes valeurs de SSA comprises entre 10 et 100 $m^2\,kg^{-1}$ et les courbes rouges avec différentes valeurs de contenu en carbone-suie comprises entre 0 et 2000 ppm.

La validation du modèle de BRDF de la neige ainsi que la comparaison entre deux collections (ou versions) des produits MODIS a été réalisée à l'aide de mesures *in situ* (Vidot et al., 2018). La Figure 3.9 montre le spectre d'albédo obtenu à partir de mesures *in-situ* (en bleu la moyenne des différents spectres mesurés sur le mois de juin 2011 et en noir les spectres à ± l'écart-type). Sur la Figure 3.9 sont aussi représentés les spectres d'albédo obtenus à partir de MODIS avec la collection 5 (en rouge) et la collection 6 (en vert). La Figure 3.9 (en bas) montre aussi le biais spectral entre les mesures *in situ* et le modèle de BRDF de RTTOV. Le modèle basé sur la collection 6 de MODIS est quasiment non biaisé par rapport aux mesures *in situ*. Cependant, cette version du modèle de BRDF n'a toujours pas été implémentée dans RTTOV par manque de temps.

3.3.2 Une nouvelle paramétrisation des propriétés optiques des cristaux de glace dans le domaine de l'infrarouge thermique

L'assimilation opérationnelle des luminances nuageuses infrarouges dans les modèles de PNT ne permet pas actuellement de prendre en compte les variables nuageuses des modèles. Les variables déduites par exemple avec la méthode du "CO_2-slicing", c'est à dire la fraction nuageuse effective et la pression au sommet de nuage

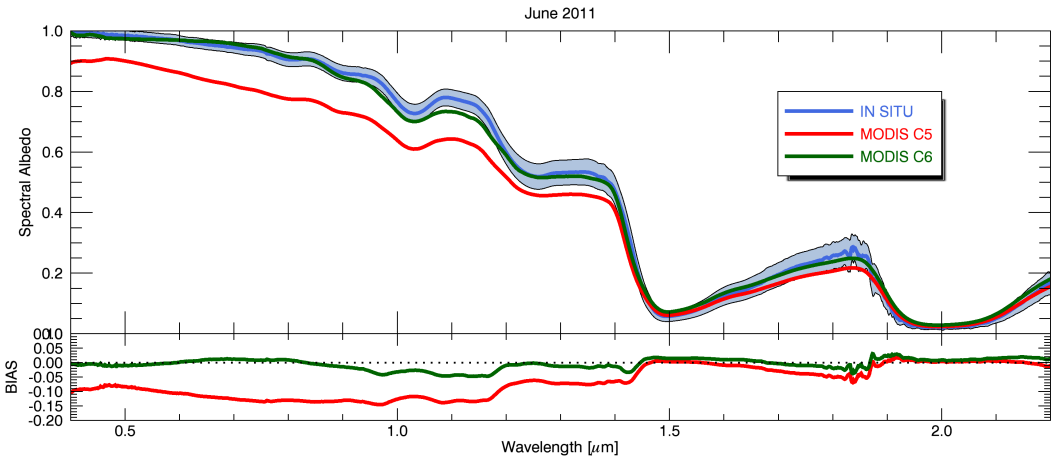

FIGURE 3.9 – En haut : Albédo spectral de la neige moyenné sur le mois de juin 2011 à partir de 11 spectres mesurés *in situ* (tracé en bleu avec ± l'écart-type tracé en noir). Albédos spectraux RTTOV obtenus à partir de la collection 5 (en rouge) et de la collection 6 (en vert) des produits MODIS. En bas : Biais d'albédos spectraux entre RTTOV et les mesures *in situ*.

sont considérées comme des variables "puit", c'est à dire n'ayant aucun effet sur le modèle de PNT mais permettent d'assimiler un peu plus d'observations et d'avoir de la sensibilité au-dessus des nuages. L'assimilation des radiances nuageuses infrarouges est pourtant un élément important d'amélioration de la PNT puisque les zones où la sensibilité de la prévision aux erreurs de l'état initial du modèle est importante correspondent souvent à des zones nuageuses (McNally, 2002; Fourrié and Rabier, 2004). Le CNRM poursuit des études dans cette direction depuis plusieurs années avec les travaux de thèse de François Faijan (Faijan et al., 2012), de Pauline Martinet (Martinet et al., 2013, 2014b) et plus récemment d'Imane Farouk (Farouk et al., 2019). Aussi, pour atteindre cet objectif ambitieux, il me semblait nécessaire au préalable de valider le modèle de transfert radiatif capable de simuler les radiances infrarouges à partir de paramétrisations des propriétés optiques des nuages en fonction des variables nuageuses des modèles de PNT (à savoir les profils de IWC, de LWC et de fraction nuageuse).

La version actuelle de RTTOV contient plusieurs modèles de propriétés optiques des nuages, et pour les domaines du visible à l'infrarouge, ces modèles sont séparés en deux catégories : nuages en phase liquide ou en phase glace. Pour les nuages en phase liquide, deux modèles de propriétés optiques des nuages sont proposés. Le premier est basé sur la base de données Optical Properties of Aerosols and Clouds (OPAC) (Hess et al., 1998). À partir de cette base de données de propriétés microphysiques (indice de réfraction spectral et distribution en taille), 5 types nuageux ont été sélectionnés par Matricardi (2005) (stratus continental ou maritime, cumulus continental (pristine ou pollué) ou maritime). Les coefficients d'absorption et de diffusion ont été précalculés à l'aide de la théorie de Mie et normalisés à une gouttelette par cm^{-3}.

Les fonctions de phase pour le calcul du coefficient de rétro-diffusion (Équation 3.16) ont été précalculées aussi. Pour obtenir les propriétés optiques totales dans chaque couche nuageuse, le profil d'IWC est alors simplement multiplié par les propriétés optiques normalisées. Dans la version 12 de RTTOV a été ajouté le deuxième modèle provenant de la base Libradtran (Emde et al., 2016) dont les propriétés optiques sont paramétrées en fonction du diamètre effectif des gouttelettes.

Pour les nuages de glace, les versions 9 à 11 de RTTOV disposaient de différentes paramétrisations selon la taille et la forme des cristaux (Matricardi, 2005). Les propriétés optiques avaient été précalculées pour deux formes (hexagonale ou agrégat) et étaient reliées au contenu en glace avec 4 paramétrisations du diamètre effectif en fonction du IWC et/ou de la température, soient Ou and Liou (1995) noté par la suite OL95, Wyser (1998) noté W98, Boudala et al. (2002) noté B02 et McFarquhar et al. (2003) noté MF03. Les comportements de ces paramétrisations sont représentés sur la Figure 3.10 où sont tracés les diamètres effectifs en fonction du IWC (en $\mathrm{g\,m^{-3}}$) et pour trois températures ($-25°$,$-35°$ et $-65°$). Les courbes de la paramétrisation OL95 (en vert) sont horizontales car cette paramétrisation ne dépend que de la température alors que la paramétrisation MF03 (en rouge) n'est représentée que par une seule courbe car elle ne dépend que du IWC. Les paramétrisations W98 (en violet) et B02 (en bleu) dépendent des deux. Il est à noter que si les 3 paramétrisations OL95, W98 et MF03 couvrent les mêmes gammes de diamètre effectif (entre 15 et 120 µm), la paramétrisation B02 donne le comportement de petits cristaux de glace (entre 15 et 40 µm).

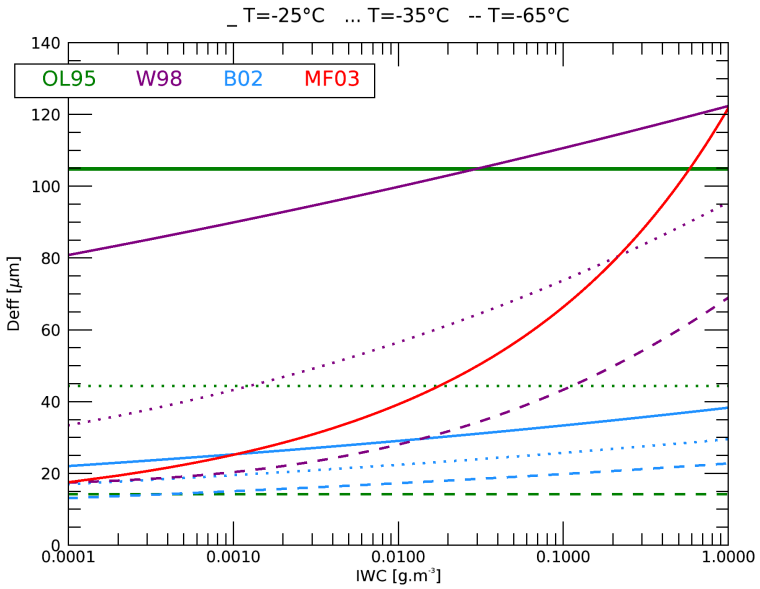

FIGURE 3.10 – Évolution du diamètre effectif des cristaux de glace (en µm) en fonction du contenu en glace (en $\mathrm{g\,m^{-3}}$) et pour trois températures (-25, -35 et $-65\,°\mathrm{C}$) provenant des 4 paramétrisations OL95, W98, B02 et MF03 de RTTOV.

J'ai voulu dans un premier temps évaluer ces 4 paramétrisations. Nous avons

alors commencé ce travail avec Gwennolé Guyot en 2011, étudiant en Master 2 de l'Université Blaise Pascal de Clermont-Ferrand et en collaboration avec Olivier Jourdan du LaMP. Cette étude préliminaire se basait sur des observations aéroportées des propriétés optiques de la glace lors de la campagne CIRCLE-2 avec des mesures *in situ* de concentrations en glace colocalisées avec le passage de CALIPSO et son radiomètre infrarouge Infrared Imager Radiometer (IIR). Cette étude a montré que la paramétrisation B02 (et ses petits cristaux) entraînait des simulations de température de brillance beaucoup trop froide par rapport aux observations de IIR de l'ordre de 10 K. Pour étendre cette étude localisée à une campagne de mesure, j'ai continué ce travail à l'échelle globale en 2014 avec Maximilien Patou, qui était alors étudiant en Master 1 à l'Université de Lille. Ce travail a permis tout d'abord de montrer qu'il y avait des erreurs systématiques de modélisation des propriétés optiques des cristaux de glace de forme agrégat avec une dépendance spectrale irréaliste entre 800 et 950 cm^{-1}, ce qui s'est traduit par une note dans le projet SAF-NWP pour recommander aux utilisateurs de ne pas utiliser cette forme de cristaux. Ensuite cette étude a permis de lancer les travaux qui ont débouché sur une nouvelle paramétrisation des cristaux de glace (Vidot et al., 2015) intégrée dans la version 11 de RTTOV.

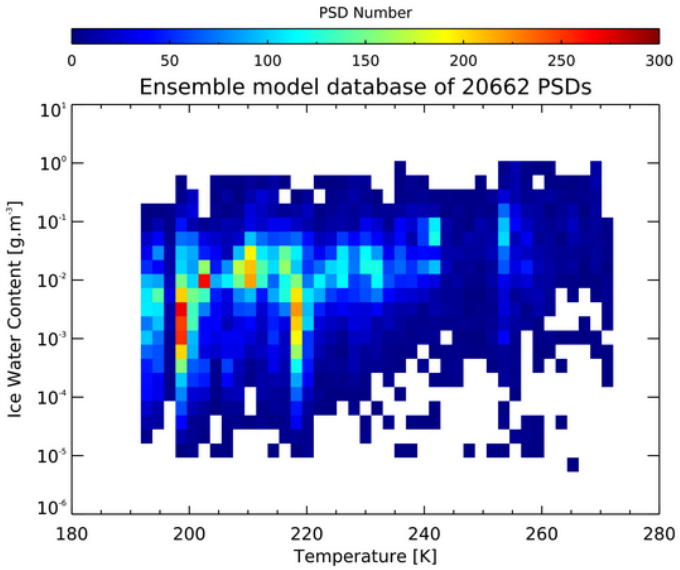

FIGURE 3.11 – Histogramme 2D du nombre de distribution en taille des cristaux de glace de la base de données du modèle d'ensemble en fonction de la température (en K) et du contenu en glace (en $\mathrm{g\,m}^{-3}$).

Contrairement aux anciennes paramétrisations, cette nouvelle paramétrisation fait l'hypothèse que les propriétés optiques des nuages de glace peuvent être déduites directement du contenu en glace et de la température, c'est à dire sans passer par le diamètre effectif. La paramétrisation s'appuie sur une large base de données

combinant mesures aéroportées et modélisation à partir d'une formulation générale de la distribution en taille des cristaux (Field et al., 2007) et d'un modèle d'ensemble de 6 formes de cristaux (hexagonale, bullet-rosette et 4 types d'agrégats) développé par Baran and Labonnote (2007). La base de données compile ainsi 20662 distributions en taille en fonction du contenu en glace et de la température (voir Figure 3.11). Les gammes de valeurs d'IWC et de température couvertes par la base de données sont très variées allant de 6×10^{-6} à $2\,\mathrm{g\,m^{-3}}$ pour le IWC et de 193 à 273 K pour la température. Pour chacune des distributions, la base de données fournit les coefficients d'absorption et de diffusion (k_a et k_s, respectivement), l'albédo de simple diffusion ω_0 et le paramètre d'asymétrie g à 145 longueurs d'ondes réparties entre 0.2 et 120 µm (Baran et al., 2014). La fonction de phase est quant à elle paramétrée à partir de g (Baran et al., 2001). Différentes formulations de paramétrisations ont été testées et j'ai retenu la formulation suivante :

$$\begin{aligned}\log_{10} k(T, IWC) = A_k + B_k T + C_k \log_{10}(IWC) \\ + D_k T^2 + E_k (\log_{10}(IWC))^2 + F_k T \log_{10}(IWC)\end{aligned} \tag{3.19}$$

$$b(T, IWC) = A_b + B_b T + C_b \log_{10}(IWC) \tag{3.20}$$

où k est soit le coefficient d'absorption soit le coefficient de diffusion et les coefficients A_k à F_k et A_b à C_b sont obtenus par une méthode de régression par moindres carrées. Un premier test de validation de cette nouvelle paramétrisation a été simplement de la comparer à une des autres paramétrisations avec des images satellites prévues. La Figure 3.12a est obtenue à partir des observations de l'instrument SEVIRI dans le canal à 10.8 µm le 5 janvier 2015 à 03h00 UTC. La Figure 3.12b est obtenue en simulant des observations à partir des sorties du modèle ARPEGE issues d'une prévision à 3 heures (correspondant à l'heure des observations de la Figure 3.12a) et en prenant la paramétrisation W98 avec des cristaux de forme hexagonaux. La Figure 3.12c montre les simulations RTTOV avec la nouvelle paramétrisation. La nouvelle paramétrisation est plus performante pour reproduire les zones de nuages élevés représentées en blanc ayant des températures de brillance inférieures à 230 K.

Ensuite pour valider cette nouvelle paramétrisation et minimiser au maximum les autres sources d'erreurs provenant des profils nuageux d'entrée et de la méthode de recouvrement nuageux, j'ai entrepris dès 2014 une étude de validation à l'aide des instruments de l'A-Train (Vidot et al., 2015). Cette étude est rentrée dans le cadre du projet EECLAT qui m'a permis de rencontrer la communauté française des lidars et radars appliqués à l'atmosphère. Ce projet soutient la future mission Earth-Care d'instruments actifs et passifs pour l'observation des aérosols et des nuages. Les informations obtenues à haute résolution verticale sont particulièrement intéressantes pour valider RTTOV car les instruments uniquement passifs ne voient qu'une information intégrée sur toute la colonne atmosphérique.

Pour m'affranchir des erreurs provenant des profils nuageux d'entrée j'ai utilisé les profils inversés d'IWC combinant des mesures spatiales des instruments actifs de

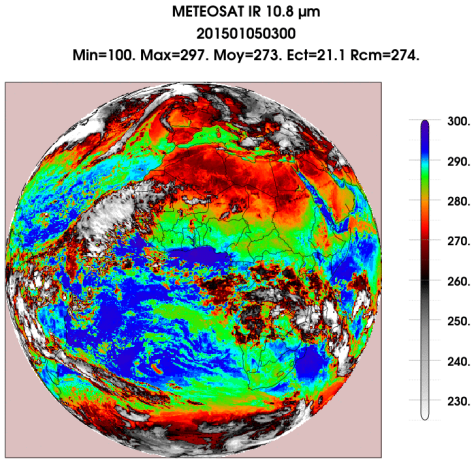

(a) Obsservations

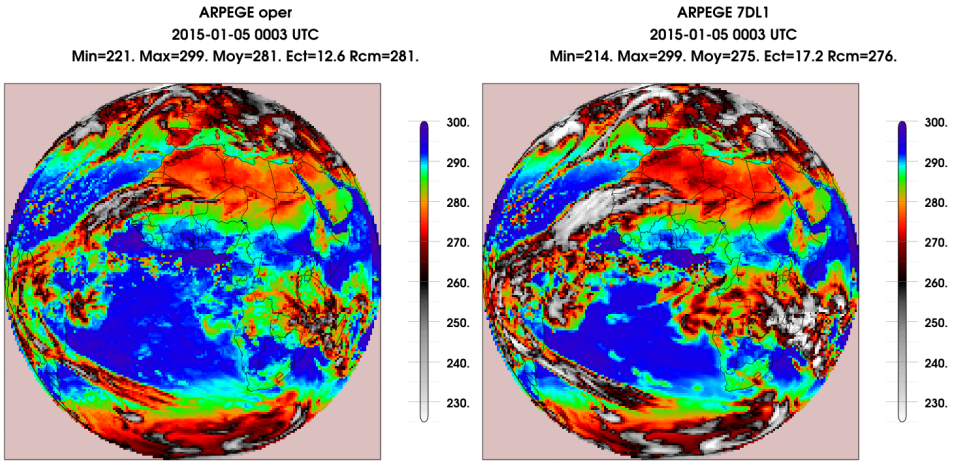

(b) RTTOV avec W98-Hex (c) RTTOV avec la n^{elle} paramétrisation

FIGURE 3.12 – (a) Observations SEVIRI en température de brillance à 10.8 µm le 5 janvier 2015 à 03 :00 UTC. (b) Simulations RTTOV avec la version opérationnelle d'ARPEGE comprenant la paramétrisation W98 et des cristaux de glace de formes hexagonales. (c) Simulations RTTOV avec ma paramétrisation de la base de données d'ensemble.

l'A-Train (radar CPR sur CloudSat et Lidar CALIOP sur CALIPSO) tels que les produits DARDAR (Delanoe and Hogan, 2010) ou 2C-ICE (Deng et al., 2010).

Pour m'affranchir des erreurs provenant de la méthode de recouvrement, j'ai utilisé les observations co-localisées du radiomètre infrarouge IIR sur CALIPSO qui a une résolution spatiale de 1 km ce qui en comparaison des 12 km des sondeurs hyperspectraux, réduit fortement la probabilité de fraction nuageuse inférieure à 1 dans les différentes couches nuageuses. Ainsi le choix a été pris de forcer les valeurs du profil de fraction nuageuse à 1 lorsqu'il y a présence de nuage de glace avec un IWC > 0 dans les couches atmosphériques.

A partir de deux semaines d'observations de l'A-Train, ont été extraites 26791 colocalisations d'observations IIR et de profils d'IWC restitués par synergie lidar-radar. L'unique présence de nuages de glace a été assurée par le masque CALIOP (v3.30) et les épaisseurs optiques des nuages à 532 nm ont été sélectionnées entre 0.03 et 4 avec des couches comprises entre 440 et 50 hPa. La Figure 3.13 montre les histogrammes des différences entre observations IIR et simulations RTTOV pour les 4 paramétrisations du diamètre effectif et pour la forme hexagonale ainsi qu'avec la nouvelle paramétrisation du modèle d'ensemble. La nouvelle paramétrisation est plus performante avec une distribution plus symétrique, un biais plus proche de zéro et un écart-type plus faible que ceux obtenus avec les anciennes paramétrisations. Les observations IIR dans les trois canaux sont reproduites globalement avec un biais de 0.43 K et un écart-type de 6.85 K. Cette nouvelle paramétrisation a depuis été utilisée dans plusieurs études d'assimilation de luminances nuageuses infrarouges avec des résultats positifs(Okamoto, 2017; Geer et al., 2019; Okamoto et al., 2019) .

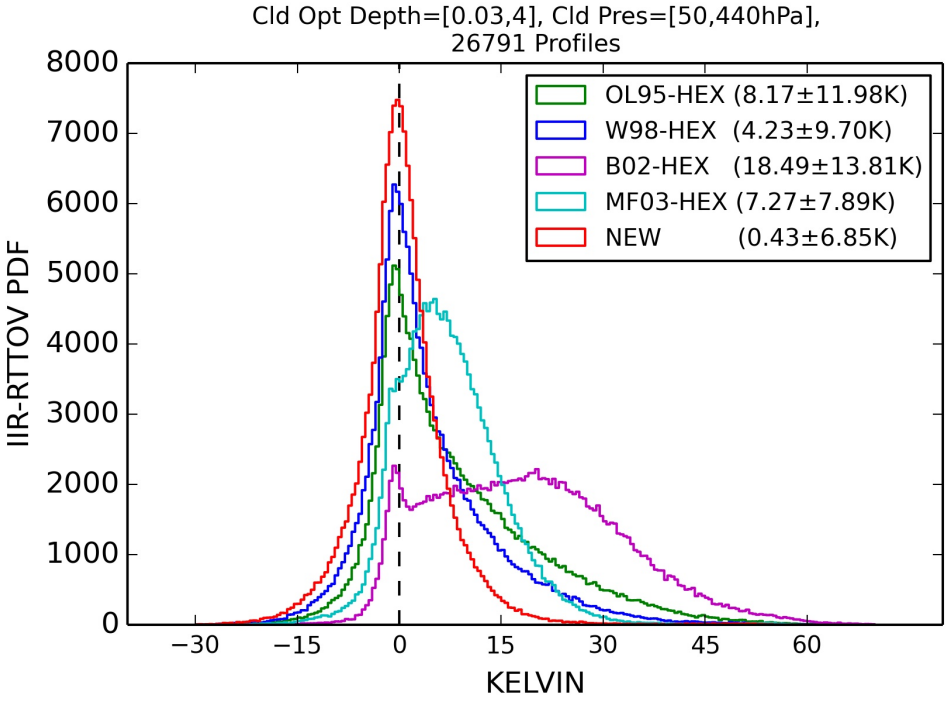

FIGURE 3.13 – Histogrammes des différences de température de brillance entre observations IIR et simulations RTTOV pour 26791 profils de nuage de glace sélectionnés sur tout le globe pendant deux semaines, ayant des épaisseurs optiques visibles comprises entre 0.03 et 4 et dont les pressions des couches nuageuses sont situées entre 440 et 50 hPa. Les paramétrisations OL95, W98, B02 et MF03 sont représentées en vert, bleu foncé, violet et bleu clair, respectivement. La nouvelle paramétrisation issue du modèle d'ensemble est représentée en rouge. Les moyennes et écart-types de chaque distribution sont donnés en légende.

3.3.3 L'instrument FORUM dans le domaine de l'infrarouge lointain

Le domaine spectral de l'infrarouge lointain a récemment montré un nouvel intérêt avec la mission FORUM, mission sélectionnée en 2019 dans le cadre de l'Earth Explorer 9 de l'European Space Agency (ESA). Le but de FORUM est de mesurer le spectre infrarouge émis par la Terre à une résolution spectrale de $0.3\,\mathrm{cm}^{-1}$ de 100 à $1600\,\mathrm{cm}^{-1}$ (ou inversement de 6.25 à 100 µm). Les objectifs scientifiques de cette mission sont la caractérisation de la vapeur d'eau dans la moyenne/haute troposphère et basse stratosphère, la caractérisation des nuages (phase thermodynamique, taille et forme des cristaux de glace), et la caractérisation de l'émissivité des surfaces en infrarouge lointain en atmosphère suffisamment sèche (c'est à dire en zones polaires). De plus, cet instrument est prévu de voler en tandem avec EPS-SG afin d'avoir des mesures colocalisées avec IASI-NG. L'originalité serait alors d'avoir des observations à résolutions spatiales équivalentes (12-15 km) et couvrant les domaines infrarouge (de 3 à 18 µm) et infrarouge lointain (de 6 à 100 µm) avec une partie en recouvrement entre 6 et 18 µm. L'intérêt des travaux engagés pour RTTOV était de montrer la capacité du modèle de paramétrisation de la transmittance atmosphérique à fonctionner dans l'infrarouge lointain et d'adapter les différents compartiments de RTTOV (modèle d'émissivité de surface et propriétés optiques des nuages) à l'infrarouge lointain. La Figure 3.14 montre des exemples de simulations de spectres FORUM simulées pour trois angles de visée (0°, 30° et 60°) avec un nuage de glace d'épaisseur optique de 2.05 à 10 µm (ou $1000\,\mathrm{cm}^{-1}$ dont le profil d'IWC est représenté sur la petite figure en haut au milieu) et sans nuage. Les deux figures en haut à droite montrent les jacobiens en IWC à $480\,\mathrm{cm}^{-1}$ et à $960.7\,\mathrm{cm}^{-1}$. On voit que même si l'infrarouge lointain est fortement absorbé par la vapeur d'eau, les canaux restent sensibles aux nuages (Yang et al., 2003) comme dans les canaux fenêtres du moyen infrarouge. Le spectre d'émissivité de surface océanique est représentée en bas de la Figure 3.14. Ces simulations montrent que la paramétrisation de la transmittance atmosphérique de RTTOV est adaptée à l'infrarouge lointain, ce qui n'est pas surprenant car cette région du spectre est essentiellement impactée par l'absorption de H_2O.

On peut noter enfin que l'adaptation de RTTOV pour la simulation d'observables du futur instrument FORUM a joué un rôle clé dans la sélection de la mission lors des présentations aux "User Consultation Meeting" qui s'est déroulé à Cambridge en juillet 2019. D'une part parce qu'on a pu montrer des restitutions de propriétés de nuages de glace sur des centaines de profils réalistes, chose qu'il aurait été impossible à faire dans le temps imparti avec des modèles plus lents. D'autre part des simulations du spectre FORUM sur le globe à partir de sorties du modèle global de PNT du UK Met-Office pour tout type de ciel (ciel clair et nuageux) afin de montrer l'intérêt de des mesures dans l'infrarouge lointain pour l'étude de la haute troposphère.

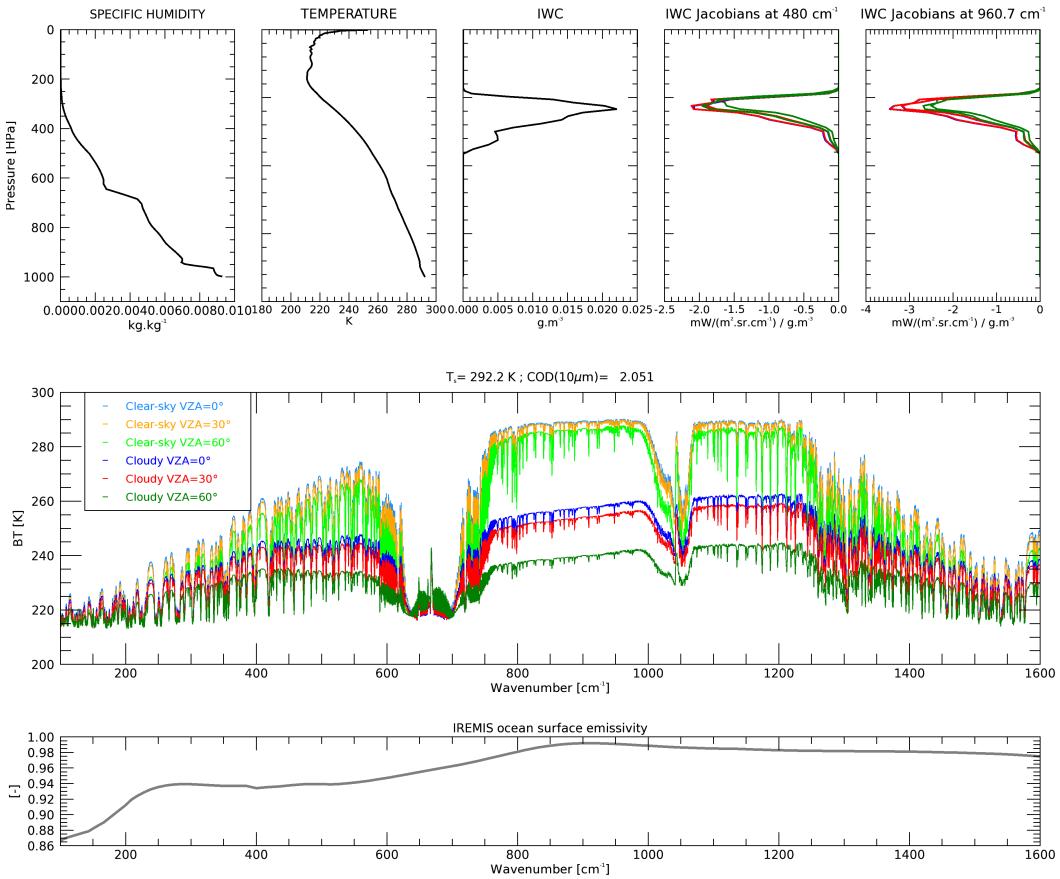

FIGURE 3.14 – Exemple de simulations RTTOV pour l'instrument FORUM de spectres de température de brillance en ciel clair et en ciel nuageux (panneau du milieu) pour trois angles d'observations (0, 30 et 60 °). Le profil nuageux d'IWC (en $\mathrm{g\,m^{-3}}$) est représenté sur la figure du haut au centre. Les jacobiens nuageux (en $\mathrm{mW/(m^2\,sr\,cm^{-1})}$ / $\mathrm{g\,m^{-3}}$) dans les canaux à $480\,\mathrm{cm^{-1}}$ et à $960.7\,\mathrm{cm^{-1}}$ sont représentés aux deux figures du haut à droite. Les profils d'humidité spécifique (en $\mathrm{kg\,kg^{-1}}$) et de température (en K) sont donnés en haut à gauche. Le spectre d'émissivité de surface est montré sur le panneau du bas.

3.4 Intercomparaison à d'autres modèles de transfert radiatif

Le modèle RTTOV est en perpétuelle évolution car il vise à intégrer régulièrement de nouveaux instruments, des nouveautés scientifiques ou des mises à jour des modèles, des atlas ou des outils sur lequel il repose. Ainsi sa confrontation avec d'autres modèles de transfert radiatif est toujours une étape importante et nécessaire d'évaluation de ses évolutions. Cependant l'intercomparaison de plusieurs modèles de transfert radiatif est un exercice long et complexe en organisation et en restitution. Peu d'études ont été faites sur ce sujet pour les modèles de transfert radiatif

rapides. On peut tout de même citer les études de Garand et al. (2001) sur le sondeur infrarouge multi-canaux HIRS et de Saunders et al. (2007) avec 8 modèles de transfert radiatif mais un seul spectre de luminance observé par l'instrument hyperspectral infrarouge AIRS.

3.4.1 Intercomparaison en ciel clair

Dans l'infrarouge et en ciel clair, j'ai engagé dès 2013 des évaluations régulières des versions de RTTOV en collaborant avec Raymond Armante du LMD pour l'intercomparer avec le modèle de transfert radiatif appelé 4A/OP. Cette collaboration s'est faite dans le cadre du projet IASI soutenu par le TOSCA. Ce projet rassemble la communauté française travaillant sur l'instrument IASI. Cet instrument est unique car il couvre tout le spectre infrarouge à haute résolution spectrale et se montre extrêmement stable radiométriquement depuis le lancement du premier instrument en 2006 (Hilton et al., 2012). De plus, il est essentiel pour Météo-France puisque c'est la première source d'observations satellites dans l'assimilation avec plus de 50 % du nombre total des observations satellites et conventionnelles dans ARPEGE (en vert kaki sur la Figure 2.2). Ainsi, la capacité de RTTOV pour simuler l'instrument IASI est primordiale. L'idée principale de confronter RTTOV à 4A/OP provient du fait que ces deux modèles reposent sur deux bases de données spectroscopiques différentes ainsi que sur des traitement différents d'effets spectroscopiques tels que les continua et les mélanges de raies d'absorptions. Ainsi cette confrontation permet aux deux équipes de mettre en avant les parties du spectre infrarouge nécessitant des convergences d'améliorations futures sur la spectroscopie. De plus, nous nous sommes reposés sur le travail important mené par le LMD depuis plusieurs années de colocalisation de profils atmosphériques Analyzed RadioSounding Archive (ARSA) avec des observations IASI. Cette base de données permet depuis plusieurs années une validation des niveaux 1 et 2 issus d'observations satellitaires (voir `https://ara.abct.lmd.polytechnique.fr/index.php?page=arsa`). Pour RTTOV, cette base colocalisée de profils atmosphériques et d'observations IASI permet de valider les nouveaux développements sur tout le domaine infrarouge que ce soit avec de nouvelles versions du modèle raie-par-raie ou d'autres aspects comme les modèles d'émissivité de surface ou les profils d'entrainement.

La Figure 3.15 représente un des nombreux résultats que nous avons obtenus grâce à ces travaux récurrents d'intercomparaison. Pour cette étude, les collocations retenues concernent les atmosphères tropicales, au-dessus des océans de jour et sur une période de 5 années. La fenêtre temporelle et spatiale utilisée est respectivement de 3 heures et 100 km. Au total 80452 colocations ont été sélectionnées. Les configurations des deux modèles sont les suivantes :

— Depuis la version 11 de RTTOV, le calcul des coefficients de la paramétrisation de la transmittance atmosphériques (Equation 3.10) est réalisé avec la version 12.2 du modèle raie-par-raie LBLRTM (Clough et al., 2005) qui combine la base de données spectroscopique AER v3.2 et le modèle de continuum d'absorption MT-CKD version 2.5.2 (voir le site `http://rtweb.aer.com/lblrtm.`

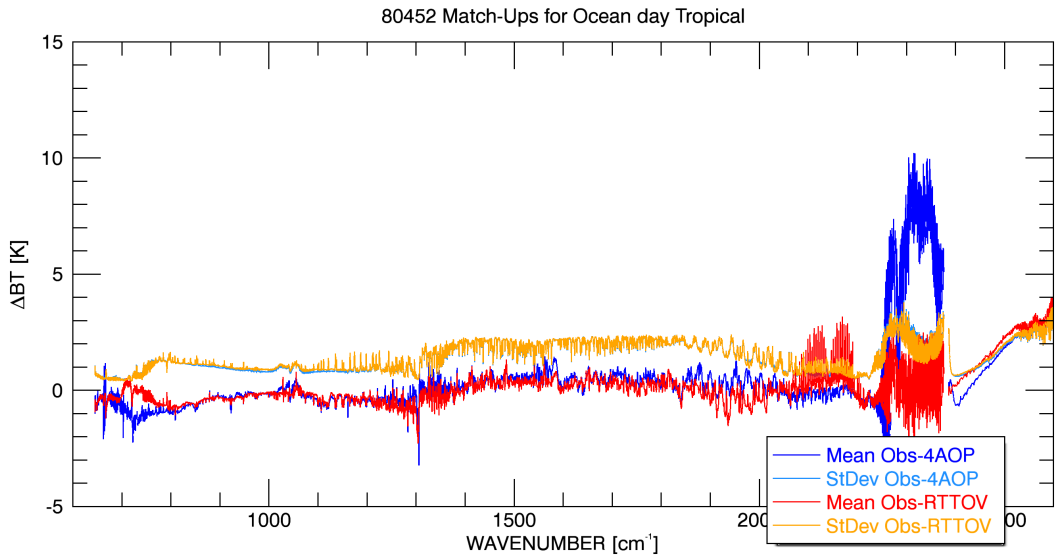

FIGURE 3.15 – Biais et écarts-types en fonction du nombre d'onde entre les observations IASI et les simulations RTTOV (en bleu foncé et bleu clair, respectivement) ou 4A/OP (en rouge et orange, respectivement). 80452 colocalisations ARSA et IASI en atmosphère tropicale de jour sur océans ont été utilisées.

`html`). La base de données spectroscopique AER v3.2 est construite à partir de HITRAN 2008 (Rothman et al., 2009) avec des améliorations notables pour H_2O, CO_2, CH_4 et O_2 (voir `http://rtweb.aer.com/line_param_whats_new.html` pour les nouveautés de chaque version). Les prédicteurs version 7 ont été utilisés car la base de données ARSA ne fournit que des profils variables en H_2O et O_3.

— La version opérationnelle du modèle LMD 4A (Scott and Chedin, 1981) développée par Noveltis (dans sa version 2012) utilise la base de données spectroscopique GEISA de 2011, les modèles de mélange de raies d'absorption de CO_2 (Niro et al., 2005) et de CH_4 (Tran et al., 2006) ainsi que des formulations du continuum pour H_2O, O_2 et N_2. Pour H_2O le continuum correspond à la version 2.1 de MT-CKD sans troncature des ailes de raie.

Les émissivités de surface ont été fixées à 0.98 pour les deux modèles. Sur la Figure 3.15 les écart-types entre les simulations des 2 modèles de transfert radiatif et les observations sont très proches avec des valeurs inférieures à 2 K sur tout le spectre excepté dans la partie solaire (au-dessus de 2400 cm^{-1}) où aucun des deux modèles n'a simulé la contribution solaire. Les biais spectraux moyens entre observations IASI et simulations sont notablement plus différents et révèlent à la fois l'impact de la spectroscopie sur les simulations mais aussi l'effet des profils d'entraînements. Tout d'abord, dans la région d'absorption du CO_2 entre 645 et 750 cm^{-1} il y a un effet important de la spectroscopie avec des différences de plus de 1 K probablement dues à la différence de spectroscopie GEISA/HITRAN et de modélisation du mélange des raies d'absorption de CO_2. On peut remarquer que RTTOV (en rouge) a

un biais plus proche de zéro que 4A/OP (en bleu). Ce biais inférieur à ± 0.5 K correspond aux résultats obtenus par Matricardi (2009) qui a comparé les observations IASI aux simulations RTTOV avec des profils du CEPMMT. Dans la bande d'absorption de l'O_3 entre 1000 et 1100 cm^{-1}, les deux modèles ont des résultats très similaires avec sans doute quelques résidus liés à la spectroscopie. Enfin, dans la large région d'absorption de H_2O entre 1300 et 2000 cm^{-1}, les multiples différences sont probablement dues au traitement différent du continuum de la vapeur d'eau et aux bases de données spectroscopiques utilisées. Une étude plus approfondie en utilisant soit les mêmes continua ou soit les mêmes bases de données spectroscopiques permettrait sans doute de mieux interpréter ces résultats. Pour finir, cette étude a aussi montré que le profil fixe de CO utilisé par RTTOV dans la génération des prédicteurs version 7 n'était pas adapté en comparaison de celui utilisé par 4A/OP avec lequel il y a un biais quasi nul entre 2000 et 2200 cm^{-1} alors que pour RTTOV, la signature spectrale de CO est très visible avec 2 K de biais positif. Ce résultat nous a notamment lancés dans une étude sur la validité des profils utilisés pour les gaz considérés comme fixes dans la génération des coefficients. Au final, cette intercomparaison montre que les deux modèles ont globalement des précisions assez similaires.

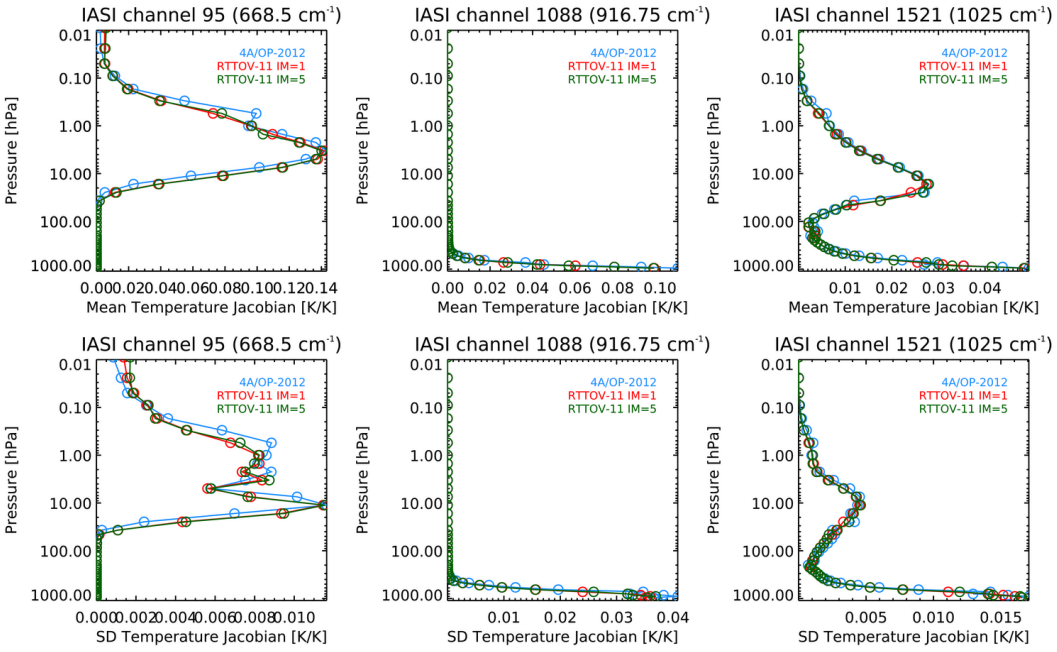

FIGURE 3.16 – Exemple de comparaison de jacobiens moyens (en haut) et d'écart-types de jacobiens (en bas) pour 3 canaux IASI (canal de sondage en température à 668.5 cm^{-1}, canal fenêtre à 916.75 cm^{-1} et canal d'absorption de l'ozone à 1025 cm^{-1}). Les moyennes et écarts-types ont été calculés à partir de 120 profils.

Dans les études de (Garand et al., 2001) et (Saunders et al., 2007), l'intercomparaison de jacobiens en température a aussi été présentée. Les jacobiens en tempéra-

ture pour les canaux de sondage en température sont généralement bien reproduits par les différents modèles mais les résultats montrent que les canaux d'absorption par l'ozone ou les canaux fenêtres ne sont pas toujours cohérents. Nous avons donc aussi comparé les jacobiens en choisissant trois canaux particuliers sur IASI : le canal de sondage de température à 668.5 cm^{-1}, le canal fenêtre à 916.5 cm^{-1} et le canal d'absorption par l'ozone à 1025 cm^{-1}. Nous avons ensuite calculé un profil de jacobien moyen en température (en $\mathrm{K\,K}^{-1}$) et un profil d'écart-type de jacobiens à partir de 120 profils de la base ARSA. La Figure 3.16 montre les résultats de cette intercomparaison de jacobiens. La première ligne montre les jacobiens moyens pour les trois canaux sélectionnés, la deuxième ligne montre les écart-types des jacobiens. Contrairement aux études citées ci-dessus c'est dans le canal de sondage que les différences entre RTTOV et 4A/OP sont les plus importantes. Ces différences pourraient être expliquées par les méthodes d'interpolations verticales internes aux modèles de transfert radiatif, notamment pour RTTOV entre les 43 niveaux des profils d'entrée et les 101 niveaux des coefficients de transmittance atmosphérique.

3.4.2 Intercomparaison en ciel nuageux

Dans l'optique de valider les développements de RTTOV sur la diffusion en infrarouge, une nouvelle collaboration avec Laurent C.-Labonnote du LOA a été engagée afin de comparer RTTOV avec le modèle de transfert radiatif LInearized Discrete Ordinate Radiative Transfer (LIDORT) (Spurr and Christi, 2014). Ce modèle est quasi unique car il prend en compte la diffusion de manière complète mais surtout il est linéarisé et donc permet de calculer aussi les jacobiens nuageux. Dans cette première étude nous avons voulu évaluer uniquement la paramétrisation de la diffusion de RTTOV. Pour cela nous nous sommes appuyés sur une base de données de profils nuageux issue du modèle Integrated Forecasting System (IFS) sur 137 niveaux du SAF-NWP (voir `https://www.nwpsaf.eu/site/software/atmospheric-profile-data/`). Cette base provient d'un échantillonnage d'une année de simulations du modèle global du CEPMMT permettant à la fois de couvrir statistiquement tout le globe mais aussi de se prémunir de profils non réalistes (Eresma and McNally, 2014). Afin de n'évaluer que la paramétrisation de la diffusion, nous avons utilisé les calculs de RTTOV en transmittance atmosphérique, en émissivité de surface et en propriétés optiques comme entrées pour LIDORT. Il est à noter que les profils de fraction nuageuse n'ont pas été pris en compte.

La Figure 3.17 est un exemple de cette intercomparaison pour un cas de nuage de glace avec une seule couche d'épaisseur optique de 1.83 à 1000 cm^{-1}. La Figure 3.17(C) montre le profil d'IWC, la Figure 3.17(A) montre le spectre IASI simulés par LIDORT et par RTTOV pour trois angles d'observations (0, 30 et 60° rappelés dans la légende de la Figure 3.17(E). Les biais spectraux aux trois angles sont représentés à la Figure 3.17(B) avec des valeurs comprise entre 0.6 et −0.4 K. Les jacobiens pour le canal fenêtre à 960.75 cm^{-1} sont représentés sur la Figure 3.17(D) et pour le canal vapeur d'eau à 1395.25 cm^{-1} sur la Figure 3.17(E). Les jacobiens des deux modèles sont très proches et on peut voir aussi que le jacobien dans le

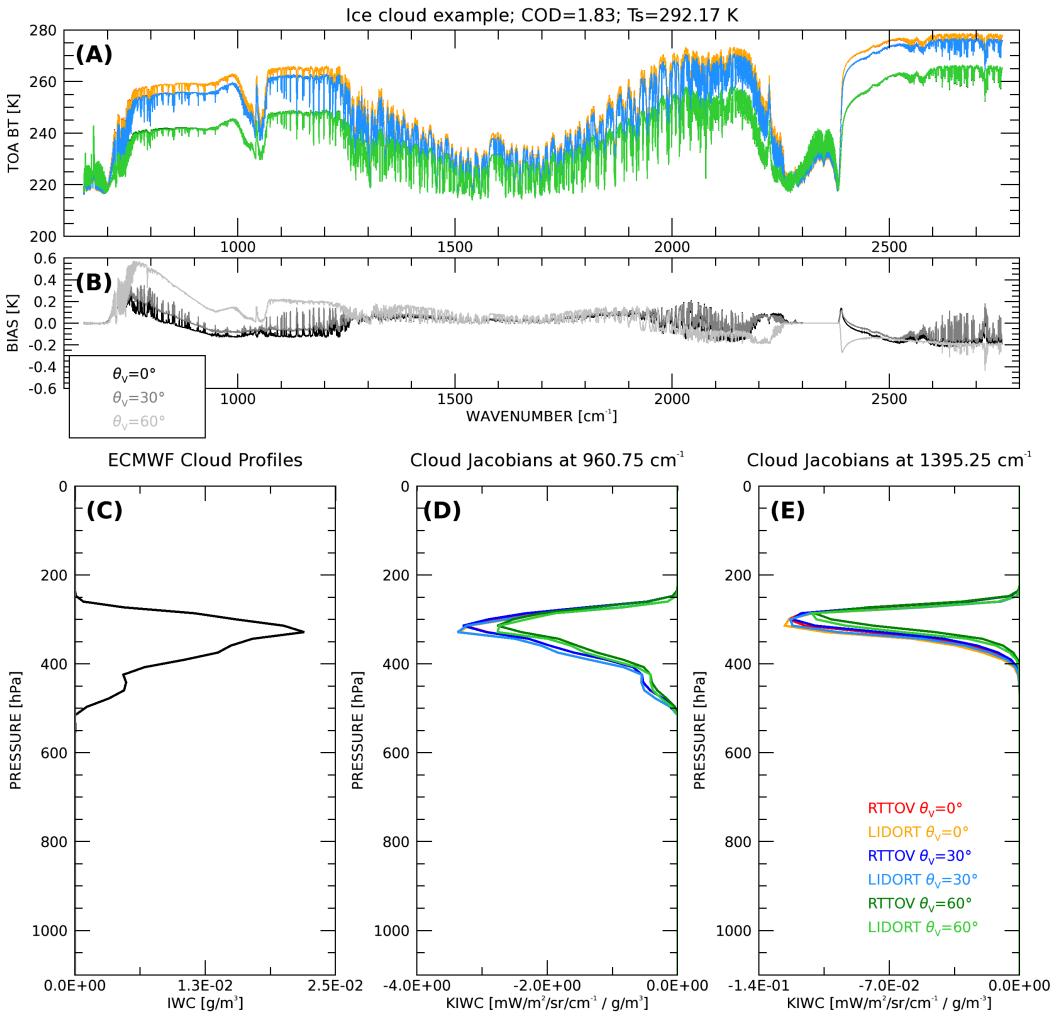

FIGURE 3.17 – Exemple de comparaison RTTOV et LIDORT pour un cas typique de nuage de glace à une couche d'épaisseur optique de 1.83 à 1000 cm^{-1}. (A) Spectres IASI simulés à trois angles de visée (0, 30 et 60°), (B) Biais spectraux RTTOV moins LIDORT aux trois angles de visées, (C) profils d'IWC, (D) jacobiens nuageux dans le canal à 960.75 cm^{-1} et (E) dans le canal à 1395.25 cm^{-1}.

canal vapeur d'eau n'est plus sensible à la partie basse du nuage contrairement au jacobien dans le canal fenêtre. Cette étude a été finalisée par une analyse statistique sur tous les profils nuageux en les séparant en trois catégories : nuages de glace uniquement, nuages d'eau liquide uniquement et nuages en phases mélangées glace et eau liquide. Les géolocalisations des profils nuageux sont représentées sur la Figure 3.18. Nous avons pu ainsi montrer que RTTOV était capable de simuler les radiances nuageuses dans l'infrarouge avec une erreur totale inférieure à 0.3 ± 0.3 K pour les nuages de glace (voir Figure 3.19), à 2 ± 1.5 K pour les nuages en phase liquide (voir Figure 3.20) et 1.5 ± 1.5 K pour les nuages en phases mélangées (voir Figure 3.21). Ces erreurs sont plus importantes aux grands angles de visée

et peuvent être globalement divisées par deux pour des angles inférieurs à 30°. La moins bonne capacité de la paramétrisation de la diffusion de RTTOV à reproduire les cas de nuages en phase liquide et phases mélangées est cohérente avec les résultats de Matricardi (2005). Elle est sans doute liée au fait que les épaisseurs optique de ces nuages sont plus importantes que dans les cas de nuage de glace uniquement. L'étude a montré aussi que les jacobiens nuageux étaient bien reproduits par la paramétrisation de la diffusion. Un article est en cours de rédaction sur ce travail (voir partie 1.3.2).

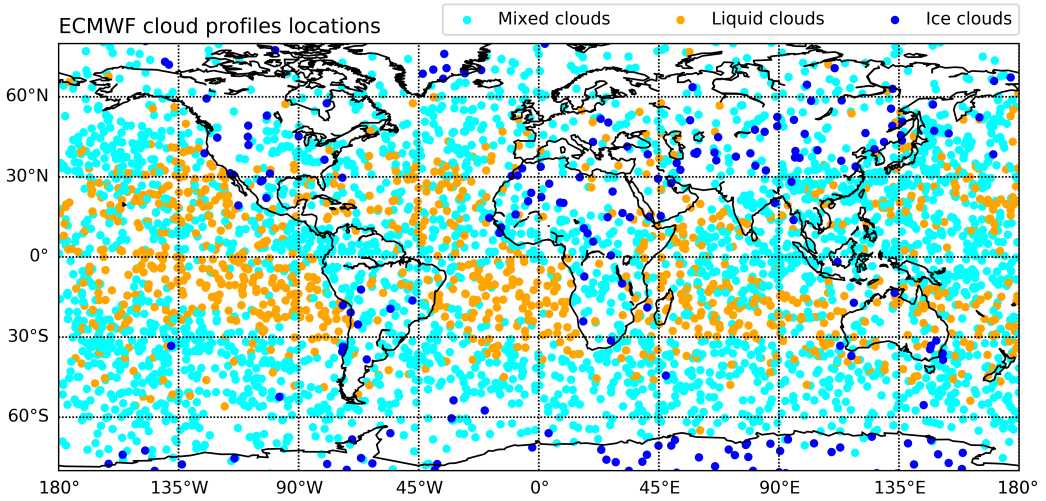

FIGURE 3.18 – Positions géographiques des profils nuageux extraits de la base de données du SAF-NWP selon les trois catégories : glace uniquement (en bleu foncé), eau liquide uniquement (en orange) et phases liquide/glace mélangées (en bleu cyan).

De manière plus générale et afin de mieux estimer les erreurs du modèle RTTOV en condition nuageuse dans l'infrarouge, un exercice d'intercomparaison de plusieurs modèles de transfert radiatif a été initié par Georges Aumann (Jet Propulsion Laboratory (JPL)) en 2016. Cet exercice a rassemblé 6 modèles de transfert radiatif internationaux et s'est limité aux comparaisons des températures de brillance simulées car la plupart des autres modèles ne proposent pas le calcul des jacobiens. La base de comparaison comprenait 7377 observations de l'instrument AIRS colocalisées avec des profils CEPMMT sur 91 niveaux verticaux (Aumann et al., 2018). L'intérêt de mener cette étude était le traitement différent par chaque modèle de transfert radiatif de la diffusion, les modèles de propriétés optiques des nuages différents et des méthodes de recouvrement nuageuses différentes aussi. La Figure 3.22 montre les biais (en traits pleins) et écart-types (en traits tiretés) spectraux pour trois modèles des 6 modèles de transfert radiatif, le modèle SARTA (Strow et al., 2003), le modèle PCRTM (Liu et al., 2016) et le modèle RTTOV. Dans le cas de RTTOV, trois configurations ont été testées :

— La paramétrisation de Chou et la méthode de recouvrement du MRO.

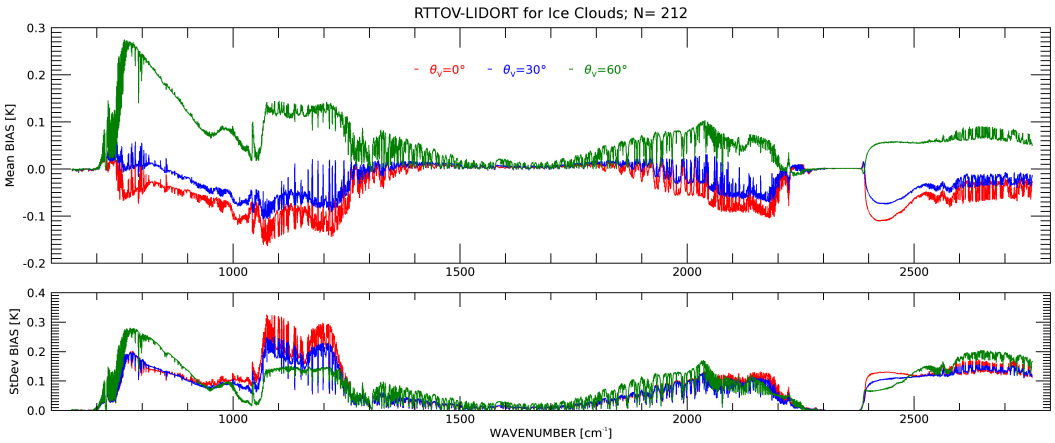

FIGURE 3.19 – Biais moyen (en haut) et écart-type (en bas) spectraux obtenus pour 3 angles d'observations (0, 30 et 60°) entre les simulations RTTOV et LIDORT à partir de 212 profils de nuage en phase glace.

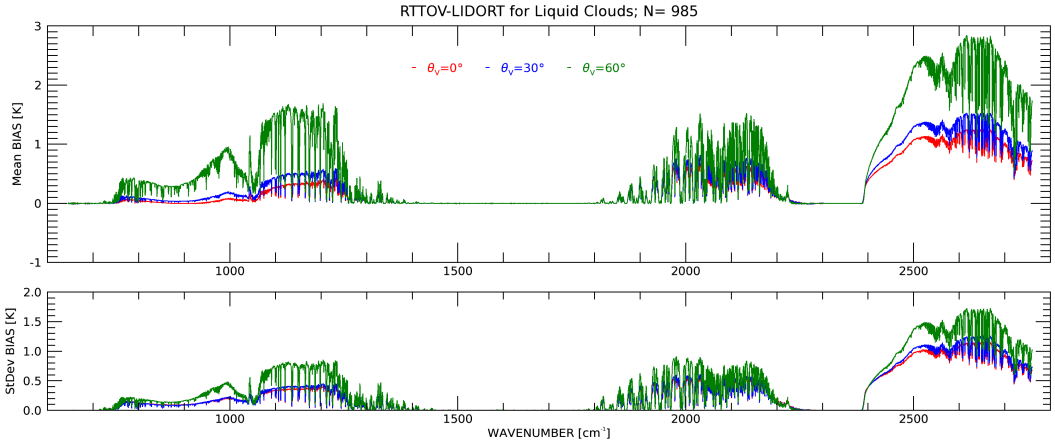

FIGURE 3.20 – Biais moyen (en haut) et écart-type (en bas) spectraux obtenus pour 3 angles d'observations (0, 30 et 60°) entre les simulations RTTOV et LIDORT à partir de 985 profils de nuage en phase liquide.

— La paramétrisation de Chou et la méthode de recouvrement du CMSS.

— La diffusion complète avec RTTOV_DOM et la méthode de recouvrement du MRO.

Dans les canaux fenêtres, les écart-types (Figure 3.22b) de tous les modèles sont de l'ordre de 18 K mais les biais (Figure 3.22a) sont plus variables entre les modèles de transfert radiatif. La version de RTTOV avec la paramétrisation de Chou et la méthode de recouvrement du CMSS est celle qui a les biais les plus faibles, montrant que la méthode de recouvrement nuageux MRO introduit des erreurs systématiques, quel que soit le traitement de la diffusion. Ce résultat est en contradiction avec les travaux de Geer et al. (2019) qui a obtenu des résultats quasiment non biaisés dans des canaux vapeur d'eau avec la méthode MRO et biaisés avec la méthode CMSS.

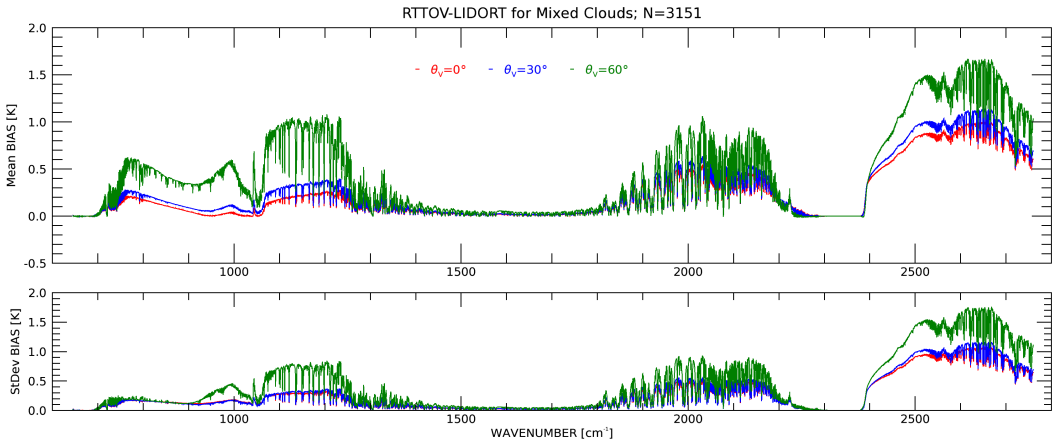

FIGURE 3.21 – Biais moyen (en haut) et écart-type (en bas) spectraux obtenus pour 3 angles d'observations (0, 30 et 60°) entre les simulations RTTOV et LIDORT à partir de 3151 profils de nuage en phases mélangées.

Une explication pourrait être la sélection des observations les plus homogènes faite par Geer et al. (2019).

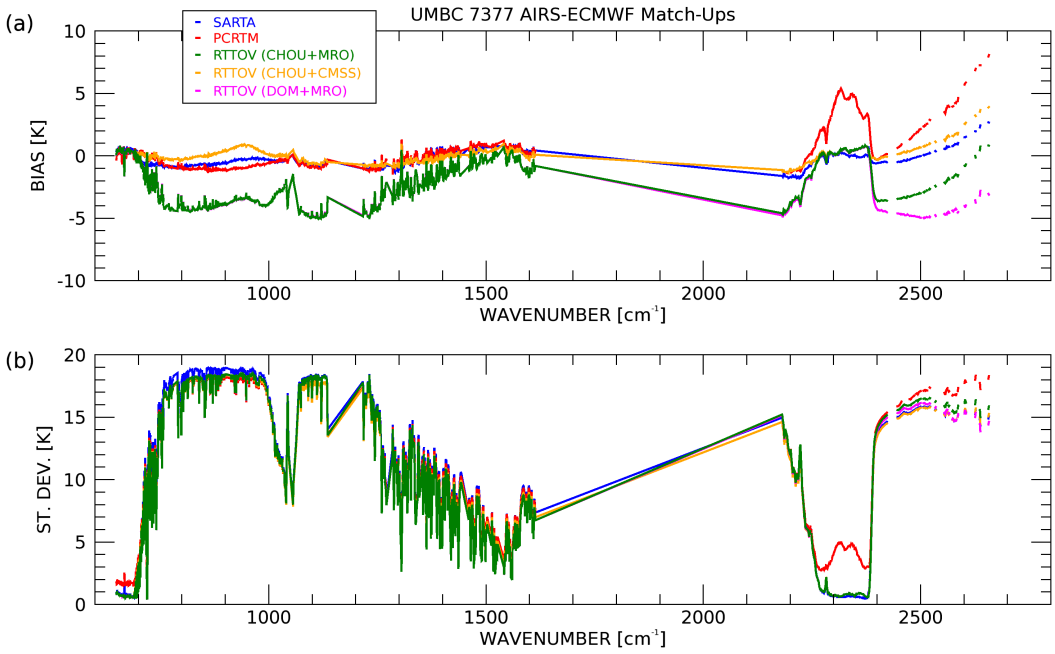

FIGURE 3.22 – Biais (a) et écart-types (b) moyens issus de l'intercomparaison de code de transfert radiatif nuageux en infrarouge à l'aide d'observations de l'instrument AIRS et de profils CEPMMT. Les simulations ont été réalisées avec SARTA (en bleu), PCRTM (en rouge) et trois configurations de RTTOV (en vert, jaune et rose).

3.5 Autres activités de recherche liées à l'observation satellitaire pour l'étude de précipitations intenses

Les autres équipes du CEMS travaillent plus particulièrement sur les observations des satellites géostationnaires. Ces instruments à haute répétivité temporelle (15 minutes pour SEVIRI sur MSG) avec des résolutions spatiales de 4 à 6 km pour SEVIRI sont une source d'information très précieuse pour étudier la dynamique de notre environnement. C'est dans cette optique que je me suis intéressé à une autre application de l'observation spatiale à haute répétivité temporelle pour l'étude de l'évolution de systèmes fortement précipitants.

L'amélioration de la prévision des précipitations sous forme de pluies intenses fait partie d'un des axes principaux de recherche du Contrat d'Objectifs et de Performances (COP) de Météo-France. Si les prévisions de précipitations sont essentiellement forcées par les observations des radars sols dans le modèle de PNT à aire limitée comme Applications de la Recherche à l'Opérationnel à Méso-Echelle (AROME), les observations satellitaires y participent aussi et notamment au-dessus des océans par l'assimilation des observations micro-ondes dans les modèles de PNT globaux comme ARPEGE. A cela pourrait aussi s'ajouter les observations dans les domaines visible, proche infrarouge et infrarouge, notamment car les instruments géostationnaires permettent d'avoir des observations à très haute fréquence temporelle contrairement aux observations micro-ondes à bord des satellites défilants limitées à quelques passages par jour. J'ai débuté cet thématique de recherche en encadrant une étudiante en 2$^{\text{ième}}$ année d'IUT de Lannion, Justine Rozé, qui a comparé des inversions de taux de pluie obtenues à partir du produit MPE (Heinemann et al., 2002) sur SEVIRI avec des observations du réseau sol de pluviomètres de Météo-France. Cette étude nous a permis de montrer que le produit MPE n'était pas assez fiable pour détecter les évènements de pluie en France. Ce produit a récemment été stoppé par EUMETSAT. Pour proposer des innovations dans cet axe de recherche, j'ai co-dirigé entre 2014 et 2018, Maximilien Patou, étudiant en thèse de l'Université de Lille avec comme directeur de thèse le Pr. Jérôme Riedi du LOA. Le sujet de la thèse était l'étude de l'évolution temporelle des propriétés physiques et optiques des nuages précédant de fortes précipitations à l'aide de SEVIRI. L'objectif de la thèse était de trouver de nouveaux indices pour prévoir la probabilité d'un système nuageux de donner lieu à un événement de pluie intense. Ces indices ont été déduits des inversions de propriétés optiques nuageuses (épaisseur optique et rayon effectif des gouttelettes d'eau, phase glace ou liquide au sommet des nuages). En outre, les travaux se sont appuyés sur les données de précipitations de Météo-France obtenues par le produit PANTHERE (Tabary, 2007) basé sur des inversions du réseau sol de radar à fréquence de 5 minutes. L'intérêt des mesures sol est de contraindre la sélection d'observations satellites sur des zones où il a effectivement plu et de remonter le temps grâce aux observations à haute fréquence temporelle de SEVIRI. Enfin, cette étude s'est étoffée avec la collaboration de Tim Garrett (Université de Salt Lake City aux USA) qui a établi une nouvelle métrique des pré-

cipitations basée sur l'évolution temporelle de la dimension spatiale des systèmes nuageux, le Cloud Perimeter to Area Ratio (CPAR). Les principaux résultats de la thèse de Maximilien ont été publiés dans Patou et al. (2018). La Figure 3.23 montre l'évolution temporelle du CPAR calculé à partir des masques nuageux du SAF for Nowcasting (SAF-NWC) de 35 événements de fortes précipitations sélectionnées entre 2011 et 2016 au-dessus de la France (voir la Table A1 de Patou et al. (2018)) et où le suivi des cellules a été réalisé à l'aide d'une méthode de recouvrement temporelle. Un choix important de l'étude était le temps de synchronisation des différents évènements qui a été fixé dans ce cas au dépassement de $3\,\mathrm{mm\,h^{-1}}$ de taux de précipitations observés depuis le sol. On remarque une diminution du CPAR entre 1 heure et deux heures avant le seuil de précipitations. Ceci est expliqué par une organisation moins fractionnée des cellules convectives avant la formation des précipitations.

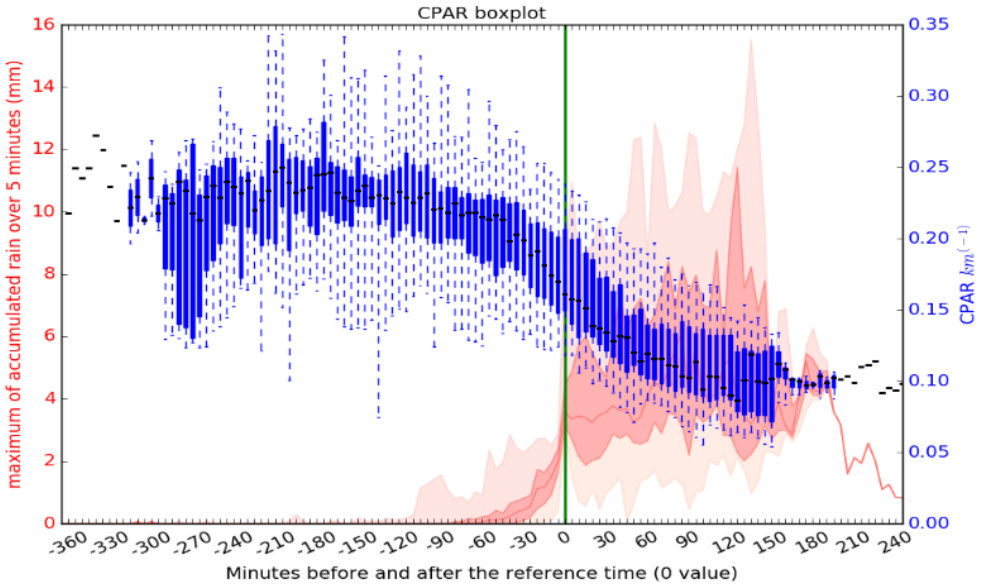

FIGURE 3.23 – Evolution temporelle du CPAR sous forme de boîte à moustaches à partir de 35 suivis de cellules pluvieuses (en bleu). Evolution temporelle des taux de pluie (en rose). La synchronisation temporelle des différents suivis a été faite lorsque les taux de précipitations dépassaient les $3\,\mathrm{mm\,h^{-1}}$.

Chapitre 4

Projet scientifique et conclusion

Sommaire

4.1 Contexte programmatique

À partir de 2022 vont être lancés les premiers satellites des deux grands nouveaux programmes d'observation de la Terre d'EUMETSAT : MTG et EPS-SG auxquels appartiendront aussi les satellites Sentinel 4 et 5 du programme Européen Copernicus (Figure 2.1). Parmi les instruments à bord de ces satellites, plusieurs nouveaux instruments seront assez similaires à ceux déjà existants en ce qui concerne la modélisation du transfert radiatif rapide comme par exemple FCI sur MTG et comme IASI-NG et METimage sur Metop-SG. Mais de nouveaux instruments, que RTTOV ne peut simuler actuellement, vont aussi arriver et nécessiteront de nouveaux développements scientifiques comme les spectromètres imageurs UV/visible/proche infrarouge Ultraviolet Visible Near-infrared (UVN) sur MTG et Sentinel-5/Ultraviolet Visible Near-infrared Shortwave (UVNS) ou comme Multi-Viewing Multi-Channel Multi-Polarisation Imaging (3MI) sur Metop-SG et ses canaux polarisés. Nous avons déjà préparé RTTOV pour simuler les instruments classiques afin que la communauté scientifique puisse se préparer à l'arrivée de ces instruments (Guedj et al., 2014; Andrey-Andrés et al., 2018). Pour les autres instruments, certains travaux de développement sont déjà prévus dans le cadre du projet SAF-NWP en CDOP-3 (jusqu'à mars 2022 comme pour les spectromètres imageurs UV/visible/proche infrarouge) ou sont en discussion dans les équipes du projet pour la prochaine phase de

CDOP-4 (de 2022 à 2027) comme par exemple la prise en compte de la polarisation pour simuler 3MI.

4.2 Projet pour la PNT

4.2.1 Exploitation des premiers satellites infrarouges

Dans le cadre d'un projet C3S qui à débuté à la fin 2018 au nom de code de "311c Lot1" ou au nom plus explicite de "Satellite data rescue", l'équipe Sondage du CEMS a la tâche de préparer et de valider les coefficients RTTOV pour des instruments infrarouges multispectraux et hyperspectraux embarqués sur des satellites ayant observé la Terre entre les années 1970 et les années 1990 (voir la page internet `https://climate.copernicus.eu/observations`). Les observations reformatées et uniformisées de ces instruments ainsi que l'opérateur d'observations satellitaires adapté à eux permettra d'utiliser ces données dans la prochaine version de la réanalyse ERA-6 du CEPMMT dont les premières simulations sont prévues en 2023. Les observations des ces instruments seront aussi proposées à la communauté scientifique par l'intermédiaire du pôle de données ICARE (partenaire du projet). Il n'y aura pas de développements scientifiques particuliers pour ces instruments puisqu'il s'agit d'instruments classiques pour RTTOV comme l'un des premiers sondeur hyperspectral infrarouge InfraRed Interferometer Spectrometer (IRIS) sur Nimbus-4 lancé en 1970 avec 862 canaux entre 400 et 1600 cm^{-1} et plusieurs sondeurs multispectraux infrarouges comme par exemple Temperature-Humidity Infrared Radiometer (THIR) sur les Nimbus-4 à -7 avec 2 canaux à 6.7 et 11.5 µm ou Medium Resolution Infrared Radiometer (MRIR) sur les Nimbus-2 et -3 lancés en 1966 avec 5 canaux. L'instrument MRIR sur Nimbus-3 est un instrument intéressant pour RTTOV car il contient deux canaux très larges, le canal 4 entre 5 et 30 µm centré sur 17 µm et le canal 5 entre 0.4 et 5 µm centré sur 0.9 µm. Les canaux des instruments multispectraux sont généralement peu larges avec des valeurs de l'ordre de quelques dixièmes de micromètre dans le domaine solaire jusqu'à 1 à 2 µm dans l'infrarouge, mais jamais de plusieurs micromètres. Ces canaux beaucoup plus larges permettront à terme de tester la robustesse de RTTOV à condition que les observations soient suffisamment de bonnes qualités. Dans un premier temps, nous avons évalué la précision de ces canaux avec la méthode classique de validation des coefficients. Cette validation des canaux infrarouges à partir des 83 profils d'entraînement est représentée sur la Figure 4.1 pour la version des prédicteurs 7 (c'est-à-dire avec des profils variables de H_2O et O_3) à 54 niveaux verticaux. On peut noter que les statistiques sont dégradées entre le canal large à 17 µm (avec un écart-type de 1 K) et les autres canaux infrarouges (avec des écart-types inférieurs à 0.25 K). Cette dernière valeur est plus typique de la validation des canaux infrarouges. Pour le canal visible, les résultats montrent un écart-type de l'ordre de 0.05 en réflectance ce qui est 10 fois supérieur aux valeurs des canaux visibles de largeurs spectrales plus fines. Pour confirmer ces résultats nous avons prévu de réaliser cette validation sur sur un jeu de profils beaucoup plus important et indépendant que les 83 profils d'entraînement ac-

tuels. Ce jeu sera composé des 25000 profils à 137 niveaux du SAF-NWP (voir la page internet `https://www.nwpsaf.eu/site/software/atmospheric-profile-data/`). Ce travail a déjà démarré par l'intermédaire de Bruna Silveira qui est en post-doc sur ce projet.

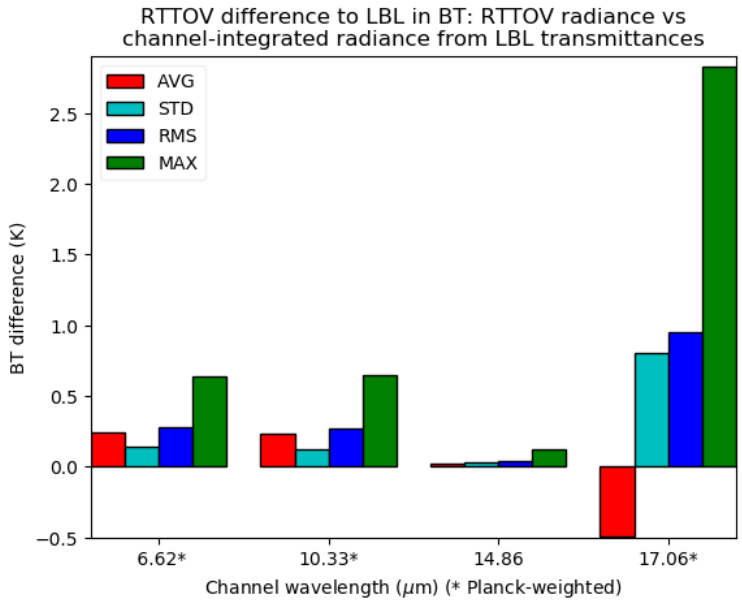

FIGURE 4.1 – Validation des coefficients RTTOV version 7 sur 54 niveaux des 4 canaux infrarouges de MRIR sur Nimbus-3. Pour chaque canal sont donnés en température de brillance les valeurs de biais moyen (en rouge), d'écart-type (en bleu ciel), d'écart quadratique moyen (en bleu foncé) et de maximum de différence (en vert). Les canaux marqués d'une astérisque sont ceux pour lesquels les températures de brillance sont corrigées de la variation spectrale de la fonction de Planck sur la SRF.

Nous avons enfin prévu de tester différentes versions de LBLRTM basées sur 3 versions de HITRAN différentes : 2004 (Rothman et al., 2005), 2008 (Rothman et al., 2009) et 2012 (Rothman et al., 2013), pour estimer les différences dues à la spectroscopie. Cette méthodologie pourra ensuite être appliquée aux instruments actuels ou futurs.

4.2.2 Exploitation du futur instrument IRS

Une nouvelle génération de sondeurs hyperspectraux infrarouges sur orbite géostationnaire est en train d'émerger dans le paysage satellitaire météorologique. Les Chinois sont les pionniers dans ce nouvel épisode spatial avec l'instrument Geostationary Interferometric Infrared Sounder (GIIRS) déjà en vol depuis 2016. L'Europe va aussi se doter d'un tel instrument appelé IRS sur MTG et dont le lancement est prévue en 2022. Cet instrument va permettre d'obtenir sur l'Europe des spectres

infrarouges de sondage toutes les 30 minutes et à 4 km de résolution spatiale au nadir. Par comparaison, les sondeurs hyperspectraux infrarouges sur orbites polaires ont une fréquence de 2 passages par jour et 12 km de résolution spatiale au nadir et 20x40 km en bord de fauchée. Sachant que ces sondeurs fournissent près d'un tiers du contenu en information dans le modèle ARPEGE, on peut logiquement s'attendre à en gagner encore plus avec cette nouvelle génération. Ceci est d'autant plus attendu pour le modèle de PNT à aire limitée AROME centré sur la France. Pour cela, il faut au préalable se préparer à simuler cet instrument et à en tirer le maximum d'information pour enfin l'assimiler. Pour RTTOV la problématique principale liée à cet instrument provient de sa fonction d'apodisation qui entraine une SRF avec de très forts lobes négatifs. La Figure 4.2 montre la SRF théorique de IRS (en bleu) dite "légère" au contraire des SRF de IASI et CrIS dites "forte" où l'on voit nettement les lobes beaucoup moins prononcés avec des valeurs négatives beaucoup moins grandes.

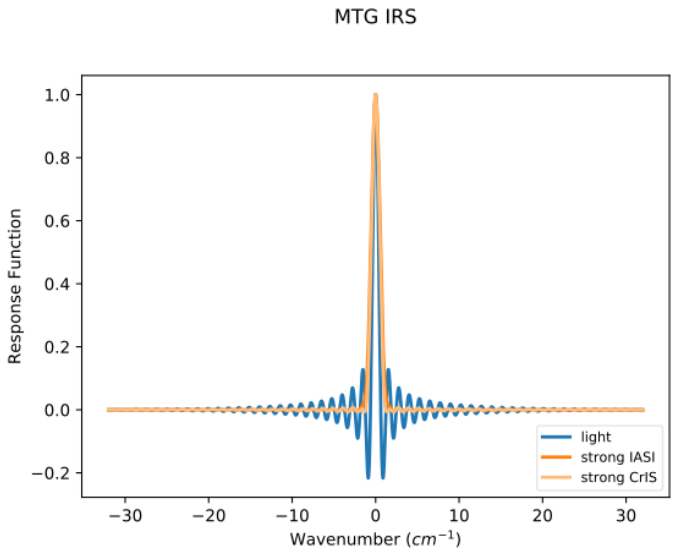

FIGURE 4.2 – SRF de l'instrument IRS en bleu obtenu à partir d'une fonction d'apodisation légère. À titre de comparaison, les fonctions d'apodisations fortes de IASI et CrIS sont aussi tracés en orange clair et foncé, respectivement.

Ces lobes négatifs entraînent des calculs de transmittances négatives lors de la convolution spectrale que la paramétrisation de la transmittance n'arrive pas à reproduire. Les statistiques de validation des coefficients sont alors dégradées. Les Figures 4.3a(a) et 4.3b(b) montrent les statistiques de validation des prédicteurs version 7 à 101 niveaux verticaux obtenues à partir des 83 profils pour IASI et IRS, respectivement. On voit presque un facteur dix entre les erreurs d'un instrument à l'autre.

Il s'agira donc dans un premier temps d'améliorer le calcul des coefficients RTTOV pour ce type de fonction d'apodisation "legère", une possibilité étant de faire 2

jeux de coefficients, un pour les lobes positifs et un pour les lobes négatifs et recombiner les luminances simulées. La demande principale des utilisateurs, notamment en PNT, est la réversibilité des spectres, c'est-à-dire d'être capable à tout moment de revenir dans l'espace des interférogrammes, pour ensuite y appliquer une nouvelle fonction d'apodisation. Cela permettra alors aux utilisateurs d'utiliser les données selon leur besoin. Il s'agira donc ensuite d'en déduire au travers d'études de contenu en information et d'OSSE toutes les informations atmosphériques que nous pourrons en extraire. Ces études se feront en collaboration avec l'équipe Groupe de Modélisation et d'Assimilation pour la Prévision (GMAP)/OBS du CNRM dans deux cadres, tout d'abord avec Olivier Coopman (Fellowship EUMETSAT) sur l'assimilation d'IRS dans AROME et ensuite avec Francesca Vittorioso que je vais co-diriger en thèse avec Nadia Fourrié sur l'apport des luminances IRS pour caractériser la composition chimique de l'atmosphère. À terme ces travaux pourront s'orienter vers le couplage prévision météorologiques et chimie de l'atmosphère qui est un des objectifs de la prospective scientifique du CNRM.

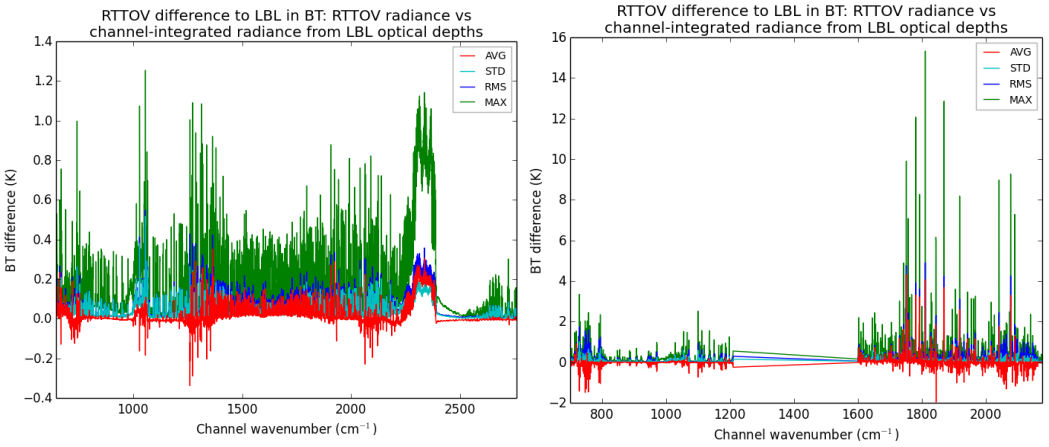

(a) IASI

(b) IRS

FIGURE 4.3 – (a) Equivalent de la Figure 4.1 pour les prédicteurs version 7 de IASI à 101 niveaux verticaux. (b) Mêmes résultats pour IRS. (*NB* : les échelles des axes des ordonnées sont différentes)

4.2.3 Vers une cohérence spectrale des propriétés optiques des nuages et du recouvrement nuageux

L'assimilation des luminances nuageuses et pluvieuses dans le domaine des micro-ondes est déjà opérationnelle dans plusieurs centre de prévision météorologiques (Geer et al., 2018). Les études de faisabilité de l'assimilation des radiances nuageuses dans le domaine infrarouge montrent toutes un impact positif sur la prévision (Martinet et al., 2014a; Okamoto, 2017; Geer et al., 2019). En revanche le modèle RTTOV n'est pas conplètement cohérent spectralement entre ces différents domaines et notamment sur les hypothèses concernant les propriétés optiques des

nuages non précipitants et les méthodes de recouvrement nuageux. Ces incohérences spectrales risquent d'introduire des erreurs lorsque les assimilations des luminances à la fois dans les domaines infrarouge et micro-ondes seront opérationnelles. Par exemple, si la paramétrisation des distributions en taille des cristaux de glace selon Field et al. (2007) est la même en micro-ondes (Geer and Baordo, 2014) et en infrarouge (Vidot et al., 2015), les modèles microphysiques et notamment les hypothèses sur les formes des cristaux sont différents entre les deux domaines spectraux. Ce sujet aura encore plus d'importance avec l'arrivée de nouveaux instruments dans de nouvelles gammes spectrales comme Ice Cloud Imager (ICI) sur EPS-SG (domaine des ondes sub-millimétriques) et FORUM (domaine de l'infrarouge lointain) et dont on sait que les sensibilités aux nuages de glace sont très importantes. Les études préparatoires sur l'instrument FORUM ont montrés aussi l'importance de prendre en compte l'effet de la température sur l'indice de réfraction de la glace dans l'infrarouge lointain. Des échanges ont déjà lieu avec Anthony Baran du UK Met-Office et Alan Geer de CEPMMT pour tenter d'avoir des modèles spectralement cohérents pour les nuages de glace. Il faudra donc envisager une paramétrisation unique sur tous les domaines spectraux en faisant des choix sur les formes et distributions en taille des nuages ainsi que sur des indices de réfraction de l'eau liquide et de la glace. De plus, plusieurs projets à venir permettront de tester ces incohérences/cohérences spectrales, notamment le projet TOSCA Infrarouge, Micro-Ondes et Transfert radiatif ensembliste pour la prévision des Extrêmes de Précipitation (IMOTEP) porté par Philippe Chambon du CNRM. Ce projet vise à développer l'assimilation des luminances nuageuses et pluvieuses micro-ondes et infrarouges et donc à étudier la cohérences spectrales des paramétrisations nuageuses ainsi que leur impact sur les restitutions à partir de ces deux types d'observations. Un autre appel à projet auquel le CNRM a répondu avec HYGEOS et le LOA propose de combiner le sondeur hyperspectral IASI-NG et le sondeur micro-ondes MicroWave Sounder (MWS) afin d'inverser les propriétés optiques des nuages avec une méthode de type 1D-Var avec l'aide de RTTOV. L'autre aspect important pour l'assimilation des luminances nuageuses et qui n'est pas spectralement cohérent dans RTTOV est la méthode de recouvrement entre les domaines infrarouge soit à l'aide de la méthode MRO (Matricardi, 2005) ou de la méthode CMSS (Geer et al., 2019) et celle du domaine des micro-ondes qui combine les profils de tous les hydrométéores (Geer et al., 2009). Il s'agira donc dans le cadre de la CDOP-4 de proposer une méthode plus cohérente spectralement et une piste à entrevoir est l'approche de colonnes indépendantes proposée par ODell et al. (2007).

4.2.4 Amélioration de la paramétrisation de la diffusion

La paramétrisation de la diffusion dans RTTOV a montré son efficacité pour simuler des spectres infrarouges de scènes contenant des nuages de glace et dans une moindre mesure des scènes contenant des nuages en phase liquide ou en phases mélangés avec des biais et écart-types inférieurs à 1 K hormis aux très grands angles de visée (voir Partie 3.4.2). Une évaluation de la paramétrisation de la diffusion dans

l'infrarouge lointain a été réalisée récemment dans le cadre du projet FORUM et les premiers résultats montrent que cette paramétrisation pour les nuages en phase glace n'est pas aussi efficace dans l'infrarouge lointain. La Figure 4.4(A) montre une comparaison, pour une visée au nadir, entre un spectre de température de brillance simulé par RTTOV pour FORUM (en rouge) et simulé par LIDORT qui permet un calcul exact de la diffusion.

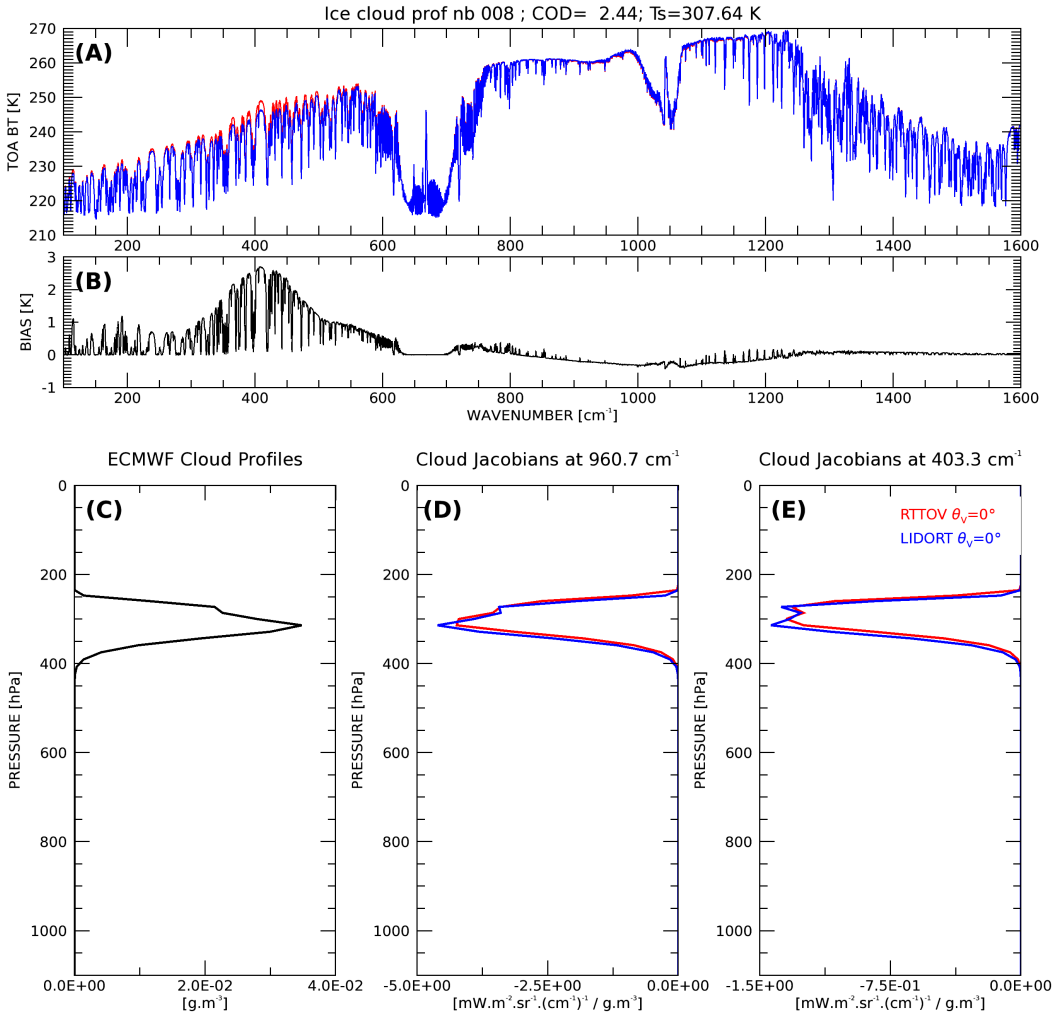

FIGURE 4.4 – (A) Simulations de spectres nuageux en température brillance FORUM à partir de RTTOV (en rouge) et à partir de LIDORT (en bleu) pour un angle de visée au nadir. L'épaisseur optique du nuage est de 2.44 à $1000\,\mathrm{cm}^{-1}$ et la température de surface est de 307.64 K. (B) Biais spectral en température de brillance RTTOV moins LIDORT. (C) Profil CEPMMT d'IWC. Jacobiens nuageux (en $\mathrm{mW/(m^2\,sr\,cm^{-1})}$ / $\mathrm{g\,m^{-3}}$) dans le canal à $960.7\,\mathrm{cm}^{-1}$ (D) et dans le canal à $403.3\,\mathrm{cm}^{-1}$ (E) calculé à partir de RTTOV (en rouge) et à partir de LIDORT (en bleu).

Un biais important de 2.5 K est visible vers $400\,\mathrm{cm}^{-1}$ alors qu'il reste très faible

dans les canaux fenêtres (Figure 4.4(B)). Les jacobiens nuageux représentés aux Figures 4.4(D) et 4.4(E) sont en revanche plutôt comparables entre les deux modèles de transfert radiatif. Ces biais plus importants dans l'infrarouge lointain sont confirmés sur la Figure 4.5. La Figure montre le biais spectral (en haut) et l'écart-type spectral (en bas) calculés à partir des 212 profils de nuage de glace au nadir. On voit nettement la dégradation entre l'infrarouge moyen et l'infrarouge lointain. Les erreurs étant déjà importantes au nadir, on peut imaginer qu'elles seront pires aux autres géométries comme pour le moyen infrarouge (voir Figure 3.19). Ces différences nécessiteront d'être évaluées à d'autres angles d'observation. L'hypothèse principale sur laquelle repose la paramétrisation de Chou et al. (1999) est de considérer le rayonnement hémisphérique isotrope dans l'infrarouge. Cette méthode permet alors de séparer le calcul de la luminance descendante et de la luminance montante. Pour améliorer les simulations, Tang et al. (2018) proposent une méthode d'ajustement basée sur une correction de la luminance descendante qui est calculée en premier lorsqu'on résout le transfert radiatif depuis le sommet de l'atmosphère jusqu'à la surface comme dans RTTOV. Cet ajustement de la paramétrisation de la diffusion donne de meilleurs résultats en comparaison avec des calculs de diffusion complète sur des flux montants aux grandes longueurs d'onde Tang et al. (2018). Cette méthode pourra être testée dans RTTOV à la fois pour l'infrarouge lointain mais aussi pour l'infrarouge moyen dans le cas des nuages en phase liquide ou en phases mélangées.

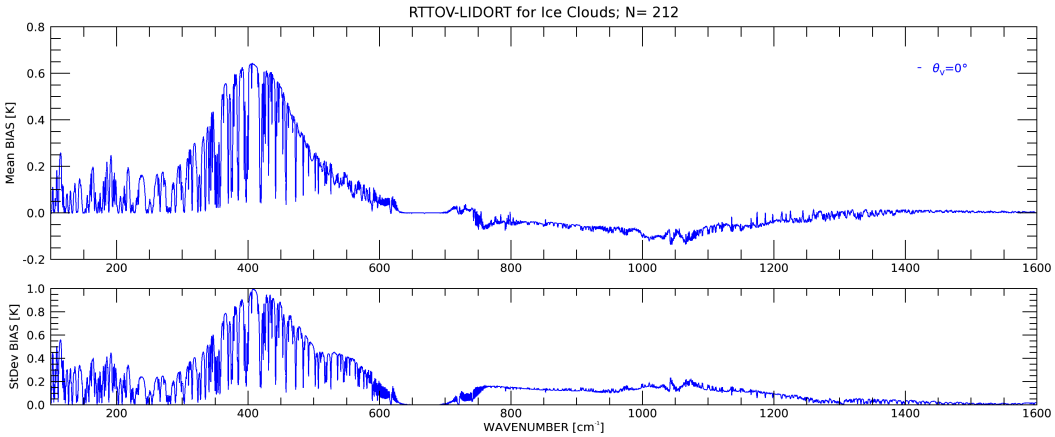

FIGURE 4.5 – Biais moyen (en haut) et écart-type (en bas) spectraux obtenus au nadir entre les simulations RTTOV et LIDORT à partir de 212 profils de nuage en phase glace pour FORUM.

4.3 Projet pour la chimie atmosphérique

4.3.1 Simulation d'instruments hyperspectraux de l'UV au proche infrarouge

L'extension des simulations de RTTOV au domaine spectral de l'UV fait partie des demandes récurrentes des utilisateurs. L'application principale concerne la forte sensibilité de l'ozone atmosphérique aux longueurs d'ondes de l'UV. Cette extension couvrira deux aspects de mon travail. Le premier concernant la capacité de la paramétrisation des transmittances atmosphériques à fonctionner dans le domaine UV mais surtout à reproduire les caractéristiques spectrales des instruments hyperspectraux tels que UVN et UVNS sur les satellites Sentinel 4 et 5, respectivement. En effet si l'extension au domaine de l'infrarouge lointain n'a pas posé de difficulté essentiellement expliquées par la prépondérance de la vapeur d'eau dans ce domaine, dans le domaine solaire d'autres molécules pourront éventuellement poser des problèmes. La Figure 4.6 montre la transmittance totale atmosphérique pour le profil moyen des profils d'entraînement (profil 83) pour les molécules les plus absorbantes. On peut voir que plusieurs molécules ont des signatures spectrales très fortes comme la vapeur d'eau (en cyan), le dioxyde de carbone (en bleu), le méthane (en rose). On peut voir aussi l'absorption par l'oxygène à 0.76 µm par exemple. Cette molécule ne devrait pas poser de problème puisque son profil est constant dans l'atmosphère. Mais il sera intéressant de voir comment la paramétrisation de la transmittance de RTTOV est capable de simuler les luminances dans les bandes d'absorption de l'oxygène à haute résolution spectrale.

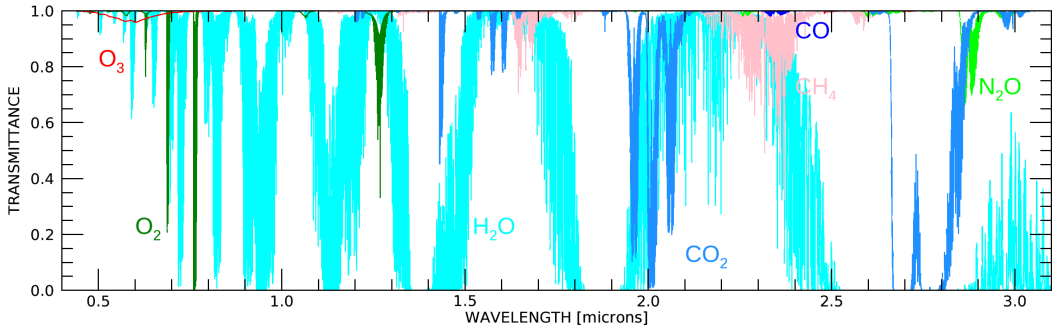

FIGURE 4.6 – Transmittance totale raie-par-raie par molécule des molécules les plus absorbantes dans le domaine solaire. Le profil 83 du jeu d'entraînement a été utilisé.

Le deuxième aspect de cette extension de RTTOVconcerne le modèle de BRDF des surfaces qui ne prend pas en compte l'UV actuellement. Il sera donc nécessaire d'étendre le modèle de BRDF à l'UV en suivant par exemple la méthodologie de Zoogman et al. (2016) qui est similaire à celle que j'ai développé mais qui utilise des spectres de réflectance issus de mesures laboratoires couvrant le domaine UV.

4.3.2 Validation des propriétés optiques des aérosols

Les aérosols atmosphériques attirent l'attention de la communauté météorologique depuis plusieurs années. L'assimilation des aérosols dans les modèles de chimie-transport dans un premier temps et dans les modèles de PNT, voire les modèles couplés atmosphère/chimie dans un deuxième temps font partie des objectifs de la prospective scientifique du CNRM du prochain quadriennal. Au CEMS, les aérosols sont aussi étudiés depuis quelques années dans l'équipe Océan dans le cadre du projet SAF for Ocean and Sea-Ice (SAF-OSI). En effet, l'impact des aérosols désertiques sur la restitution des Température de Surface de la Mer (TSM) à partir de radiomètres infrarouges est très important compte-tenu de la précision requise sur les restitutions (de l'ordre de 0.5 K). Pour corriger l'effet des aérosols désertiques sur la TSM, un indice a été développé par Merchant et al. (2006)) à partir de simulations RTTOV. En effet, les aérosols sont pris en compte dans RTTOV depuis la version 9. Les premiers modèles implémentés par Matricardi (2005) étaient basés sur OPAC (Hess et al., 1998). Par la suite d'autres modèles ont été implémentés comme pour les poussières volcaniques et les modèles Copernicus Atmospheric composition Monitoring Service (CAMS) (Saunders et al., 2018). En revanche ces modèles d'aérosols n'ont jamais été véritablement validés, si ce n'est le travail de Matricardi (2005) avec une simulation de spectre infrarouge pour chaque type d'aérosols. Pour aller plus loin, j'ai entrepris un travail de validation dès 2015 dans le cadre du projet EECLAT avec une méthodologie similaire à celle développée pour la validation des propriétés optiques des nuages de glace. En effet, les observations du lidar CALIOP colocalisées avec IIR sont aussi une mine d'information très importante pour la détection et la caractérisation des aérosols et pour la validation des simulations RTTOV. Cependant, les inversions à partir de CALIOP ne permettent pas d'obtenir les profils de concentration en aérosols nécessaires en entrée de RTTOV et j'ai donc utilisé les champs du modèle de chimie du CEPMMT CAMS. Un premier travail de validation a été réalisé à partir de 3887 observations IIR sélectionnées à partir du masque aérosols de CALIOP du produit v4.10 (Getzewich et al., 2018). La Figure 4.7 montre les épaisseurs optiques des aérosols à 532 nm des 3887 cas sélectionnés à partir du masque aérosols dans la semaine du 22 au 27 avril 2015 sur l'océan Atlantique au large de l'Afrique de l'Ouest.

On voit clairement un panache d'aérosols désertiques provenant des déserts africains se propager sur l'océan Atlantique. Il est à noter qu'un seuil d'épaisseur optique supérieur à 0.1 a été choisi pour la sélection des cas. La Figure 4.8 montre les températures de brillance au sommet de l'atmosphère simulées par RTTOV en fonction de celles observées par IIR dans le canal à 8.7 µm. Pour les simulations RTTOV, trois configurations ont été testées : sans aérosols (en vert), avec aérosols et la paramétrisation de la diffusion (en bleu), avec aérosols et la diffusion complète avec RTTOV_DOM (en rouge).

La prise en compte des aérosols permet de réduire le biais de 0.61 K à 0.05 K avec la paramétrisation de la diffusion et à 0.09 K avec la diffusion complète. Les écarts-types ne sont pas modifiés mais les histogrammes montrent en revanche deux pics

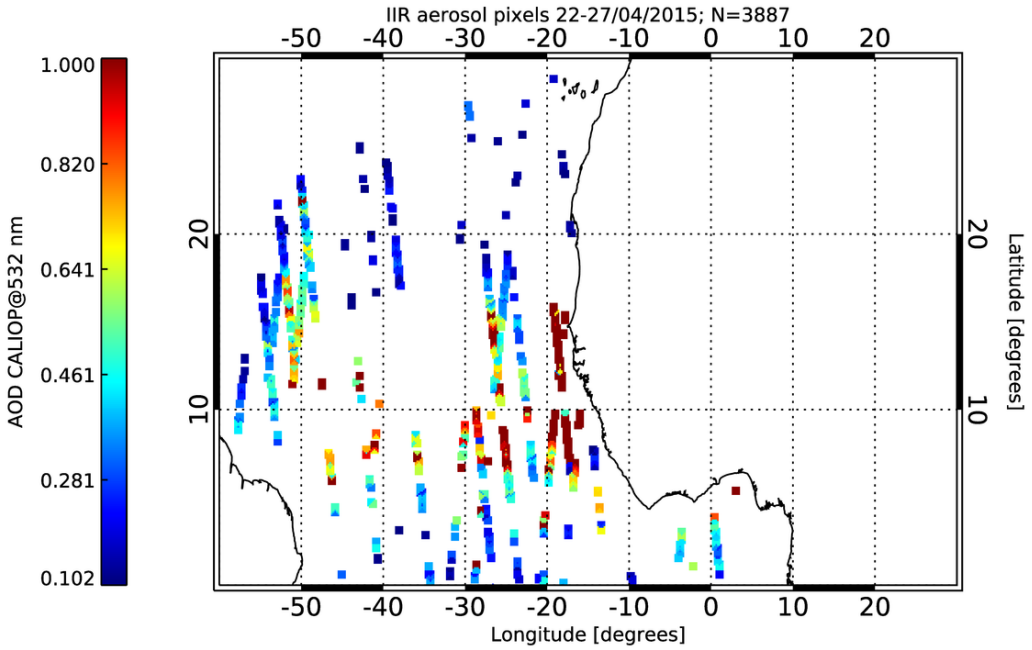

FIGURE 4.7 – Epaisseur optique des aérosols restituées par Caliop à 532 nm des 3887 observations sélectionnées dans la semaine du 22 au 27 avril 2015 pour la validation des simulations RTTOV.

avec les aérosols et semblent plus élargis. La comparaison dans les autres canaux IIR confirme la réduction de biais d'environ 0.6 K mais avec un basculement dans les biais négatifs puisque sans les aérosols, les biais ne sont que 0.3 K. L'élargissement des histogrammes est confirmé dans les autres canaux (non montrés). L'étape suivante de la validation des aérosols de RTTOV a été de comparer les épaisseurs optiques CALIOP avec celles estimées par RTTOV. La Figure 4.9 montre les histogrammes des épaisseurs optiques aérosols issues de CALIOP à 532 nm et les épaisseurs optiques à 550 nm (calculées en simulant MODIS plutôt que IIR). On peut noter qu'à la fois les faibles et les fortes épaisseurs optiques ne sont pas bien simulées par RTTOV. Ces résultats nécessiteront d'être confirmés sur un nombre d'observations plus important et de comprendre si ces différences d'épaisseurs optiques proviennent des profils d'entrée CAMS ou si elles proviennent des propriétés optiques de RTTOV. Il est à noter que les premiers résultats de cet exercice nous confirme la robustesse de la paramétrisation de la diffusion par les aérosols mais il s'agira aussi de confirmer cela sur une plus large base de données en fonction de l'épaisseur optique par exemple. Lorsque la méthode d'ajustement de la paramétrisation de la diffusion de Tang et al. (2018) sera intégrée pour les nuages, elle pourra être facilement testée pour les aérosols.

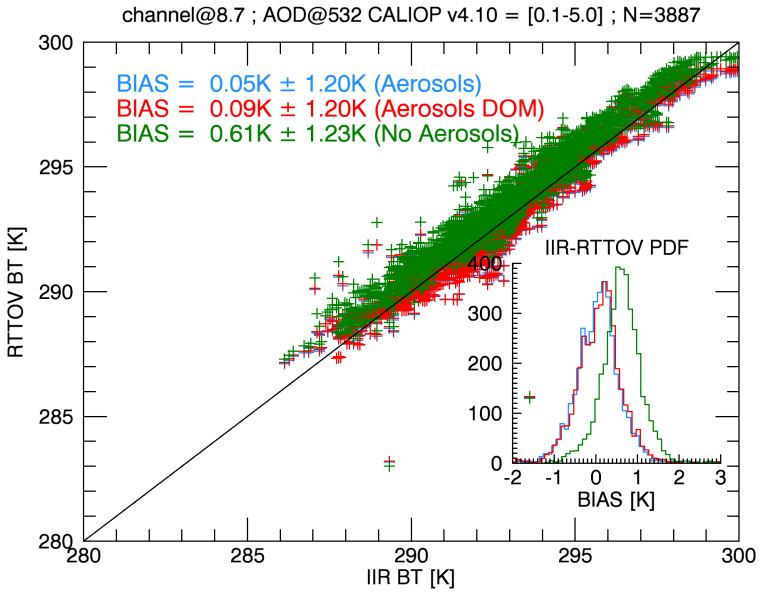

FIGURE 4.8 – Températures de brillance (en K) simulées par RTTOV et observées par IIR dans le canal à 8.7 µm pour trois configurations de RTTOV : sans aérosols (en vert), avec aérosols et la paramétrisation de la diffusion (en bleu) et avec aérosols et la diffusion complète avec RTTOV_DOM. Les histogrammes des différences entre observations et simulations sont aussi montrés.

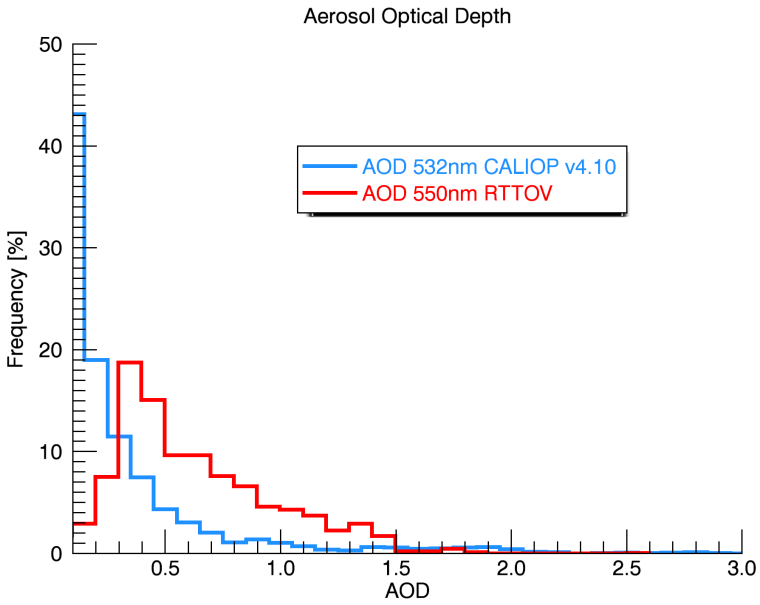

FIGURE 4.9 – Histogrammes des épaisseurs optiques des aérosols à 532 nm issues des produits de niveau 2 de CALIOP v4.10 (en bleu) et des épaisseurs optiques des aérosols à 550 nm issues des simulations RTTOV pour MODIS (en rouge).

4.4 Conclusion

Depuis mon arrivée au CEMS en 2010, les activités de mes recherches se sont essentiellement centrées sur le modèle de transfert radiatif rapide RTTOV. Ce modèle développé depuis plusieurs dizaines d'années pour les besoins opérationnels en assimilation d'observations satellites des centres de prévisions météorologiques est considéré par la communauté météorologique internationale comme un modèle de référence, tant par sa précision que par sa rapidité et sa large applicabilité. Ceci est fondamentalement lié à la méthode de paramétrisation de la transmittance atmosphérique qui date du milieu des années 1970 et permet toujours d'assimiler un nombre considérable de luminances en ciel clair à partir d'observations spatiales dans les domaines infrarouges et micro-ondes.

La structuration des développements du modèle est unique grâce au soutien d'EUMETSAT par le projet SAF-NWP. Les différentes équipes qui travaillent sur RTTOV jouissent d'un cadre favorisant les développements scientifiques dans plusieurs thématiques et ceux-ci sont assurés pour encore plusieurs années avec les futurs programmes spatiaux MTG et EPS-SG.

Dans ce projet, les thématiques de recherche de mon travail se sont rapidement orientées vers le domaine infrarouge et, compte-tenu de mes expériences passées, vers l'extension du modèle au domaine visible et proche infrarouge. Ainsi, j'ai pu rapidement proposer deux travaux importants, un premier sur un modèle de BRDF hyperspectral dont l'utilisation reste encore marginale mais qui est encouragée par le UK Met-Office avec la production opérationnelle d'images satellites prévues. Le deuxième concerne une paramétrisation des propriétés optiques des nuages de glace, au départ dans l'infrarouge mais maintenant sur plusieurs domaines spectraux allant du visible à l'infrarouge lointain. Cette nouvelle paramétrisation permettra à terme d'assimiler de manière opérationnelle les luminances infrarouges nuageuses dans les modèles de PNT. Les premiers résultats des travaux d'assimilation qui utilisent cette paramétrisation sont très encourageants.

La confrontation du modèle RTTOV à d'autres modèles de transfert radiatif est une étape importante de validation. Les différentes intercomparaisons que j'ai pu réaliser, que ce soit en ciel clair ou en ciel nuageux ont permis de réaffirmer la qualité du modèle mais aussi de mettre en évidence certains défauts qu'il faudra améliorer dans le futur.

Par ailleurs, les travaux d'assimilation des luminances infrarouges nuageuses et pluvieuses dans les modèles de PNT amènent des questions élémentaires sur la modélisation du transfert radiatif, notamment sur la cohérence spectrale de RTTOV entre les différents domaines spectraux. En effet, la cohérence spectrale des propriétés microphysiques et optiques mais aussi du recouvrement nuageux sont des enjeux très importants et un travail conséquent sera nécessaire dans les années à venir. De plus, si la paramétrisation de la diffusion dans l'infrarouge est très efficace pour certains types de nuage comme les nuages de glace, il faudra aussi l'améliorer pour la rendre plus précises dans tous les domaines infrarouges et pour tous les diffusants, nuages comme aérosols.

Enfin il faudra se préparer aux enjeux apportés par les nouveaux instruments comme les sondeurs hyperspectraux infrarouges sur satellites géostationnaires dont les retombées scientifiques sont nombreuses ou les spectromètres UV/visible/proche infrarouge. Dans toutes ces nouvelles orientations scientifiques, il s'agira encore de transférer des travaux fondamentaux vers des applications opérationnelles en s'appuyant sur mon expertise mais aussi sur les compétences de la communauté scientifique.

Chapitre 5

Mes principales publications

Sommaire

5.1 Vidot et Borbas (2014)

Cet article publié en 2014 dans *Quarterly Journal of the Royal Meteorological Society* (facteur d'impact de 3.198) est le premier article que j'ai publié sur le modèle RTTOV. Ce travail est le fruit d'une collaboration avec Eva Borbas (Cooperative Institute for Meteorological Satellite Studies (CIMSS)) qui m'avait invité à venir passer une semaine aux USA pour démarrer cette étude. Les résultats ont été montrés dans deux conférences (ITSC-18, IRS-2012) et m'a permis d'intégrer le groupe de travail international sur les surfaces terrestres ISWG. Ce travail est maintenant utilisé au UK Met-Office pour la production opérationnelle d'images satellites prévues.

Quarterly Journal of the Royal Meteorological Society Q. J. R. Meteorol. Soc. 140: 2186–2196, October 2014 A DOI:10.1002/qj.2288

RMetS
Royal Meteorological Society

Land surface VIS/NIR BRDF atlas for RTTOV-11: model and validation against SEVIRI land SAF albedo product

Jérôme Vidot[a]* and Éva Borbás[b]
[a]*Centre de Météorologie Spatiale, DP/Météo-France, Lannion, France*
[b]*SSEC/CIMSS, Madison, WI, USA*

*Correspondence to: J. Vidot, Centre de Météorologie Spatiale, DP/Météo-France, Avenue de Lorraine, 22300, Lannion, France.
E-mail: jerome.vidot@meteo.fr

This study describes the scientific approach and the validation of the visible and near-infrared snow-free land surface Bidirectional Reflectance Distribution Function (BRDF) atlas for Version 11 of the Radiative Transfer for the Television Infrared Observation Satellite (TIROS) Operational Vertical Sounder (TOVS) (RTTOV) Forward Model. The atlas provides a global (at a spatial resolution of 0.1°) and monthly mean land surface BRDF for any instrument containing channels with a central wavelength between 0.4 and 2.5 μm, as well as a quality index of the BRDF. It is based on the reconstructed hyperspectral BRDF from the seven channels of the operational and global Moderate Resolution Imaging Spectroradiometer (MODIS) 16 days BRDF kernel-driven product MCD43C1: a principal component analysis regression method was applied between the seven channels of the MODIS BRDF products and a set of the US Geological Survey hyperspectral reflectance measurements for soils, rocks, and mixtures of both and vegetation surfaces. The comparison of the RTTOV BRDF atlas against the Spinning Enhanced Visible and Infrared Imager (SEVIRI) surface black-sky albedo products of the European Organization for the Exploitation of Meteorological Satellites (EUMETSAT) Land Satellite Application Facility on Land Surface Analysis (Land-SAF) shows good spatial and temporal consistency of the RTTOV BRDF atlas when applied on three SEVIRI visible and near-infrared channels. The RTTOV narrowband black-sky albedo is retrieved within ±0.01 in absolute accuracy at 0.6 and 1.6 μm and is overestimated by something between 0.01 and 0.03 at 0.8 μm. The temporal variation of the RTTOV broadband black-sky albedo is consistent with the EUMETSAT Land-SAF SEVIRI products but overestimated by somewhere between 0.01 and 0.02 when considering the best quality index of the RTTOV BRDF atlas. Less agreement is found in two cases: (i) for extreme geometrical conditions when the satellite zenith angle is greater than 65° and (ii) for lower quality indices of the RTTOV BRDF atlas.

Key Words: radiative transfer; solar domain; satellite retrievals; surface properties

Received 29 August 2012; Revised 22 October 2013; Accepted 29 October 2013; Published online in Wiley Online Library 12 February 2014

1. Introduction

Since the early 1990s, the direct assimilation of satellite radiances into the numerical weather prediction (NWP) models led operational meteorological centres to develop fast radiative transfer models. The Radiative Transfer for the Television Infrared Observation Satellite (TIROS) Operational Vertical Sounder (TOVS) (RTTOV) model emerged in Europe at this time (Eyre and Woolf, 1988; Eyre, 1991) and has been continuously supported by the NWP Satellite Applications Facility (SAF) team since then to simulate the new generation of instruments in terms of computational cost, accuracy and spectral characteristics (Saunders *et al.*, 1999; Matricardi *et al.*, 2004; Bauer *et al.*, 2006; Matricardi, 2009). The last version of RTTOV (Version 10) covers the spectral range of 500–3300 cm^{-1} in the infrared and the frequency range of 10–200 GHz in the microwave region. The model uses a linear combination of profile-dependent predictors for computing the gaseous transmittance and is able to take into account both clouds and aerosols using simplified scattering schemes (Saunders *et al.*, 2010). These methods ensure the efficiency of the RTTOV model in the NWP environment for the fast computation of both the direct top of atmosphere (TOA) radiances and the gradient of the radiances with respect to the atmospheric state vector (or Jacobian) that is necessary in the data assimilation variational scheme (English *et al.*, 2000; Pavelin *et al.*, 2008; Bauer *et al.*, 2010; Geer *et al.*, 2010).

At the lower boundary of the RTTOV model, treatment of the surface emissivity is realized through different possibilities,

either by using fixed standard values or by using different atlases and/or models. In the infrared, the surface emissivity is provided by the Infrared Surface Emissivity Model (ISEM: Sherlock, 1999) over water and by the University of Wisconsin infrared land surface emissivity atlas (UWIREMIS: Borbas and Ruston, 2010) for land surfaces. In the microwave, the surface emissivity is provided by an atlas from the Centre National de la Recherche Météorologique (CNRM: Karbou *et al.*, 2005) or from the Tool to Estimate Land Surface Emissivities in the Microwave (TELSEM: Aires *et al.*, 2011) for land surfaces and from the fast microwave emissivity model (FASTEM: Liu *et al.*, 2011) for water surfaces. The UWIREMIS, CNRM and TELSEM databases were developed from satellite measurements in order to better characterize the spatial and temporal variability of natural surfaces as seen from a satellite.

In the next version of RTTOV (Version 11), users will be able to simulate clear-sky satellite observations in the visible and in the near-infrared (VIS/NIR) spectral regions. Even if assimilating VIS/NIR radiances is not a priority for improving numerical weather prediction, the scientific community has recognized that fast radiative transfer models simulating satellite observations in VIS/NIR are needed. For example, the current assimilation of satellite-based cloud and precipitation products lacks information about mean particle size (Errico *et al.*, 2007). The NIR radiances are known to be sensitive to effective particle radius at the top of the cloud (Nakajima and King, 1990). Furthermore, in nowcasting and very short-term forecasting, both solar and thermal spectral regions are used for cloud detection and classification (see e.g. Derrien and LeGléau, 2005). It is also known that solar channels are very sensitive to aerosols, and VIS/NIR have been used for many years to retrieve aerosols' optical properties (King *et al.*, 1999).

In cloud-free situations over land, the major contribution to the TOA VIS/NIR radiances comes from the surface. As for thermal infrared or microwave spectral regions, the surface optical properties exhibit strong spectral signatures that depend on the surface type. Furthermore, in the VIS/NIR, the surface optical properties also exhibit a strong geometrical dependency that varies by geometries of the solar and the satellite directions. To describe the spectral and the geometrical dependencies of the surface, the surface optical properties are represented by the Bidirectional Reflectance Distribution Function (BRDF). Additionally, the surface optical properties of vegetation-covered areas present a non-negligible seasonal dependency. In order to take into consideration the spectral, geometrical and temporal dependencies of the land surface VIS/NIR BRDF, we combined hyperspectral reflectance laboratory measurements (to account for the spectral variability of land surfaces) and global and seasonal satellite-based retrievals of the BRDF (to account for both surface type and geometrical and seasonal variability of the surface optical properties). The methodology was derived from the work of Borbas *et al.* (2007) and Seemann *et al.* (2008) for infrared land-surface emissivity and was developed similar to the RTTOV UWIREMIS atlas (Borbas and Ruston, 2010). The UWIREMIS atlas has already been demonstrated successfully in different applications (Vogel *et al.*, 2011; De Wachter *et al.*, 2012; Pavelin and Candy, 2013), and this work represents a natural extension of the model to BRDF.

The concept is to reconstruct hyperspectral BRDF spectra by constraining/fitting the satellite-derived BRDF retrievals at specific channels with the principal components (PC) of a representative set of hyperspectral surface reflectance spectra. The BRDF of any instrument with channels having central wavelengths in the VIS/NIR is then estimated by interpolation from the reconstructed hyperspectral BRDF spectra. The principal components analysis (PCA) is based on the assumption that the reflectance (or emissivity) of an area observed from a satellite is a linear combination of the different types of terrestrial materials found in that area (Tobin *et al.*, 2006). Therefore, the set of hyperspectral surface reflectance spectra must be representative of materials that can be found on Earth. For this purpose, we used the hyperspectral laboratory measurements database from the US Geological Survey (USGS) and the BRDF retrieval products from the Moderate Resolution Imaging Spectroradiometer (MODIS) Land Science Team. The MODIS 16 days BRDF (called MCD43C1) products at 0.05° spatial resolution provide three model parameters that allow the full description of the BRDF at seven VIS and NIR channels (at 0.470, 0.555, 0.659, 0.865, 1.24, 1.64 and 2.13 μm). The central wavelengths of the MODIS channels have been chosen as fitting points for the PCA regression method. The study is as follows: section 2 presents the global MODIS Level 3 BRDF kernel-driven product; section 3 presents the USGS laboratory spectra selected for VIS and NIR spectral regions and gives a description of the PCA regression method; section 4 gives details of the resampling of the MODIS dataset at 0.05° spatial resolution to a new database of global monthly mean BRDF parameters at 0.1° spatial resolution and an associated quality index; in section 5 we perform a validation of the RTTOV BRDF atlas by comparing monthly mean RTTOV narrowband black-sky albedo (BSA) with the Land SAF surface albedo daily products from the Spinning Enhanced Visible Infra-Red Imager (SEVIRI) in VIS/NIR channels (at 0.6, 0.8 and 1.6 μm), as well as by comparing the temporal variation of broadband BSA over 9 months; our conclusions and perspectives are given in section 6.

2. The MODIS Level 3 BRDF kernel-driven product

The MODIS Level 3 BRDF kernel-driven product (named MCD43C1, see https://lpdaac.usgs.gov/products/modis_products_table/mcd43c1) is one of the operational MODIS land-surface products (Schaaf *et al.*, 2002). The MODIS land-surface products have been validated against *in situ* measurements (Jin *et al.*, 2003; Wang *et al.*, 2010; Cescatti *et al.*, 2012) or have been compared with other satellite-based land-surface albedo from the Multiangle Imaging SpectroRadiometer instrument (Pinty *et al.*, 2011). Globally, the MODIS products are able to capture the seasonal cycle of snow-free surface albedo with an accuracy better than 0.05 but are less satisfactory for high solar zenith angles (Liu *et al.*, 2009). The MODIS surface products have been widely used for many applications, e.g. for land-surface energy budgets (Wang *et al.*, 2004; Barlage *et al.*, 2005) or for climate models (Roesch *et al.*, 2004; Houldcroft *et al.*, 2009). The MCD43C1 product combines both Terra and Aqua satellites over a 16 day period of acquisition and is provided globally at 0.05° of spatial resolution. This product was derived from the original 1 km spatial resolution of MODIS data and was developed for the global modelling community (Gao *et al.*, 2005). We used collection 5 of the product that contains three retrieved BRDF model parameters (f_{iso}, f_{vol} and f_{geo}) for each MODIS VIS/NIR channel and three associated pieces of information on quality and inputs. The MODIS BRDF is modelized by using the semi-empirical linear model of Ross-Li (Lucht *et al.*, 2000), which is given by:

$$R(\theta_{sat}, \theta_{sol}, \Delta\phi, \lambda) = f_{iso}(\lambda) + f_{vol}(\lambda)K_{vol}(\theta_{sat}, \theta_{sol}, \Delta\phi) + f_{geo}(\lambda)K_{geo}(\theta_{sat}, \theta_{sol}, \Delta\phi), \quad (1)$$

where θ_{sat}, θ_{sol} and $\Delta\phi$ are the satellite zenith angle, the solar zenith angle, and the azimuth difference between satellite and solar directions, respectively, and λ is the wavelength. The first BRDF model parameter f_{iso} is due to isotropic scattering; the second, f_{vol}, is due to volumetric scattering from horizontally homogeneous leaf canopies; the third, f_{geo}, is due to geometric–optical surface scattering as from scenes containing three-dimensional objects that cast shadows and are mutually obscured from view at off-nadir angles. The formulation of the BRDF model kernels K_{vol} and K_{geo} can be found in Lucht *et al.* (2000) and were derived from previous works (Roujean *et al.*, 1992; Wanner *et al.*, 1995).

The three MCD43C1 collection-5 associated pieces of information are: (i) the collection-5 simplified albedo quality

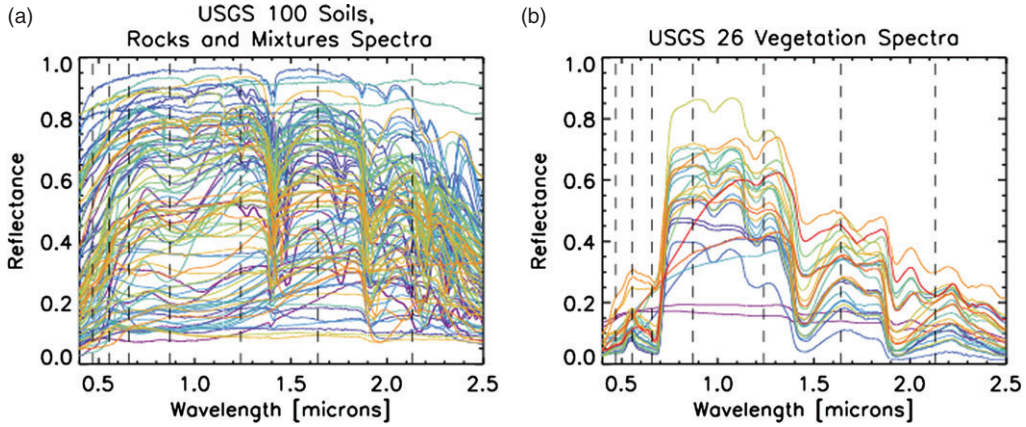

Figure 1. Spectral reflectance for (a) soils, rocks and mixtures and (b) vegetation surface types selected from the USGS Digital Spectral Library 06. Central wavelengths of the seven VIS/NIR MODIS channels are represented by dashed lines.

(called hereafter QA) that provides information about the quality of the retrieval; (ii) the percentage of inputs (from the native MODIS spatial resolution of ∼1 km) between 0 and 100% (called hereafter PI); and (iii) the percentage of snow coverage between 0 and 100% (called hereafter PS). The collection-5 simplified albedo quality QA has five different values:

- QA = 0 for best quality retrieval, i.e. for 75% or more with best full inversions;
- QA = 1 for good quality retrieval, i.e. for 75% or more with full inversions;
- QA = 2 for mixed retrieval, i.e. for 75% or fewer full inversions and 25% or fewer filled values;
- QA = 3 for inversions of all magnitudes or 50% or fewer filled values;
- QA = 4 for 50% or more filled values.

3. Principal component analysis on selected USGS laboratory spectra

The USGS Digital Spectral Library Version 6 is freely available at http://speclab.cr.usgs.gov/spectral-lib.html. It is a compilation of over 1300 hyperspectral reflectance spectra of natural and man-made materials measured in the laboratory, during field campaigns or from aircraft instrumentations (Clark *et al.*, 2007). The database provides reflectance spectra for six classes of surface types (mineral, soil/rock/mixture, coating, water, man-made and vegetation). The database covers ultraviolet to mid-infrared spectral regions (from 0.2 to 150 μm) at different spectral resolutions (between 0.002 and 0.03 μm), but the spectral range of each laboratory spectrum differs by surface type. To apply those VIS/NIR spectra in the RTTOV forward model over land surfaces, we considered all the spectra that cover the spectral range between 0.4 and 2.5 μm for soils, rocks, and mixtures of both and vegetation surface types. After this spectral range criteria and some visual inspection, we selected a total number of 126 spectra (100 spectra for soils, rocks, and mixtures of both and 26 spectra for vegetation). It is worth noting that the spectral reflectance measurements were obtained in two different configurations: (i) in the laboratory, where the spectrometer uses an integrating sphere and where the incident beam was normal to surface sample; and (ii) during field campaigns, where the data where collected around noon with an incident angle of the spectrometer between 20° and 40°. The proportion of spectra obtained within these two configurations is half-half for soils, rocks and mixtures and is one-third to two-thirds for vegetation, respectively, for the configurations listed above. The spectral resolution of the selected 126 spectra has been made uniform to 0.01 μm, leading to 2101 spectral points for each spectrum. Figure 1 shows the spectral variation of reflectances for soils, rocks, and mixtures of (a) both and (b) vegetated surface types. The vertical dashed lines represent the central wavelength of the seven VIS/NIR MODIS channels. As compared with soil, rocks and mixtures of both surfaces, most vegetation surface spectra exhibit clear spectral signatures with low reflectance in the visible (with a small chlorophyll peak signature at 0.55 μm) and high reflectance between 0.8 and 1 μm. We noticed that even for vegetation spectra, the USGS selected spectra provide a large variability of reflectance over the entire spectral domain.

As a next step, the PCA regression method was applied. The PCs (or eigenvectors) of the 126 selected laboratory spectra were regressed against the satellite-derived BRDF for a given location as follows:

$$\mathbf{R} = \mathbf{c}\mathbf{U}, \tag{2}$$

where **R** is the vector of the BRDF at the MODIS VIS/NIR bands, **c** is the regression coefficient vector and **U** is the matrix of the first few PCs of the high spectral resolution laboratory spectra on the MODIS VIS/NIR bands. To obtain the PCs on the resolution of the MODIS VIS/NIR bands, the high spectral resolution eigenvectors were convolved with the spectral response functions of the MODIS bands. Those first few PCs should represent the variation of the laboratory measurements with good accuracy.

To finally reconstruct the hyperspectral BRDF spectra at any latitude and longitude from the retrieved MODIS BRDF, the regression coefficients **c** are calculated as follows:

$$\mathbf{c} = \mathbf{R}\mathbf{U}^{\mathrm{T}}(\mathbf{U}\mathbf{U}^{\mathrm{T}})^{-1}. \tag{3}$$

The reconstructed hyperspectral BRDF values are then determined by using Eq. (2), where the PCs obtained from the laboratory spectra are on the original high spectral resolution.

The number of PCs is limited by the total number of available channels of the 16 days MODIS BRDF products (i.e. seven channels) that were chosen and resampled in our study. After preliminary tests (see more information in Borbas *et al.*, 2007) the most optimal number of PCs resulting in the best agreement between the original laboratory measurements and reconstructed spectra was found to be six. This number of PCs was therefore used in this study.

4. The RTTOV BRDF atlas

The monthly mean RTTOV BRDF atlas at 0.1° of spatial resolution was obtained by resampling the MODIS MCD43C1 products and combining the retrieval quality, inputs and snow information. It is based on the selection of the best pixels from MCD43C1 data by applying iterative tests. The methodology was as follows: for all original MODIS MCD43C1 data within a month, we extracted the information for a 4 by 4 pixel box (from an original pixel resolution at 0.05° to a final grid at 0.1°). The iterative tests combine the value of the retrieval quality and

Table 1. Iterative test criteria for the quality index and the calculation of the RTTOV BRDF atlas.

Quality index	Name	Criteria			Description
		QA	PI (%)	PS (%)	
0	WATER				Land/water mask from UWIREMIS atlas
1	GOOD	0–1	≥80	0	No snow, best and good MCD43C1 quality for 80% inputs or more
2	MEDIUM	2–3	≥80	0	No snow, medium MCD43C1 quality for 80% inputs or more
3	LOW	0–4	<80	0	Remaining no snow pixels
4	SNOW	0–4	0–100	100	Full snow
5	BAD	0–4	0–100	≠ 0 or ≠100	Remaining pixels containing snow
6	NO DATA				Remaining pixel from land/water mask with no BRDF retrieval

Table 2. Coefficients g in Eq. (4) for the calculation of the RTTOV narrowband BSA.

g	Isotropic	Volumetric	Geometric
0	1.0	−0.007574	−1.284909
1	0.0	−0.070987	−0.166314
2	0.0	−0.307588	−0.041840

the percentages of inputs and snow (see Table 1). First of all, the land/water mask from the UWIREMIS atlas, which is based on the official MODIS MOD44 Vegetation Cover Conversion product (http://modis-land.gsfc.nasa.gov/), is used. Then the first test is applied, i.e. by looking for pixels with QA = 0 or 1, with more than or equal to 80% inputs and without snow. If at least one pixel is found within the final grid over a month, then the quality index is associated and the values of the three BRDF model parameters f are calculated using the value of the best original pixel or the mean value if more than one original pixel is found. If no pixel is found, then the second test is applied, and so on, until all pixels are tested. The MODIS BRDF parameters can be averaged because of the linearity of the semi-empirical BRDF model retrieved (Gao *et al.*, 2005). The panels of Figure 2 show the monthly RTTOV BRDF quality index for (a) January 2010, (b) April 2010, (c) July 2010 and (d) October 2010. Night-persistent areas at high latitudes (see e.g. Figure 2(a)) or cloud-persistent areas (such as in India in July, Figure 2(c)) are classified as having no BRDF data. Antarctic and Arctic areas, as well as snow-covered areas in the winter, are well classified (most of Europe and the United States experienced heavy snowfalls in this year). Areas often classified with a medium quality index, as in the northern part of South America, in Central Africa or in Asia, are explained by the difficulty to retrieve BRDF model parameters in the presence of clouds (Salomon *et al.*, 2006). The RTTOV BRDF products classified as good quality index represent 29.2% in January 2010 and 74.3% in July 2010 of the global land surfaces (i.e. all surfaces not classified as water or no data). The percentages are 9.2 and 14% for medium quality index, 5.3 and 6.3% for filled quality index, 56.3 and 5.2% for snow and 0.3 and 0.2% for bad quality index, respectively.

5. Validation of the RTTOV BRDF atlas with the land SAF black-sky albedo product

For the validation of the RTTOV BRDF atlas, we simulated land-surface BRDF using SEVIRI VIS/NIR channels and compared them with land-surface albedo products (Geiger *et al.*, 2008) from the EUMETSAT Land-SAF. We were not able to validate the BRDF

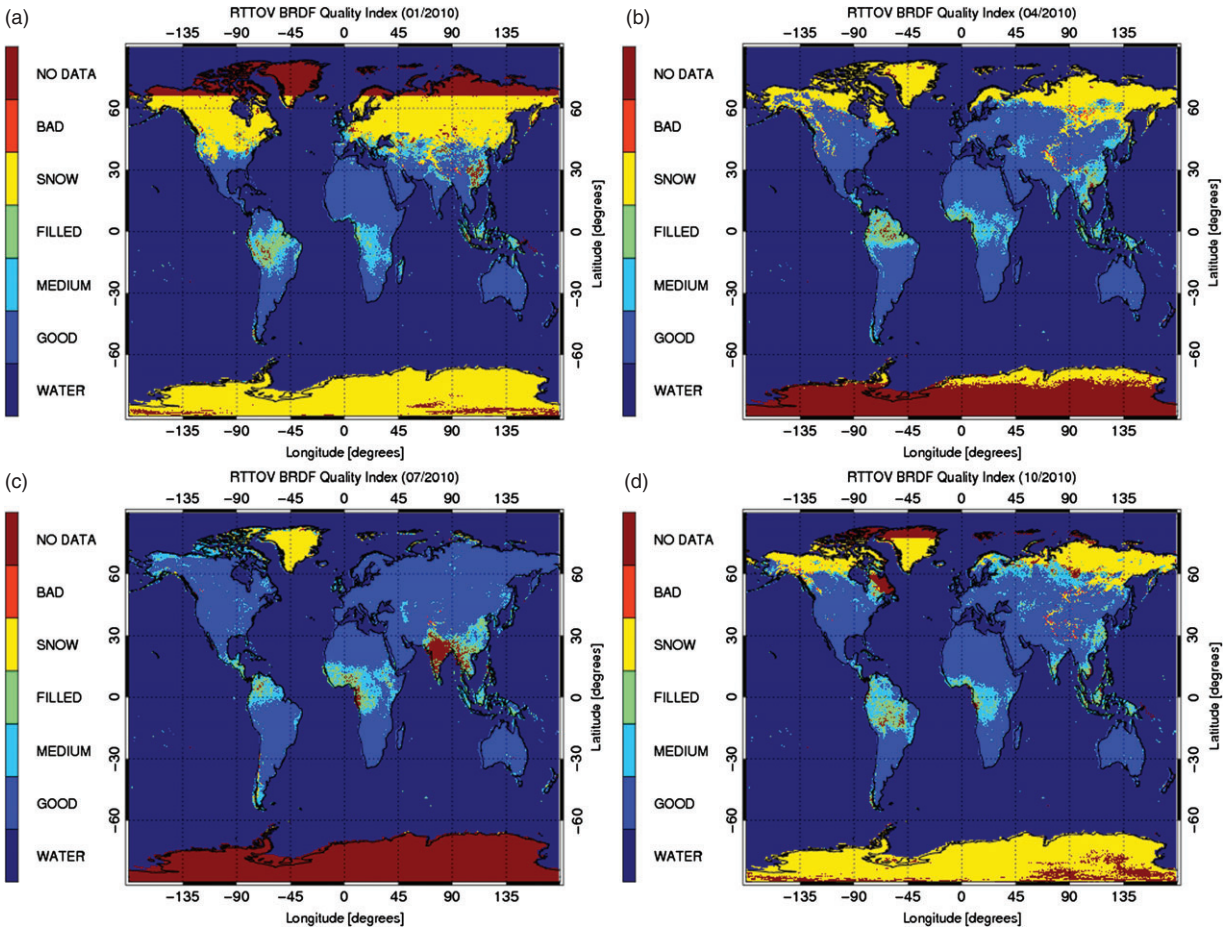

Figure 2. RTTOV BRDF quality index for 2010: (a) January, (b) April, (c) July and (d) October.

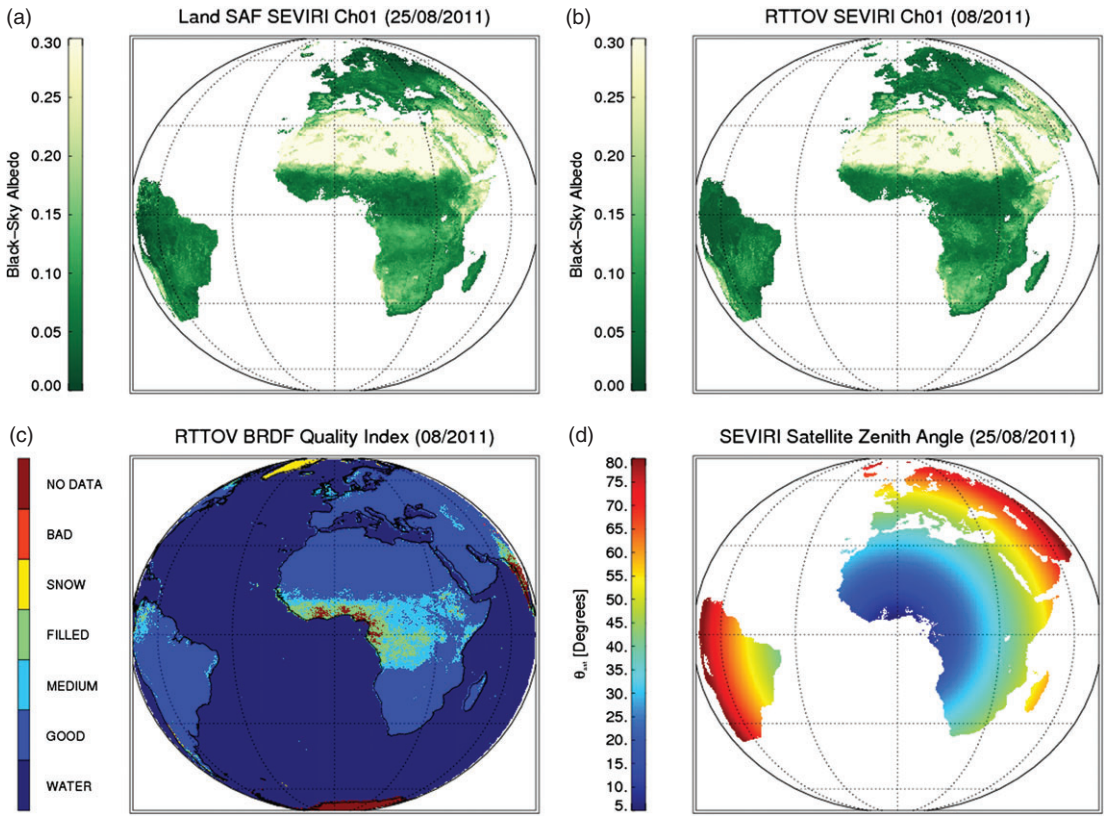

Figure 3. Land SAF narrowband black-sky albedo (BSA) product on 25 August 2011 for (a) SEVIRI channel 1 at 0.6 μm, (b) RTTOV narrowband BSA on August 2011 for SEVIRI channel 1, (c) RTTOV BRDF quality index for SEVIRI-like observation in August 2011 and (d) SEVIRI satellite zenith angle in degrees on 25 August 2011.

itself because the BRDF is not an operational product from the Land SAF team. We used the Land SAF directional hemispherical reflectance (DHR) or black-sky albedo (BSA) products for both narrowband and broadband, averaged at 0.1° spatial resolution from the original spatial resolution of SEVIRI. The Land SAF surface albedo product is documented at the Land SAF website (http://landsaf.meteo.pt) and has been validated with ground measurements and MODIS collection-4 products (Carrer *et al.*, 2010). Here, the validation was conducted as follows. First, we compared one daily Land SAF narrowband BSA product (called MDAL) that is provided in three SEVIRI channels (0.6, 0.8 and 1.6 μm) with simulated RTTOV narrowband BSA. Second, we compared the seasonal variation of mean broadband BSA calculated from 9 months (from January to September 2010) of the 10 days Land SAF product (called MTAL).

The RTTOV narrowband BSA α_{bs} values were calculated from the MODIS BRDF kernel-driven product (Lucht *et al.*, 2000) using the following equation:

$$\begin{aligned}\alpha_{\mathrm{bs}}(\theta_{\mathrm{ref}},\lambda) = {} & f_{\mathrm{iso}}(\lambda)(g_{0\mathrm{iso}} + g_{1\mathrm{iso}}\theta_{\mathrm{ref}}^2 + g_{2\mathrm{iso}}\theta_{\mathrm{ref}}^3) \\ & + f_{\mathrm{vol}}(\lambda)(g_{0\mathrm{vol}} + g_{1\mathrm{vol}}\theta_{\mathrm{ref}}^2 + g_{2\mathrm{vol}}\theta_{\mathrm{ref}}^3) \\ & + f_{\mathrm{iso}}(\lambda)(g_{0\mathrm{geo}} + g_{1\mathrm{geo}}\theta_{\mathrm{ref}}^2 + g_{2\mathrm{geo}}\theta_{\mathrm{ref}}^3) \qquad (4)\end{aligned}$$

where the different coefficients g are given in Table 2 and θ_{ref} is the reference angle at local solar noon. Figure 3(a) depicts the SEVIRI channel 1 (at 0.6 μm) Land SAF narrowband BSA product on 25 August 2011 averaged on a 0.1° grid. In Figure 3(b) the monthly mean RTTOV narrowband BSA for August 2011 in channel 1 is depicted. Vegetation-covered areas (with lower albedos) and desert areas (with higher albedos) are well retrieved with the RTTOV BRDF atlas as compared with the Land SAF product. However, some discrepancies between RTTOV and Land SAF appear in the Middle East and over Central Africa. Figure 3(c) illustrates the monthly mean RTTOV BRDF quality index for August 2011. The quality index reveals that in Central Africa the quality of the MODIS BRDF retrieval is lower. This result is explained by the lower quality of the MODIS BRDF retrieval in the presence of clouds (Salomon *et al.*, 2006), which is confirmed by the MODIS level 3 monthly mean cloud product with a mean cloud fraction above 70% (not shown). To take into account this problem and to differentiate surface types in the interpretation of the results, we then divided the SEVIRI full disc into three latitudinal areas, i.e.:

1. Mid-latitude areas in Europe (above 38°N), in South Africa and South America (below 15°S).
2. Desert areas in Northern Africa and the Middle East (between 15°N and 38°N).
3. Equatorial areas in Central Africa and Central America (between 15°S and 15°N).

The scatterplot of RTTOV BSA and Land SAF BSA for mid-latitude areas depicted in Figure 4(a) shows a good correlation between RTTOV and Land SAF, with a correlation coefficient $R = 0.756$ and a bias of ∼0.011. However, the scatterplot also shows some outliers. These outliers are explained by the difficulty to retrieve BRDF parameters at high zenith angles, which is more critical for geostationary satellites such as SEVIRI at the edge of the disc. By removing data for satellite zenith angles greater than 65° (see Figure 3(d)), most outliers are removed (Figure 4(b)) and the correlation coefficient increases to $R = 0.919$ and the bias is reduced to 0.0023.

Scatterplots for channel 2 (at 0.8 μm) and for channel 3 (at 1.6 μm) for mid-latitude areas are depicted in Figure 4(c) and (d), respectively. A threshold of 65° for the satellite zenith angle is applied. The correlation coefficients are 0.887 and 0.95 for channel 2 and 3, respectively with a larger bias in channel 2 (of ∼0.014) than in channel 1 and a low bias in channel 3 (0.004).

The results for channels 1, 2 and 3 are depicted in Figure 5(a), (c) and (e) for the equatorial areas and in Figure 5(b), (d), and (f) for the desert areas, respectively. Here again, a threshold of 65° for the satellite zenith angle is applied. For the equatorial areas, the correlation coefficients are better for all the channels as compared with mid-latitude areas, but the biases are slightly increased for all

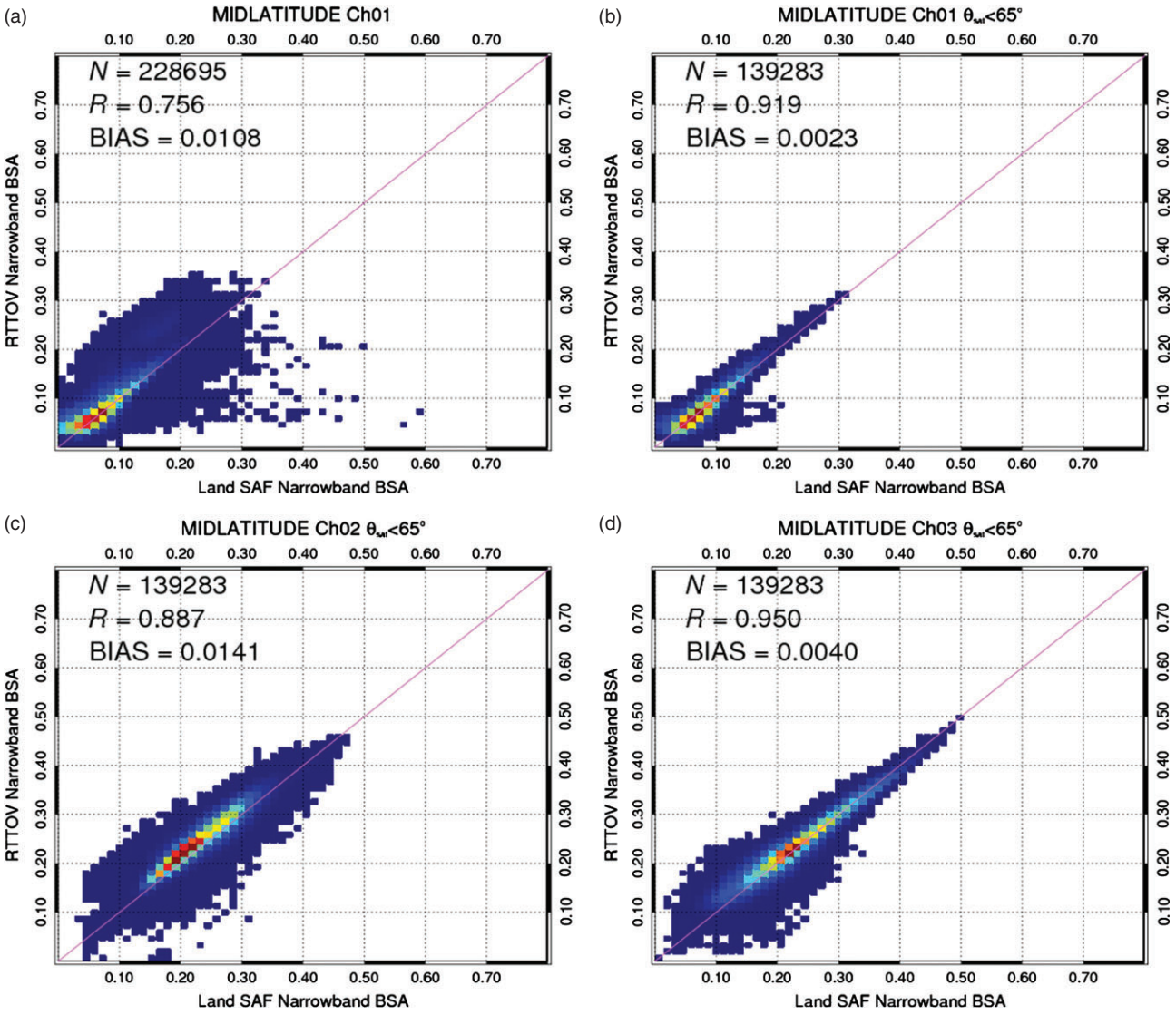

Figure 4. (a) Scatterplot of monthly mean RTTOV narrowband black-sky albedo (BSA) for August 2011 versus daily Land SAF narrowband BSA on 25 August 2011 for SEVIRI channel 1 in mid-latitude areas. (b) Scatterplot when satellite zenith angle <65°. Same as (b) in (c) channel 2 at 0.8 μm and (d) channel 3 at 1.6 μm. The number of points N, the correlation coefficients R and biases are given in each figure.

the channels. For the desert areas, the correlation coefficients are even better, with biases on the same order of magnitude as for the equatorial areas (with opposite sign for channels 1 and 3). Overall, we have found very good consistency in the RTTOV narrowband BSA as compared with the Land SAF product, with higher biases between 0.01 and 0.03 in channel 2. The higher biases in channel 2 have been also noticed by Carrer *et al.* (2010) in the left column of their figure 4. These biases might be explained by the larger difference in the channel's central wavelength between MODIS and SEVIRI for channel 2 (of ∼0.5 μm) compared with channels 1 and 3 (less than 0.2 μm), or by the differences in spectral sensitivities of the sensors.

To check the temporal consistency of the RTTOV BRDF atlas, we exploited 9 months of Land SAF products. In this study, the 10 days LSAF albedo product (called MTAL), which is provided every 5th, 15th and 25th of each month between January and September 2010, was used. As compared with the Land SAF daily product, the 10 days product provides broadband albedo and not narrowband albedo. The Land SAF broadband BSAs are defined for the VIS between 0.4 and 0.7 μm, NIR between 0.7 and 4 μm and short-wave (SW) between 0.3 and 4 μm ranges. They are calculated by a linear combination of the SEVIRI narrowband (van Leeuwen and Roujean, 2002). In order to avoid misinterpretation due to the difference between the MODIS and SEVIRI narrowband to broadband conversion factors, we applied the SEVIRI narrowband to broadband coefficients to

Table 3. Narrowband to broadband conversion coefficients C in Eq (5) for the SEVIRI channels.

Spectral range (μm)	C_0	C_1	C_2	C_3
SW (0.3, 4)	0.004724	0.537	0.2805	0.1297
VIS (0.4, 0.7)	0.009283	0.9606	0.0497	−0.1245
NIR (0.7, 4)	−0.000426	0.117	0.51	0.3971

RTTOV narrowband BSA using equation (39) of the LSA–SAF Surface Albedo Algorithm Theoretical Basis Document (available at http://landsaf.meteo.pt):

$$a_\gamma = C_{O\gamma} + \sum_\beta C_{\beta\gamma}\alpha_\beta, \tag{5}$$

where a is the broadband BSA, C are the coefficients given in Table 3 and where γ stands for the VIS, NIR or SW and β stands for channel 1, 2 or 3.

The panels of Figure 6 represent the statistical comparison between the RTTOV broadband BSA and the Land SAF product for the mid-latitude areas. In order to take into account the quality index of the RTTOV BRDF atlas and the satellite zenith angle effect, we compared the broadband BSA in three classes: for good quality index pixels with $\theta_{sat} < 65°$, for good quality index pixels with $\theta_{sat} > 65°$ and for medium or filled quality indices.

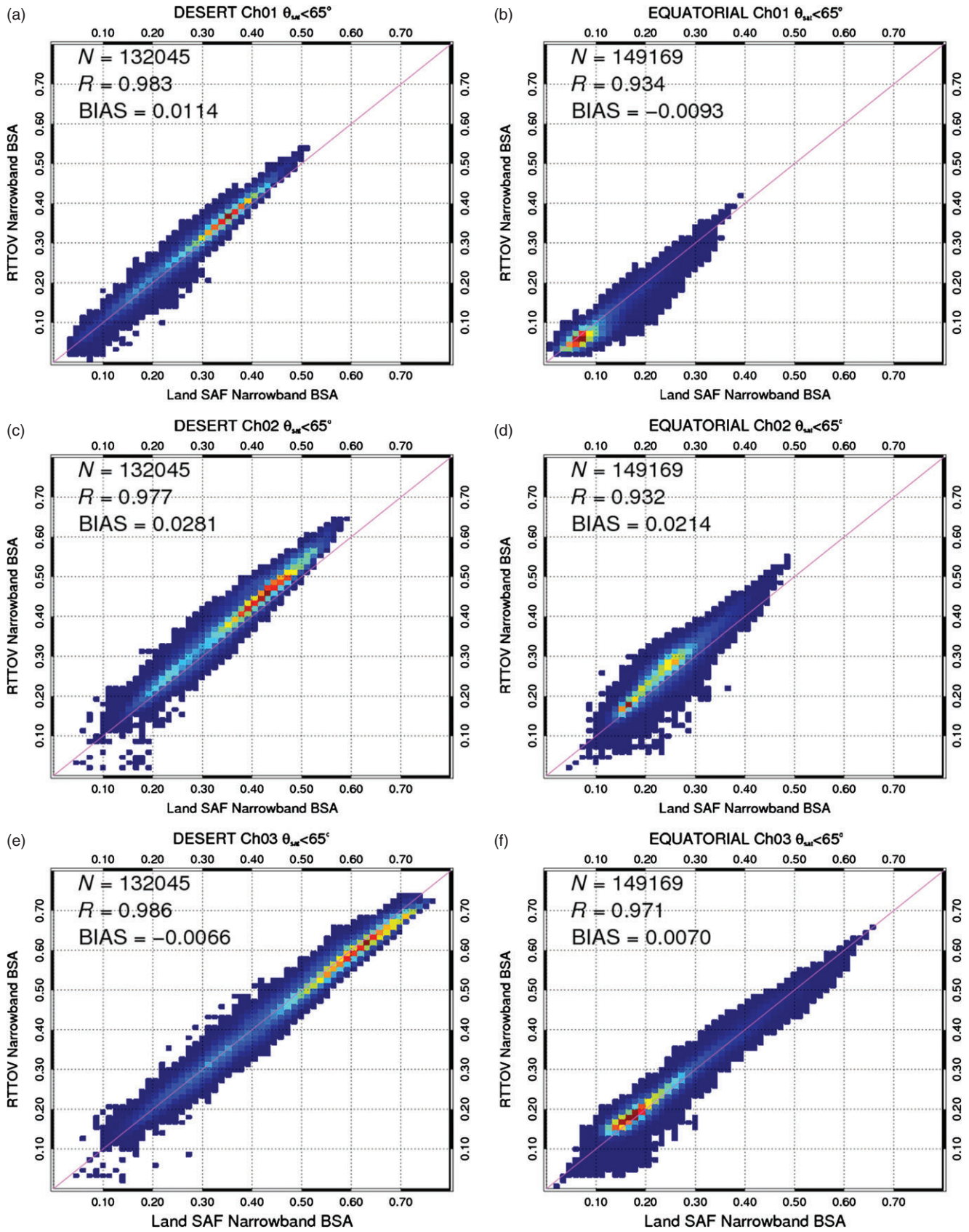

Figure 5. Same as Figure 4(b) but for desert areas at (a) 0.6 μm, (c) 0.8 μm and (e) 1.6 μm and for equatorial areas at (b) 0.6 μm, (d) 0.8 μm and (f) 1.6 μm.

Figure 6(a) depicts the temporal variation of the percentage of pixels for each class. In mid-latitude areas, two-thirds of the surfaces are mainly classified as good pixels for $\theta_{sat} < 65°$ and one-third for $\theta_{sat} > 65°$, and a substantial number are classified as medium or filled in the beginning of the year. In Figure 6(b)–(j) the temporal variation of the mean, residual and standard deviation of RTTOV and Land SAF broadband BSA for each class are represented for each broadband spectral domain (represented by different colours: see figure caption for definitions). For good quality indices with $\theta_{sat} < 65°$ (Figure 6(b)–(e)), we found good temporal agreement between RTTOV and Land SAF, with an overestimation lower than 0.02 generally and with smaller residuals for VIS (Figure 6(e) in blue) than for NIR (Figure 6(e) in red). The standard deviations of the RTTOV broadband BSA are slightly lower than the Land SAF BSA values (Figure 6(h)). When $\theta_{sat} > 65°$, overestimations are increased

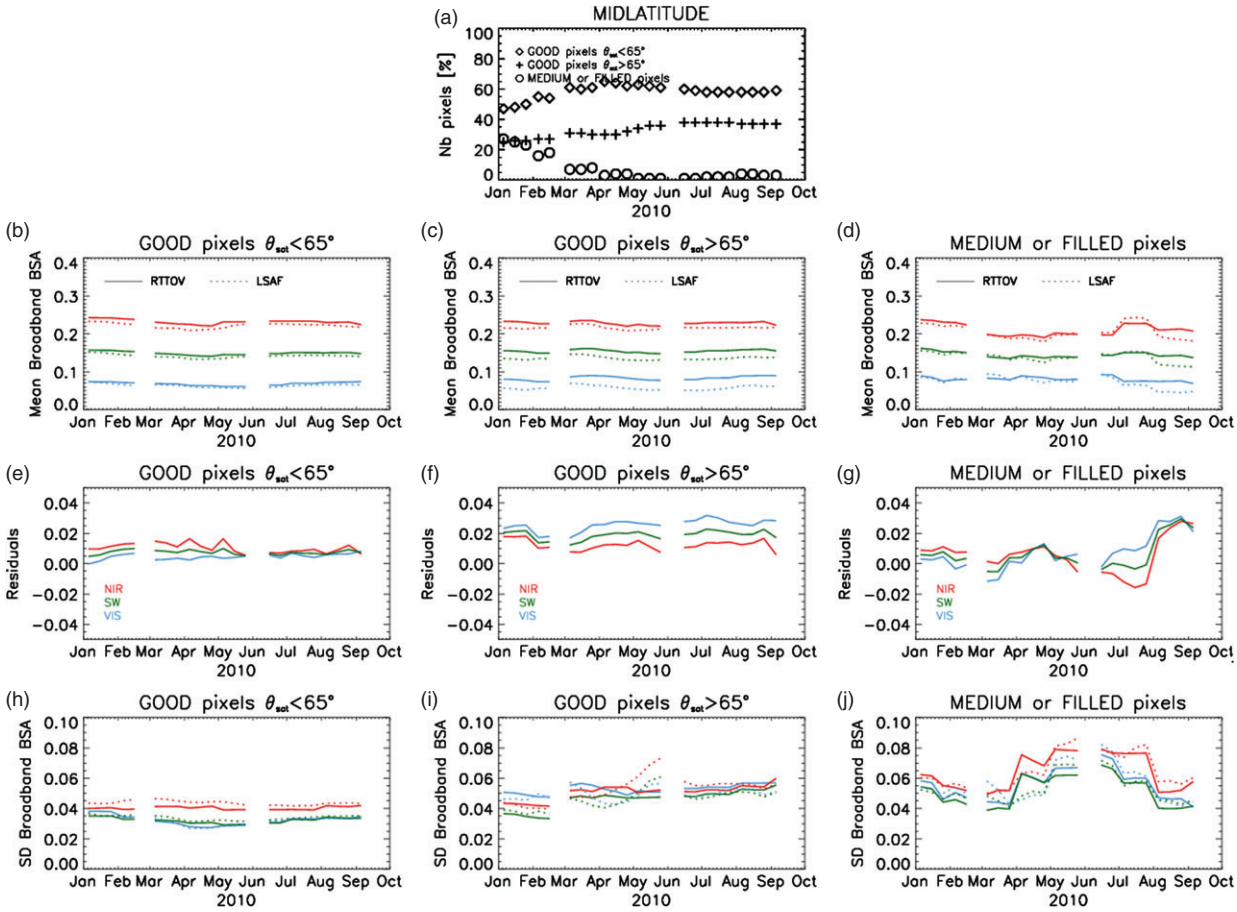

Figure 6. Broadband black-sky albedo (BSA) temporal variation of different quality indices for the time period between 1 January and 30 September 2010 over the mid-latitude areas. (a) Percentage temporal variation of each class of quality index pixels. Mean values of RTTOV (solid line) and Land SAF products (dashed line) are plotted for (b) good pixels with satellite zenith angles <65°, (c) for good pixels with satellite zenith angles >65° and (d) for medium or filled quality pixels. Colors indicate the spectral ranges, i.e., red stands for the near infrared, green for the short-wave and blue for the visible spectral ranges. Residuals are represented in (e)–(g) and the standard deviations of the Broadband BSA are illustrated in (h)–(j), for the same three categories respectively.

for the visible, and hence for the short-wave region (Figure 6(f)). For medium or filled quality indices, the residuals are less stable (Figure 6(g)) and standard deviations of the broadband BSA are increased, with a stronger seasonal dependence than other classes (Figure 6(j)).

The results for desert areas are presented in the panels of Figure 7. In this case, 80% of desert surfaces over the same period are classified as good quality indices with $\theta_{sat} < 65°$, and less than 5% are classified as medium or filled (see Figure 7(a)). For good quality indices with $\theta_{sat} < 65°$, good temporal agreement between broadband BSA is found (Figure 7(b)), with overestimations again below 0.02, but with higher values for VIS than for NIR (Figure 7(e)). Standard deviations of the Land SAF broadband BSA are slightly lower than the RTTOV values (Figure 7(h)). For the two other classes, residuals are less stable (Figure 7(f) and (g)), with underestimations up to 0.1 for the medium- or filled-quality indices category. Seasonal dependencies of the standard deviation are obtained again for medium and filled pixels (Figure 7(j)), and also only for Land SAF BSAs classified as having good quality indices with $\theta_{sat} > 65°$ (Figure 7(i)). Finally, results for equatorial areas are represented in the panel of Figure 8. Almost half of the equatorial surfaces are classified as having good quality indices and almost half as having medium or filled quality indices (Figure 8(a)). A better temporal agreement is found for good quality indices with $\theta_{sat} < 65°$, with overestimations lower than 0.01 (Figure 8(e)) but higher standard deviations (Figure 8(h)). As for desert surfaces, seasonal dependencies of the standard deviation are obtained for medium and filled pixels (Figure 8(j)), and also only for the Land SAF products classified with good quality indices with $\theta_{sat} > 65°$ (Figure 8(i)). These seasonal dependencies require further investigation.

6. Conclusion and perspectives

A BRDF model for land surfaces has been developed for RTTOV-11. Although it is not a perfect model of the reflectance properties of Earth, it is a practical tool for approximating these at a global scale. It is based on a combination of 126 USGS Digital Spectral Library Version 6 of hyperspectral reflectance measurements of soil, rocks and mixtures of both and vegetation surfaces and the MODIS Level 3 BRDF MCD43C1 products. This model allows the estimation of the BRDF for any instrument with channels having a central wavelength between 0.4 and 2.5 μm. The model provides a global and monthly mean BRDF at 0.1° spatial resolution. It also provides a quality index of the BRDF obtained from MCD43C1 retrieval quality and inputs information. Comparison with one global daily SEVIRI Land SAF product at 0.6, 0.8 and 1.6 μm shows good agreement for narrowband BSA, with correlation coefficients greater than 0.9 for all latitudinal areas when observations at high satellite zenith angles are removed. An accuracy of ±0.01 of the narrowband BSA is found for SEVIRI channels 1 and 3 (at 0.6 and 1.6 μm) and a positive bias of 0.02–0.03 is found in SEVIRI channel 2 (at 0.8 μm). We may expect larger errors for wavelengths that move away from MODIS bands, but further investigations need to be done. By comparing 9 months of the 10 days Land SAF surface albedo products, we found good temporal agreement for broadband BSA, with a positive bias lower than 0.02 when good quality indices of the RTTOV BRDF atlas are used and the satellite zenith angle is lower than 65° – which represents 50–60% of the SEVIRI targets in mid-latitude areas, 80% in desert areas and 50% in equatorial areas. The overestimation of the broadband BSA estimated from MODIS and reported here runs contrary to the result found by Carrer *et al.* (2010),

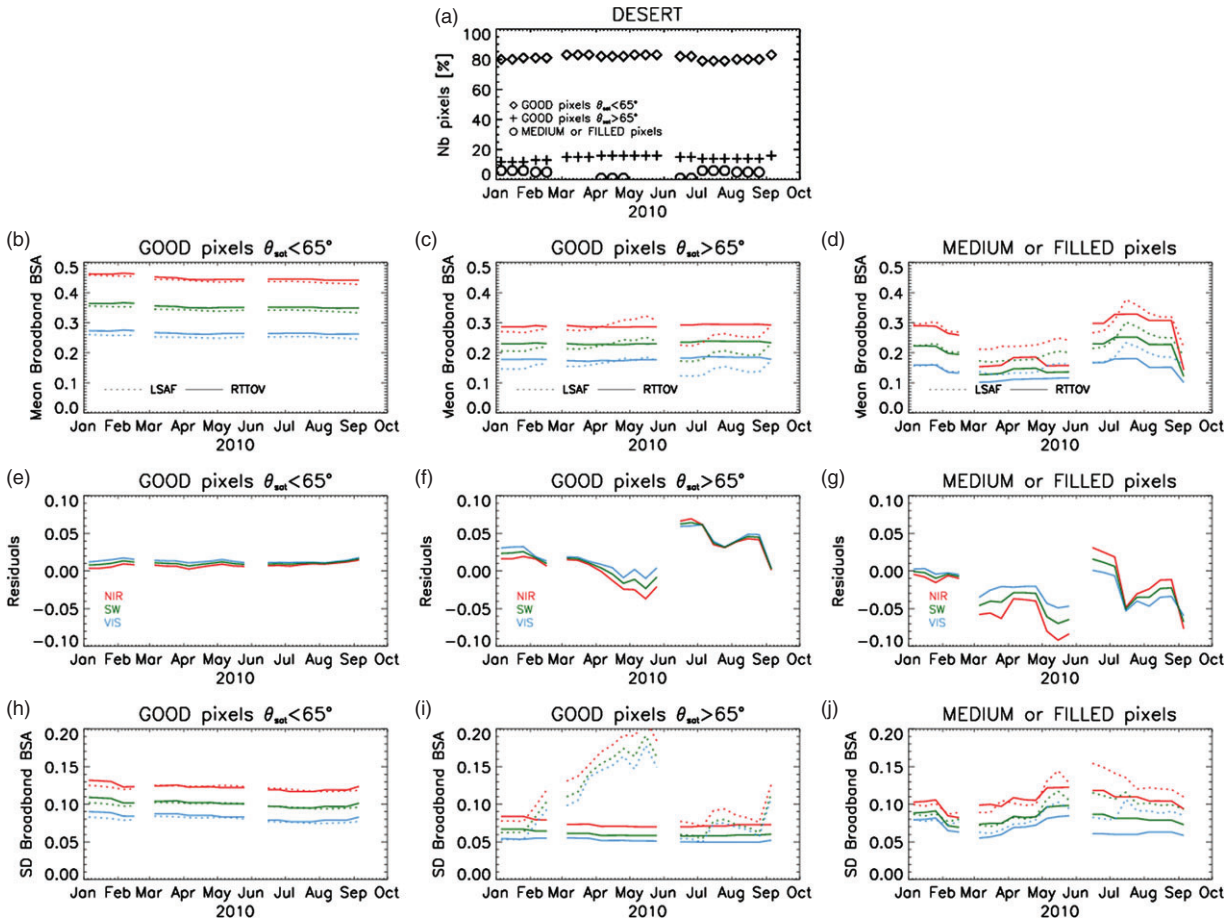

Figure 7. Same as Figure 6 but for desert areas.

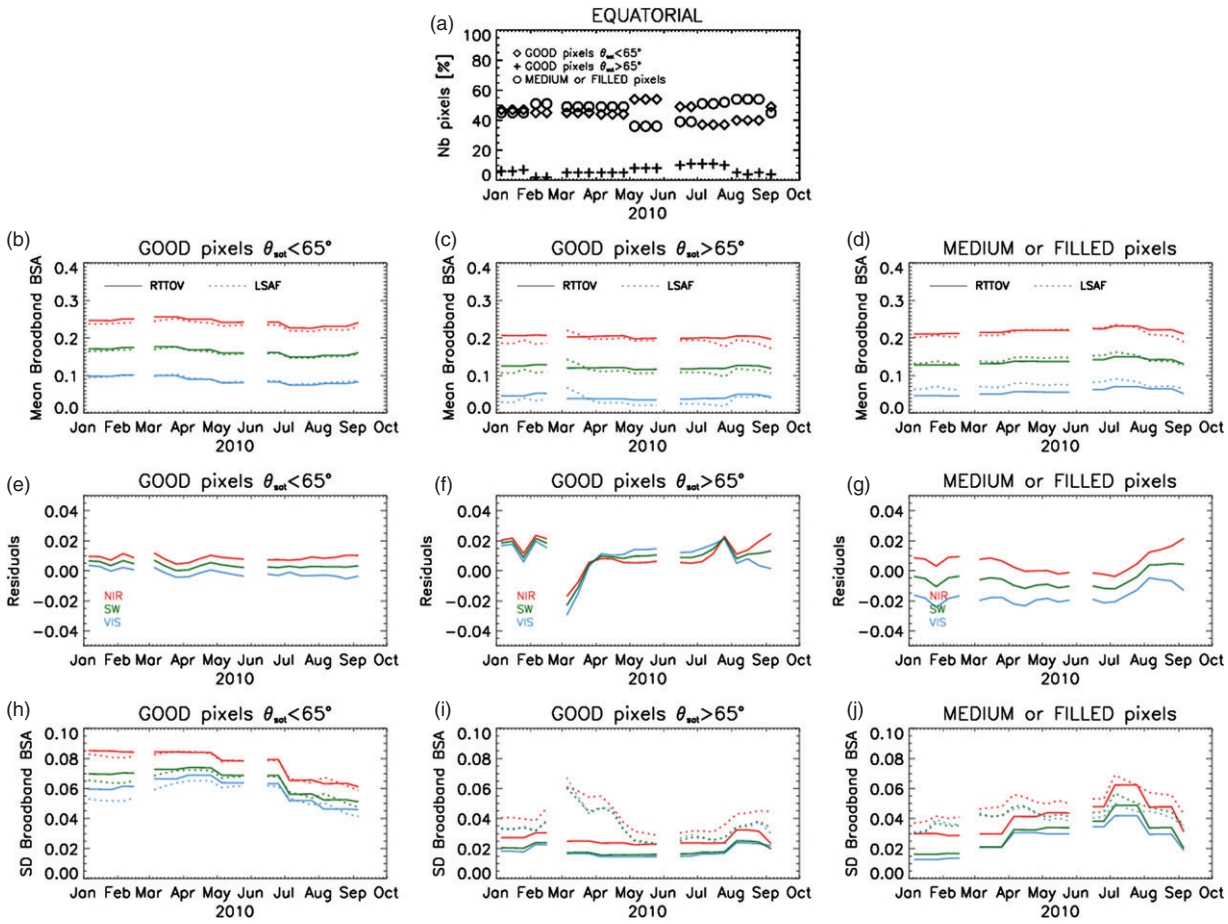

Figure 8. Same as Figure 6 but for equatorial areas.

but this difference might be explained by the different dataset (MODIS collection, MODIS spatial resolution product and pixel selection) or other sources (calibration accuracy of instruments, atmospheric correction schemes and spatial heterogeneity of sampling). Further investigations are needed to identify this consistently positive bias. Less agreement is obtained at satellite zenith angles higher than 65°, probably due to the lack of geometrical sampling for Land SAF products at the edge of the SEVIRI disc. This effect is more important for desert surfaces, but these surfaces in these extreme geometrical conditions represent less than 20% of the SEVIRI desert surfaces. Less agreement is also found for lower quality indices in equatorial areas that represent 50% of the SEVIRI observations. This decline in agreement is explained by the quasi-permanent presence of clouds that reduces the capability of satellite-based observations to retrieve surface optical properties in VIS and NIR spectral region. In the near future further improvements will be included in the RTTOV BRDF atlas: first by processing the full period between 2001 and 2010 in order to provide the interannual variations of the surface reflectance properties; and second by updating the atlas with collection 6 of the MODIS products. We are also planning to investigate the use of a multiyear approach in order to obtain more high quality pixels, especially in areas where currently no data are available (as for example over India, see Figure 2(c)), and we will study whether there is any temporal trend in the BRDF over many years.

Acknowledgements

The MODIS MCD43C1 data were obtained through the online Data Pool at the NASA Land Processes Distributed Active Archive Center (LP DAAC), USGS/Earth Resources Observation and Science (EROS) Center, Sioux Falls, South Dakota (https://lpdaac.usgs.gov/get_data). The authors are greatful to Leanne Avila for editing the English and to the two anonymous reviewers for their comments.

References

Aires F, Prigent C, Bernardo F, Jiménez C, Saunders R, Brunel P. 2011. A Tool to Estimate Land-Surface Emissivities at Microwave frequencies (TELSEM) for use in numerical weather prediction. *Q. J. R. Meteorol. Soc.* **137**: 690–699, doi: 10.1002/qj.803.

Barlage M, Zeng X, Wei H, Mitchell KE. 2005. A global 0.05 maximum albedo dataset of snow-covered land based on MODIS observations. *Geophys. Res. Lett.* **32**: L17405, doi: 10.1029/2005GL022881.

Bauer P, Moreal E, Chevallier F, O'keeffe U. 2006. Multiple-scattering microwave radiative transfer for data assimilation applications. *Q. J. R. Meteorol. Soc.* **132**: 1259–1281, doi: 10.1256/qj.05.153.

Bauer P, Geer AJ, Lopez P, Salmond D. 2010. Direct 4D-Var assimilation of all-sky radiances. Part I: Implementation. *Q. J. R. Meteorol. Soc.* **136**: 1868–1885, doi: 10.1002/qj.659.

Borbas E, Ruston BC. 2010. 'The RTTOV UWiremis IR land surface emissivity module', Report NWPSAF-MO-VS-042. EUMETSAT Associate Visiting Mission Report. http://research.metoffice.gov.uk/research/interproj/nwpsaf/vs.html (accessed 8 January 2014).

Borbas E, Knuteson RO, Seemann SW, Weisz E, Moy L, Huang H-L. 2007. 'A high spectral resolution global land surface infrared emissivity database'. In *Joint 2007 EUMETSAT Meteorological Satellite Conference and the 15th Satellite Meteorology and Oceanography Conference of the American Meteorological Society*, 24–28 September 2007. Amsterdam, The Netherlands. http://www.eumetsat.int/Home/Main/AboutEUMETSAT/Publications/ConferenceandWorkshopProceedings/2007/groups/cps/documents/document/pdf_conf_p50_s10_03_borbas_p.pdf (accessed 8 January 2014).

Carrer D, Roujean J-L, Meurey C. 2010. Comparing operational MSG/SEVIRI land surface albedo products from land SAF with ground measurements and MODIS. *IEEE Trans. Geosci. Remote Sens.* **48**: 1714–1728.

Cescatti A, Marcolla B, Santhana Vannan SK, Yun Pan J, Román MO, Yang X, Ciais P, Cook RB, Law BE, Matteucci G, Migliavacca M, Moors E, Richardson AD, Seufert G, Schaaf CB. 2012. Intercomparison of MODIS albedo retrievals and *in situ* measurements across the global FLUXNET network. *Remote Sens. Environ.* **121**: 323–334, doi: 10.1016/j.rse.2012.02.019.

Clark RN, Swayze GA, Wise R, Livo E, Hoefen T, Kokaly R, Sutley SJ. 2007. USGS Digital Spectral Library splib06a', *Digital Data Series* 231. U.S. Geological Survey. http://speclab.cr.usgs.gov/spectral.lib06/ds231 (accessed 8 January 2014).

Derrien M, LeGléau H. 2005. MSG/SEVIRI cloud mask and type from SAFNWC. *Int. J. Remote Sens.* **26**: 4707–4732.

De Wachter E, Barret B, Le Flochmoën E, Pavelin E, Matricardi M, Clerbaux C, Hadji-Lazaro J, George M, Hurtmans D, Coheur P-F, Nedelec P, Cammas JP. 2012. Retrieval of MetOp-A/IASI CO profiles and validation with MOZAIC data. *Atmos. Meas. Tech.* **5**: 2843–2857, doi: 10.5194/amt-5-2843-2012.

English SJ, Renshaw RJ, Dibben PC, Smith AJ, Rayer PJ, Poulsen C, Saunders FW, Eyre JR. 2000. A comparison of the impact of TOVS arid ATOVS satellite sounding data on the accuracy of numerical weather forecasts. *Q. J. R. Meteorol. Soc.* **126**: 2911–2931, doi: 10.1002/qj.49712656915.

Errico RM, Ohring G, Weng F, Bauer P, Ferrier B, Mahfouf J-F, Turk J. 2007. Assimilation of satellite cloud and precipitation observations in numerical weather prediction models: Introduction to the JAS special collection. *J. Atmos. Sci.* **64**: 3737–3741.

Eyre JR. 1991. 'A fast radiative transfer model for satellite sounding systems', ECMWF Tech. Memo 176.

Eyre JR, Woolf HM. 1988. Transmittance of atmospheric gases in the microwave region: A fast model. *Appl. Opt.* **27**: 3244–3249.

Gao F, Schaaf C, Strahler A, Roesch A, Lucht W, Dickinson R. 2005. MODIS bidirectional reflectance distribution function and albedo Climate Modeling Grid products and the variability of albedo for major global vegetation types. *J. Geophys. Res.* **110**: D01104, doi: 10.1029/2004JD005190.

Geer AJ, Bauer P, Lopez P. 2010. Direct 4D-Var assimilation of all-sky radiances. Part II: Assessment. *Q. J. R. Meteorol. Soc.* **136**: 1886–1905, doi: 10.1002/qj.681.

Geiger B, Carrer D, Franchisteguy L, Roujean J-L, Meurey C. 2008. Land surface albedo derived on a daily basis from meteosat second generation observations. *IEEE Trans. Geosci. Remote Sens.* **46**: 3841–3856.

Houldcroft CJ, Grey WMF, Barnsley M, Taylor CM, Los SO, North PRJ. 2009. New vegetation albedo parameters and global fields of soil background albedo derived from MODIS for use in a climate model. *J. Hydrometeorol.* **10**: 183–198, doi: 10.1175/2008JHM1021.1.

Jin Y, Schaaf CB, Woodcock CE, Gao F, Li X, Strahler AH, Lucht W, Liang S. 2003. Consistency of MODIS surface bidirectional reflectance distribution function and albedo retrievals: 2. Validation. *J. Geophys. Res.* **108**: 4159, doi: 10.1029/2002JD002804.

Karbou F, Prigent C, Eymard L, Pardo J. 2005. Microwave land emissivity calculations using AMSU-A and AMSU-B measurements. *IEEE Trans. Geosci. Remote Sens.* **43**: 948–959.

King MD, Kaufman YJ, Tanré D, Nakajima T. 1999. Remote sensing of tropospheric aerosols from space: Past, present, and future. *Bull. Am. Meteorol. Soc.* **80**: 2229–2259.

van Leeuwen WJD, Roujean J-L. 2002. Land surface albedo from the synergistic use of polar (EPS) and geo-stationary (MSG) observing systems: An assessment of physical uncertainties. *Remote Sens. Environ.* **81**: 273–289.

Liu J, Schaaf CB, Strahler AH, Jiao Z, Shuai Y, Zhang Q, Roman M, Augustine JA, Dutton EG. 2009. Validation of Moderate Resolution Imaging Spectroradiometer (MODIS) albedo retrieval algorithm: Dependence of albedo on solar zenith angle. *J. Geophys. Res.* **114**: D01106, doi: 10.1029/2008JD009969.

Liu Q, Weng F, English SJ. 2011. An improved fast microwave water emissivity model. *IEEE Trans. Geosci. Remote Sens.* **49**: 1238–1250, doi: 10.1109/TGRS.2010.2064779.

Lucht W, Schaaf CB, Strahler AH. 2000. An algorithm for the retrieval of albedo from space using semiempirical BRDF models. *IEEE Trans. Geosci. Remote Sens.* **38**: 977–998.

Matricardi M. 2009. Technical note: An assessment of the accuracy of the RTTOV fast radiative transfer model using IASI data. *Atmos. Chem. Phys.* **9**: 6899–6913, doi: 10.5194/acp-9-6899-2009.

Matricardi M, Chevallier F, Kelly G, Thépaut J-N. 2004. An improved general fast radiative transfer model for the assimilation of radiance observations. *Q. J. R. Meteorol. Soc.* **130**: 153–173, doi: 10.1256/qj.02.181.

Nakajima T, King MD. 1990. Determination of the optical thickness and effective particle radius of clouds from reflected solar radiation measurements. Part I: Theory. *J. Atmos. Sci.* **47**: 1878–1893.

Pavelin EG, Candy B. 2013. Assimilation of surface-sensitive infrared radiances over land: Estimation of land surface temperature and emissivity. *Q. J. R. Meteorol. Soc.*, doi: 10.1002/qj.2218.

Pavelin EG, English SJ, Eyre JR. 2008. The assimilation of cloud-affected infrared satellite radiances for numerical weather prediction. *Q. J. R. Meteorol. Soc.* **134**: 737–749.

Pinty B, Taberner M, Haemmerle VR, Paradise SR, Vermote E, Verstraete MM, Gobron N, Widlowski J-L. 2011. Global-scale comparison of MISR and MODIS land surface albedos. *J. Clim.* **24**: 732–749, doi: http://dx.doi.org/10.1175/2010JCLI3709.1.

Roesch A, Schaaf CB, Gao F. 2004. Use of Moderate-Resolution Imaging Spectroradiometer bidirectional reflectance distribution function products to enhance simulated surface albedos. *J. Geophys. Res.* **109**: D12105, doi: 10.1029/2004JD004552.

Roujean J-L, Leroy M, Deschamps P-Y. 1992. A bidirectional reflectance model of the Earth's surface for the correction of remote sensing data. *J. Geophys. Res.* **97**: 20455–20468, doi: 10.1029/92JD01411.

Salomon JG, Schaaf CB, Strahler AH, Gao F, Jin Y. 2006. Validation of the MODIS bidirectional reflectance distribution function and albedo retrievals using combined observations from the aqua and terra platforms. *IEEE Trans. Geosci. Remote Sens.* **44**: 1555–1565.

Saunders R, Matricardi M, Brunel P. 1999. A improved fast radiative transfer model for assimilation of satellite radiance observations. *Q. J. R. Meteorol. Soc.* **125**: 1407–1425.

Saunders R, Matricardi M, Geer A, Rayer P, Embury O, Merchant C. 2010. 'RTTOV-9 science and validation report', NWP Technical Report NWPSAF-MO-TV. http://research.metoffice.gov.uk/research/interproj/nwpsaf/rtm/rtm_rttov9.html (accessed 8 January 2014).

Schaaf CB, Gao F, Strahler AH, Lucht W, Li X, Tsang T, Strugnell NC, Zhang X, Jin Y, Muller J-P, Lewis P, Barnsley M, Hobson P, Disney M, Roberts G, Dunderdale M, Doll C, d'Entremont RP, Hu B, Liang S, Privette JL, Roy D. 2002. First operational BRDF, albedo nadir reflectance products from MODIS. *Remote Sens. Environ.* **83**: 135–148, doi: 10.1016/S0034-4257(02)00091-3.

Seemann SW, Borbas EA, Knuteson RO, Stephenson GR, Huang H-L. 2008. Development of a global infrared land surface emissivity database for application to clear sky sounding retrievals from multispectral satellite radiance measurements. *J. Appl. Meteorol. Climatol.* **47**: 108–123.

Sherlock V. 1999. 'ISEM-6: infrared surface emissivity model for RTTOV-6', Report 299. Met Office NWP SAF report 299: Exeter, UK, p 17.

Tobin DC, Revercomb HE, Knuteson RO, Lesht BM, Strow LL, Hannon SE, Feltz WF, Moy LA, Fetzer EJ, Cress TS. 2006. Atmospheric Radiation Measurement site atmospheric state best estimates for Atmospheric Infrared Sounder temperature and water vapor retrieval validation. *J. Geophys. Res.* **111**: D09S14, doi: 10.1029/2005JD006103.

Vogel RL, Liu Q, Han Y, Weng F. 2011. Evaluating a satellite-derived global infrared land surface emissivity data set for use in radiative transfer modeling. *J. Geophys. Res.* **116**: D08105, doi: 10.1029/2010JD014679.

Wang Z, Zeng X, Barlage M, Dickinson RE, Gao F, Schaaf CB. 2004. Using MODIS BRDF and albedo data to evaluate global model land surface albedo. *J. Hydrometeorol.* **5**: 3–14.

Wang K, Liang S, Schaaf CB, Strahler AH. 2010. Evaluation of Moderate Resolution Imaging Spectroradiometer land surface visible and shortwave albedo products at FLUXNET sites. *J. Geophys. Res.* **115**: D17107, doi: 10.1029/2009JD013101.

Wanner W, Li X, Strahler AH. 1995. On the derivation of kernels for kernel-driven models of bidirectional reflectance. *J. Geophys. Res.* **100**: 21077–21089, doi: 10.1029/95JD02371.

5.2 Vidot et al. (2015)

Cet article publié en 2015 dans *Journal of Geophysical Research* (facteur d'impact de 3.63) est le deuxième article que j'ai publié sur le modèle RTTOV. Ce travail est le fruit d'une collaboration avec Anthony Baran (UK Met-Office) que j'ai eu l'occasion de rencontrer plusieurs fois lors des réunions du projet RTTOV. Les résultats ont aussi été montrés dans différentes conférences (ITSC-20, EUMETSAT-2013, IASI-2013, IRS-2016) et relayés dans le rapport recherche annuel de Météo-France. Les premiers retours que j'ai eu sur l'utilisation de ces travaux en assimilation pré-opérationnelle ont été très positifs.

AGU PUBLICATIONS

JGR

Journal of Geophysical Research: Atmospheres

RESEARCH ARTICLE
10.1002/2015JD023462

Key Points:
- A new ice cloud parameterization for infrared fast RTM is proposed
- It does not need information about the size and the shape of ice particles
- Validation with ice cloud profile retrieval products is conducted

Correspondence to:
J. Vidot,
jerome.vidot@meteo.fr

Citation:
Vidot, J., A. J. Baran, and P. Brunel (2015), A new ice cloud parameterization for infrared radiative transfer simulation of cloudy radiances: Evaluation and optimization with IIR observations and ice cloud profile retrieval products, *J. Geophys. Res. Atmos.*, *120*, 6937–6951, doi:10.1002/2015JD023462.

Received 2 APR 2015
Accepted 28 JUN 2015
Accepted article online 1 JUL 2015
Published online 21 JUL 2015

A new ice cloud parameterization for infrared radiative transfer simulation of cloudy radiances: Evaluation and optimization with IIR observations and ice cloud profile retrieval products

Jérôme Vidot[1], Anthony J. Baran[2], and Pascal Brunel[1]

[1]Centre de Météorologie Spatiale, DP/Météo-France, Lannion, France, [2]Met Office, Exeter, UK

Abstract A new ice cloud optical property database in the thermal infrared has been parameterized for the RTTOV radiative transfer model. The Self-Consistent Scattering Model (SCSM) database is based on an ensemble model of ice crystals and a parameterization of the particle size distribution. This convolution can predict the radiative properties of cirrus without the need of a priori information on the ice particle shape and an estimate of the ice crystal effective dimension. The ice cloud optical properties are estimated through linear parameterizations of ambient temperature and ice water content. We evaluate the new parameterization against existing parameterizations used in RTTOV. We compare infrared observations from Imaging Infrared Radiometer, on board CALIPSO, against RTTOV simulations of the observations. The simulations are performed using two different products of ice cloud profiles, retrieved from the synergy between space-based radar and lidar observations. These are the 2C-ICE and DARDAR products. We optimized the parameterization by testing different SCSM databases, derived from different shapes of the particle size distribution, and weighting the volume extinction coefficient of the ensemble model. By selecting a large global data set of ice cloud profiles of visible optical depths between 0.03 and 4, we found that the simulations, based on the optimized SCSM database parameterization, reproduces the observations with a mean bias of only 0.43 K and a standard deviation of 6.85 K. The optimized SCSM database parameterization can also be applied to any other radiative transfer model.

1. Introduction

The assimilation of infrared cloudy radiances from satellite observations is a major goal in improving numerical weather prediction (NWP) models [*Errico et al.*, 2007]. In the microwave spectral domain (10–100 GHz), the operational assimilation of satellite observations is already performed in all-weather conditions [*Bauer et al.*, 2011]. In the infrared spectral domain (3–20 μm), the assimilation of satellite observations is only performed in clear-sky and in overcast cloudy conditions [*Pavelin et al.*, 2008; *McNally*, 2009; *Guidard et al.*, 2011]. The limitation to overcast cloudy conditions is mainly due to the large nonlinear sensitivity of infrared radiances to cloud parameters of the simplified single-layer cloud model (cloud fraction and cloud top height) used in the operational assimilation of infrared radiances. Furthermore, the advantage of assimilating overcast cloudy radiances is to exclude the modeling of multiple scattering. However, fast radiative transfer models (RTMs) developed for the assimilation of satellite observations in NWP models are also able to simulate infrared radiances in more complex cloudy conditions. For that, they use NWP model cloud variables (ice and liquid water content profiles and cloud fraction profiles) as input information together with parameterization of cloud particle optical properties. This capability has shown encouraging results in improving assimilation of infrared cloudy radiances [*Stengel et al.*, 2010, 2013; *Martinet et al.*, 2013a; *Okamoto et al.*, 2013] using the radiative transfer model for TOVS (RTTOV) [*Saunders et al.*, 1999; *Matricardi et al.*, 2004]. This improvement has been achieved by more accurate modeling of cloud scattering and multilayer clouds.

A key step in better simulating infrared cloudy radiances for RTTOV is to improve the parameterization of cirrus optical properties from NWP model cloud variables. For ice cloud, the version 9 of RTTOV [*Saunders et al.*, 2009] provides eight different parameterizations. These parameterizations come from four different empirical relationships, which were derived from different cloud studies and were based on aircraft measurements located in different geographical areas [*Ou and Liou*, 1995; *Wyser*, 1998; *Boudala et al.*, 2002; *McFarquhar et al.*, 2003]. These parameterizations are named hereafter OL95, W98, B02, and MF03,

respectively. These empirical relationships relate the ice crystal effective diameter (D_{eff}) to the ice water content (IWC) and/or the ambient temperature (T). The ice cloud optical properties were then parameterized as functions of D_{eff} and IWC for two shapes of ice crystals, i.e., the randomly oriented hexagonal ice column and ice aggregate. A full description of the parameterizations can be found in *Matricardi* [2005] and in *Saunders et al*. [2009]. However, these previous parameterizations developed for RTTOV are based on particle size distributions (PSDs) which are highly likely to be biased toward smaller ice crystals due to ice crystal shattering on or at the inlets of microphysical probes [*Korolev et al*., 2011]. Additionally to these eight parameterizations, two more parameterizations were provided in an updated RTTOV version 10.2, which allows the user to input directly vertical profiles of D_{eff} to RTTOV for each assumed ice crystal shape [*Saunders et al*., 2012]. Hereafter, this parameterization is named DE.

The current problem with the RTTOV ice parameterizations is that users are provided with a wide choice of parameterizations which leads to difficulties in deciding which might be best for their particular application. For instance, simulations of one typical top-of-atmosphere (TOA) infrared brightness temperature (BT) spectra show few tens of kelvin's difference in window channels for the same ice cloud profile using the different parameterizations [*Faijan et al*., 2012; *Vidot et al*., 2013]. However, *Faijan et al*. [2012] show also that no parameterization globally provides a unique choice of parameterization when simulating many Infrared Atmospheric Sounding Interferometer (IASI) spectra in the presence of semitransparent clouds. Inversely, *Martinet et al*. [2013b] preferred the B02 parameterization, with randomly oriented hexagonal ice column crystals, for channel selection of the Infrared Atmospheric Sounding Interferometer (IASI) instrument in cloudy retrievals. In other studies, the W98 parameterization, which assumes aggregate ice crystals, was chosen [*Stengel et al*., 2013; *Okamoto et al*., 2013]. However, it is worth mentioning here that care must be taken with the aggregate shape of ice crystals from RTTOV, since it has been shown by simulated infrared spectra that the parameterization leads to unphysical spectral behavior between 10 and 12 μm [*Faijan et al*., 2012; *Vidot et al*., 2013].

In this study, we attempt to evaluate these ice cloud parameterizations together with a new parameterization provided in RTTOV version 11 [*Saunders et al*., 2013]. The new parameterization is based on a new database of bulk ice optical properties derived from the Self-Consistent Scattering Model (SCSM) for cirrus, called the ensemble model of ice crystals, and this model is fully described in the work of *Baran and Labonnote* [2007]. In this paper, we test a new SCSM bulk ice optical property database. This database combines the ensemble model of atmospheric ice particles with a particle size distribution (PSD) scheme that is consistent with microphysical observations, and this new SCSM optical property database is described in *Baran et al*. [2014a] and *Baran et al*. [2014b]. Alternative bulk ice optical property databases have been provided for the infrared spectral range [*Hess and Wiegner*, 1994; *Hess et al*., 1998; *Yang et al*., 2005; *Baum et al*., 2007; *Yang et al*., 2013; *Baum et al*., 2014, and references cited herein]. These databases were never incorporated into RTTOV, which is why they are not considered in this paper. We concentrate on RTTOV ice cloud parameterizations that are used in operational NWP centers. The novelty of this new parameterization is that the radiative properties of ice cloud can be predicted without the need for a priori information on the ice particle shape and an ice crystal effective diameter.

To compare and evaluate the RTTOV parameterizations, we used a large selection of products comprising of ice cloud profiles, retrieved from a combination of CloudSat [*Stephens et al*., 2002] and CALIPSO [*Winker et al*., 2009] observations. These ice cloud profiles are used to simulate infrared TOA BT. We then compare the simulations to the BT measured by the Imaging Infrared Radiometer (IIR) instrument, on board CALIPSO [*Garnier et al*., 2012], at 8.65, 10.6, and 12.05 μm. This comparison was motivated by two reasons: first, the better accuracy of ice cloud profiles retrieved by active sensors as compared to NWP outputs. Second, the fine spatial resolution of IIR (~1 km) allows the neglect of the effect of the vertical cloud fraction within a single pixel. Furthermore, this selection of ice cloud profiles and IIR BT observations was used to optimize the new ice cloud parameterization by modifying the calculation of the ice cloud optical property database by minimizing the difference between RTTOV simulations and IIR observations.

Section 2 of this article presents the new RTTOV-11 ice cloud parameterization and the modification of the SCSM database to optimize the new ice cloud parameterization. Section 3 is devoted to the selection of the ice cloud profiles, and the results are outlined in section 4. Conclusions and perspectives are given in section 5.

2. The RTTOV Ice Cloud Parameterization and the SCSM Databases

The infrared TOA BT of satellite-based observations in the presence of cloud is simulated by RTTOV using the Chou-scaling approximation [*Chou et al*., 1999]. The Chou-scaling approximation simplifies the cloud-scattering effect by estimating an effective extinction β_{eff}, at a wavelength λ of each cloud layer, given by

$$\beta_{\text{eff}}(\lambda, T, \text{IWC}) = \beta_{\text{abs}}(\lambda, T, \text{IWC}) + b(\lambda, T, \text{IWC})\beta_{\text{sca}}(\lambda, T, \text{IWC}), \quad (1)$$

where β_{abs} and β_{sca} are the volumetric absorption and scattering coefficients, respectively. The coefficient b is the backscattering fraction calculated from the phase function (see equation (32) of *Matricardi* [2005]).

In RTTOV-9, the ice cloud optical properties (β_{abs}, β_{sca}, and b) within each cloud layer are estimated from parameterization of IWC and D_{eff} profiles (see equations (35)–(37) of *Saunders et al*. [2009]) and where D_{eff} is parameterized as functions of T only (OL95) or IWC only (MF03) or T and IWC (W98 and B02).

In RTTOV-11 [*Saunders et al*., 2013], we have added a new parameterization of β_{abs}, β_{sca}, and b from T and IWC without the need of D_{eff}. The new parameterization is based on the Self-Consistent Scattering Model (SCSM) database of ice cloud optical properties. The SCSM database is based on the ensemble model of cirrus ice crystals shown in Figure 1 of *Baran and Labonnote* [2007]. The ensemble model consists of six habit members. The first habit is the hexagonal ice column of aspect ratio unity, where the aspect ratio is the quotient between the length and the diameter of the three-dimensional hexagon. The second habit is assumed to be the six-branched bullet rosette, followed by three-, five-, eight-, and ten-element hexagonal ice aggregates. For each of the hexagonal ice aggregates, the hexagonal monomers are arbitrarily attached to each other, forming compact and spatial ice aggregates. The orientation-averaged aspect ratio of each of these aggregate habits is given in Table 6 of *Baran and Labonnote* [2007]. To obtain the bulk-scattering optical properties, the ensemble model single-scattering properties were integrated over a moment estimation parameterization of the PSD due to *Field et al*. [2007], named hereafter F07. To generate the PSDs, a total number of 20,662 in situ estimates of IWC and in-cloud temperature measurements are applied to the F07 parameterization, given a mass-dimensional relationship. The PSD parameterization is further described below. The in situ estimates and measurements were obtained from a number of aircraft-based field campaigns located in the tropics and midlatitudes. The construction of the database used in this paper is fully described in *Baran et al*. [2011a] and *Baran et al*. [2014a] and so will not be repeated here. Each member of the ensemble can be assigned to a particular size bin. However, since the distribution of ensemble shapes throughout the PSD is unknown, the ensemble members are distributed into six equal intervals of the PSD, with the hexagonal columns being distributed into the first interval, and the last interval is occupied by the ten-element ice aggregate. The computation of the single-scattering SCSM optical property database is described in *Baran et al*. [2014a].

The F07 PSD parameterization is based on 10,000 in situ PSDs, which were filtered, by using particle interarrival times as described by *Field et al*. [2003] and *Field et al*. [2007], to reduce shattered ice artifacts distorting the shape of the small ice mode. Due to the shattering problem, the F07 parameterization ignored in situ measurements of ice crystal size less than 100 μm. To complete the PSD, the F07 parameterization assumes an exponential PSD to represent ice crystal size less than 100 μm, and this is added to a gamma function, for sizes greater than that. The F07 parameterization is shown to fit well to several cases of in situ measured-averaged PSDs obtained in the tropics [*Baran et al*., 2011a]. In the F07 parameterization, the second moment (i.e., the IWC) is linked to any other moment via polynomial fits to the in-cloud temperature. Thus, for any given IWC and in-cloud temperature, the original PSD can be estimated. It has been previously demonstrated by *Baran et al*. [2014a] that for several cases of ice cloud the SCSM bulk optical properties successfully simulated active and passive measurements from the UV to the microwave regions of the spectrum, while maintaining microphysical consistency across the spectrum.

The SCSM database consists of 20,662 PSDs (the compilation of the PSD database is described in *Baran et al*. [2014a]), that were generated from the F07 parameterization, using different in situ measured T and estimated IWC observations, and their distribution is shown in Figure 1. Figure 1 shows that the SCSM database covers a large range of both IWC and T values. The SCSM database provides for each PSD the simulated volumetric extinction and scattering coefficients and the asymmetry parameter at 145 wavelengths between 0.2 and 120 μm. In this paper, we utilize the database between 3 and 18 μm. The phase function is given by a linear

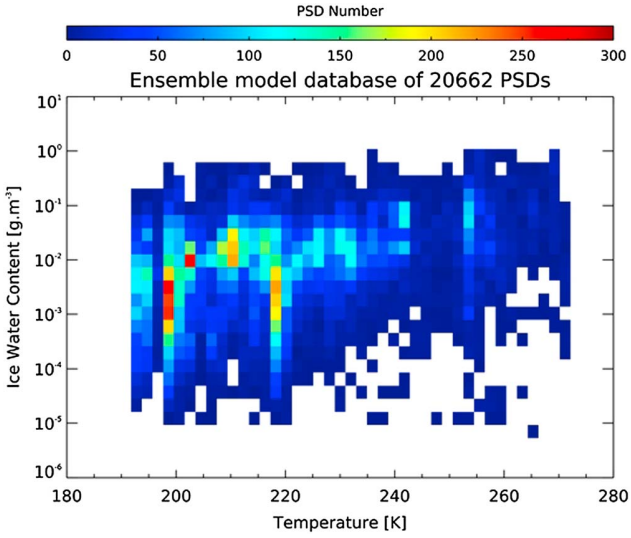

Figure 1. Two-dimensional histogram of ice water content (in g m^{-3}) versus temperature (in K) of the 20,662 PSD databases.

piecewise parameterization of the Henyey-Greenstein phase function, which depends only on the asymmetry parameter [*Baran et al.*, 2001], and is used to calculate the backscattering fraction coefficient *b*. The physical justification of using a phase function parameterization based on the Henyey-Greenstein phase function lies in the fact that in infrared range, the ice crystal phase function tends to be smooth in the backscattering region, with a strong diffraction peak in the forward scattering direction [*Yang et al.*, 2001]. The *Baran et al.*'s [2001] parameterization of the Henyey-Greenstein phase function has been shown to replicate short-wave multiangle satellite and aircraft observations of cirrus [*Baran et al.*, 2001; *Baran and Francis*, 2004] as well as high-resolution infrared observations of cirrus between 3.0 and 18.0 μm [*Baran and Francis*, 2004]. Therefore, for the purposes of this paper the *Baran et al.*'s [2001] parameterization of the Henyey-Greenstein phase function is sufficiently accurate.

It was found that the following equations gave the best fit to the distribution of bulk optical properties shown in Figure 1. The new parameterization has been implemented into RTTOV-11 and is given by the following equations:

$$\log_{10}[\beta_{\mathrm{abs}}(\lambda,T,\mathrm{IWC})] = A_a + B_aT + C_a\log_{10}(\mathrm{IWC}) + D_aT^2, + E_a(\log_{10}(\mathrm{IWC}))^2 + F_aT\log_{10}(\mathrm{IWC}) \quad (2)$$

$$\log_{10}[\beta_{\mathrm{sca}}(\lambda,T,\mathrm{IWC})] = A_s + B_sT + C_s\log_{10}(\mathrm{IWC}) + D_sT^2 + E_s(\log_{10}(\mathrm{IWC}))^2 + F_sT\log_{10}(\mathrm{IWC}), \quad (3)$$

$$b(\lambda,T,\mathrm{IWC}) = A_b + B_bT + C_b\log_{10}(\mathrm{IWC}). \quad (4)$$

The set of parameterization coefficients for β_{abs} (A_a to F_a), β_{sca} (A_s to F_s), and b (A_b to C_b) were calculated by using a nonlinear least squares fitting procedure over the SCSM database and are also functions of wavelength (omitted in equations for clarity). More details of this procedure can be found in *Saunders et al.* [2013].

It has been shown by *Baran et al.* [2011a] that the ensemble model predicts a mass-dimensional relationship of the form $m = aD^2$, where the prefactor a has a value of 0.04 and D is the maximum dimension of the ice crystal, where m and D are both in SI units [*Baran et al.*, 2011b]. This mass-dimensional relationship is applied to the F07 parameterization to generate the 20,662 PSDs, from which the bulk optical properties are obtained. We named, hereafter, this set of parameterization coefficients BV11. The BV11 parameterization was first improved by increasing the integration over the edges of the PSDs, leading to an improved SCSM database. An improved set of parameterization coefficients was then obtained, and this improved set is named B004. We tested new sets of parameterization coefficients afterward. This was achieved by changing the value of the prefactor and keeping the improvement of the integration over the PSD edges. In this paper, the values of the prefactor are assumed to be 0.015, 0.06, and 0.08. This range in prefactor value generates different shapes of the PSD. These new sets of parameterization coefficients are named hereafter B0.015, B0.06, and B0.08, respectively. A further SCSM database was also tested assuming a prefactor value of 0.0257, which corresponds to the value proposed by

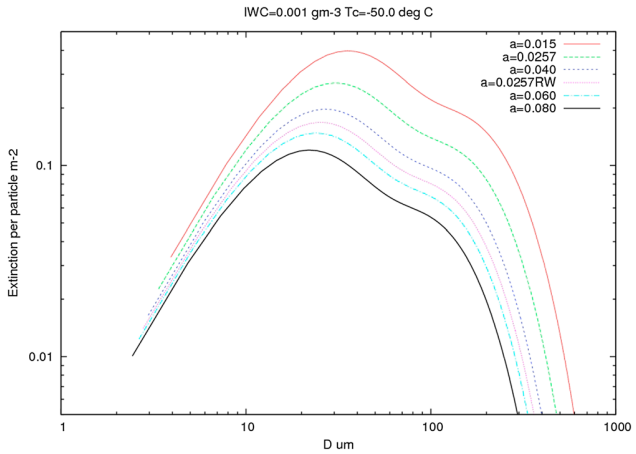

Figure 2. Extinction per particle in m^{-2} versus the maximum dimension of ice crystal D in μm for different values of the prefactor a of the mass-dimensional relationship throughout the exponent is set to a value of 2.0 (see text for explanation).

Cotton et al. [2013], and this other set of parameterization coefficients is named hereafter B0.0257. The use of this prefactor convolved with the F07 parameterization is microphysically consistent with the current cloud scheme used in the operational Met Office high-resolution NWP model [*Field et al*., 2014]. We finally tested a last SCSM database, where the scattering and absorption coefficients of the B0.0257 database were scaled by a fixed value of 0.49, hereafter named B0.0257RW, where RW stands for reweighting. The motivation for reweighting the ensemble model is to obtain an SCSM database between those of parameterizations B0.04 and B0.06 while preserving the *Cotton et al*.'s [2013] observed values of the prefactor and exponent in the mass-dimensional relationship (i.e., $m = 0.0257\ D^2$). In this case, the weightings of the ensemble model volumetric extinction coefficient β_{ext} were achieved at each size bin of the PSD using the following equation:

$$\beta_{ext} = \int_{D_{min}}^{D_{max}} \left[\sum_{j=1}^{j=6} w_j \beta_{ext,j}(D) \right] n(D) dD, \tag{5}$$

where D_{min} and D_{max} are the minimum and maximum values of the ice crystal maximum dimension in the F07 PSDs and w_j is the weight applied to each member of the ensemble model at each size bin. By definition, $\Sigma w_j = 1$ at each size bin. Finally, $n(D)$ is the ice crystal number concentration at each size bin predicted by the F07 PSD parameterization. To preserve the shape of the PSD using the constrain mass-dimensional relationship it was necessary to reweight the ensemble model using equation (5). If we assume the *Cotton et al*.'s [2013] observed microphysics (i.e., B0.0257) to be the best estimate of the mass-dimensional relationship, and applying this to the F07 parameterization, we will fix the underlying shape of the PSD. Given a fixed underlying shape of the PSD, the particle concentration per bin size can change, given the different profiles of IWC and T. Given the fixed underlying shape of the PSD, the ensemble model members were reweighted, such that the scattering and absorption coefficients were equivalent to the coefficients using a prefactor of between 0.04 and 0.06. This equivalence is achieved by using equation (5). The percentage contribution of each of the ensemble model members to the extinction coefficient (i.e., scattering plus absorption) per bin size was found to be 30% hexagonal columns; 30% six-branched bullet rosettes; and 10%, 20%, and finally 10% of three- to eight-branched ice aggregates, respectively. This idealized habit-weighted distribution may not represent the microphysical constitution of actual cirrus, but may simulate radiative equivalent cirrus, given a fixed underlying shape of the PSD.

The different prefactors were used to either broaden the F07 PSD or narrow the PSD to change the transmission properties of the cloud. The exponent of the mass-dimensional relationship was kept constant at a value of 2.0, as this value is consistent with the literature (see *Cotton et al*. [2013] for details and references therein). Figure 2 shows the extinction per particle versus the maximum dimension of ice crystal D for an assumed IWC value of 0.001 g m^{-3} and an assumed cloud temperature value of −50°C. The figure shows that on increasing the prefactor, the extinction becomes less, due to the need for fewer larger-sized particles to conserve IWC. On the other hand, on decreasing the prefactor, to lower values, increases the extinction, due to the need for larger particles being required to conserve IWC. In this way, the transmission properties of the cloud can be varied, and from the measurements, the best optimized convolution of ensemble model weighting and shape of the PSD can be found.

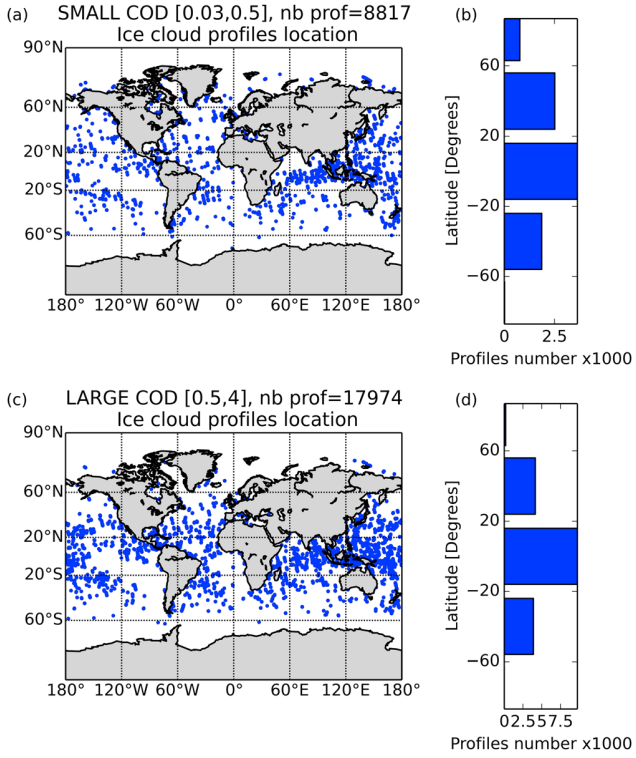

Figure 3. Global maps of selected ice cloud profiles for (a) small cloud optical depth and (c) large cloud optical depth for the two periods (22–28 February 2010 and 25–31 August 2010). (b and d) Zonal profiles number distributions are provided, respectively.

3. Selection of Ice Clouds

To evaluate the different RTTOV ice cloud parameterizations, we selected two different retrieval products of ice cloud profiles. The two products were retrieved from combined Lidar CALIOP (on board CALIPSO) and Radar CPR (on board CloudSat) instruments. The two products used in this paper are 2C-ICE [*Deng et al.*, 2010] and DARDAR [*Delanoë and Hogan*, 2010]. The two products provide information on the IWC and D_{eff} profiles, as well as the visible cloud optical depth (COD). The main differences between 2C-ICE and DARDAR are the vertical resolution of the product (CPR vertical resolution for 2C-ICE and CALIOP vertical resolution for DARDAR) and different assumptions for multiple scattering, lidar backscatter to extinction ratio, and parameterizations of radar and lidar signals [*Deng et al.*, 2013].

We selected the ice cloud profiles from 2 weeks (one in February and one in August 2010) of 2C-ICE and DARDAR product databases by using the DARDAR cloud mask product [*Delanoë and Hogan*, 2010]. The DARDAR cloud mask product was found to be better at removing aerosol-contaminated profiles than the CloudSat mask product. We also selected only profiles over oceans, to reduce potential land surface emissivity errors in our simulations, and when the pressures of the ice cloud layers were between 440 hPa (for the lowest layer) and 50 hPa (for the highest layer). We finally separated the selection into two groups of optical depth, one for COD between 0.03 and 0.5 (named small COD) and one for COD between 0.5 and 4 (named large COD).

Figures 3a and 3c represent the global location of ice cloud profiles for small and large CODs, respectively. The total number of profiles is 8817 profiles for small COD and 17,974 profiles for large COD. The zonal number of the profile distribution is shown in Figures 3b and 3d for each of the COD classifications, respectively. We separated the latitudes into the following five areas: High-Latitude North (90°N–60°N), Midlatitude North (60°N–20°N), Tropical Latitudes (20°N–20°S), Midlatitude South (20°S–60°S), and High-Latitude South (HLS) [60°S–90°S]. Most of the profiles are located in the tropics (with 41.2% and 54.2% of the total number of profiles for small and large CODs, respectively), and the profile distribution decreases toward the higher latitudes. For both COD classifications, there are significantly fewer profiles located at high latitudes (9% and 1.1% for small and large CODs, respectively). Figures 4a–4d show the mean and standard deviation profiles of IWC and D_{eff}, calculated from 2C-ICE (blue) and DARDAR (red). Figures 4a and 4b show the IWC and D_{eff} profiles for small COD, respectively, while Figures 4c and 4d show the same but for large COD. DARDAR generally retrieves more IWC and larger D_{eff} than 2C-ICE, except for D_{eff} in the highest layers. The difference between the two products mean and standard deviation profiles is more important for small COD, especially for IWC in the upper layers of ice clouds (see Figure 4a), above about 300 hPa.

4. Results

We compared the RTTOV TOA-simulated BT with TOA-observed BT, as measured by the IIR instrument on board CALIPSO in three channels. The response function of each of the IIR channels is centered on 8.65 μm

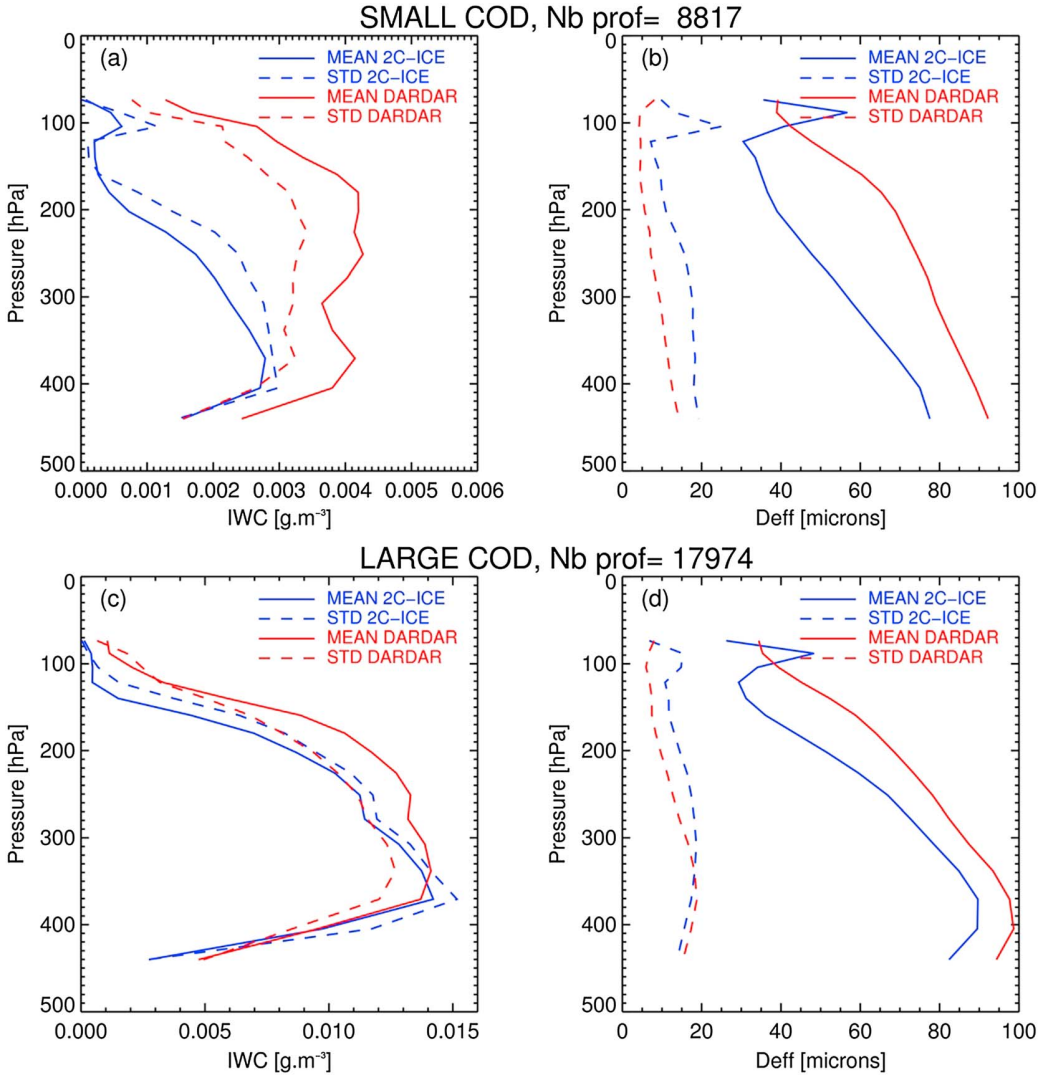

Figure 4. Mean and standard deviation profiles of (a) IWC and (b) D_{eff} from selected 2C-ICE profiles (in blue) and from selected DARDAR profiles (in red) for small COD. Mean and standard deviation profiles of (c) IWC and (d) D_{eff} for large COD, respectively.

(1156 cm^{-1}), 10.6 μm (943 cm^{-1}), and 12.05 μm (830 cm^{-1}). The absolute accuracy of the IIR channels is considered to be better than 1 K [*Corlay et al.*, 2000]. For all RTTOV simulations, we assume a cloud fraction of unity in any cloud layer. This assumption is supported by the fine spatial resolution of IIR (~1 km). To complete the needed inputs for RTTOV, we used collocated European Centre for Medium-Range Weather Forecasts (ECMWF) meteorological profiles (for pressure, temperature, specific humidity, and ozone mixing ratio) and collocated ECMWF surface pressure and 2 m temperature (ECMWF-AUX CloudSat product). We finally used collocated skin temperature from the Operational Sea Surface Temperature and Sea Ice Analysis (OSTIA) product [*Donlon et al.*, 2011]. This product was chosen because it was better to simulate clear-sky IIR observations as compared with the ECMWF skin temperature product (not shown here for reasons of brevity), and it provides a mask of sea ice for ice cloud cases in the high latitudes. The accuracy of RTTOV simulations in cloud-free situations was estimated by selecting 6629 clear-sky profiles for 22 February 2010. The biases and standard deviations between IIR observations minus RTTOV simulations were found to be -0.35 ± 0.76 K, -0.13 ± 0.82 K, and -0.23 ± 0.83 K for channels 1, 2, and 3, respectively.

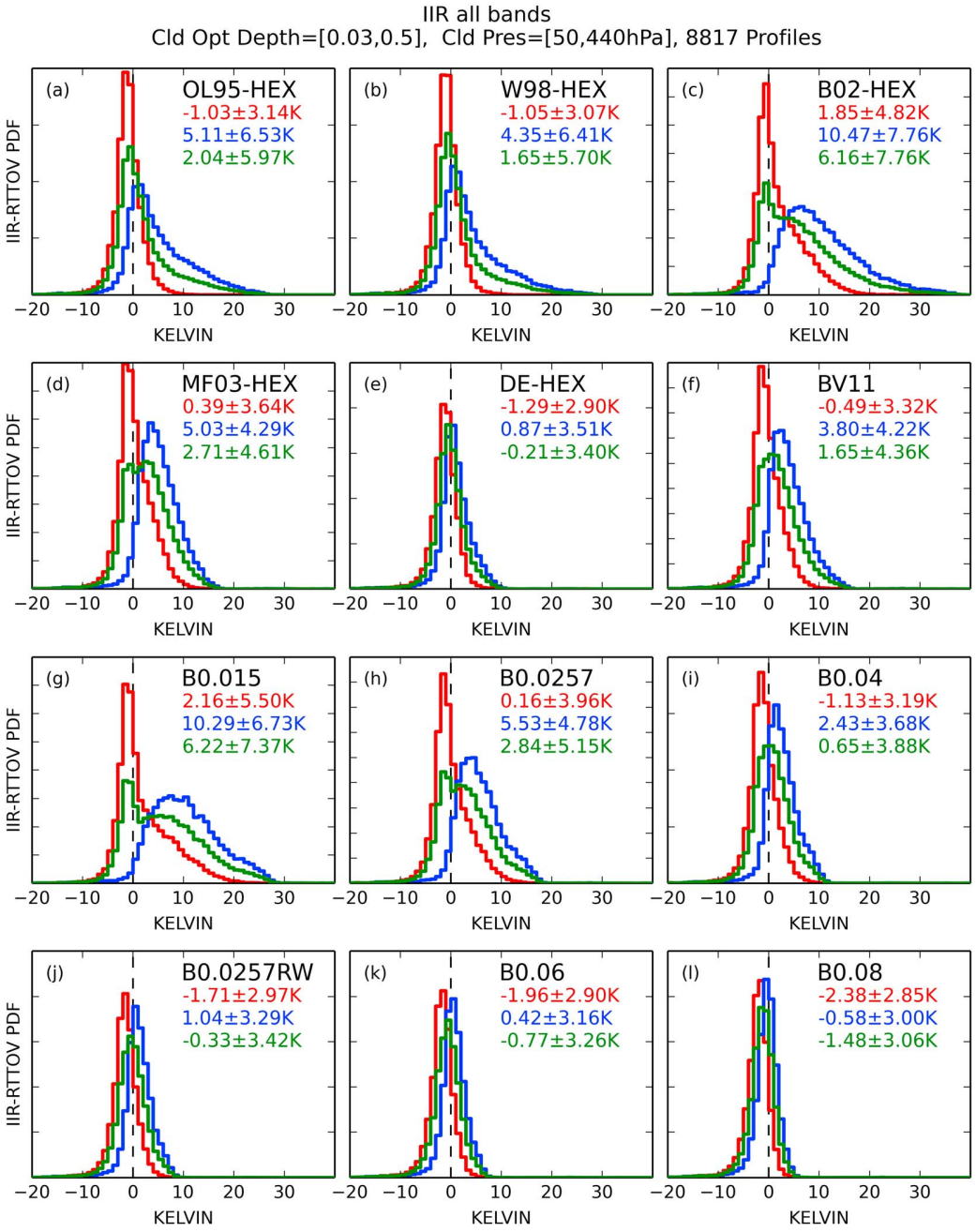

Figure 5. The normalized PDFs of IIR BT observations in all bands minus RTTOV BT simulations for the different ice cloud parameterizations, for small COD and from 2C-ICE (in red), from DARDAR (in blue), and from both 2C-ICE and DARDAR (in green) and the zero bias (black dashed line). Values of mean biases and standard deviations are provided in the legend. (a) OL95-HEX, (b) W98-HEX, (c) B02-HEX, and (d) MF03-HEX stand for the *Ou and Liou* [1995], *Wyser* [1998], *Boudala et al.* [2002], and *McFarquhar et al.* [2003] parameterizations, respectively. These parameterizations express the bulk optical properties as a function of the ice crystal effective diameter and IWC and/or temperature. (e) DE-HEX stands for the case where ice crystal effective diameter retrieved from satellite measurements was used together with hexagonal crystal optical parameterization. (f) BV11 stands for the current RTTOV version 11 parameterization of the SCSM model, and (g) B0.015, (h) B0.0257, (i) B0.04, (j) B0.0257RW, (k) B0.06, and (l) B0.08 stand for the parameterizations of the SCSM model with a prefactor of 0.015, 0.0257, 0.04, 0.0257 reweigthed, 0.06, and 0.08, respectively.

4.1. Global Results

Figures 5a–5l are IIR observations minus RTTOV simulations (O-B) represented as normalized probability density functions (PDFs) for small COD and for each of the parameterizations. The normalization is defined as the integral of the histogram summed to unity. The PDFs were calculated from the aggregation of the three O-B data sets corresponding to each of the IIR channels, leading to 3 times the number of selected profiles for each PDF. We simulated TOA BT by using 2C-ICE ice cloud profiles (in red), DARDAR ice cloud profiles (in blue), and both 2C-ICE and DARDAR (in green). The mean biases (μ) and standard deviations (σ) of the PDFs, derived from each of the parameterizations, shown in the panels, are given by

$$\mu = \frac{1}{3n}\sum_{i=1}^{3n}(O_i - B_i), \tag{6}$$

where n is the number of selected profiles and

$$\sigma = \sqrt{\frac{1}{3n}\sum_{i=1}^{3n}(O_i - \mu)^2}, \tag{7}$$

respectively.

Figures 5a–5f show the results for the current RTTOV-11 ice cloud parameterizations (excluding the aggregate shape for reasons given in section 1). The zero bias is shown by the vertical dashed lines. The results show that the PDFs are different when using 2C-ICE or DARDAR, except for the parameterization using the D_{eff} profiles as input (DE-HEX), see Figure 5e. With 2C-ICE ice cloud profile inputs (in red), RTTOV simulations are overestimated for OL95-HEX (Figure 5a), W98-HEX (Figure 5b), DE-HEX (Figure 5e), and BV11 (Figure 5f), with negative biases between −0.49 K and −1.29 K. RTTOV simulations are underestimated for B02-HEX (Figure 5c) and MF03-HEX (Figure 5d), with positive biases of 1.85 K and 0.39 K, respectively. With DARDAR ice cloud profiles (in blue), RTTOV simulations are more underestimated for most of the parameterizations (with positive biases between 3.8 K and 10.47 K), except for DE-HEX (Figure 5e), which has a bias of 0.87 K. Standard deviations (SDs) are also larger with DARDAR inputs. These results confirm the mean ice cloud profiles shown in Figure 4a, where the mean and standard deviation IWC profiles for small COD from DARDAR are greater than those from the 2C-ICE product, leading to lower BT simulations. Similarly, the lower difference between the DARDAR and 2C-ICE mean D_{eff} profiles (Figure 4b) is also obtained in the O-B PDF (see Figure 5e). These results also show that the comparison is very sensitive to the products of ice water content profiles used as inputs for RTTOV. To reduce this dependence on the ice cloud product, we aggregated TOA simulations from both products into the same data set. In the plot of Figure 5, the green lines represent the PDFs, when combining both products. The values of the mean biases and standard deviations are given in the legends. When combining 2C-ICE and DARDAR, and for most of the parameterizations, the O-B overestimation from 2C-ICE (due to lower IWC inputs) is cancelled out with the O-B underestimation from DARDAR IWC inputs. Figure 5e shows that the DE-HEX parameterization gave the lowest mean bias of −0.21 K with a SD of 3.4 K out of all current RTTOV parameterizations. However, this model was shown by *Baran and Francis* [2004] not to be a suitable model to use for the simultaneous simulation of high-resolution solar and infrared radiances measured from above and below the cirrus. Furthermore, the PSDs on which the DE-HEX parameterization is based were highly likely to have been affected by ice crystal shattering. This means that the overestimation of the occurrence of small ice crystals when convolved with the geometry of the hexagonal column could lead to a cancellation of error. Excluding the DE-HEX parameterization for the reasons given above means that the best agreement is found with the BV11 parameterization with $\mu = 1.65$ K and $\sigma = 4.36$ K (Figure 5f).

We experimented with further parameterizations to minimize O-B differences, to see if an optimal combination of PSD shape and optical properties could be found. This was achieved by modifying the SCSM database with the change of the mass-dimensional prefactor, as previously described in section 2. The effect of increasing the prefactor is (1) to change the mean bias from 6.22 K (for $a = 0.015$; Figure 5g) to −1.48 K (for $a = 0.08$; Figure 5i) and (2) to reduce the standard deviation from 7.37 K to 3.06 K, respectively. The best compromise is found for B0.0257RW, which represents the reweighted ensemble model, made to be consistent with the most current microphysics (Figure 5j). Using this parameterization, we found that $\mu = -0.33$ K and $\sigma = 3.42$ K. It is interesting to note here that the unweighted ensemble model results, assuming a prefactor of 0.0257 (Figure 5h), gives a combined $\mu = 2.84$ K and combined

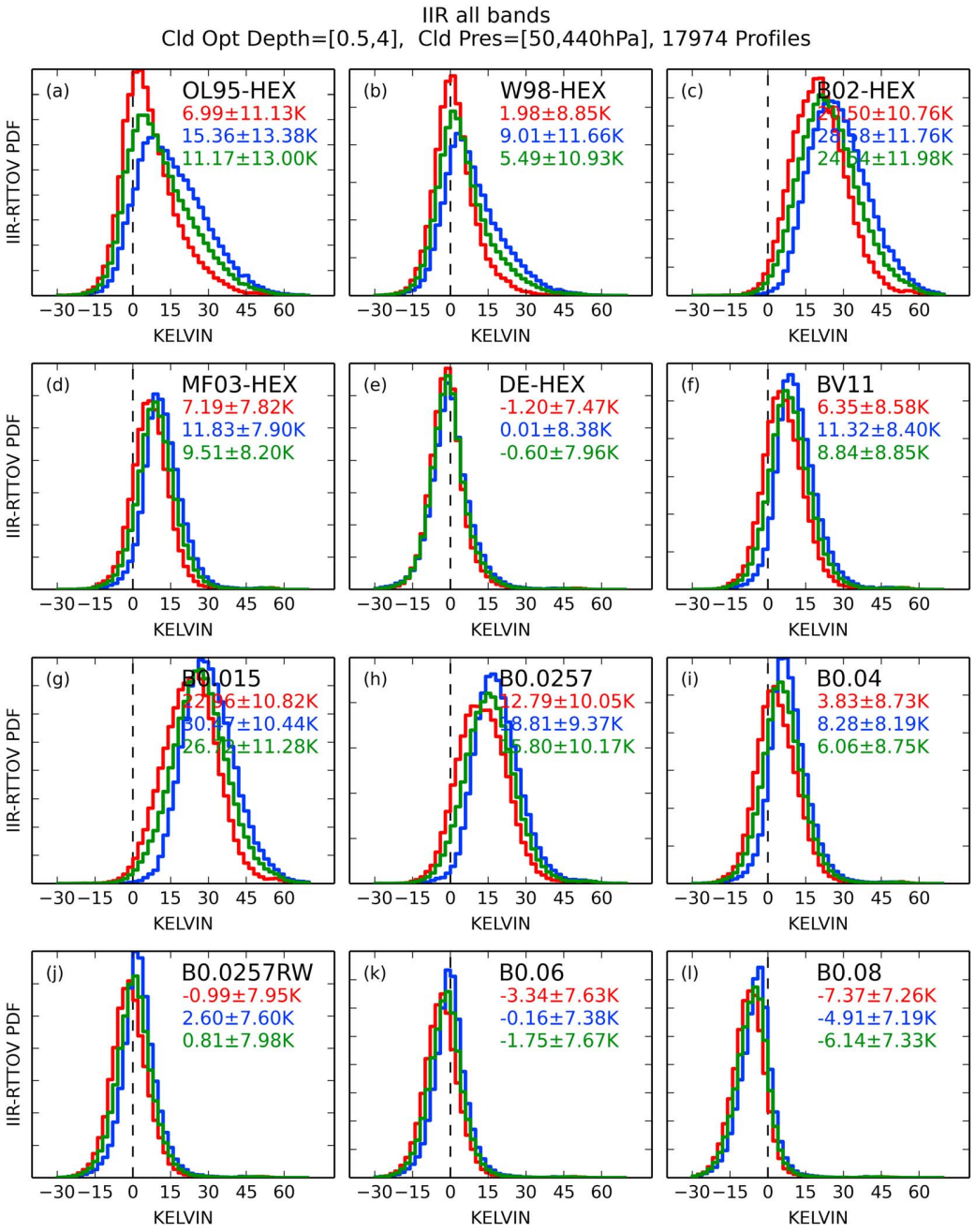

Figure 6. (a–l) Same as Figure 5 for large COD.

$\sigma = 5.15$ K, which means that, for small COD, the model was too biased toward the hexagonal ice column. The reason for this bias toward the hexagonal ice column is because it has been assigned to the first interval of the six equally divided intervals of the PSD, and it is over the first interval that the ice crystal number concentration is a maximum, which when convolved with the broader PSD (as can be seen from Figure 2), biased the simulated cloud BT's to colder temperatures.

Figures 6a–6l show the same comparison but for large COD. As compared to small COD, the differences between the distributions when using DARDAR or 2C-ICE is less important; however, standard deviations are much larger. These results confirm also the mean ice cloud profiles shown in Figures 4c and 4d, where the differences were found to be less between DARDAR and 2C-ICE IWC. When combining DARDAR and

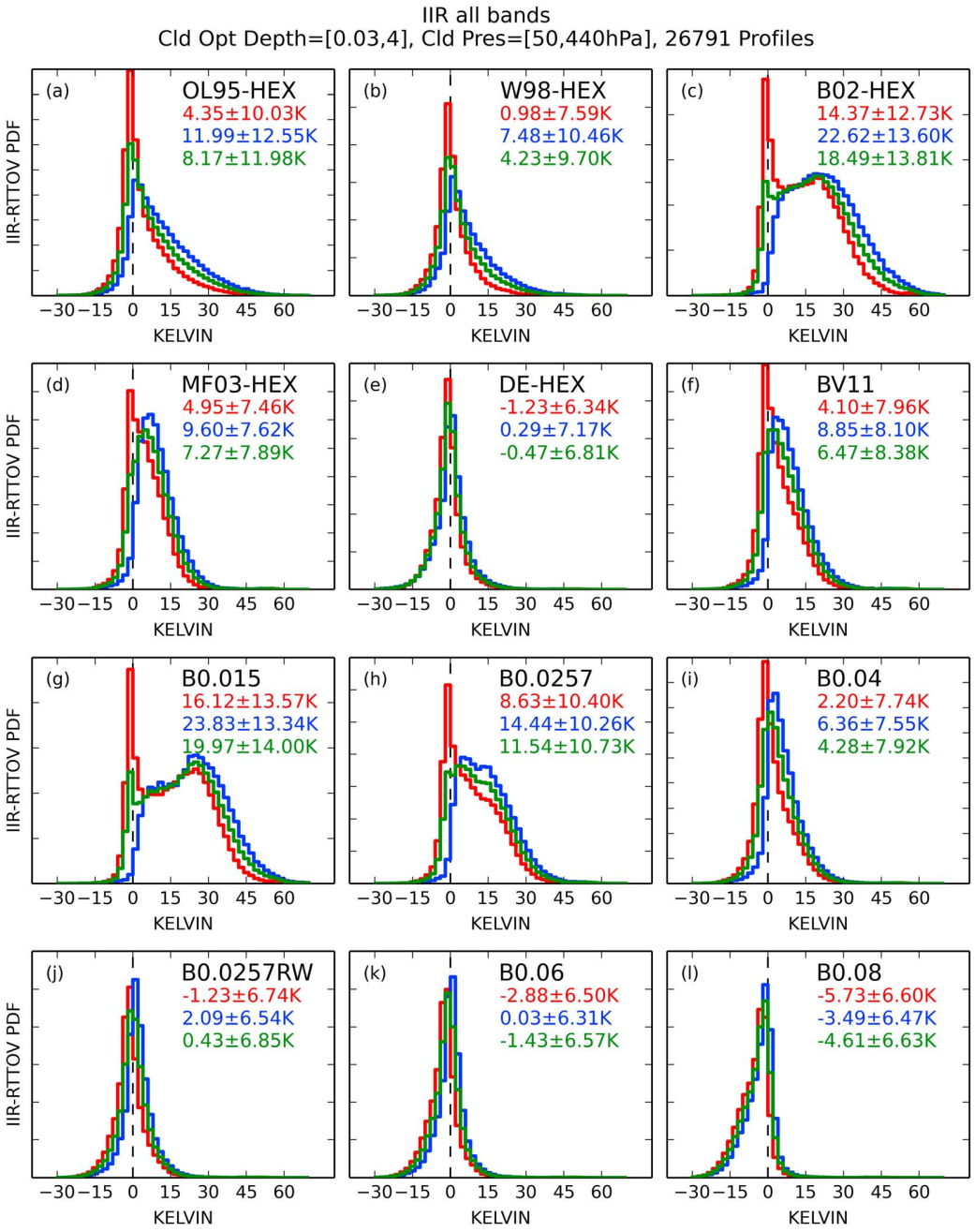

Figure 7. (a–l) Same as Figure 5 for all COD.

2C-ICE, the best agreement for the current RTTOV-11 ice cloud parameterizations (Figures 6a–6f) is again DE-HEX (Figure 6e) with $\mu = -0.6$ K and $\sigma = 7.96$ K (with caveats regarding previous comments about consistency and PSDs). If D_{eff} is not inputted, the second best agreement is found for the W98-HEX parameterization, with $\mu = 5.49$ K and $\sigma = 10.93$ K (Figure 6b). The same caveats apply to this parameterization with regard to geometry and the PSDs being affected by ice crystal shattering. By experimenting with the prefactor of the mass-dimensional relationship applied to the SCSM database, we can again improve the correlation with the same effect as for small COD, when increasing the prefactor and reweighting the ensemble model. For large COD, the best compromise is also found for B0.0257RW (Figure 6j), with $\mu = 0.81$ K and $\sigma = 7.98$ K, which is consistent with the results found for small COD.

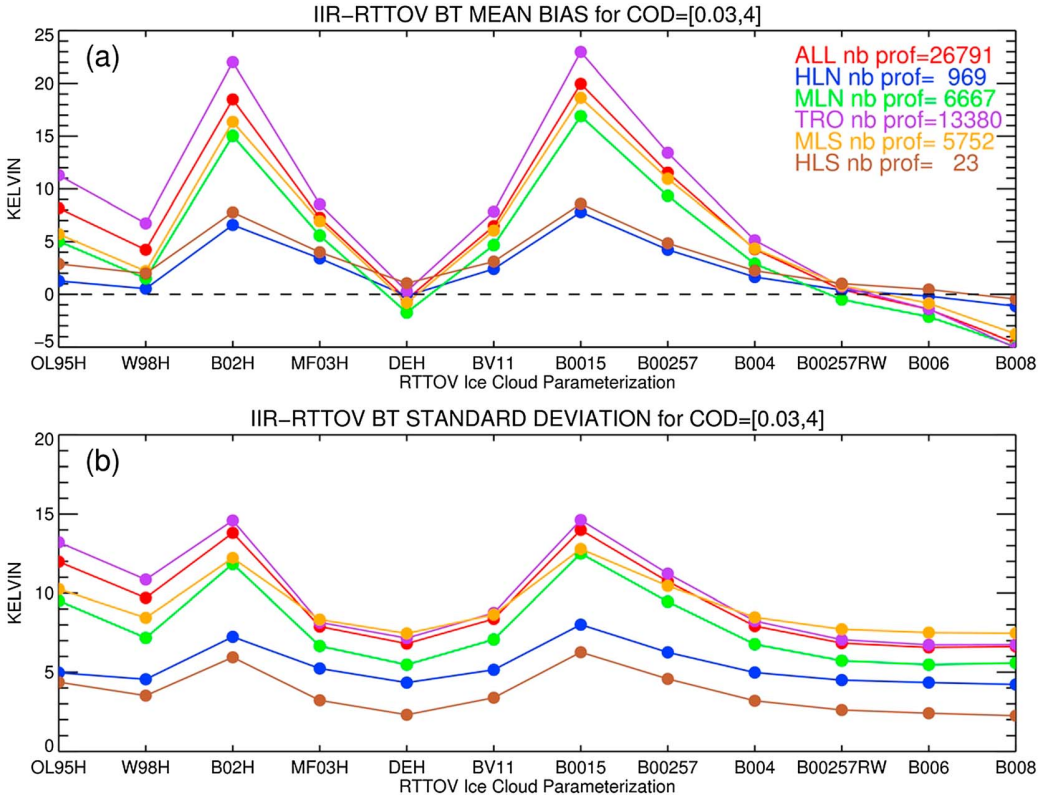

Figure 8. IIR BT observations minus RTTOV simulations (a) mean bias and (b) standard deviation versus RTTOV ice cloud parameterization from all COD profiles in all zonal areas (in red), in High-Latitude North (blue), in Midlatitude North (green), in Tropical Latitudes (purple), in Midlatitude South (orange), and in High-Latitude South (brown). The number of profiles for each area is given in Figure 8a legend.

Finally, we evaluated the comparison when adding the two COD groups to find out which one of the current RTTOV-11 parameterizations provides the best agreement. The results are depicted in Figures 7a–7l. The DE-HEX parameterization with $\mu = -0.47$ K and $\sigma = 6.81$ K (Figure 7e) is still the best of the current RTTOV-11 ice cloud parameterizations, and the W98-HEX parameterization with $\mu = 4.23$ K and $\sigma = 9.70$ K (Figure 7b), when D_{eff} is not inputted. Again, the previously stated caveats apply to these parameterizations.

The impact of changing the transmission properties of the SCSM, by increasing the prefactor in the mass-dimensional relationship to change the shape of the PSD, is also shown in Figure 7. The combined results show that the effect is to move the mean bias from underestimation to overestimation of the RTTOV BT simulations and to systematically reduce the standard deviation. Consistent with the results found for small and large CODs, the combined results show that the B0.0257RW parameterization provides the best agreement with the observations, with $\mu = 0.43$ K and $\sigma = 6.85$ K (Figure 7j). The remaining rather high value of the standard deviation may have different sources, as the uncertainties from IWC products or the error due to the RTTOV scattering approximation. As a comparison, other fast RTMs have shown similar standard deviations when comparing infrared observations and simulations in ice cloud situations [*Chen et al.*, 2008]. The results show that the B0.0257RW parameterization is closest to the current RTTOV-11 DE-HEX parameterization (Figure 7e). However, the B0.0257RW parameterization is the most consistent with current cirrus microphysics observations, in terms of PSDs, mass-dimensional relationships, and does not include significant biases in the small ice mode of the PSD due to ice crystal shattering. Moreover, simulations with this optimized parameterization are statistically very close to the simulations with the parameterization, when D_{eff} profile is inputted, and are statistically better than simulations with the other current RTTOV-11 ice cloud parameterizations. This section has shown that given a best-estimated PSD, from the latest observations of the mass-dimensional relationship [*Cotton et al.*, 2013], the ensemble model can be reweighted to find the

best optimal fit to the measurements. In principle, this can be applied to any shape of the PSD while maintaining microphysical consistency.

4.2. Zonal Results

We next studied whether the parameterizations have any zonal dependence. The results of this analysis are shown in Figure 8, which show the mean bias (Figure 8a) and standard deviation (Figure 8b) values for each of the parameterizations. As for Figure 7, the two groups of COD and all IIR channels were combined. The different colors shown in Figure 8 represent the different zonal areas, and the number of profiles in each zonal area defined in section 3 is given in the legend. The red line corresponds to values from Figure 7. The results found at the global scale can be applied for all zonal areas, even for HLS where very few profiles were selected. From Figure 8, it can be seen that the least zonally biased parameterization is B0.0257RW. Therefore, whatever the zone, the optimized B0.0257RW parameterization better simulates the IIR TOA BT in the presence of ice clouds.

5. Conclusions

A Self-Consistent Scattering Model (SCSM) database of ice cloud optical properties in the thermal infrared has been parameterized and implemented into RTTOV-11. This new parameterization allows a direct estimation of the cloud optical properties from the IWC and the ambient temperature T profiles, avoiding the choice of an effective diameter relationship and the shape of ice crystals. To evaluate this new parameterization, with other RTTOV ice cloud parameterizations, we selected a data set of ice cloud profiles from 2C-ICE and DARDAR products. The comparison of simulated TOA brightness temperatures against collocated IIR observations showed that the best parameterizations to apply are DE-HEX and B0.0257RW, where, in the case of DE-HEX, the effective size profile of ice cloud has to be provided as input to RTTOV. We point out here that the B0.0257RW parameterization is directly related to the NWP or climate model prognostic variable IWC, whereas D_{eff} has to be diagnosed, usually within the radiation scheme of NWP or climate models, and this diagnosis depends on empirical fits between D_{eff} and environmental temperature and/or IWC. Moreover, the single hexagonal column cannot be applied across the electromagnetic spectrum as demonstrated by *Baran and Francis* [2004]. Furthermore, the older RTTOV-11 parameterizations are based on PSDs which are highly likely to have been affected by ice crystal shattering, thereby resulting in underestimated D_{eff} values [*Mitchell et al.*, 2011]. Nevertheless, for all parameterizations, the mean biases between simulated and observed brightness temperatures are still up to a few kelvins. A recent paper by *Fauchez et al.* [2014] has shown that cirrus heterogeneities can impact simulations of brightness temperatures in the terrestrial window region by several kelvins when compared against RTM assuming plane-parallel and homogeneous layers. Therefore, the remaining biases shown in this paper could be due to 3-D cloud effects, which should be taken into account in future simulations through some form of parameterization.

To obtain the B0.0257RW parameterization, which is fundamentally based on the SCSM database, we used the selected data set of ice cloud profiles to minimize the bias between simulations and observations. We demonstrated that by modifying the prefactor of the mass-dimensional law of the PSD, to match the *Cotton et al.*'s [2013] observationally derived mass-dimensional relationship, we could reduce the bias from 6.47 K to 0.43 K and the standard deviation from 8.38 K to 6.85 K for the complete range of visible COD used in this study. Indeed, the B0.0257RW parameterization was demonstrated to be the least zonally biased out of all the current RTTOV-11 parameterizations. As a result of this finding, in the next version of RTTOV, we will replace the current SCSM parameterization (BV11) with the optimized SCSM database parameterization (B0.0257RW). This parameterization can also be applied to any other fast radiative transfer model [see for example *Havemann et al.*, 2009; *Thelen et al.*, 2012]. This parameterization may also be applied to general circulation models, since the SCSM database has already been parameterized in a simplistic manner and tested in the Met Office Unified Model Global Atmosphere configuration 5.0 setup [*Baran et al.*, 2014b]. In future studies, the RTTOV parameterizations will be tested at wavelengths ranging from the visible to the near infrared.

Acknowledgments
This study was accomplished in the frame of the NWP-SAF project funded by EUMETSAT and was also supported by the French national program LEFE/INSU. We gratefully acknowledge the NASA CloudSat project for providing 2C-ICE and CloudSat products (http://www.cloudsat.cira.colostate.edu/data-products). We also thank the ICARE data and service center for providing the DARDAR cloud and mask products (http://www.icare.univ-lille1.fr/drupal/projects/dardar) and the Met Office for maintaining and providing the OSTIA products in the frame of the MyOcean European Project (http://ghrsst-pp.metoffice.com/pages/latest_analysis/ostia.html). The optical properties on which the optimized SCSM database parameterization is based are freely available upon request to Anthony Baran. We would like also to thank anonymous reviewers for helping to improve the manuscript.

References

Baran, A. J., and P. N. Francis (2004), On the radiative properties of cirrus cloud at solar and thermal wavelengths: A test of model consistency using high-resolution airborne radiance measurements, *Q. J. R. Meteorol. Soc.*, *130*, 763–778.

Baran, A. J., and L.-C. Labonnote (2007), A self-consistent scattering model for cirrus. I: The solar region, *Q. J. R. Meteorol. Soc.*, *133*, 1899–1912.

Baran, A. J., P. N. Francis, L.-C. Labonnote, and M. Doutriaux-Boucher (2001), A scattering phase function for ice cloud: Tests of applicability using aircraft and satellite multi-angle multi-wavelength radiance measurements of cirrus, *Q. J. R. Meteorol. Soc.*, *127*, 2395–2416.

Baran, A. J., P. J. Connolly, A. J. Heymsfield, and A. Bansemer (2011a), Using in situ estimates of ice water content, volume extinction coefficient, and the total solar optical depth obtained during the tropical ACTIVE campaign to test an ensemble model of cirrus ice crystals, *Q. J. R. Meteorol. Soc.*, *137*, 199–218, doi:10.1002/qj.731.

Baran, A. J., A. Bodas-Salcedo, R. Cotton, and C. Lee (2011b), Simulating the equivalent radar reflectivity of cirrus at 94 GHz using an ensemble model of cirrus ice crystals: A test of the Met Office global numerical weather prediction model, *Q. J. R. Meteorol. Soc.*, *137*, 1547–1560.

Baran, A. J., R. Cotton, K. Furtado, S. Havemann, L.-C. Labonnote, F. Marenco, A. Smith, and J.-C. Thelen (2014a), A self-consistent scattering model for cirrus. II: The high and low frequencies, *Q. J. R. Meteorol. Soc.*, doi:10.1002/qj.2193.

Baran, A. J., P. Hill, K. Furtado, P. Field, and J. Manners (2014b), A coupled cloud physics–radiation parameterization of the bulk optical properties of cirrus and its impact on the Met Office Unified Model Global Atmosphere 5.0 configuration, *J. Clim.*, *27*, 7725–7752, doi:10.1175/JCLI-D-13-00700.1.

Bauer, P., et al. (2011), Satellite cloud and precipitation assimilation at operational NWP centres, *Q. J. R. Meteorol. Soc.*, *137*, 1934–1951, doi:10.1002/qj.905.

Baum, B. A., P. Yang, S. Nasiri, A. K. Heidinger, A. Heymsfield, and J. Li (2007), Bulk scattering properties for the remote sensing of ice clouds. Part III: High-resolution spectral models from 100 to 3250 cm^{-1}, *J. Appl. Meteorol. Climatol.*, *46*, 423–434, doi:10.1175/JAM2473.1.

Baum, B. A., P. Yang, A. J. Heymsfield, A. Bansemer, A. Merrelli, C. Schmitt, and C. Wang (2014), Ice cloud bulk single-scattering property models with the full phase matrix at wavelengths from 0.2 to 100 μm, *J. Quant. Spectrosc. Radiat. Transfer*, *146*, 123–139, doi:10.1016/j.jqsrt.2014.02.029.

Boudala, F. S., G. A. Isaac, Q. Fu, and S. G. Cober (2002), Parameterization of effective ice particle size for high-latitude clouds, *Int. J. Clim.*, *22*, 1267–1284.

Chen, Y., F. Weng, Y. Han, and Q. Liu (2008), Validation of the community radiative transfer model by using CloudSat data, *J. Geophys. Res.*, *113*, D00A03, doi:10.1029/2007JD009561.

Chou, M. D., K. T. Lee, S. C. Tsay, and Q. Fu (1999), Parameterization for cloud longwave scattering for use in atmospheric models, *J. Clim.*, *12*, 159–169.

Corlay, G., M.-C. Arnolfo, T. Bret-Dibat, A. Lifferman, and J. Pelon (2000), The infrared imaging radiometer for PICASSOCENA. [Available at http://smsc.cnes.fr/CALIPSO/IIR_ICSO00_S2-06.pdf.]

Cotton, R. J., P. R. Field, Z. Ulanowski, P. H. Kaye, E. Hirst, R. S. Greenaway, I. Crawford, J. Crosier, and J. Dorsey (2013), The effective density of small ice particles obtained from in situ aircraft observations of mid-latitude cirrus, *Q. J. R. Meteorol. Soc.*, *139*, 1923–1934.

Delanoë, J., and R. J. Hogan (2010), Combined CloudSat-CALIPSO-MODIS retrievals of the properties of ice clouds, *J. Geophys. Res.*, *115*, D00H29, doi:10.1029/2009JD012346.

Deng, M., G. G. Mace, Z. Wang, and H. Okamoto (2010), Tropical Composition, Cloud and Climate Coupling Experiment validation for cirrus cloud profiling retrieval using CloudSat radar and CALIPSO lidar, *J. Geophys. Res.*, *115*, D00J15, doi:10.1029/2009JD013104.

Deng, M., G. G. Mace, Z. Wang, and R. P. Lawson (2013), Evaluation of several A-Train ice cloud retrieval products with in situ measurements collected during the SPARTICUS campaign, *J. Appl. Meteorol. Climatol.*, *52*, 1014–1030, doi:10.1175/JAMC-D-12-054.1.

Donlon, C. J., M. Martin, J. D. Stark, J. Roberts-Jones, E. Fiedler, and W. Wimmer (2011), The Operational Sea Surface Temperature and Sea Ice Analysis (OSTIA), *Remote Sens. Environ.*, doi:10.1016/j.rse.2010.10.017.

Errico, R. M., G. Ohring, F. Weng, P. Bauer, B. Ferrier, J.-F. Mahfouf, and J. Turk (2007), Assimilation of satellite cloud and precipitation observations in numerical weather prediction models: Introduction to the JAS special collection, *J. Atmos. Sci.*, *64*, 3737–3741.

Faijan, F., L. Lavanant, and F. Rabier (2012), Towards the use of cloud microphysical properties to simulate IASI spectra in an operational context, *J. Geophys. Res.*, *117*, D22205, doi:10.1029/2012JD017962.

Fauchez, T., C. Cornet, F. Szczap, P. Dubuisson, and T. Rosambert (2014), Impact of cirrus clouds heterogeneities on top-of-atmosphere thermal infrared radiation, *Atmos. Chem. Phys.*, *14*, 5599–5615, doi:10.5194/acp-14-5599-2014.

Field, P. R., R. Wood, P. R. A. Brown, P. H. Kaye, E. Hirst, R. Greenaway, and J. A. Smith (2003), Ice particle interarrival times measured with a fast FSSP, *J. Atmos. Oceanic Technol.*, *20*, 249–261, doi:10.1175/1520-0426(2003)020<0249:IPITMW>2.0.CO;2.

Field, P. R., A. J. Heymsfield, and A. Bansemer (2007), Snow size distribution parameterization for midlatitude and tropical ice clouds, *J. Atmos. Sci.*, *64*, 4346–4365.

Field, P. R., R. J. Cotton, K. McBeath, A. P. Lock, S. Webster, and R. P. Allan (2014), Improving a convection-permitting model simulation of a cold air outbreak, *Q. J. R. Meteorol. Soc.*, *140*, 124–138, doi:10.1002/qj.2116.

Garnier, A., J. Pelon, P. Dubuisson, M. Faivre, O. Chomette, N. Pascal, and D. P. Kratz (2012), Retrieval of cloud properties using CALIPSO Imaging Infrared Radiometer. Part I: Effective emissivity and optical depth, *J. Appl. Meteorol. Climatol.*, *51*, 1407–1425, doi:10.1175/JAMC-D-11-0220.1.

Guidard, V., N. Fourrié, P. Brousseau, and F. Rabier (2011), Impact of IASI assimilation at global and convective scales and challenges for the assimilation of cloudy scenes, *Q. J. R. Meteorol. Soc.*, *137*, 1975–1987, doi:10.1002/qj.928.

Havemann, S., J.-C. Thelen, J. P. Taylor, and A. Keil (2009), The Havemann–Taylor fast radiative transfer code: Exact fast radiative transfer for scattering atmospheres using principal components (PCs), in *Proceedings of the International Radiation Symposium (IRC/IAMAS)*, AIP Conf. Proc., vol. 1100, pp. 38–40, doi:10.1063/1.3117000.

Hess, M., and M. Wiegner (1994), COP: A data library of optical properties of hexagonal ice crystals, *Appl. Opt.*, *33*, 7740–7746.

Hess, M., P. Koepke, and I. Schult (1998), Optical properties of aerosols and clouds: The software package OPAC, *Bull. Am. Meteorol. Soc.*, *79*, 831–844, doi:10.1175/1520-0477(1998)079<0831:OPOAAC>2.0.CO;2.

Korolev, A. V., E. F. Emery, J. W. Strapp, S. G. Cober, G. A. Isaac, M. Wasey, and D. Marcotte (2011), Small ice particles in tropospheric clouds: Fact or artifact? Airborne icing instrumentation evaluation experiment, *Bull. Am. Meteorol. Soc.*, *92*, 967–973, doi:10.1175/2010BAMS3141.1.

Martinet, P., N. Fourrié, V. Guidard, F. Rabier, T. Montmerle, and P. Brunel (2013a), Towards the use of microphysical variables for the assimilation of cloud-affected infrared radiances, *Q. J. R. Meteorol. Soc.*, *139*, 1402–1416, doi:10.1002/qj.2046.

Martinet, P., L. Lavanant, N. Fourrié, F. Rabier, and A. Gambacorta (2013b), Evaluation of a revised IASI channel selection for cloudy retrievals with a focus on the Mediterranean basin, *Q. J. R. Meteorol. Soc.*, doi:10.1002/qj.2239.

Matricardi, M. (2005), The inclusion of aerosols and clouds in RTIASI, the ECMWF fast radiative transfer model for the infrared atmospheric sounding interferometer, ECMWF Tech. Memo., 474.

Matricardi, M., F. Chevallier, G. Kelly, and J.-N. Thépaut (2004), An improved general fast radiative transfer model for the assimilation of radiance observations, *Q. J. R. Meteorol. Soc.*, *130*, 153–173, doi:10.1256/qj.02.181.

McFarquhar, G. M., S. Iacobellis, and R. C. J. Somerville (2003), SCM simulations of tropical ice clouds using observationally based parameterizations of microphysics, *J. Clim.*, *16*, 1643–1664.

McNally, A. P. (2009), The direct assimilation of cloud-affected satellite infrared radiances in the ECMWF 4D-Var, *Q. J. R. Meteorol. Soc.*, *135*, 1214–1229, doi:10.1002/qj.426.

Mitchell, D. L., R. P. Lawson, and B. Baker (2011), Understanding effective diameter and its application to terrestrial radiation in ice clouds, *Atmos. Chem. Phys.*, *11*, 3417–3429, doi:10.5194/acp-11-3417-2011.

Okamoto, K., A. P. McNally, and W. Bell (2013), Progress towards the assimilation of all-sky infrared radiances: An evaluation of cloud effects, *Q. J. R. Meteorol. Soc.*, doi:10.1002/qj.2242.

Ou, S. C., and K. N. Liou (1995), Ice microphysics and climatic temperature feedback, *Atmos. Res.*, *35*, 127–138.

Pavelin, E. G., S. J. English, and J. R. Eyre (2008), The assimilation of cloud-affected infrared satellite radiances for numerical weather prediction, *Q. J. R. Meteorol. Soc.*, *134*, 737–749.

Saunders, R., M. Matricardi, and P. Brunel (1999), A improved fast radiative transfer model for assimilation of satellite radiance observations, *Q. J. R. Meteorol. Soc.*, *125*, 1407–1425.

Saunders, R., M. Matricardi, A. Geer, P. Rayer, O. Embury, and C. Merchant (2009), RTTOV-9 Science and Validation Report. [Available at https://nwpsaf.eu/deliverables/rtm/rttov9_files/rttov9_svr.pdf.]

Saunders, R., J. Hocking, P. Rayer, M. Matricardi, A. Geer, and N. Bormann (2012), RTTOV-10 Science and Validation Report. [Available at https://nwpsaf.eu/deliverables/rtm/docs_rttov10/rttov10_svr_1.11.pdf.]

Saunders, R., J. Hocking, D. Rundle, P. Rayer, M. Matricardi, A. Geer, C. Lupu, P. Brunel, and J. Vidot (2013), RTTOV-11 Science and Validation Report. [Available at https://nwpsaf.eu/deliverables/rtm/docs_rttov11/rttov11_svr.pdf.]

Stengel, M., M. Lindskog, P. Undén, N. Gustafsson, and R. Bennartz (2010), An extended observation operator in HIRLAM 4D-VAR for the assimilation of cloud-affected satellite radiances, *Q. J. R. Meteorol. Soc.*, *136*, 1064–1074, doi:10.1002/qj.621.

Stengel, M., M. Lindskog, P. Undén, and N. Gustafsson (2013), The impact of cloud-affected IR radiances on forecast accuracy of a limited-area NWP model, *Q. J. R. Meteorol. Soc.*, *139*, 2081–2096, doi:10.1002/qj.2102.

Stephens, G. L., et al. (2002), The CloudSat mission and the A-Train, *Bull. Am. Meteorol. Soc.*, *83*, 1771–1790, doi:10.1175/BAMS-83-12-1771.

Thelen, J.-C., S. Havemann, and J. P. Taylor (2012), Atmospheric correction of shortwave hyperspectral imagery using a fast, full-scattering 1DVar retrieval scheme, in *Algorithms and Technologies for Multispectral, Hyperspectral, and Ultraspectral Imagery XVIII*, Proc. SPIE, 839010, edited by S. S. Shen and P. E. Lewis, doi:10.1117/12.918012.

Vidot, J., P. Brunel, and A. J. Baran (2013), A new ice cloud optical properties database in RTTOV for IASI, Third International IASI Conference, Hyères, France, 4–8, poster 40, 4–8 February. [Available at http://smsc.cnes.fr/IASI/PDF/conf3/posters/40_Vidot_J.pdf.]

Winker, D. M., M. A. Vaughan, A. Omar, Y. Hu, K. A. Powell, Z. Liu, W. H. Hunt, and S. A. Young (2009), Overview of the CALIPSO mission and CALIOP data processing algorithms, *J. Atmos. Oceanic Technol.*, *26*, 2310–2323, doi:10.1175/2009JTECHA1281.1.

Wyser, K. (1998), The effective radius in ice clouds, *J. Clim.*, *11*, 1793–1802.

Yang, P., B.-C. Gao, B. A. Baum, Y. X. Hu, W. J. Wiscombe, S.-C. Tsay, D. M. Winker, and S. L. Nasiri (2001), Radiative properties of cirrus clouds in the infrared (8–13 μm) spectral region, *J. Quant. Spectrosc. Radiat. Transfer*, *70*, 473–504, doi:10.1016/S0022-4073(01)00024-3.

Yang, P., H. Wei, H. Huang, B. Baum, Y. Hu, G. Kattawar, M. Mishchenko, and Q. Fu (2005), Scattering and absorption property database for nonspherical ice particles in the near- through far-infrared spectral region, *Appl. Opt.*, *44*, 5512–5523.

Yang, P., L. Bi, B. A. Baum, K.-N. Liou, G. Kattawar, M. Mishchenko, and B. Cole (2013), Spectrally consistent scattering, absorption, and polarization properties of atmospheric ice crystals at wavelengths from 0.2 μm to 100 μm, *J. Atmos. Sci.*, *70*, 330–347.

5.3 Saunders et al. (2018)

Cet article publié en 2018 dans *Geoscientific Model Development* (facteur d'impact de 5.154) fait suite à une volonté de l'équipe projet RTTOV de rassembler et de promouvoir scientifiquement les nouveaux développements de RTTOV et ainsi d'avoir un nouvel article de référence, le dernier datant de 1999 a été cité plus de 500 fois.

Geosci. Model Dev., 11, 2717–2737, 2018
https://doi.org/10.5194/gmd-11-2717-2018

Geoscientific Model Development
Open Access
EGU

An update on the RTTOV fast radiative transfer model (currently at version 12)

Roger Saunders[1], James Hocking[1], Emma Turner[1], Peter Rayer[1], David Rundle[1], Pascal Brunel[2], Jerome Vidot[2], Pascale Roquet[2], Marco Matricardi[3], Alan Geer[3], Niels Bormann[3], and Cristina Lupu[3]

[1]Met Office, Fitzroy Rd., Exeter, UK
[2]MeteoFrance/CMS, Avenue de Lorraine, Lannion, France
[3]ECMWF, Shinfield Park, Reading, UK

Correspondence: Roger Saunders (roger.saunders@metoffice.gov.uk)

Received: 7 March 2018 – Discussion started: 22 March 2018
Revised: 5 June 2018 – Accepted: 8 June 2018 – Published: 10 July 2018

Abstract. This paper gives an update of the RTTOV (Radiative Transfer for TOVS) fast radiative transfer model, which is widely used in the satellite retrieval and data assimilation communities. RTTOV is a fast radiative transfer model for simulating top-of-atmosphere radiances from passive visible, infrared and microwave downward-viewing satellite radiometers. In addition to the forward model, it also optionally computes the tangent linear, adjoint and Jacobian matrix providing changes in radiances for profile variable perturbations assuming a linear relationship about a given atmospheric state. This makes it a useful tool for developing physical retrievals from satellite radiances, for direct radiance assimilation in NWP models, for simulating future instruments, and for training or teaching with a graphical user interface. An overview of the RTTOV model is given, highlighting the updates and increased capability of the latest versions, and it gives some examples of its current performance when compared with more accurate line-by-line radiative transfer models and a few selected observations. The improvement over the original version of the model released in 1999 is demonstrated.

1 Introduction

Over the past 2 decades fast radiative transfer models have become an indispensable tool for a variety of applications including data assimilation in numerical weather prediction (NWP; for a list of abbreviations, please see the list in Appendix A) models (Eyre et al., 1993), enabling physical retrievals from satellite data (Li et al., 2000), producing simulated imagery from NWP models (Blackmore et al., 2014; Lupu and Wilhelmsson, 2016) and for assessing the performance of proposed instruments to fly on future satellites (Andrey-Andrés et al., 2018). The RTTOV (Radiative Transfer for TOVS) model was developed to enable the direct assimilation of radiances during the 1990s at the European Centre for Medium-Range Weather Forecasts (ECMWF) when it was implemented within their variational system (Andersson et al., 1998). The development of RTTOV was subsequently taken on within the EUMETSAT-funded Numerical Weather Prediction Satellite Application Facility (NWP SAF) in 1998. There are over 1000 users worldwide of RTTOV, and it is now used in many NWP centres around the world as part of their data assimilation system both for weather forecasting and producing atmospheric reanalyses. Although initially developed for the TIROS Operational Vertical Sounder (TOVS) radiometers, RTTOV can now simulate around 90 different satellite sensors measuring in the microwave (MW), infrared (IR) and visible (VIS) regions of the spectrum. Some of these instruments flew in the 1970s, and now RTTOV enables their radiances to be assimilated into historical atmospheric reanalyses exploiting these data, for the first time, with modern data assimilation methods (Poli et al., 2017). RTTOV can also be used in climate model simulations to provide top-of-atmosphere radiances for evaluating climate models as demonstrated by Turner and Tett (2014) and to facilitate this, it is now included in the CFMIP Observation Simulator Package (COSP) (Bodas-Salcedo et al., 2011).

There have been several other fast models developed over the years, notably the Community Radiative Transfer Model (CRTM) (Chen et al., 2008; Ding et al., 2011), which is also used in several NWP models, the Optimal Spectral Sampling (OSS) model (Moncet et al., 2015) and many others which have taken part in several inter-comparisons with RTTOV (e.g. Garand et al., 2001; Saunders et al., 2007; Aumann et al., 2018). These fast models are not only forward models (i.e. compute the top-of-atmosphere radiance from a given atmospheric state) but also compute the Jacobian matrix which gives the change in radiance for a change in any element of the atmospheric state assuming a linear relationship about a given atmospheric state. Not all applications require the full Jacobian matrix to be stored, and so tangent-linear and adjoint versions of the code are also provided as options. The performance of these models is not only assessed for the forward calculations but also for the Jacobian computations in terms of speed and accuracy (e.g. Saunders et al., 2007).

The initial version of RTTOV developed at ECMWF (version 3) which was made available to the community was documented in the open literature (Saunders et al., 1999), but since then there have been many upgrades (it is now at version 12, described in detail by Saunders et al., 2017), and so this paper is intended to provide an updated overview description of RTTOV in the peer review literature, taking into account all the changes in the interim period. The full documentation of the latest supported versions of RTTOV is available from the NWP SAF website,[1] and there have been papers on various aspects of the RTTOV development which are referenced here for more details. Section 2 provides a brief history of the different versions of RTTOV, Sect. 3 describes the latest capabilities of the model at version 12, Sect. 4 shows how well it reproduces the line-by-line models on which it is trained, and Sect. makes some comparisons with observations. A summary and future plans are given in Sect. 6.

2 A brief history of RTTOV

With the advent of satellite sounding radiometers in the 1970s and the need to derive atmospheric profile retrievals efficiently in near real time, activities were initiated to develop fast radiative transfer models for this application. An initial study reported by McMillin and Fleming (1976) showed that the layer transmittance of the atmosphere, for a region with only well-mixed gaseous absorption, can be parameterized by functions of the mean layer temperature. Further work developed formulations for water vapour and ozone where the gas concentration was also taken into account (Eyre and Woolf, 1988), and gradient versions of the model were developed for profile retrievals and assimilation applications which culminated in the first version of the RTTOV model maintained at ECMWF in the early 1990s (Eyre, 1991). During the mid-1990s EUMETSAT were setting up their SAFs one of which was the NWP SAF led by the Met Office (UK) which aimed to provide software packages to enable NWP centres to better exploit satellite data in their NWP systems. RTTOV was adopted by the NWP SAF as one of its main packages and has been developed within the SAF ever since and distributed to users worldwide, with currently over 1000 users of RTTOV in 2017.

The ECMWF version of RTTOV in 1999 was described in Saunders et al. (1999). Since then there have been many enhancements developed under the NWP SAF activities, and the interested reader is referred to the RTTOV website and the various science and validation reports for full details. For example one new innovation in recent years has been to compute the infrared spectrum as principal component (PC) scores (e.g. PCRTM, Liu et al., 2006; HT-FRTC, Havemann et al., 2009; and PC-RTTOV, Matricardi, 2010). PC-RTTOV and HT-FRTC have been adopted as options within RTTOV and this has enabled experiments to assimilate the PCs directly in NWP systems (Matricardi and McNally, 2014). This is potentially a way to make use of more of the spectrum measured by the new advanced IR sounders such as the Infrared Atmospheric Sounding Interferometer (IASI) as traditional methods can only assimilate a few hundred spectral channels efficiently with fast models. Another major development has been the addition of scattering effects for simulating cloudy and aerosol-affected radiances in the IR in version 9 (Matricardi, 2005) and a wrapper code for computing scattering from hydrometeors at MW frequencies introduced in version 8 (Bauer et al., 2006).

Table 1 gives a summary of the major upgrades for each version of the model, culminating in version 12 released to users in February 2017. In addition to these, each version benefitted from improved transmittances computed from the latest line-by-line models for the IR and MW wavelength regions (i.e. LBLRTM (Clough et al., 2005, Rothman et al., 2013) or AMSUTRAN (Liebe et al., 1989, Saunders et al., 2017)) and also improved computational speed through continuous optimization of the code for parallel computing architecture. After every new version of the code was developed an extensive validation campaign was undertaken to ensure the code was not slower or less accurate (when compared with line-by-line models) than the previous version. Checks were also made to ensure the tangent-linear, adjoint and full Jacobian versions of the code were all consistent with each other. Another constraint was that the code had to be backward compatible so users could reproduce the results of the previous version with the new code to enable a controlled transition to the new model in their operational systems.

Initially RTTOV only supported the NOAA TOVS radiometers (HIRS, MSU), but with the number of sounding radiometers increasing as more nations launched instruments and as TOVS was upgraded to the Advanced TOVS

[1] http://nwp-saf.eumetsat.int (last access: 6 July 2018)

Table 1. Major enhancements to RTTOV since the initial versions developed at ECMWF in mid 1990s.

RTTOV version	Release date	Major enhancements
1–4	Mid1990s	– TOVS only on 40 atmospheric levels. Clear sky and black cloud. Surface emissivity provided by user.
5	1999 (pre-NWP SAF)	– ATOVS, METEOSAT, GOES imagers. Clear sky and grey cloud, 43 atmospheric layers
6	March 2000	– Revised water vapour transmittance calculation – More sensors supported (e.g. ATSR, GOES, AVHRR, MODIS, GMS, SSM/I) – Addition of SSIREM IR and FASTEM MW ocean surface emissivity models – Addition of MW cloud liquid water absorption (English et al., 2000)
7	January 2002	– New clear-air transmittance formulation introduced – Improved cloud simulations for multi-layers – FASTEM version 2 introduced
8	November 2005	– Revised transmittance calculations for more variable gases and separate continuum – FASTEM version 3 introduced to allow simulation of polarimetric radiometers – Addition of RTTOV-SCATT wrapper for MW scattering from hydrometeors
9	March 2008	– Addition of reflected solar radiation for SWIR channels – IR cloud and aerosol scattering added using parameterization from Chou et al. (1999) and maximum random cloud overlap – Radiative transfer computation possible on user input pressure levels – Coefficient files for advanced IR sounders provided on 100 levels – Internal profile interpolation added
10	January 2011	– First land surface emissivity atlases UWIREMIS and TELSEM and CNRM (Karbou et al., 2006). – Introduction of FASTEM versions 4 and (later) 5 – Computation of principal components for advanced IR sounders added (PC-RTTOV) – Number of atmospheric layers increased from 43 to 51 for radiometers – Included Zeeman effect for high-peaking channels
11	May 2013	– Ability to simulate VIS/NIR radiances for clear sky and basic cloud – Land surface BRDF atlas – FASTEM version 6 introduced – Number of atmospheric layers increased from 51 to 54 for radiometers – Improved profile interpolation options – NLTE parameterization introduced for shortwave IR channels – RTTOV graphical user interface (GUI) created
12	February 2017	– VIS/NIR/IR scattering using discrete ordinates. Developments to existing microwave emissivity atlases. – New IR sea surface emissivity model – New IR land surface emissivity atlas (CAMEL) – Added SO_2 as a variable gas – First version of another PC model HT-FRTC included as an option – NLTE parameterization updated for shortwave IR channels

(ATOVS) the demand for RTTOV to simulate different satellite radiometers grew. Also, with the recent extension of RTTOV to cover the VIS and near IR parts of the spectrum, more radiometers can be simulated which cover this region of the spectrum.

The list of satellites now supported by RTTOVv12 is up to 50 and increasing, and the full list of instruments, up to 90, currently supported is given on the RTTOV website and in the latest RTTOV user guide (Hocking et al., 2017). Users can request any satellite nadir-viewing radiometer be supported by RTTOV as long as the channel spectral response functions or passbands are provided. Many of the instruments are now retired, but they provide measurements since 1969 and are required in support of the global atmospheric reanalysis efforts which are under way. This has enabled satellite data to be used for climate monitoring applications.

3 Model formulation

The details of the formulation of the RTTOV model are documented in various reports over the past 20 years, and it is not possible to reproduce all aspects of the model here. However, an overview is given here with references for the more detailed aspects given where necessary. The main framework of the formulation is given in Saunders et al. (1999) and has not changed in the latest versions of RTTOV although there are many additional capabilities added.

3.1 Atmospheric profile and surface variables

3.1.1 Input state vector

The classical temperature and water vapour profiles are the default input profiles to RTTOV, but in addition the capability to simulate the transmittance from several variable atmospheric gases has been added for infrared sensors. RTTOV can also include in the state vector concentration profiles of ozone, carbon dioxide, nitrous oxide, methane, carbon monoxide and sulfur dioxide. For microwave sensors ozone is included as a mixed gas. Cloud liquid/ice water profiles and aerosol profiles can also optionally be provided to enable absorption/scattering calculations at IR and VIS wavelengths and cloud liquid water absorption to be computed for MW frequencies. The cloud fraction profile can also be provided to enable simulations for atmospheres partially covered by clouds. In that case the radiative transfer is solved by using the maximum random overlap method. The profiles can be input on any user-defined pressure levels, and these input profiles are then interpolated to the levels on which the RTTOV coefficients are supplied to compute the gaseous transmittance. The vertical layering for the coefficients has been optimized from the 40 layers used in the original version of RTTOV to 53 layers from 1050 to 0.005 hPa for multichannel radiometers with fairly wide spectral response functions and for all MW radiometers. These are defined in Table 1 of Hocking et al. (2017). For the new IR hyperspectral sounders (e.g. IASI on Metop) coefficients on 100 layers (1100 to 0.005 hPa) are the optimal configuration provided to users although 53 layer coefficient files are also available to reduce the run time of the model at the expense of accuracy. Once the gas optical depth profiles have been computed (see Sect. 3.2), they are interpolated back to the user levels for the radiative transfer computation (see Sect. 3.3), which is more accurate.

For the surface variables, skin temperature, 2 m temperature and water vapour concentration, wind speed (over ocean only), surface type, and elevation all have to be defined. To account for viewing angle effects, the satellite zenith and optionally azimuth angles (for MW and VIS/NIR channels) at the surface are required. The nadir scan angle is also computed internally for the MW instruments where the mixing of the polarizations is a function of scan angle. The solar zenith and azimuth angles are also required if solar-affected simulations are required.

The surface emissivity/reflectance can be either input by the user or RTTOV can calculate it, for instance over the ocean using physical models such as ISEM (Sherlock and Saunders, 2000) or IREMIS (Saunders et al., 2017) for IR emissivities. A sea surface solar BRDF model (Matricardi, 2003) is used for solar-affected channels, and FASTEM or TESSEM2 models (Prigent et al., 2017) are used at MW frequencies. The FASTEM model has had several updates during the development of RTTOV as the parameterization has been improved to be valid for a wider range of frequencies (Liu et al., 2011; Bormann et al., 2012; Kazumori and English, 2015). MW radiometers measure polarized radiances in a polarization plane that can be either (or both) of vertical and horizontal polarization or a mixture of the two. Models like FASTEM initially calculate emissivity and reflectivity in vertical and horizontal planes and then take account of the scan geometry to rotate (if needed) into the observation polarization plane. The emissivity is modified by ocean roughness on all scales from small ripples to large-scale swell and is also modified by foam arising from breaking waves. Most changes to the FASTEM model have involved representing more accurately these two aspects. In addition to measuring the amplitude in single or dual polarization plane, some MW radiometers (e.g. Windsat) provide observations of the full Stokes vector. FASTEM has an empirical formulation for the third and fourth elements of the Stokes vector but has no rigorous capability for handling the full Stokes vector. Reflectance/emissivity atlases are provided over the land for visible and near-infrared wavelengths (Vidot and Borbás, 2014; Vidot et al., 2018), for infrared UWIREMIS (Borbas and Ruston, 2010) and CAMEL (Borbas et al., 2017), and for the microwave TELSEM (Aires et al., 2011) and the CNRM atlas (Karbou et al., 2006, 2010), which are all provided as part of the RTTOV package.

3.1.2 Profile training datasets

In order to compute the regression coefficients for RTTOV, layer-to-space transmittances computed from line-by-line radiative transfer models using a diverse set of atmospheric profiles are used. For the visible and infrared transmittances, they are stored in a database, whereas for the microwave region, they are produced at run time. The version of RTTOV in 1999 (Saunders et al., 1999) was trained on a dataset of 32 radiosonde profiles with 40 levels (Chevallier et al., 2000). Now diverse temperature, water vapour and ozone profiles which are thermodynamically consistent are sampled from the ECMWF reanalysis fields (Chevallier et al., 2006), and for the variable trace gas profiles the Copernicus Atmosphere Model reanalysis fields were also used (http://www.copernicus-atmosphere.eu/). Currently, 83 atmospheric profiles on 101 or 54 levels are used to compute the layer-to-space transmittances (Matricardi, 2008).

The line-by-line model calculations are performed with some minor constituents that do not vary with profiles; these are called "fixed gases". The fixed gases included for RTTOVv11 are O_2, NO, NO_2, HNO_3, OCS, N_2, CCL_4, CFC-11, CFC-12, CFC-14. In RTTOVv12, NH_3, OH, HF, HCl, HBr, HI, ClO, H_2CO, HOCl, HCN, CH_3Cl, H_2O_2, C_2H_2, C_2H_6 and PH_3 were added. The microwave line-by-line calculation includes only N_2, O_2 and O_3 as fixed gases. The profile concentrations are from the U.S. Standard Atmosphere (1976). The new variable gas profile sets have been constructed to cover the variability observed since the 1970s taking into account the fact that the mean profile should also be representative of the current state of the atmosphere. It is worth being aware of which year the CO_2 profile used for the transmittance calculations is valid for, as it has changed significantly during the satellite era. Similar considerations apply to the CH_4 and CFC profiles assumed in the coefficient generation. More details on the latest variable gas profile datasets can be found in the RTTOVv12 science and validation report (Saunders et al., 2017).

3.2 Transmittance model

The physical basis of the fast model to compute atmospheric transmittance has not changed much since the original ideas of McMillin and Fleming (1976) and Eyre and Woolf (1988), where the layer optical depth for a specific gas and channel is parameterized in terms of layer mean temperature, absorber amount, pressure and viewing angle, which are predictors for the optical depth for layer j and σ_j is the level j to space optical depth for that gas using the following formulation:

$$\sigma_j = \sigma_{j-1} + \sum_{k=1}^{k=m} a_{j-1,\,k} X_{j-1,\,k} \quad j = 2 \text{ to } n, \tag{1}$$

where j is the level number where there are n levels, m is the number of predictors indexed by k, $X_{j,\,k}$ are the predictors, and a are the coefficients for n levels and k predictors. The diverse profile datasets are used to compute layer optical depths for each gas and combinations of gases from a line-by-line model. The LBLRTMv12.2 model (Clough et al., 2005) with the AER v3.2 molecular database and MT-CKD2.5.2 for continuum absorption is used to calculate the VIS/near IR layer optical depths in the range 2000–25500 cm^{-1} at a spectral resolution of 0.01 cm^{-1} and in the IR (175–3300 cm^{-1}) at 0.001 cm^{-1} on 54 and 101 levels. The AMSUTRAN model, which takes its spectroscopic parameters from the 1989 version of the Liebe Millimeter wave Propagation Model (MPM89) (Liebe et al., 1989) and is based on the earlier work of Rayer (1995), is used for microwave instruments at all frequencies below 1000 GHz with a parameterization to include the Zeeman effect for high-peaking channels around the 50–60 GHz oxygen lines. Spectroscopic parameters have been updated for the 22 and 183 GHz water vapour lines based on half-width data from Liljegren et al. (2005) and Payne et al. (2008), respectively. All oxygen line parameters are updated to those from Tretyakov et al. (2005), and 35 ozone lines below 300 GHz from the HITRAN 2016 molecular database (Gordon et al., 2017) have been added. The strategy has been to update the reference line-by-line model calculations at least once every 5 years to benefit from improved spectroscopic databases and diverse profiles. The transmittance calculations are computed for all the diverse sets of atmospheric profiles resulting in a large database of level-to-space transmittances and associated profile variables used for the statistical regression and hence coefficient generation. In the fast model, the optical depths for mixed gases and each variable gas are computed from Eq. (1), converted into transmittances and then combined into "effective" transmittances as ratios, according to the following formulation originally recommended by McMillin et al. (1995):

$$\tau^{\text{tot}}_{i,\,j} = \tau^{\text{mix}}_{i,\,j} \cdot \frac{\tau^{\text{mix+wv}}_{i,\,j}}{\tau^{\text{mix}}_{i,\,j}} \cdot \frac{\tau^{\text{mix+wv+oz}}_{i,\,j}}{\tau^{\text{mix+wv}}_{i,\,j}}. \tag{2}$$

This ratioing of transmittances can prove cumbersome when adding more variable gases, and a more recent paper by McMillin et al. (2006) suggests a simpler approach may be feasible, but this has not been implemented in RTTOV to date. The layer optical depths for mixed gases and each variable gas are combined to give the total layer transmittance as in Eq. (2).

Over the years there has been research on improving the predictors used, and there are now three possible sets of predictors, $X_{j,\,k}$, which can be invoked when running RTTOV.

- The original predictors: H_2O and O_3 variable, all other gases fixed (referred to as v7 in the RTTOV guide).
- Updated predictors that include CO_2 as a variable gas (referred to as v8 in the RTTOV guide).
- Updated predictor set (referred to as v9 in the RTTOV guide), optimized for water vapour channels, allows for additional optional variable trace gases and is designed to enable the inclusion of solar radiation and zenith angles beyond 60°.

The original v7 predictors defined in Table 2 of Saunders et al. (1999) and the profile variables in Table 3 predict the classical mixed gas, water vapour and ozone absorption and are still optimal for radiometers such as HIRS and AMSU. The v8 predictors described in Matricardi (2003) separates out the water vapour continuum from the line absorption and includes carbon dioxide as an additional variable gas which can be useful for historical instruments allowing for the increasing carbon dioxide. The most recent v9 predictor set described in Matricardi (2008) is focused on getting the best optical depths from the hyperspectral IR sounder channels and can optionally include CO_2, N_2O, CO, CH_4 and more recently SO_2 as variable gases. It also extends the range of zenith angles the regression is valid for in the shortwave IR.

Here there is a complex mix of transmittance ratios used depending on which spectral region is being predicted and which is the dominant absorbing gas, and so there are many different combinations of variable gas transmittance ratios used in Eq. (2). This predictor set is the only one used for solar-affected radiances due to the large range of zenith angles the ray path can traverse in this case. Users are warned if any input profile variables are outside the range of the training dataset. In practice, tests have shown that for profile variables, up to 10 % outside the training set still allows an accurate calculation of the layer optical depth to be made.

3.3 Radiative transfer

The radiative transfer calculation in RTTOV is now performed on the user-defined pressure levels input to RTTOV, which is a change from the original version, where the input layers and the levels on which the transmittance was computed were the same. This allows more accurate calculations for cloud-affected radiances as the cloud top can be defined by the user at the required level. To enable this, the input/output profiles must be interpolated from/to user levels to/from the levels on which the RTTOV coefficients are provided (normally 54 or 101). There are various options for the interpolation which can take as input a fixed vertical pressure grid or a variable pressure grid to allow "sigma" coordinates commonly used in NWP models to be used. A tangent linear and adjoint of the interpolation scheme are also included with one option described by Rochon et al. (2007). A description of the interpolation options used in RTTOV is given in Hocking (2014), and its application in the ECMWF model is found in Lupu and Geer (2015).

A radiative transfer model for simulating top-of-atmosphere satellite radiances has to compute the following radiative transfer equation:

$$L(\nu,\theta_{\rm sat},\theta_{\rm sun}) = (1-N)\,L^{\rm Clr}(\nu,\theta_{\rm sat},\theta_{\rm sun}) + N L^{\rm Cld}(\nu,\theta_{\rm sat},\theta_{\rm sun}), \quad (3)$$

where $L^{\rm Clr}(\nu,\theta_{\rm sat},\theta_{\rm sun})$ and $L^{\rm Cld}(\nu,\theta_{\rm sat},\theta_{\rm sun})$ are the clear-sky and overcast sky radiances at a frequency ν and zenith angle $\theta_{\rm sat}$ and solar zenith $\theta_{\rm sun}$. N is the effective fractional cloud amount (i.e. the product of the fractional cloud amount and the cloud emissivity assuming it is grey body). The top-of-atmosphere clear-sky radiance includes the emitted radiation from the surface and reflected downward radiation (emitted, solar and diffuse) and the emitted radiation from the atmosphere:

$$L^{\rm Clr}(\nu,\theta_{\rm sat},\theta_{\rm sun}) = \tau_{\rm s}(\nu,\theta)\cdot\epsilon_{\rm s}(\nu,\theta)\,B(\nu,T_{\rm s}) + \int_{\tau_{\rm s}}^{1} B(\nu,T)\,{\rm d}\tau + (1-\epsilon_{\rm s}(\nu,\theta_{\rm sat}))\,\tau_{\rm s}^2(\nu,\theta_{\rm sat}) \int_{\tau_{\rm s}}^{1}\frac{B(\upsilon,T)}{\tau^2{\rm d}\tau} + L_{\rm Sol}(\nu,\theta_{\rm sat},\theta_{\rm sun}), \quad (4)$$

where $\tau_{\rm s}$ is the surface to space transmittance, $\epsilon_{\rm s}$ is the surface emissivity and $B(\nu,T_{\rm s})$ is the Planck function for the defined frequency and skin temperature. $L_{\rm Sol}(\nu,\theta_{\rm sat},\theta_{\rm sun})$ is the direct and diffuse solar radiation reflected from the surface given by:

$$L_{\rm Sol}(\nu,\theta_{\rm sat},\theta_{\rm sun}) = \int_{\tau_{\rm s}}^{1} J^{\uparrow}(\nu,\theta_{\rm sat},\theta_{\rm sun})\,{\rm d}\tau + r_{\rm s}(\nu,\theta_{\rm sat})\,\tau_{\rm s}^2 \int_{\tau_{\rm s}}^{1}\frac{J^{\downarrow}(\nu,\theta_{\rm sat},\theta_{\rm sun})}{\tau^2}{\rm d}\tau, \quad (5)$$

where $J^{\uparrow}$ is the upwelling source function, $r_{\rm s}(\nu,\theta_{\rm sat})$ is the surface reflectance for the downward incoming radiance and upward outgoing radiance along the satellite line of sight. In fact, this value is not available within RTTOV, so the input BRDF for the incoming solar and outgoing satellite surface zenith angles (multiplied by the cosine of the satellite zenith angle) is used instead. In general this should not cause significant errors since the surface-reflected downwelling radiation is very much smaller in magnitude than the upward-scattered component except for highly reflective surfaces. The upwelling and downwelling contributions are calculated for each layer of the input user level profile. The solar and satellite angles (and hence the phase function) are assumed to be constant through each layer. A value for the source term for atmospheric layer i (bounded by levels i and $i+1$) is obtained by integrating over the layer:

$$J_i^{\uparrow\downarrow}(\nu,\theta_{\rm sat},\theta_{\rm sun}) = F_{\rm sun}\tau_{{\rm sun},i}\frac{P\left(\theta_i^{\uparrow\downarrow}\right)}{4\pi}\frac{\sigma_s}{\cos\left(\theta_{{\rm sat},i}\right)}\int_{z_{i+1}}^{z_i} N\left(z'\right){\rm d}z', \quad (6)$$

where $F_{\rm sun}$ is the solar irradiance at the top of the atmosphere, $\tau_{{\rm sun},\,i}$ is the transmittance from space to level i, $\sigma_{\rm s}$ is the Rayleigh scattering cross section, $P(\theta_i^{\uparrow\downarrow})$ are the upward and downward scattering phase functions calculated for layer i, $\theta_{{\rm sat},\,i}$ is the satellite zenith angle in layer i, and z_i is the height of level i. $N(z)$ is the number of particles per unit volume and height z. The factor of 4π normalizes the phase function, and the dependence on the sun-satellite azimuth is omitted here.

In the original RTTOV, it was assumed the atmospheric layer was optically thin so that equal weight can be given to the radiance emitted from all points within the layer, so the average value of the Planck function was used, which is sufficient for clear-sky calculations. For optically thick layers (e.g. with cloud) only the upper regions of the layer give a significant contribution to the radiance. In this case the use of the average value of the Planck function would put too much weight on the radiance coming from the lower part of the layer. To improve the accuracy a parameterization of the Planck function based on the linear in τ assumption that the source function throughout the layer is a linear function of

Table 2. Options in RTTOV for simulating the effects of cloud, precipitation and aerosols.

Option in RTTOV	Microwave	Infrared	Visible
Simple cloud (no scattering)			
Grey optically thick cloud	No	Yes	Yes
Liquid water absorption	Yes (through normal RTTOV interface)	No	No
Scattering solutions			
Delta-Eddington	Yes (through RTTOV-SCATT interface)	No	No
Chou scaling	No	Yes	No
Discrete ordinates	No	Yes	Yes

Table 3. The parameters assumed for RTTOVv12.1 vs. line-by-line model comparisons.

Parameters	RTTOVv12 simulations
Number of layers for optical depth calculation	VIS/IR/MW 54 (0.005–1050 hPa), IASI 101 (0.005–1100 hPa)
Input profile sets	Dependent: 83 profiles; independent: 52 profiles
VIS/IR transmittances	
Spectroscopic data	LBLRTMv12.2/AER 3.2, MTCKD2.5.2
Surface emissivity assumed	1.0
Surface reflectance assumed	BRDF of $0.3/\pi$
Optical depth predictors	Version 7 for HIRS and version 9 for IASI and VIS channels
MW transmittances	
Spectroscopic data	Liebe et al. (1989) update/Tretyakov et al. (2005)
Surface emissivity assumed	1.0
Optical depth predictors	Version 7

the optical depth, τ is used:

$$B\left[T\left(\tau\right)\right] = B_0 + \left(B_1 - B_0\right)\frac{\tau}{\tau_*}, \quad (7)$$

where B_0 is the Planck function for the top of the layer, B_1 is the Planck function at the bottom of the layer and τ_* is the optical depth of the layer.

RTTOV can also estimate daytime non-local thermodynamic equilibrium (NLTE) effects in the CO_2 ν_3 band (around 4.3 µm). Here, local thermodynamic equilibrium breaks down due to the absorption of the incident solar radiation. The effect can add around 10 K to the measured brightness temperatures at midday. NLTE effects are introduced in the RTTOV calculations by adding a correction to the standard LTE radiances for affected channels (between 2200 and 2400 cm^{-1}) of high-resolution IR sounders. The most recent NLTE correction is computed using a predictor-based regression scheme (Matricardi et al., 2018). The predictors consist of various combinations of the solar zenith angle, the sensor zenith angle and the average kinetic temperature in two broad layers above ∼ 51 hPa. The regression has been trained using a database of accurate vibrational temperatures computed using the Granada NLTE population algorithm (Funke et al., 2012).

3.4 Cloud, precipitation and aerosol-affected radiance simulations

RTTOV offers a number of approaches for simulating the radiative effect of cloud, precipitation and aerosols, each tailored to its own frequency domain as defined in Table 2. In the microwave and infrared regions, there are options to treat clouds as simple absorbers (English et al., 2000); such approaches are fast, but their validity is limited mainly to water clouds. To accurately simulate the effect of liquid and frozen precipitation in the microwave region, and cloud and aerosol in the visible and infrared regions, it is necessary to represent the effects of multiple scattering. Hence, a number of more sophisticated models are also available.

3.4.1 Cloud and aerosol radiance simulations at infrared wavelengths

For the cloudy-sky radiances there are two options: a simple uniform grey cloud assumption and a more complex scattering calculation for complex clouds. The "simple" cloudy radiance model is given by

$$L^{\mathrm{Cld}}(\nu, \theta_{\mathrm{sat}}) = \tau_{\mathrm{Cld}} B(\nu, T_{\mathrm{Cld}}) + \int_{\tau_{\mathrm{Cld}}}^{1} B(\nu, T)\, \mathrm{d}\tau, \quad (8)$$

where τ_{Cld} is the transmittance from the uniform cloud top to the top of the atmosphere and T_{Cld} is the cloud top temperature. This formulation can be used for simulating radiances over uniform grey cloud and has been used to extend the use of clear-sky radiances in data assimilation to uniform cloud situations.

For more complex cloudy fields, the parameterization of multiple scattering in the IR, introduced in RTTOVv9, is designed to avoid solving the full scattering equation but instead to solve a modified version of Eq. (4) in which the absorption optical depth is replaced by an effective optical depth for the extinction. This approximation enables the efficiency of the RTTOV layer optical depth computation to be retained.

The RTTOV parameterization of multiple scattering is based on the approach proposed by Chou et al. (1999), who originally developed a scheme to compute approximate fluxes in a scattering atmosphere. In the scheme by Chou et al. (1999), the radiative transfer equation is identical to the one with no scattering but, crucially, the optical depth for absorption, τ, is replaced by an effective optical depth for extinction, τ_{e}:

$$\tau_{\mathrm{e}} = \tau + b\tau_{\mathrm{sc}}, \quad (9)$$

where τ_{sc} is the optical depth for scattering and b is the mean fraction of the radiation scattered in the upward direction for isotropic radiation incident from above (see Chou et al., 1999, for details). To derive their approximated form of the scattering transfer equation, Chou et al. (1999) have folded the effect of backscattering into a contribution to atmospheric emission and absorption. In addition, they have assumed that the diffuse radiance field is isotropic and can be approximated by the local Planck function.

To compute b, a knowledge of the phase function of the atmospheric particulates to be considered is needed which can be from aerosols, water droplets or ice crystals. For RTTOVv12 IR radiances in the presence of 13 different types of aerosol components, 5 different types of water clouds and 2 options for ice cloud properties can be computed.

To solve the radiative transfer for an atmosphere partially covered by clouds, a stream method is used that divides the field of view into a number of horizontally homogeneous columns, each column containing either cloud-free layers or totally cloudy layers. Each column is assigned a fractional coverage and the number of columns is determined by the cloud-overlapping assumption (maximum random overlap) and the number of layers the atmosphere is divided up into. The total radiance is then obtained as the sum of the radiances for the single columns weighted by the column fractional coverage.

For aerosols, the range and shape vary from quasi-spherical to highly irregular with a size typically less than 1 µm although particles as large as 10 to 20 µm have been observed. A database of optical properties assuming spherical particles has been generated using the microphysical properties assembled in the Optical Properties of Aerosols and Clouds (OPAC) software package (Hess et al., 1998) with some additional components added (old and new volcanic ash and Asian dust). This database provides the microphysical properties (size distribution and refractive indices) for 13 aerosol components (insoluble, water soluble, soot), 2 sea salt components (accumulation mode and coarse mode) and 4 mineral components (nucleation, accumulation, coarse modes, transported sulfated droplets, and volcanic ash). Additionally, a new volcanic ash and Asian dust component were provided in RTTOVv11. Some components are hydrophilic, and so the properties are interpolated according to the local relative humidity. For water clouds a cloud liquid water content must be provided in one or more atmospheric layers. It is then converted into a particle number concentration, and the absorption, scattering and extinction optical depths can be derived from the normalized values of the optical parameters. RTTOV has parameters from OPAC for two stratus cloud types (stratus continental and stratus maritime) and three cumulus clouds (cumulus continental clean, cumulus continental polluted and cumulus maritime) with the size distribution described by the modified gamma distribution.

There are two ice cloud optical property parameterizations included in RTTOV for the VIS and IR wavelengths. The first uses the ice crystal properties dataset developed by Baum et al. (2011), which is interpolated to obtain the scattering properties used in RTTOV (i.e. extinction coefficient, β_{ext}; single-scattering albedo, ω_0) from the input profile of ice crystal effective diameter. Users can explicitly provide ice effective diameter or can choose among four parameterizations in terms of ice water content and temperature (Ou and Liou, 1995; Wyser, 1998; Boudala et al., 2002; McFarquhar et al., 2003). The second scheme uses the methodology developed initially for the IR (Vidot et al., 2015) by using a large database of optical properties of ice clouds provided by Baran et al. (2014). It consists of 20 662 particle size distributions using different in situ measured temperature (T) and estimated ice water content (IWC) observations; this simulates an ensemble of different ice cloud particle shapes and is expected to be more realistic than just assuming specific shapes, as was done previously. It allows a direct parameterization of the optical properties from the cloud temperature and the ice water content. For each pair of ice water content and temperature observations, the database contains the absorption and scattering coefficients, the asymmetry parameter (to compute the phase function) and also b (Eq. 9) used for the Chou parameterization at wavelengths between 0.2 and 19 µm. The formulation that has been implemented in RTTOV is given by the following equations:

$$\log_{10}\left[\beta_{\text{ext}}(\lambda, T, \text{IWC})\right] = A_\beta(\lambda) + B_\beta(\lambda)\,T + C_\beta(\lambda)\log_{10}(\text{IWC}) + D_\beta(\lambda)\,T^2 + E_\beta(\lambda)\left(\log_{10}(\text{IWC})\right)^2 + F_\beta(\lambda)T\log_{10}(\text{IWC}), \quad (10)$$

$$\overline{\omega_0}(\lambda, T, \text{IWC}) = A_{\overline{\omega_0}}(\lambda) + B_{\overline{\omega}_0}(\lambda)\,T + C_{\overline{\omega}_0}(\lambda)\log_{10}(\text{IWC}), \quad (11)$$

$$g(\lambda, T, \text{IWC}) = A_{\text{g}}(\lambda) + B_{\text{g}}(\lambda)\,T + C_{\text{g}}(\lambda)\log_{10}(\text{IWC}). \quad (12)$$

The parameterization coefficients A to F of β_{ext}, ω_0 and g (the asymmetry parameter) were calculated by using a non-linear least squares fitting procedure over the database, and they are also functions of wavelength. Note that the size distributions of the ice crystals assumed by the user (or their cloud model) should be consistent with the cloud parameterization scheme used in RTTOV. Users can input aerosol and/or cloud optical properties explicitly, so they are not restricted to the optical properties assumed in RTTOV. The full details of this parameterization of the scattering as implemented in RTTOV are documented in Matricardi (2005) and Saunders et al. (2017).

3.4.2 Cloudy and aerosol radiance simulations for solar radiation

For solar radiation, multiple scattering due to aerosols/clouds using the discrete ordinates method or DOM (Chandrasekhar, 1960) has been implemented in RTTOV for treating solar radiation and thermal emission. The choice of solver for the thermal emission and solar source terms can be selected independently: for thermal emission, the choice is between the existing "Chou-scaling" parameterization and DOM. For solar radiation only the DOM should be used.

The implementation of DOM is very similar to that in the DISORT model (Stamnes et al., 1988), such that the radiances from RTTOV agree to at least four significant figures with those from DISORT when equivalent inputs are used. The details of the DOM algorithm are given in Hocking (2015). There is one significant difference between the RTTOV and DISORT implementations of DOM: for solar simulations, RTTOV takes the full phase functions as input and directly interpolates them at the scattering angle where required. In contrast, DISORT reconstructs the phase function from the full Legendre expansion. This is not a practical solution for some phase functions at VIS wavelengths which may require many thousands of Legendre terms in order to be accurately reconstructed. RTTOVv12, therefore, only requires as many Legendre coefficients as there are discrete ordinates (or "streams") in the calculation. The DOM implementation treats thermally emitted (IR) and solar radiation separately for reasons of efficiency. The surface is assumed to be Lambertian and in the IR the surface albedo is calculated as 1−emissivity. For solar calculations the surface albedo is calculated as $\pi \cdot \text{BRDF}$, and this value is capped at 1 to prevent unphysical albedo values being used. For each layer, the absorption and scattering coefficients (the Legendre coefficients corresponding to the phase function), and, for solar channels, the phase function itself have to be specified. The cloud and aerosol coefficient files include these properties for the aerosol and water cloud particle types defined in Sect. 3.4. As for the IR, the Baran et al. (2014) or Baum et al. (2011) scattering property datasets can be selected for ice cloud. The phase function is calculated from the asymmetry parameter following Baran et al. (2001), and the Legendre expansion of the phase function is calculated internally in RTTOV.

DOM is a solver for monochromatic radiances. However, RTTOV simulates radiances with a finite spectral bandwidth, and the standard RTTOV gaseous absorption optical depths are used as inputs to the DOM algorithm. The errors resulting specifically from applying DOM to polychromatic quantities were of the order of 1–2 % in radiance for VIS/near-IR channels, and the errors are dominated by variability in optical properties (especially the phase function) across the channel (Hocking, 2015). In the IR, the errors are dominated by the variability of gas absorption across the channel, and as the amount of scattering material in the atmosphere increases, the errors decrease because the optical properties of clouds/aerosols vary relatively slowly across the sensor channels and this begins to dominate over the gas absorption.

The DOM algorithm does not currently treat atmospheric Rayleigh scattering. It would be very expensive to compute as it would imply the presence of scattering particles in (almost) every layer. It is also the case that currently the LBLRTM simulations used to train RTTOV include extinction due to Rayleigh scattering. If this was disabled, it would require an additional parameterization of the Rayleigh extinction to be developed for clear-sky VIS/near-IR simulations. The existing Rayleigh single-scattering calculation is included as an "additive" effect alongside DOM, so there is no interaction between the Rayleigh scattered radiation and the clouds/aerosols except for increased extinction by Rayleigh scattering (included in the gaseous optical depths used in DOM) and by clouds/aerosols (included in the Rayleigh single-scattering calculation). This leads to an underestimation of the top-of-atmosphere reflectances as the optical thickness of the scattering layers increases and as the wavelength decreases (Scheck, 2016). Improvements to the treatment of Rayleigh scattering will be investigated for a future version of RTTOV. A faster scattering model at VIS wavelengths, MFASIS (Scheck et al., 2016), is being developed for future versions of RTTOV, which will allow VIS channel radiances to be used for real-time data assimilation applications.

3.4.3 Scattering at microwave frequencies

Although scattering by hydrometeors (e.g. rain and snow) at MW frequencies is not included in the core RTTOV package, there is a wrapper programme (RTTOV-SCATT; Bauer

et al., 2006) that provides this capability outside RTTOV. Full details of the initial formulation of the model are given in the RTTOV-8 Science and Validation Report (Saunders et al., 2006). RTTOV-SCATT is a multiple-scattering radiative transfer model which enables all-sky MW radiance assimilation in numerical weather prediction models and, as for the core RTTOV code, includes forward, tangent-linear, adjoint and Jacobian models. The all-sky brightness temperature is calculated, as in Eq. (3), as the combination of independent clear and cloudy columns weighted by an effective cloud fraction. The gaseous absorption component of both columns is computed by RTTOV. The scattering calculation in the cloudy column is based on the Delta-Eddington approximation (Joseph et al., 1976) so that only one angle (i.e. the observation angle) is needed, and the anisotropic radiance field is decomposed into an isotropic and anisotropic component. Compared to reference doubling-adding simulations, this produces mean errors of less than 0.5 K at the targeted MW frequencies between 10 and 200 GHz, based on a dataset of 8290 model profiles located in tropical areas to ensure the presence of deep clouds and intense precipitation so that multiple scattering is maximized (Bauer et al., 2006).

The hydrometeor types assumed in RTTOV-SCATT are rain, snow, cloud liquid water and cloud ice. Tables of hydrometeor optical properties are pre-calculated for the required frequencies, temperatures and hydrometeor classes. As a function of hydrometeor water content, these give the bulk (i.e. integrated over an assumed particle size spectra) extinction coefficient, single-scattering albedo and asymmetry parameter as required to perform the radiative transfer calculations. The optical properties are stored in sensor-specific coefficient files, with calculations valid at the centre frequency of the channel, or if a channel is composed of multiple sidebands, the optical properties are an average of those at the centre frequencies of the sidebands. Cloud ice, cloud water and rain hydrometeors are represented by spheres, with their optical properties computed from Mie theory. Details of the underlying assumptions required for different hydrometeor types, i.e. particle permittivity as a function of frequency, temperature and water/ice content, as well as the particle size distributions, can be found in Bauer (2001). Since the original implementation of RTTOV-SCATT, the representation of snow hydrometeors has been changed to use discrete dipole simulations of non-spherical particles described by Liu (2008). This more realistic representation of the complex 3-D shapes of frozen particles has led to improved simulations of deep convective clouds, validated by comparing observations with simulations from the ECMWF model (Geer and Baordo, 2014). The code used to compute the optical property lookup tables is available as part of RTTOV, which gives the user the possibility to adjust the microphysical representations of hydrometeors if required.

An additional development since the original implementation of RTTOV-SCATT has been the revised calculation of the effective cloud fraction in Eq. (3). The original approach used the maximum cloud fraction in the profile, which would be a plausible choice for visible radiative transfer applications but generates excessive beamfilling at microwave frequencies. Geer et al. (2009) changed this to a hydrometeor-weighted average across the vertical profile of input cloud fraction; this decreased rms errors by 40 % compared to reference simulations.

Although the treatment of microwave scattering is highly simplified, including the treatment of sub-grid-scale cloud cover, the "one shape fits all" hydrometeor optical properties, and the use of essentially a two-stream solver for scattering, this model is used successfully at some centres for "all-sky" MW radiance assimilation. It gives errors much smaller than the many other uncertainties involved, and, critically, it is fast enough for operational use (e.g. Bauer et al., 2010; Geer et al., 2017).

3.5 Simulating principal components of the infrared spectrum

A major update to RTTOV at version 10 was the introduction of the capability of simulating radiances from the IR spectrum in the form of PCs, which is a useful way to represent all the measurements from the advanced IR sounders such as IASI. The method used for the simulation of the PC scores for clear skies is described in Matricardi (2010) and referred to as PC-RTTOV. The dataset of atmospheric profiles used to train the PC model consists of profiles generated using the operational suite of the ECMWF forecast model. It comprises 12 500 vertical profiles of temperature, water vapour, ozone and ancillary information on surface properties over all surface types. Aerosols, trace gases and NLTE effects are all included in the latest version. The PC scores obtained from the eigenvectors of the covariance matrix of the simulated radiances are used in a linear regression scheme where they are expressed as a linear combination of profile-dependent predictors. The predictors consist of a selected number of polychromatic radiances computed using the standard RTTOV transmittance model described in Sect. 3.2. The linear regression scheme can then be used to simulate PC scores and consequently reconstruct radiances for any input atmospheric profile.

The principal component option in RTTOV is much more computationally efficient for sensors like the advanced IR sounders with many channels. The user can select the number of predictors used in the PC score regression algorithm and the number of eigenvectors used in the reconstruction of the radiances. The different combinations of eigenvectors/predictors can provide a trade-off between more accurate but less computationally efficient simulations. PC score regression coefficients are available based on 300, 400, 500 and 600 predictors for IASI whereas the number of eigenvectors can be up to 400. A detailed description of the PC-RTTOV model and an assessment of its accuracy can be found in Matricardi (2010).

HT-FRTC is another model that calculates transmittance and radiance spectra using PCs (Havemann et al., 2009) and has been included as an optional module called from the RTTOV interface. The PCs cover the spectrum at very high spectral resolution, similar to that of conventional line-by-line models, so that individual spectral lines are resolved. This approach allows very fast calculations of spectra with line-by-line-like accuracy for clear scenes. The PCs are derived from high spectral-resolution data using a diverse set of atmospheres and surface conditions. Monochromatic calculations at these frequencies are used to predict the PC scores (Havemann, 2006). The liquid cloud optical properties are parameterized in terms of the droplet effective radius. The cirrus optical properties are based on Baran et al. (2014) and scattering by frozen and liquid water and aerosols are approximated by modifications to the transmittances using the Chou approximation (Chou et al., 1999). An assessment of the HT-FRTC model for advanced IR sounder simulations is underway using the Met Office NWP model.

4 Performance of RTTOV compared with line-by-line models

There are several ways to assess the performance of a fast radiative transfer model: firstly, to investigate the accuracy of the fast model itself by comparing the primary outputs from RTTOV with the corresponding values computed using an accurate line-by-line model, which is described in this section; secondly, to compare the computed radiances with observations where an underlying atmospheric state can be provided usually from an NWP model analysis or short-range forecast for input to the fast model covered in the following section. The parameters assumed for the comparison between RTTOV and the line-by-line models for the VIS, IR and MW regions are given in Table 3. The coefficients are computed from the 83-profile diverse set (Matricardi, 2008), and comparisons were also made for the MW channels on an independent 52-profile diverse set although the results were similar for both profile sets. RTTOVv12.1 is used throughout for these comparisons. The changes in brightness temperature due to updated spectroscopic parameters in the line-by-line models can change the computed values by several tenths of a degree, but here we just document the accuracy of RTTOV reproducing the line-by-line model optical depth values for VIS, IR and MW radiometers and advanced IR sounders. Note that these comparisons assume a surface emissivity of unity as we are only assessing the accuracy of the atmospheric layer optical depths here.

In their Fig. 3, Saunders et al. (1999) showed results for the AMSU MW sounder to demonstrate the performance of RTTOVv5 for MW radiometers, and so a similar comparison for RTTOVv12 is given in Fig. 1, which shows the differences for the AMSU channels for the 52-profile independent set. The upper-tropospheric water vapour channel of AMSU-B (channel 18) has the largest standard deviation with the line-by-line reference (0.04 K), but this is an order of magnitude below the instrument noise. The largest bias for channel 20 is only 0.002 K. The equivalent results shown in Saunders et al. (1999) show much higher standard deviation values for all AMSU channels (e.g. channel 18 is 0.2 K). The big improvement is mainly due to improved predictors for water vapour absorption described in Matricardi et al. (2004) introduced from RTTOVv7 onwards (referred to as version 7 predictors), but better and more diverse profile datasets with more profiles (32 TIGR vs. 83 ECMWF) and more levels (40 vs. 54) have also helped.

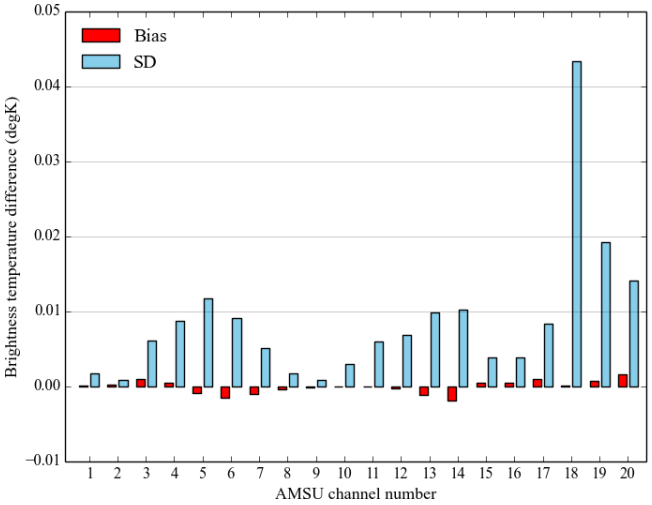

Figure 1. The mean differences and standard deviations for AMSU(1-15)/MHS(1-5) channels between the AMSUTRAN line-by-line model and RTTOVv12 for the 52-profile independent set for viewing angles out to 63° using version 7 predictors.

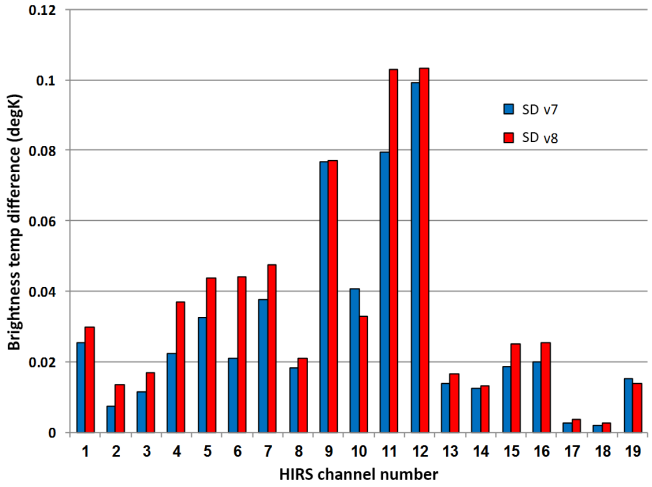

Figure 2. The mean standard deviation of the difference for Metop-A HIRS channels between the LBLRTM line-by-line model and RTTOVv12 for the 83-profile set for all nadir views up to 63° using version 7 and 8 predictors with a surface emissivity of 1.

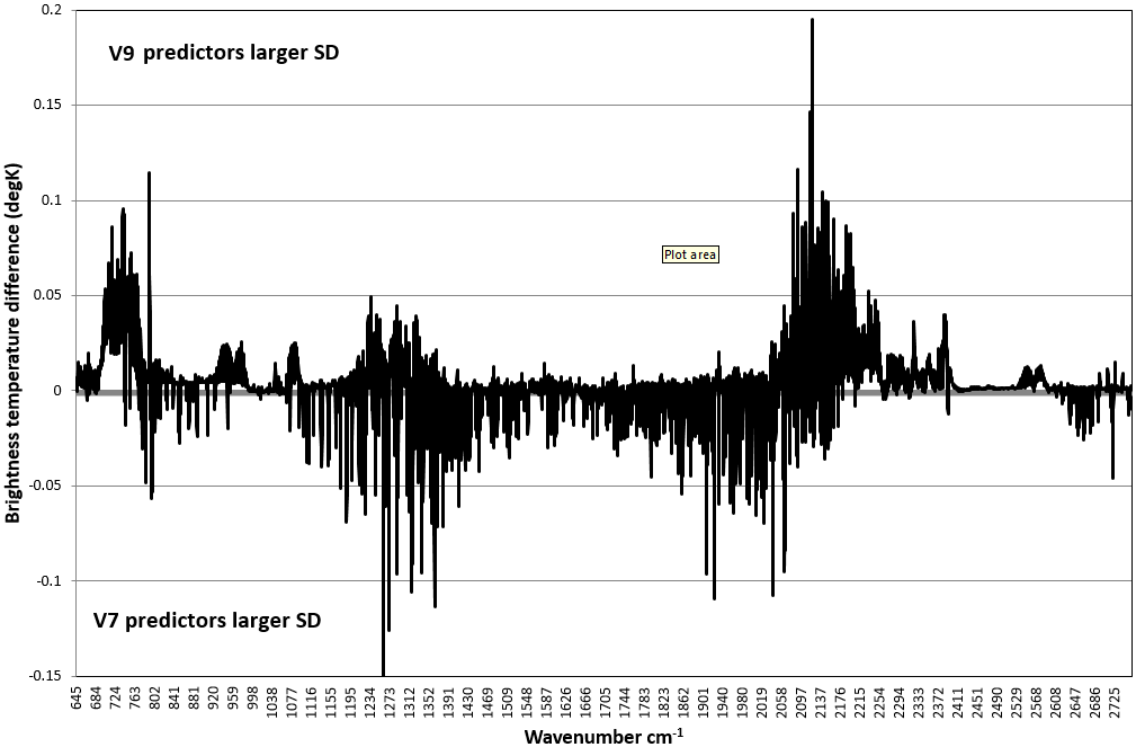

Figure 3. For selected IASI channels, the difference of the standard deviations of the brightness temperature fit between the LBLRTM line-by-line channel-integrated optical depth model and RTTOVv12-computed optical depths for the 83-profile dependent set for all views up to 63° with version 7 and version 9 predictors. Version 7 predictors have smaller differences for positive values, and version 9 predictors have smaller differences for negative values. Note that the version 9 predictors are also computing the optical depths of the trace gases whereas for version 7 only water vapour and ozone are considered.

For HIRS the differences to the line-by-line model are shown in Fig. 2, this time for the 83-profile dependent set though the results are similar for the independent profiles. The results are harder to compare with those shown in Fig. 1 of Saunders et al. (1999) as the profile dataset they used then was much bigger. An unpublished report at the time showing standard deviations of the differences with a 32-profile dataset for RTTOVv5 shows that the errors for the HIRS temperature sounding channels are only slightly improved in RTTOVv12, but the errors for the water vapour channels have been reduced by a factor of 2 using the version 7 predictors.

Radiances from the advanced IR sounders are now a key part of the satellite observing system, and RTTOV has been developed to simulate these accurately (Matricardi, 2003, 2005). An example of simulations for the IASI sounder is shown in Fig. 3, using both the older version 7 and the new version 9 predictors (Matricardi, 2008), which allow transmittances from a variety of trace gases to be computed in addition to water vapour and ozone (see Sect. 3.2). In terms of the standard deviation of the differences, the version 9 predictors are more accurate for the water-vapour-sensitive channels, but the version 7 predictors are better for the temperature sounding channels and window regions of the spectrum. However, it has to be borne in mind that version 9 predictors have to explain the variability of trace gases in addition to temperature, water vapour and ozone whereas version 7 predictors do not. The differences seen are generally below the IASI instrument noise at all wavelengths. Version 9 predictors are mandatory if you want to include the simulation of traces gases which are not fixed in amount and also for simulations which include solar-affected channels due to the larger zenith angles involved.

For simulations of imager radiances, Fig. 4 shows the comparison for the VIIRS VIS channels in terms of reflectance for the range of satellite and solar zenith angles used to train the coefficients with a relative azimuth of 180°. They include contributions from atmospheric Rayleigh scattering and surface reflection, assuming a surface BRDF of $0.3/\pi$ located at the bottom level of the coefficient pressure profile (1050 hPa for 54 L coefficients). The 83-profile set of profiles was used here. The channels affected by water vapour are the ones with higher standard deviations, but the differences are all small. Note that the 0.65 µm channel is for the much wider-band day–night channel. Similar differences are seen for the ABI VIS/NIR channels on GOES.

Another aspect of the RTTOV radiance computations is to evaluate the gradient of the radiances as a function of changes in the state vector as this is important for data as-

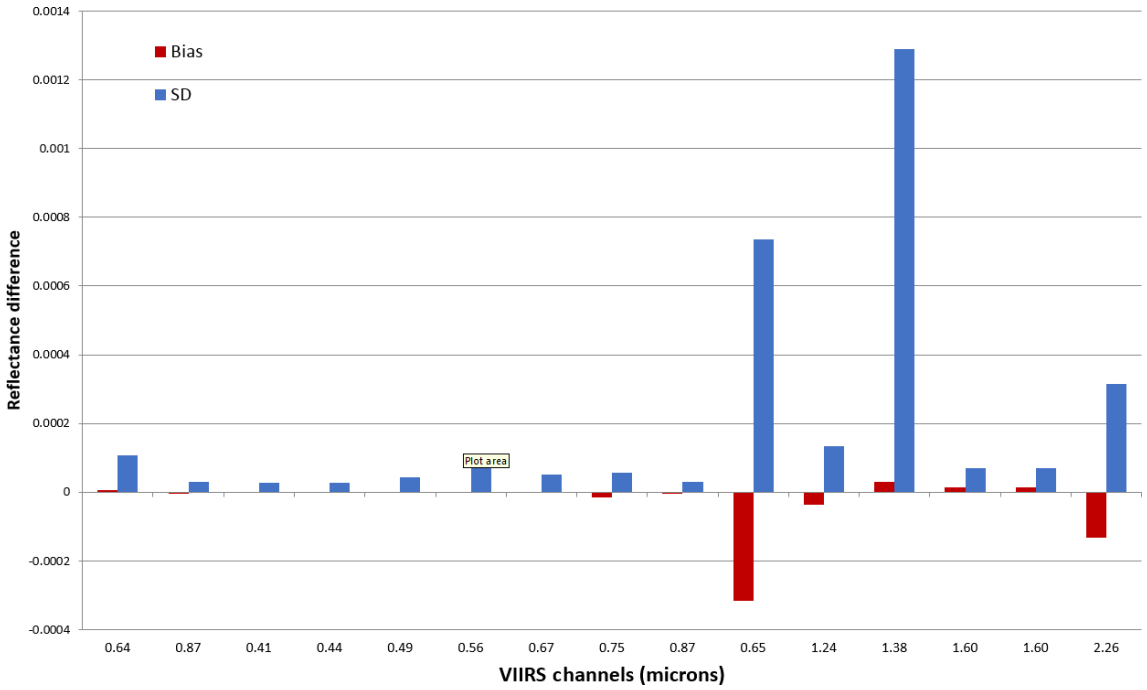

Figure 4. The mean difference for VIIRS visible/near IR channels between the HITRAN line-by-line model and RTTOVv12 for the 83-profile set for all clear-sky views with zenith angles up to 84° using version 9 predictors.

similation applications where the adjoint or Jacobian is used. A comparison of Jacobians from a set of line-by-line and fast radiative transfer models was undertaken by Garand et al. (2001) for HIRS and AMSU and by Saunders et al. (2007) for AIRS, showing that RTTOVv6 did match the line-by-line models well in these cases. Computing Jacobians from line-by-line models is costly, requiring a separate run for each level and parameter in the state vector where they are perturbed relative to the reference profile. Figure 5 shows the temperature Jacobian for a temperature sounding channel of AMSU-A (channel 6, 54.4 GHz) and a water vapour Jacobian for a channel of AMSU-B (channel 3, 183 ± 1 GHz) for a typical 50-level tropical standard atmosphere together with those computed from the MW line-by-line model, AMSUTRAN. The agreement between the line-by-line model and the equivalent RTTOV-generated Jacobian is close.

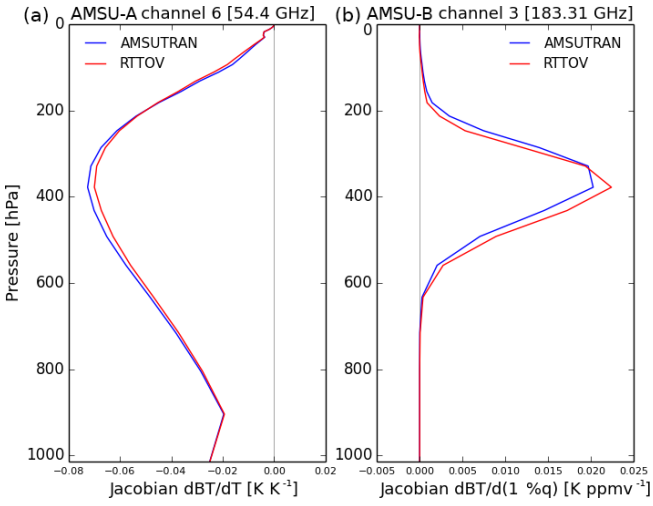

Figure 5. Temperature Jacobian for AMSU-A channel 5 **(a)** and water vapour Jacobian for AMSU-B channel 3 **(b)** for U.S. Standard Atmosphere (1976). AMSUTRAN (blue) is from the line-by-line code, and RTTOV (red) uses the RTTOV predictors to compute the transmittances for the Jacobians.

5 Comparisons with measurements

Another way to evaluate RTTOV is to compare the simulated radiances with real observations from a variety of sensors using a global NWP model to provide the atmospheric state coincident with the observation locations for input to RTTOV. This ensures that a wide range of atmospheric conditions are sampled but, biases due to instrument calibration and NWP model errors are all included in the difference statistics. A reduction in the standard deviation of the differences, however, can be used as a measure of the improvement of the radiative transfer model performance if only the RT model in the system has changed. The observations compared with the model first-guess profiles are from a 6 h forecast. To demonstrate this, experiments have been run using the ECMWF model for a 1-month period (2 May–2 June 2016) at reduced (TCo399) horizontal resolution and 137 vertical levels, with the model

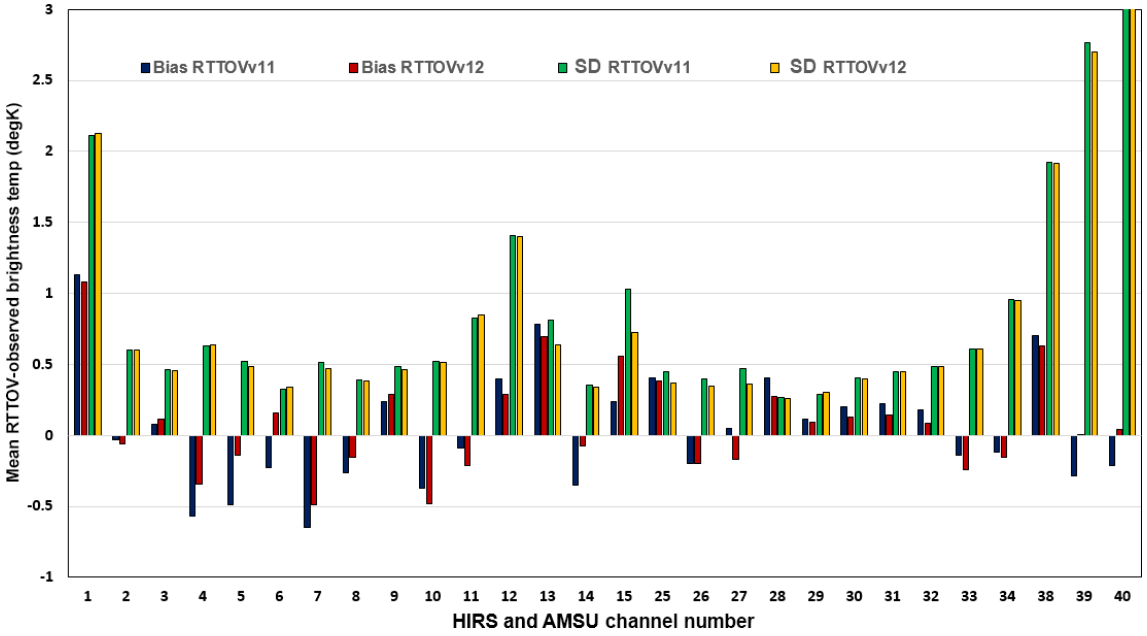

Figure 6. Mean global RTTOV minus observed statistics before bias correction for HIRS (channels 1–20) and AMSU-A (channels 5–14 or 25–34 here) and MHS (channels 3–5 or 38–40 here) for the period 2 May–2 June 2016 for RTTOV versions 11 and 12 in the ECMWF IFS NWP model.

top pressure at 0.01 hPa. Version 7 optical depth predictors are used for all IR and MW observations, except for IASI, CrIS and AIRS, where version 8 predictors were used, which are different for the water vapour optical depth calculations. For HIRS only those instruments on Metop-A and Metop-B were considered, but for AMSU-A, instruments on six satellites (NOAA-15, NOAA-18, NOAA-19, Metop-A, Metop-B, Aqua) were included, and for MHS, instruments on NOAA-18, NOAA-19, Metop-A and Metop-B were used to generate the statistics. Figure 6 shows the mean differences over the month for a selection of HIRS and AMSU sounding channels. The HIRS and AMSU-A temperature sounding channels have mean biases and standard deviations of differences all within 0.5 K. The water vapour channels of HIRS (channels 11 and 12) and AMSU (channels 38–40) have larger standard deviations (1–3 K) mainly due to the water vapour fields from the NWP model not being so accurate. HIRS channel 1 peaks high in the stratosphere, and so NWP model uncertainties again dominate the errors here.

Another factor for those channels which see the surface is the uncertainty in the surface emissivity assumed. In terms of bias, the differences between the RTTOVv11- and RTTOVv12-computed radiances were slightly reduced for v12, but in terms of standard deviation the differences were in most cases negligible. The reduction in the bias is due to improved spectroscopy in this case. Figure 7 shows calculations for a selection of IASI channels across the spectrum for RTTOVv11 and v12 with coefficients that are based on different versions of the line-by-line models (the main reason for the differences).

The biases were generally within ± 1 K and the RTTOVv12 values with updated spectroscopy reduced the bias with the model relative to RTTOVv11. The coefficients used with RTTOVv11 have been computed using the kCARTA line-by-line model while the newly released IR coefficient files with RTTOVv12 are based on LBLRTMv12.2. Other changes in the IR coefficient files include updated concentrations of CO_2 to current values in the mixed gas transmissions and a different training set of diverse atmospheric profiles. The biases in Fig. 7 are considerably larger than the comparisons of RTTOV with the line-by-line model (Fig. 3) and are due to instrumental calibration biases and also biases in the NWP model temperature and humidity fields. The reduction in bias for RTTOVv12 shows that improvements in the underlying transmittances from the line-by-line models can significantly reduce the biases with measurements motivating further improvements in the spectroscopic parameters. NWP centres apply a bias correction to remove these mean biases before assimilation.

6 Summary and future plans

The RTTOV fast radiative transfer model was first developed in the early 1990s and made available to researchers working with satellite sounding data for their physical retrievals and development of direct radiance assimilation in NWP models. Since that time the model development has been continuous under the auspices of the EUMETSAT NWP SAF, and its capabilities have greatly increased both in terms of wavelengths

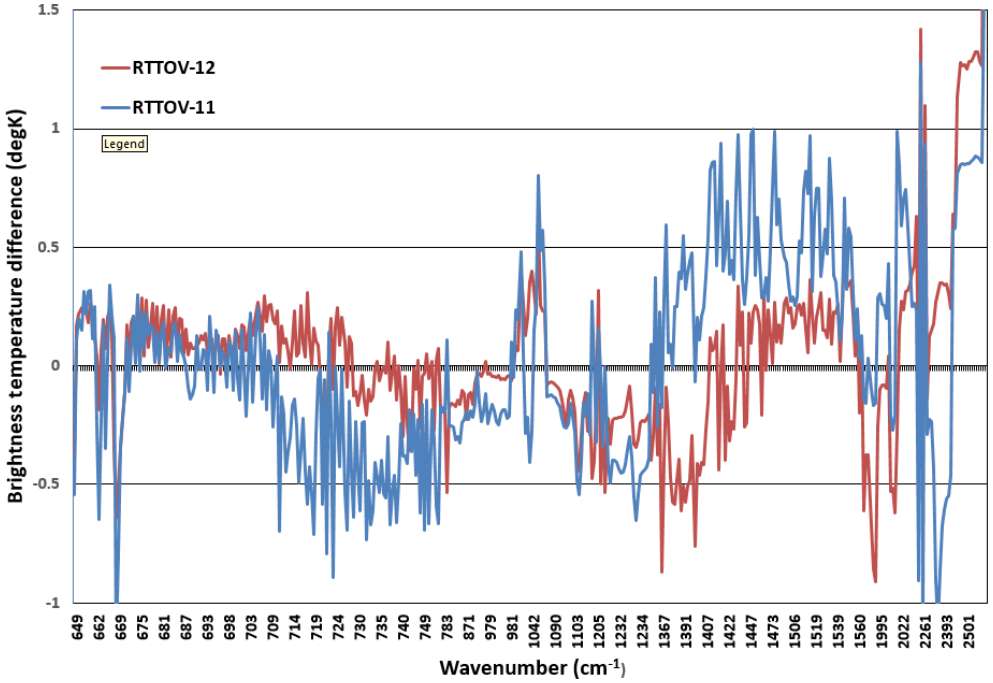

Figure 7. Mean global RTTOV minus observed statistics before bias correction for selected IASI channels for the period 2 May–2 June 2016 for RTTOV versions 11 and 12 in the ECMWF IFS NWP model.

covered but also through the use of updated spectroscopic parameters and improved diverse profiles. The computation of the layer optical depths has also been updated several times, improving their accuracy and hence top-of-atmosphere radiances. RTTOV now has a user base which is truly worldwide, with over 1000 registered users, and it is used at many operational NWP centres for their radiance assimilation. The accuracy of the model at MW frequencies is shown to be much better than the instrument noise of the current MW radiometers. At IR wavelengths, its accuracy is generally below the instrument noise of the current IR hyperspectral sounders, but improvements for the water-vapour-affected channels are still needed for the clear-sky radiative transfer. It is important to note that the largest differences between versions are often due to changes in the transmittances from the underlying line-by-line models where spectroscopic parameters have been updated. Other improvements in the clear-air radiative transfer include the representation of NLTE effects in the shortwave IR region during daylight and the inclusion of the Zeeman splitting of the oxygen lines around 60 GHz for upper-stratosphere channels.

Concerning simulating cloudy radiances, the original version of RTTOV could only compute the radiance from a fractional cover of uniform grey cloud layer at a defined level. The inclusion of cloud and hydrometeor scattering and absorption at each level and at all wavelengths within RTTOV has allowed cloudy radiances, often referred to as all-sky, to be computed for more complicated cloud regimes which match the observed radiances well (Aumann et al., 2018). This has proven useful for producing simulated satellite imagery from model fields to compare with the real imagery (Blackmore et al., 2014) and for developing an all-sky radiance assimilation system (Geer et al., 2017).

The representation of the land surface using emissivity models for RTTOV radiative transfer calculations was requested by users, and this is an area continually under development, with parameterized models used over the ocean and atlases available over land. Improved surface models are allowing more of the surface sensing channels to be used actively for data assimilation and model validation.

To optimize the simulation of radiances from the advanced IR sounders, RTTOV has included two options to compute principal components from the full IR spectrum, which is computationally much more efficient than computing the entire spectral range with thousands of channels. This capability is now being used to more fully exploit the measurements from the hyperspectral sounders for data assimilation applications; see, e.g., Matricardi and McNally (2014).

RTTOV will continue to be developed as part of the NWP SAF activities, with new major versions planned every 3 years in response to user needs. In addition, minor releases are made every year which fix bugs and provide some limited upgrades which do not change the user interface. The RTTOV web pages (nwp-saf.eumetsat.int) also provide bug fixes, coefficients for new instruments which can be downloaded by users, and a variety of documentation for using RTTOV and associated studies.

The following improvements to aspects of RTTOV are planned for the coming years:

- assessing if the current layer optical depth prediction scheme can be further optimized in terms of accuracy, linearity and run time
- extending the range of clear-sky simulations into the ultraviolet range to allow the ozone sounding instruments to be simulated
- extending the MW simulations up to at least 700 GHz, including scattering, to allow new sensors which are planned to be modelled
- incorporating the MFASIS fast visible cloud scattering parameterization into RTTOV
- updating the scattering and absorption properties of different aerosol types and incorporating them into the MFASIS fast model
- adding 3-D effects for cloud and hydrometeor scattering calculations
- implementing a more efficient option for treating cloud overlap in VIS/IR cloud simulations
- developing the capability to simulate active MW sensors (e.g. radars) in RTTOV-SCATT
- extending PC-RTTOV and the interface to HT-FRTC to enable the simulation of more situations (for example, additional trace gases).

In addition to the above, improvements to the underlying spectroscopy at all wavelengths will be taken into account at each major RTTOV version as will the coefficients regenerated using this updated spectroscopy.

Code and data availability. The latest version of the RTTOV model can be downloaded free of charge from the NWP SAF website (http://nwp-saf.eumetsat.int, last access: 6 July 2018) once users have registered on the site to agree to the licence conditions. Updates to the code and coefficients for new instruments are also posted on the site. There is also a discussion forum for RTTOV (under the support tab) for users to share experiences with using the RTTOV model.

Appendix A: List of abbreviations

AER	Atmospheric and Environmental Research
AIRS	Atmospheric InfraRed Sounder
AMSU	Advanced Microwave Sounding Unit
ATOVS	Advanced TIROS Operational Vertical Sounder
ATSR	Along-track Scanning Radiometer
AVHRR	Advanced Very High Resolution Radiometer
BRDF	Broadband reflectance distribution function
CFMIP	Cloud Feedback Model Intercomparison Project
CNRM	Centre National de Recherches Météorologiques
COSP	CFMIP Observation Simulator Package
CrIS	Cross-track Infrared Sounder
CRTM	Community Radiative Transfer Model
DOM	Discrete ordinates method
ECMWF	European Centre for Medium-Range Weather Forecasts
EUMETSAT	European Organisation for the Exploitation of Meteorological Satellites
GMS	Geostationary meteorological satellite
GOES	Geostationary Operational Environmental Satellite
GUI	Graphical user interface
HIRS	High Resolution Infrared Sounder
HT-FRTC	Havemann–Taylor Fast Radiative Transfer Code
IASI	Infrared Atmospheric Sounding Interferometer
IR	Infrared
IWC	Ice water content
MFASIS	Method for FAst Satellite Image Synthesis
MHS	Microwave Humidity Sounder
MODIS	MODerate resolution Imaging Spectroradiometer
MSU	Microwave sounding unit
MT-CKD	Mlawer–Tobin_Clough– Kneizys–Davies continuum
MW	Microwave
NLTE	Non-local thermodynamic equilibrium
NOAA	National Oceanic and Atmospheric Administration
NWP	Numerical weather prediction
OPAC	Optical properties of aerosols and clouds
PC	Principal components
RTTOV	Radiative Transfer for TOVS
SAF	Satellite application facility
SSM/I	Special Sensor Microwave Imager
TELSEM	Tool to Estimate Land-Surface Emissivities at Microwave frequencies
TESSEM	Tool to Estimate Sea-Surface Emissivities at Microwave frequencies
TIGR	Thermodynamic Initial Guess Retrieval
TIROS	Television infrared observation satellites
UWIREMIS	University of Wisconsin IR emissivity atlas
VIS	Visible

Competing interests. The authors declare that they have no conflict of interest.

Acknowledgements. Most of the RTTOV development has been funded by the EUMETSAT NWP SAF over many years. Visiting scientists funded by the NWP SAF have contributed over the years to various aspects of the development, and their contributions are gratefully acknowledged.

Edited by: Tim Butler
Reviewed by: Sid Boukabara and Benjamin Ruston

References

Aires, F., Prigent, C., Bernardo, F., Jiménez, C., Saunders, R., and Brunel, P.: A Tool to Estimate Land-Surface Emissivities at Microwave frequencies (TELSEM) for use in numerical weather prediction, Q. J. Roy. Meteor. Soc., 137, 690–699, 2011.

Andersson, E., Haseler, J., Undén, P., Courtier, P., Kelly, G., Vasiljevic, D., Brankovic, C., Gaffard, C., Hollingsworth, A., Jakob, C., Janssen, P., Klinker, E., Lanzinger, A., Miller, M., Rabier, F., Simmons, A., Strauss, B., Viterbo, P., Cardinali, C., and Thépaut, J.-N.: The ECMWF implementation of three-dimensional variational assimilation (3D-Var). III: Experimental results, Q. J. Roy. Meteor. Soc., 124, 1831–1860, https://doi.org/10.1002/qj.49712455004, 1998.

Andrey-Andrés, J., Fourrié, N., Guidard, V., Armante, R., Brunel, P., Crevoisier, C., and Tournier, B.: A simulated observation database to assess the impact of the IASI-NG hyperspectral infrared sounder, Atmos. Meas. Tech., 11, 803–818, https://doi.org/10.5194/amt-11-803-2018, 2018.

Aumann, H., Xiuhong, C., Fishbein, E., Geer, A., Havemann, S., Huang, X., Liu, X., Liuzzi, G., DeSouza-Machado, S., Manning, E. M., Masiello, G., Matricardi, M., Moradi, I., Natrai, V., Serio, C., Strow, L., Vidot, J., Wilson, C., Wu, W., Yang, Q., and Yung, Y. L.: Evaluation of Radiative Transfer Models with Clouds, J. Geophys. Res.-Atmos., 123, https://doi.org/10.1029/2017JD028063, online first, 2018.

Baran, A. J., Francis, P. N., Labonnote, L.-C., and Doutriaux-Boucher, M.: A scattering phase function for ice cloud: Tests of applicability using aircraft and satellite multi-angle multi-wavelength radiance measurements of cirrus, Q. J. Roy. Meteor. Soc., 127, 2395–2416, 2001.

Baran, A. J., Cotton, R., Furtado, K., Havemann, S., Labonnote, L.-C., Marenco, F., Smith, A., and Thelen, J.-C.: A self-consistent scattering model for cirrus. II: The high and low frequencies, Q. J. Roy. Meteor. Soc., 140, 1039–1057, https://doi.org/10.1002/qj.2193, 2014.

Baum, B. A., Yang, P., Heymsfield, A. J., Schmitt, C., Xie, Y., Bansemer, A., Hu, Y. X., and Zhang, Z.: Improvements to shortwave bulk scattering and absorption models for the remote sensing of ice clouds, J. Appl. Meteorol. Clim., 50, 1037–1056, 2011.

Bauer, P.: Including a melting layer in microwave radiative transfer simulation for clouds, Atmos. Res., 67, 9–30, 2001.

Bauer, P., Moreau, E., Chevallier, F., and O'Keeffe, U.: Multiple-scattering microwave radiative transfer for data assimilation applications, Q. J. Roy. Meteor. Soc., 132, 1259–1281, https://doi.org/10.1256/qj.05.153, 2006.

Bauer, P., Geer, A. J., Lopez, P., and Salmond, D.: Direct 4D-Var assimilation of all-sky radiances. Part I: Implementation, Q. J. Roy. Meteor. Soc., 136, 1868–1885, https://doi.org/10.1002/qj.659, 2010.

Blackmore, T. A., Saunders, R., and Keogh, S. J.: Verifying NWP model analyses and forecasts using simulated satellite imagery, in: Proceedings of the 2014 EUMETSAT Meteorological Satellite Conference, 22–26 September 2014, Geneva, available at: https://www.eumetsat.int/website/home/News/ConferencesandEvents/DAT_2076129.html (last access: 22 June 2018), Session 8: Oral proceedings, 2014.

Bodas-Salcedo, A., Webb, M. J., Bony, S., Chepfer, H., Dufresne, J., Klein, S. A., Zhang, Y., Marchand, R., Haynes, J. M., Pincus, R., and John, V. O.: COSP: Satellite simulation software for model assessment, B. Am. Meteorol. Soc., 92, 1023–1043, https://doi.org/10.1175/2011BAMS2856.1, 2011.

Borbas, E. E. and Ruston, B. C.: The RTTOV UWiremis IR land surface emissivity module, NWP SAF report, available at: http://nwpsaf.eu/vs_reports/nwpsaf-mo-vs-042.pdf (last access: 22 June 2018), 2010.

Borbas, E. E, Hulley, G., Knuteson, R., and Feltz, M.: MEaSUREs Unified and Coherent Land Surface Temperature and Emissivity (LST&E) Earth System Data Record (ESDR): The Combined ASTER and MODIS Emissivity database over Land (CAMEL) User's guide, Technical documentation, 30 pp., available at: https://lpdaac.usgs.gov/sites/default/files/public/product_documentation/cam5k30_v1_user_guide_atbd.pdf (last access: 2 July 2018), 2017.

Bormann, N., Geer, A., and English, S. J.: Evaluation of the microwave ocean surface emissivity model FASTEM-5 in the IFS, ECMWF, Technical Memorandum 667, 18 pp., 2012.

Boudala, F. S., Isaac, G. A., Fu, Q., and Cober, S. G.: Parameterization of effective ice particle size for high-latitude clouds, Int. J. Climatol., 22, 1267–1284, 2002.

Chandrasekhar, S.: Radiative Transfer, Dover, New York, 1960.

Chen, Y., Weng, F., Han, Y., and Liu, Q.: Validation of the community radiative transfer model (CRTM) by using CloudSat Data, J. Geophys. Res., 113, 2156–2202, 2008.

Chevallier, F., Chédin, A., Chéruy, F., and Morcrette, J. J.: TIGR-like atmospheric profile databases for accurate flux computation, Q. J. Roy. Meteor. Soc., 126, 777–785, 2000.

Chevallier, F., Di Michele, S., and Mc Nally A.: Diverse profile datasets from the ECMWF 91-level short-range forecasts, ECMWF, NWP SAF Technical Report, 10, 14 pp., 2006.

Chou, M.-D., Lee, K.-T., Tsay, S.-C., and Fu, Q.: Parameterization for Cloud Longwave scattering for use in Atmospheric Models, J. Climate, 12, 159–169, 1999.

Clough, S. A., Shephard, M. W., Mlawer, E. J., Delamere, J. S., Iacono, M. J., Cady-Pereira, K., Boukabara, S., and Brown, P. D.: Atmospheric radiative transfer modeling: a summary of the AER codes, Short Communication, J. Quant. Spectrosc. Ra., 91, 233–244, 2005.

Ding, S., Yang, P., Weng, F., Liu, Q., Han, Y., Van Delst, P., Li, J., and Baum, B.: Validation of the community radiative transfer model, J. Quant. Spectrosc. Ra., 112, 1050–1064, 2011.

English, S. J., Poulsen, C., and Smith, A. J.: Forward modelling for liquid water cloud and land surface emissivity. Proceedings of

ECMWF/EUMETSAT workshop on the use of ATOVS data for NWP assimilation, ECMWF, Reading, RG2 9AX, UK, 91–96, 2000.

Eyre, J. R.: A fast radiative transfer model for satellite sounding systems, ECMWF, Technical Memorandum, 176, 28 pp., 1991.

Eyre, J. R. and Woolf, H.: Transmittance of atmospheric gases in the microwave region, Appl. Optics, 27, 3244–3249, 1988.

Eyre, J. R., Kelly, G. A., McNally, A. P., Andersson, E., and Persson, A.: Assimilation of TOVS radiance information through one-dimensional variational analysis, Q. J. Roy. Meteor. Soc., 119, 1427–1463, https://doi.org/10.1002/qj.49711951411, 1993.

Funke, B., López-Puertas, M., García-Comas, M., Kaufmann, M., Höpfner, M., and Stiller G. P.: GRANADA: A Generic RAdiative traNsfer AnD non-LTE population algorithm, J. Quant. Spectrosc. Ra., 113, 1771–1817, 2012.

Garand, L., Turner, D. S., Larocque, M., Bates, J., Boukabara, S., Brunel, P., Chevallier, F., Deblonde, G., Engelen, R., Hollingshead, M., Jackson, D., Jedlovec, G., Joiner, J., Kleespies, T., McKague, D. S., McMillin, L., Moncet, J.-L., Pardo, J. R., Rayer, P. J., Salathe, E., Saunders, R., Scott, N. A., Van Delst, P., and Woolf, H.: Radiance and Jacobian intercomparison of radiative transfer models applied to HIRS and AMSU channels, J. Geophys. Res., 106, 24017–24031, https://doi.org/10.1029/2000JD000184, 2001.

Geer, A. J. and Baordo, F.: Improved scattering radiative transfer for frozen hydrometeors at microwave frequencies, Atmos. Meas. Tech., 7, 1839–1860, https://doi.org/10.5194/amt-7-1839-2014, 2014.

Geer, A. J., Bauer, P., and O'Dell, C. W.: A revised cloud overlap scheme for fast microwave radiative transfer in rain and cloud, J. Appl. Meteorol. Clim., 48, 2257–2270, 2009.

Geer, A. J., Baordo, F., Bormann, N., Chambon, P., English, S. J., Kazumori, M., Lawrence, H., Lean, P., Lonitz, K., and Lupu, C.: The growing impact of satellite observations sensitive to humidity, cloud and precipitation, Q. J. Roy. Meteor. Soc., 143, 3189–3206, https://doi.org/10.1002/qj.3172, 2017.

Gordon, I. E., Rothman, L. S., Hill, C., et al.: The HITRAN2016 Molecular Spectroscopic Database, J. Quant. Spectrosc. Ra., 203, 3–69, https://doi.org/10.1016/j.jqsrt.2017.06.038, 2017.

Havemann, S.: The development of a fast radiative transfer model based on an empirical orthogonal functions (EOF) technique, SPIE, 6405, 348–358, 2006.

Havemann, S., Thelen, J.-C., and Taylor, J. P.: The Havemann-Taylor Fast Radiative Transfer Code: Exact fast radiative transfer for scattering atmospheres using Principal Components (PCs), Current problems in atmospheric radiation (IRS 2008) Edited by: Nakajima, T; Yamasoe, MA Book Series: AIP Conference Proceedings Volume: 1100 Pages: 38-40, 2009.

Hess, M., Koepke, P., and Schult, I. : Optical Properties of Aerosols and Clouds: the software package OPAC, B. Am. Meteorol. Soc., 79, 831–844, 1998.

Hocking, J.: Interpolation methods in the RTTOV fast radiative transfer model, Met Office Forecasting Research Technical Report 590, available at: http://www.metoffice.gov.uk/binaries/content/assets/mohippo/pdf/i/k/frtr590.pdf (last access: 2 July 2018), 2014.

Hocking, J.: A visible/infrared multiple-scattering model for RTTOV, NWP SAF report, available at: http://nwpsaf.eu/publications/tech_reports/nwpsaf-mo-tr-031.pdf (last access: 2 July 2018), 2015.

Hocking, J., Rayer, P., Rundle, D., Saunders, R. W., Matricardi, M., Geer, A., Brunel, P., and Vidot, J.: RTTOV v12 User Guide, NWP SAF, available at: https://www.nwpsaf.eu/site/software/rttov/documentation/ (last access: 2 July 2018), 2017.

Joseph, J. H., Wiscombe, W. J., and Weinman, J. A.: The Delta-Eddington Approximation for Radiative Flux Transfer, J. Atmos. Sci., 33, 2452–2459, 1976.

Karbou, F., Gérard, E., and Rabier, F.: Microwave land emissivity and skin temperature for AMSU-A and -B assimilation over land, Q. J. Roy. Meteor. Soc., 132, 2333–2355, https://doi.org/10.1256/qj.05.216, 2006.

Karbou, F., Gérard, E., and Rabier, F. : Global 4DVAR assimilation and forecast experiments using AMSU observations over land. Part I: Impacts of various land surface emissivity parameterizations, Weather Forecast., 25, 5–19, 2010.

Kazumori, M. and English, S. J.: Use of the ocean surface wind direction signal in microwave radiance assimilation, Q. J. Roy. Meteor. Soc., 141, 1354–1375, 2015.

Li, J., Wolf, W. W., Menzel, W. P., Zhang, W., Huang, H. L., and Achtor, T. H.: Global soundings of the atmosphere from ATOVS measurements: The algorithm and validation, J. Appl. Meteorol., 39, 1248–1268, 2000.

Liebe, H. J., Manabe, T., and Hufford, G. A.: Millimeter-wave attenuation and delay rates due to fog/cloud conditions, IEEE T. Antenn. Propag., 37, 1617–1612, 1989.

Liljegren, J. C., Boukabara, S. A., Cady-Pereira, K., and Clough, S. A.: The effect of the half-width of the 22-GHz water vapor line on retrievals of temperature and water vapor profiles with a 12-channel microwave radiometer, IEEE T. Geosci. Remote, 43, 1102–1108, 2005.

Liu, G.: A database of microwave single-scattering properties for non-spherical ice particles, B. Am. Meteorol. Soc., 111, 1563–1570, 2008.

Liu, X., Smith, W. L., Zhou, D. K., and Larar, A.: Principal component-based radiative transfer model for hyperspectral sensors: Theoretical concept, Appl. Optics, 45, 201–209, 2006.

Liu, Q., Weng, F., and English, S.: An improved fast microwave water emissivity model, IEEE, T. Geosci. Remote, 49, 1238–1250, 2011.

Lupu, C. and Geer, A. J.: Operational implementation of RTTOV-11 in the IFS, ECMWF, Research Dept., Technical Memorandum, 748, 19 pp., 2015.

Lupu, C. and Wilhelmsson T.: A guide to simulated satellite images in the IFS, ECMWF Research Department Memorandum RD16-064, 10 pp., available at: https://software.ecmwf.int/wiki/display/FCST/Simulated+satellite+data?preview=/55127736/97382070/A_guide_to_simulated_satellite_images_in_the_IFS.pdf (last access: 2 July 2018), 2016.

Matricardi, M.: RTIASI-4, a new version of the ECMWF fast radiative transfer model for the infrared atmospheric sounding intererometer, ECMWF, Technical Memorandum, 425, 63 pp., 2003.

Matricardi, M.: The inclusion of aerosols and clouds in RTIASI, the ECMWF fast radiative transfer model for the Infrared Atmospheric Sounding Interferometer, ECMWF, Technical Memorandum, 474, 53 pp., 2005.

Matricardi, M.: The generation of RTTOV regression coefficients for IASI and AIRS using a new profile training set and a new line-by-line database, ECMWF, Technical Memorandum, 564, 47 pp., 2008.

Matricardi, M.: A principal component based version of the RTTOV fast radiative transfer model, Q. J. Roy. Meteor. Soc., 136, 1823–1835, https://doi.org/10.1002/qj.680, 2010.

Matricardi, M. and McNally, A.: The direct assimilation of principal components of IASI spectra in the ECMWF 4D-Var, Q. J. Roy. Meteor. Soc., 140, 573–582, 2014.

Matricardi, M., Chevallier, F., Kelly, G., and Thepaut, J.-N.: An improved general fast radiative transfer model for the assimilation of radiance observations, Q. J. Roy. Meteor. Soc., 130, 153–173, 2004.

Matricardi, M., López Puertas, M., and Funke, B.: Modeling of nonlocal thermodynamic equilibrium effects in the principal component based version of the RTTOV fast radiative transfer model, J. Geophys. Res.-Atmos., 123, 5741–5761, https://doi.org/10.1029/2018JD028657, 2018.

McFarquhar, G. M., Iacobellis, S., and Somerville, R. C. J.: SCM simulations of tropical ice clouds using observationally based parameterizations of microphysics, J. Climate, 16, 1643–1664, 2003.

McMillin, L. M. and Fleming, H. E.: Atmospheric Transmittance of an Absorbing Gas: A Computationally Fast and Accurate Transmittance Model for Absorbing Gases with Constant Mixing Ratios in Inhomogeneous Atmospheres, Appl. Optics, 15, 358–363, 1976.

McMillin, L. M., Crone, L. J., and Kleespies, T. J.: Atmospheric transmittance of an absorbing gas. 5. Improvements to the OPTRAN approach, Appl. Optics, 34, 8396–8399, 1995.

McMillin, L. M., Xiong, Han, X., Y., Kleespies, T. J., and Van Delst, P.: Atmospheric transmittance of an absorbing gas. 7. Further improvements to the OPTRAN 6 approach, Appl. Optics, 45, 2028–2034. https://doi.org/10.1364/AO.45.002028, 2006.

Moncet, J., Uymin, G., Liang, P., and Lipton, A. E.: Fast and Accurate Radiative Transfer in the Thermal Regime by Simultaneous Optimal Spectral Sampling over All Channels, J. Atmos. Sci., 72, 2622–2641, https://doi.org/10.1175/JAS-D-14-0190.1, 2015.

Ou, S. C. and Liou, K. N.: Ice microphysics and climatic temperature feedback, Atmos. Res., 35, 127–138, 1995.

Payne, V. H., Delamere, J. S., Cady-Pereira, K. E., Gamache, R. R., Moncet, J.-L., Mlawer, E. J., and Clough, S. A.: Air-broadened half-widths of the 22- and 183-GHz water-vapor lines, IEEE T. Geosci. Remote, 46, 3601–3617, 2008.

Poli, P., Dee, D., Saunders, R., John, V., Rayer, P., Schulz, J., Holmlund, K., Coppens, D., Klaes, D., Johnson, J., Esfandiari, A., Gerasimov, I., Zamkoff, E., Al-Jazrawi, A., Santek, D., Albani, M., Brunel, P., Fennig, K., Schröeder, M., Kobayashi, S., Oertel, D., Döehler, W., Späenkuch, D., and Bojinski, S.: Recent advances in satellite data rescue, B. Am. Meteorol. Soc., 98, 1471–1484, https://doi.org/10.1175/BAMS-D-15-00194.1, 2017.

Prigent, C., Aires, F., Wang, D., Fox, S., and Harlow, C.: Sea-surface emissivity parametrization from microwaves to millimetre waves, Q. J. Roy. Meteor. Soc., 143, 596–605, https://doi.org/10.1002/qj.2953, 2017.

Rayer, P. J.: Fast transmittance model for satellite sounding, Appl. Optics, 34, 7387–7394, 1995.

Rochon, Y. J., Garand, L., Turner, D. S., and Polavarapu, S.: Jacobian mapping between vertical coordinate systems in data assimilation, Q. J. Roy. Meteor. Soc., 133, 1547–1558, https://doi.org/10.1002/qj.117, 2007.

Rothman, L. S., Gordon, I. E., Babikov, Y., et al.: The HITRAN2012 molecular spectroscopic database, J. Quant. Spectrosc. Ra., 130, 4–50, https://doi.org/10.1016/j.jqsrt.2013.07.002, 2013.

Saunders, R., Matricardi, M., and Brunel, P.: An improved fast radiative transfer model for assimilation of satellite radiance observations, Q. J. Roy. Meteor. Soc., 125, 1407–1425, https://doi.org/10.1002/qj.1999.49712555615, 1999.

Saunders, R., Brunel, P., English, S., Bauer, P., O'Keefe, U., Francis, P. N., and Rayer, P.: RTTOV-8 science and validation report, 46 pp., available at: https://nwpsaf.eu/oldsite/deliverables/rtm/rttov8_svr.pdf (last access: 2 July 2018), 2006.

Saunders, R., Rayer, P., Brunel, P., von Engeln, A., Bormann, N., Strow, L., Hannon, S., Heilliette, S., Liu, X., Miskolczi, F., Han, Y., Masiello, G., Moncet, J.-L., Uymin, G., Sherlock, V., and Turner, D. S.: A comparison of radiative transfer models for simulating Atmospheric Infrared Sounder (AIRS) radiances, J. Geophys. Res., 112, D01S90, https://doi.org/10.1029/2006JD007088, 2007.

Saunders, R., Hocking, J., Rundle, D., Rayer, P., Havemann, S., Matricardi, M., Geer, A., Lupu, C., Brunel, P., and Vidot, J.: RTTOV v12 science and validation report, 78 pp., available at: https://www.nwpsaf.eu/site/download/documentation/rtm/docs_rttov12/rttov12_svr.pdf (last access: 2 July 2018), 2017.

Scheck, L.: Comparison of MFASIS and RTTOV-DOM, NWP SAF report, 18 pp., available at: http://nwpsaf.eu/vs_reports/nwpsaf-mo-vs-054.pdf (last access: 2 July 2018), 2016.

Scheck, L., Frerebeau, P., Buras-Schnell, R., and Mayer, B.: A fast radiative transfer method for the simulation of visible satellite imagery, J. Quant. Spectrosc. Ra., 175, 54–67, 2016.

Sherlock, V. and Saunders, R.: ISEM-6: Infrared surface emissivity model for RTTOV-6, in: Tech. Proc. 11th Int. ATOVS Study Conf., 20–26 September 2000, Bureau of Meteorology Research Centre, Budapest, Hungary, 383–389, 2000.

Stamnes, K., Tsay, S.-C., Wiscombe, W., and Jayaweera, K.: Numerically stable algorithm for discrete-ordinate-method radiative transfer in multiple-scattering and emitting layered media, Appl. Optics, 27, 2502–2509, 1988.

Tretyakov, M. Yu., Koshelev, M. A., Dorovskikh, V. V., Makarov, D. S., and Rosenkranz, P. W.: 60-GHz oxygen band: precise broadening and central frequencies of fine structure lines, absolute absorption profile at atmospheric pressure, and revision of mixing coefficients', J. Mol. Spectrosc., 231, 1–14, https://doi.org/10.1016/j.jms.2004.11.011, 2005.

Turner, E. C. and Tett, S. F. B.: Using longwave HIRS radiances to test climate models, Clim. Dynam., 43, 1103, https://doi.org/10.1007/s00382-013-1959-6, 2014.

U.S. Standard Atmosphere: U.S. Government Printing Office, Washington, D.C., 1976.

Vidot, J. and Borbás, É.: Land surface VIS/NIR BRDF atlas for RTTOV-11: model and validation against SEVIRI land SAF albedo product, Q. J. Roy. Meteor. Soc., 140, 2186–2196, https://doi.org/10.1002/qj.2288, 2014.

Vidot, J., Baran, A. J., and Brunel, P.: A new ice cloud parameterization for infrared radiative transfer simulation of cloudy radiances:

Evaluation and optimization with IIR observations and ice cloud profile retrieval products, J. Geophys. Res.-Atmos., 120, 6937–6951, https://doi.org/10.1002/2015JD023462, 2015.

Vidot, J., Brunel, P., Dumont, M., Carmagnola, C., and Hocking, J.: The VIS/NIR Land and Snow BRDF Atlas for RTTOV: Comparison between MODIS MCD43C1 C5 and C6, Remote Sens., 10, 21, https://doi.org/10.3390/rs10010021, 2018.

Wyser, K.: The effective radius in ice clouds, J. Climate, 11, 1793–1802, 1998.

5.4 Aumann et al. (2018)

Cet article publié en 2018 dans *Journal of Geophysical Research* (facteur d'impact de 3.63) est le fruit d'une coordination internationale lancée en 2016 par Georges Aumann (JPL) qui proposait une base de données comprenant des observations hyperspectrales infrarouges de l'instrumentAIRS sur une demi-journée contenant des nuages et des profils nuageux d'entrée du CEPMMT colocalisés pour comparer des codes de transfert radiatif. Les premiers résultats avaient été discutés lors de la session "Advances in hyperspectral remote sensing in the cloudy atmospheres" de la conférence American Geophysical Union (AGU) en décembre 2016.

Journal of Geophysical Research: Atmospheres

RESEARCH ARTICLE
10.1029/2017JD028063

Evaluation of Radiative Transfer Models With Clouds

Hartmut H. Aumann[1], Xiuhong Chen[2], Evan Fishbein[1], Alan Geer[3], Stephan Havemann[4], Xianglei Huang[2], Xu Liu[5], Giuliano Liuzzi[6], Sergio DeSouza-Machado[7], Evan M. Manning[1], Guido Masiello[6], Marco Matricardi[3], Isaac Moradi[8], Vijay Natraj[1], Carmine Serio[6], Larrabee Strow[7], Jerome Vidot[9], R. Chris Wilson[1], Wan Wu[5], Qiguang Yang[5], and Yuk L. Yung[1,10]

[1]Jet Propulsion Laboratory, California Institute of Technology, Pasadena, CA, USA, [2]Department of Climate and Space Science, University of Michigan, Ann Arbor, MI, USA, [3]European Center for Medium-Range Weather Forecasting, Reading, UK, [4]UK Met Office, Exeter, UK, [5]NASA Langley Research Center, Hampton, VA, USA, [6]School of Engineering, University of Basilicata, Potenza, Italy, [7]Department of Physics, University of Maryland, Baltimore County, Catonsville, MD, USA, [8]ESSIC, University of Maryland, College Park, MD, USA, [9]Meteo France, Toulouse, France, [10]Department of Planetary Science, California Institute of Technology, Pasadena, CA, USA

Key Points:
- In the 900-cm^{-1} atmospheric window channel several Radiative Transfer Models have a better than 0.95 correlation between the histogram derived from the observations and those derived from the calculations
- Differences in the bias between observations and calculations for the 2,616-cm^{-1} atmospheric window channel are not inconsistent with results at 900 cm^{-1} if the daytime calculations use full scattering
- Differences in the cloud physics and cloud overlap assumptions between Radiative Transfer Models result in a standard deviation of the pairwise difference of between 6 and 12 K; differences due to the cloud overlap assumption alone result in a 3-K standard deviation

Correspondence to:
H. H. Aumann,
aumann@jpl.nasa.gov

Citation:
Aumann, H. H., Chen, X., Fishbein, E., Geer, A., Havemann, S., Huang, X., et al. (2018). Evaluation of radiative transfer models with clouds. *Journal of Geophysical Research: Atmospheres*, *123*, 6142–6157. https://doi.org/10.1029/2017JD028063

Received 14 NOV 2017
Accepted 4 APR 2018
Accepted article online 16 APR 2018
Published online 13 JUN 2018

Abstract Data from hyperspectral infrared sounders are routinely ingested worldwide by the National Weather Centers. The cloud-free fraction of this data is used for initializing forecasts which include temperature, water vapor, water cloud, and ice cloud profiles on a global grid. Although the data from these sounders are sensitive to the vertical distribution of ice and liquid water in clouds, this information is not fully utilized. In the future, this information could be used for validating clouds in National Weather Center models and for initializing forecasts. We evaluate how well the calculated radiances from hyperspectral Radiative Transfer Models (RTMs) compare to cloudy radiances observed by AIRS and to one another. Vertical profiles of the clouds, temperature, and water vapor from the European Center for Medium-Range Weather Forecasting were used as input for the RTMs. For nonfrozen ocean day and night data, the histograms derived from the calculations by several RTMs at 900 cm^{-1} have a better than 0.95 correlation with the histogram derived from the AIRS observations, with a bias relative to AIRS of typically less than 2 K. Differences in the cloud physics and cloud overlap assumptions result in little bias between the RTMs, but the standard deviation of the differences ranges from 6 to 12 K. Results at 2,616 cm^{-1} at night are reasonably consistent with results at 900 cm^{-1}. Except for RTMs which use full scattering calculations, the bias and histogram correlations at 2,616 cm^{-1} are inferior to those at 900 cm^{-1} for daytime calculations.

Plain Language Summary Getting the right clouds of the right type, at the right time and location in Global Circulation Models, is key to getting the local energy balance right. This is key to an accurate forecast. If the clouds are of the wrong type or at the wrong location or time, the accuracy of the forecast is degraded. We evaluate the accuracy of the best currently available cloud description (produced by the European Center for Medium-Range Weather Forecasting) by comparing the radiances calculated using Radiative Transfer Models (RTMs) from six major development teams to cloudy radiances observed by the Atmospheric Infrared Sounder at the same location and time. The better RTMs fit statistically reasonably well in the 11-μm atmospheric window area, with little latitude (zonal) and day/night cloud-type related bias. None of the RTMs fit well in the 4-μm atmospheric window area during daytime, unless the calculations use full scattering. With the current state of art, all major RTMs would be suitable to start the validation of cloud effects in the National Weather Center models using just one 11-μm atmospheric window channel.

1. Introduction

Clouds are a key component of the Earth's weather and climate system. The data from hyperspectral infrared sounders have the information content to sense the vertical distribution of temperature and water vapor in clear air and of ice and liquid water inside semitransparent clouds. The data from four hyperspectral sounders in polar orbit are routinely ingested by the National Weather Centers (NWCs; e.g., Collard & McNally, 2009): The Atmospheric Infrared Sounder (AIRS; Aumann et al., 2003) on the Earth Observing System Aqua satellite, the Crosstrack Infrared Sounder (CrIS, Glumb et al., 2003) on the Suomi National Polar-orbiting Platform satellite, and the Infrared Atmospheric Sounder Interferometer (IASI, Blumstein et al., 2008; Hilton et al., 2012) on MetOp A and B each makes more than 2 million observations of the state of the atmosphere and the clouds each day. The NWCs predominantly use the cloud-free portion of these data to initialize forecasts that

Table 1
Cloudy RTM Developers Who Participated in the Comparison

RTM name	Base model spectroscopy	Participant	Organization
SARTA	HITRAN2008	DeSouza-Machado Strow	UMBC
RTTOV	HITRAN2008	Vidot Matricardi	NWPSAF (France) ECMWF (EU)
HT-FRTC	HITRAN2008	Havemann	UK Met Office
PCRTM	HITRAN2008	Xianglei Huang	University of Michigan
		Xu Liu	LARC
CRTM	HITRAN2008	Moradi, Wilson	NASA GMAO NASA JPL
σ-IASI-as	HITRAN2012	Liuzzi Masiello	U. Basilicata, Italy

provide temperature, water vapor, water cloud, and ice cloud profiles on a global grid every 3 hr. Using cloudy observations in forecast models is difficult (Bennartz & Greenwald, 2011; Errico et al., 2007; McNally, 2009; McNally & Watts, 2003; Okamoto et al., 2014; Pavelin et al., 2008), and although all-sky microwave radiances are now used (e.g., Geer et al., 2017), the use of infrared radiances represents a harder problem. NWCs make use of some cloudy scenes, such as low-level cloud or fully overcast scenes, but the cloud information is still not used to initialize forecasts (Guidard et al., 2011; Lavanant et al., 2011). A number of NWCs and university research groups have developed fast and accurate Radiative Transfer Models (RTMs) for infrared sounders, which include the effects of cloud and aerosol scattering. The names and associated organizations of the RTM developers are summarized in Table 1. Summaries of the RTMs are found in Appendix A3. While each RTM has been subject to its own validation, our paper is the first to compare results from major RTMs for cloudy hyperspectral infrared applications on the same data set to collocated observations and to each other.

The objective of our paper was to evaluate the degree to which the radiative effects of clouds in NWC models agree with collocated hyperspectral observation. The availability of RTMs with a high degree of radiometric fidelity relative to observation, or at least the availability of tools to assess this fidelity, is expected to lead to the increased utilization of hyperspectral sounder data in the forecast. We selected AIRS observations and AIRS RTMs for our analysis to follow the Saunders et al. (2007) RTM analysis under cloud-free conditions.

2. Data, Participants, and Evaluation

2.1. Data

We selected data provided by the European Center for Medium-Range Weather Forecasting (ECMWF; European Center for Medium-Range Weather Forecasting (ECMWF), 2009) as representative for the definition of the atmospheric states with clouds. The ECMWF description of the atmospheric state (temperature, water vapor and cloud vertical profiles, and surface temperature) has been widely documented and validated (e.g., Kazumori et al., 2016; Köhler et al., 2011; Tiedtke, 1989, 1993; Tompkins et al., 2007). Details are in Appendix A1.

For the intercomparison of RTMs we used AIRS observations from 1 March 2009 and the matching atmospheric state defined by ECMWF. A subset of this data was created using the difference between the ECMWF estimate of the surface temperature (stemp) and the brightness temperature measured in the 1,231-cm^{-1} window channel (bt1231; stemp-bt1231). This difference is a measure of the radiometric effect of clouds. Under clear conditions the difference is less than 2 K, but the difference can increase to as much as 100 K in the presence of cold clouds in the tropics. We limited the size of this data set to control the magnitude of the computational effort involved in scattering calculations by using stratified sampling. This method selected a representative mix of cloudy conditions from the AIRS data, which resulted in 7,377 unique cases. The surface emissivity and surface reflectance were obtained from a monthly climatology (Zhou et al., 2012). The surface reflectance was assumed to be Lambertian. Details of the selection algorithm are given in Appendix A2.

2.2. Participants and RTM Methodology

Table 1 summarizes the affiliation of the developers of cloud-capable RTMs at major NWCs, government, and university facilities. Six RTMs were used: (1) Stand Alone Radiative Transfer Algorithm (SARTA), (2) Radiative Transfer for TOVS (RTTOV), (3) Havemann-Taylor Fast Radiative Transfer Code (HT-FRTC), (4) Principal Component-based RTM (PCRTM), (5) Community RTM (CRTM), and (6) σ-IASI. Largely based on discussions at the 2016 AGU meeting, every RTM team, except the RTTOV teams, submitted revised results. Five of the RTM developers generated variants related to details of how cloud overlap, cloud type, and scattering were handled. Details on the individual RTMs are summarized in Appendix A3.

All RTMs calculated cloudy radiances using a linear combination of clear-sky calculations and scattering calculations for one or more cloud columns. The results of the clear-sky column calculations from all these RTMs

were nearly identical, consistent with Saunders et al. (2007). The cloudy spectra were calculated as the linear combination of clear and cloudy columns based on the cloud fraction. The maximum overlap (MO) model is the simplest case:

$$R_{MO} = CF\ R_{FO} + (1 - CF)\ R_{CLR} \quad (1)$$

R_{MO} is the spectrum calculated with the MO assumption and CF is defined as the maximum cloud fraction in the cloud coverage profile. Some RTMs set CF equal to the total cloud cover (tcc) specified in the ECMWF record. R_{CLR} is the clear-sky spectrum, and R_{FO} is the spectrum assuming full overcast (i.e., clouds fill the entire satellite footprint). Some RTMs allow the user to make more complicated overlap assumptions. The maximum random overlap (MRO) assumption states that any continuous vertical cloud profile is maximally overlapped, and the discontinuous parts of the vertical cloud profile are randomly overlapped (Hogan & Illingworth, 2000). If two cloud slabs are used, the MRO radiance is

$$R_{MRO} = CF_1\ (1 - CF_2)\ R_{C1} + CF_2\ (1 - CF_1)\ R_{C2} + CF_1\ CF_2\ R_{CLD} + (1 - CF_1)\ (1 - CF_2)\ R_{CLR} \quad (2)$$

where CF_1 is the maximum cloud fraction of the first cloud slab, CF_2 is the maximum cloud fraction of the second cloud slab, R_{C1} is the calculation where only the first cloud slab is included, R_{C2} is the calculation where only the second cloud slab is included, R_{CLD} is the calculation where both clouds are included, and R_{CLR} is the clear-sky calculation. There are several variants of the overlap assumption, including MO, exponential random overlap (ERO), and the random overlap (RO). We indicated these variants in the names of the models; for example, CRTM_mro is the cloudy spectrum calculated using CRTM with the MRO assumption. Most RTM developers submitted results with a number of variants.

2.3. Evaluation

The intercomparison of the RTMs used three methods.

1. The pairwise comparison of the observed AIRS spectra with the calculated spectra. We calculated the mean and standard deviation (stddev). This comparison is complicated by several factors: (a) The collocation error: The location and local time of the AIRS data obtained with a 12-km footprint (effectively 1/8 degree latitude/longitude in the tropics) is not a good match to the temporal (3 hr) and spatial grid (approximately 25 km) of the ECMWF data available to this study. (b) The tcc is specified in the ECMWF data; the cloud fraction, liquid water, and ice water content are specified for each level, but the cloud overlap is not specified. Each RTM can handle the cloud overlap with different assumptions. (c) The ECMWF description of the cloud in 91 levels is itself subject to random and systematic errors. (d) The liquid water and ice cloud particle size distributions are not directly specified. For a sufficiently large data set, factor (a) should have zero bias but will cause a large stddev. Factors (b), (c), and (d) may create a bias as well as a large stddev.
2. Characterization of the radiometric effect of clouds using histograms of (stemp-bt). Here stemp is the surface temperature from ECMWF and bt is the AIRS observed or RTM-calculated brightness temperature in an atmospheric window channel. In the absence of a solar reflected component, (stemp-bt) increases from near zero under clear conditions to 100 K with increasing cloudiness. Under ideal conditions of a perfect matchup between AIRS and ECMWF, perfect clouds and thermodynamic profiles in the ECWMF model, and a perfect RTM, the two histograms will be identical. We evaluate the closeness of the match between observations and calculations by calculating the histogram correlation. Small residual biases that result from compensatory large positive and negative differences between AIRS and the RTM calculations under different conditions of cloudiness (or cloud types) are revealed as distortions of the histograms, resulting in a lowered correlation with the observations. This approach is not sensitive to random errors in the ECMWF cloud forecasts (e.g., the miss-location of clouds) but remains vulnerable to systematic errors; nevertheless, known systematic errors in ECMWF cloud forecasts are globally infrequent and limited to specific meteorological conditions (Kazumori et al., 2016). Infrequent ECMWF cloud errors are not likely to impact the histogram correlation because of the wide variety of cloud conditions in our data set.
3. The pairwise comparison of results from different RTMs. This approach has the advantage that it sidesteps matchup uncertainties with ECMWF. All RTMs use the same cloud model description. The comparison reveals the radiometric effect of differences between RTMs in cloud microphysics assumptions, cloud overlap assumptions, and scattering algorithms.

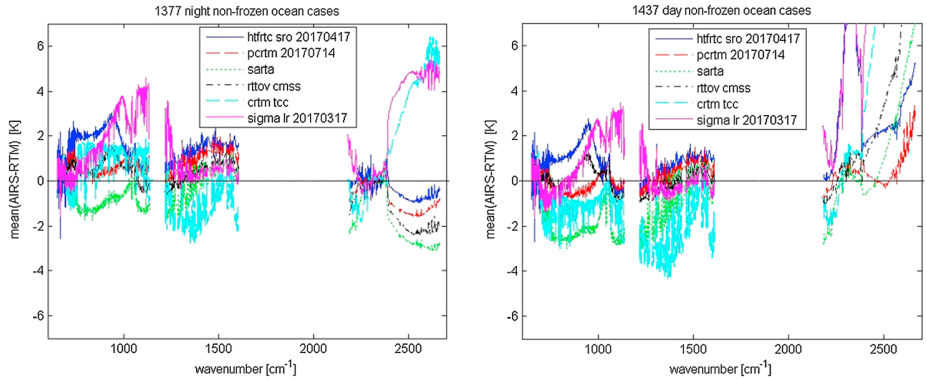

Figure 1. (a, b) Mean difference between Atmospheric Infrared Sounder (AIRS) and six Radiative Transfer Model (RTM) implementations for nonfrozen ocean cases.

3. Results

Figure 1 illustrates typical spectral patterns in the mean of the pairwise difference between AIRS spectra and the spectra calculated using six representative RTMs for 1,377 night and 1,437 day nonfrozen ocean cases, respectively. For wavenumbers lower than 1,700 cm^{-1} there is a relatively day/night independent, spectrally correlated pattern in the mean of the difference between AIRS and different RTMs. For wavenumbers above 2,200 cm^{-1} the pattern for the different RTMs is inconsistent even for the nighttime data. This inconsistency is even larger for the daytime data due to the differences in the way the RTMs deal with scattering and solar-reflected radiation. For the detailed evaluation of the RTMs we focus on the two representative atmospheric window channels at 900 and 2,616 cm^{-1}.

Figure 2 illustrates the comparison between AIRS and three RTMs at 900 cm^{-1} for the same two cases as Figure 1 using histograms of (stemp-bt900). The peak of the histogram in all cases is near +10 K, that is, relatively little cloudiness or low clouds. The coldest cloud tops are 100 K colder than stemp. The black trace is derived from the AIRS observation. HT_CRO and HT_SRO results are nearly identical, even though HT_CRO uses Chou scaling, while HT_SRO uses a full scattering calculation (both RTMs use the RO assumption). SARTA traced the AIRS histogram somewhat better than either HT variant for nighttime cases with (stemp-bt900) between 40 and 70 K, with SARTA finding many more cases than AIRS, while the HT RTMs had less cases. SARTA uses Chou scaling and the RO assumption similar to HT_CRO. However, SARTA takes multileveled clouds and converts them into two single layer clouds, one for ice clouds and one for water clouds.

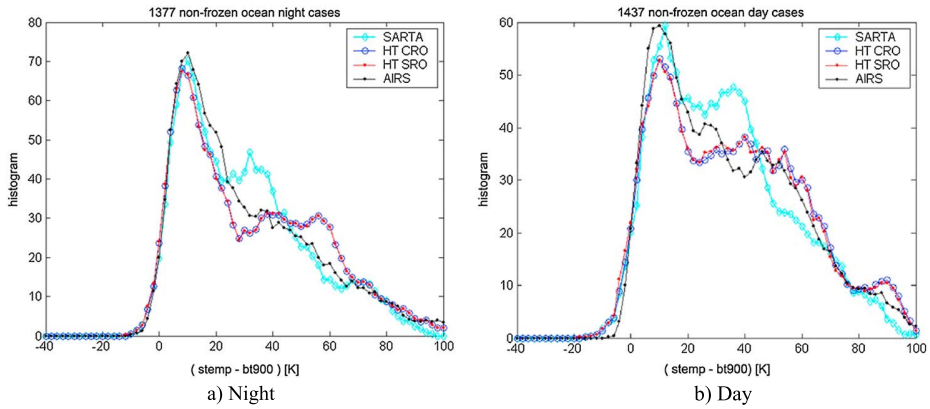

Figure 2. (a, b) Histograms for (stemp-bt900) observed by Atmospheric Infrared Sounder (AIRS) and calculated by three representative Radiative Transfer Models.

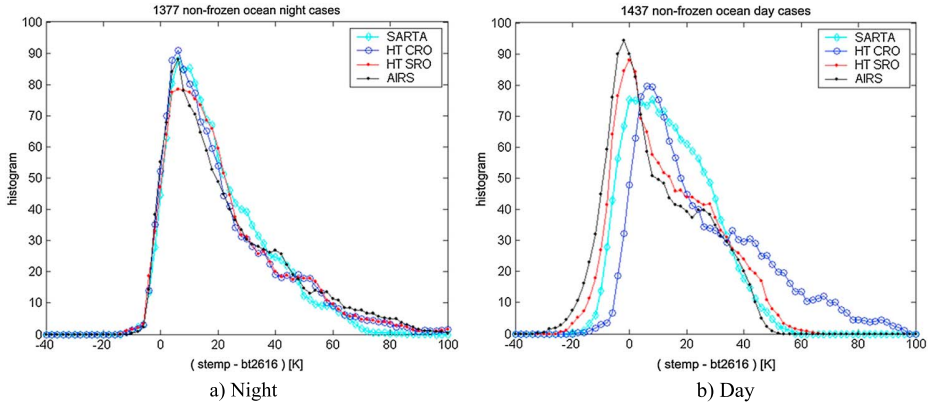

Figure 3. (a, b) Histograms for stemp-bt2616 observed by Atmospheric Infrared Sounder (AIRS) and calculated by three representative Radiative Transfer Models.

For daytime cases (Figure 2b), both SARTA and HT RTMs deviated from the AIRS trace for (stemp-bt900) cases between 15 and 70 K. Similar to the nighttime case, SARTA had more cases than AIRS in this range, while both versions of HT had less cases than AIRS between 15 and 30 K.

Figure 3 illustrates the histogram comparison using the same three RTMs and the same day and night non-frozen ocean cases as Figure 2 but at 2,616 cm^{-1}. In this figure the agreement between the RTMs and AIRS at night is much better than during the day. In fact, the histograms from SARTA and both HT RTMs are more closely matched to the AIRS histogram for cases between 15 and 70 K than the histograms at 900 cm^{-1} (Figure 2a). During the day the full scattering calculations used by HT_SRO result in histograms without the long tail for high clouds (stemp-bt2616 $>$ 60 K) seen in the HT_CRO histogram.

3.1. Numerical Summary of Histogram Correlations, Bias, and Standard Deviations

Table 2 summarizes the histogram correlations and the bias relative to AIRS for the day and night nonfrozen ocean cases at 900 cm^{-1}. The results shown are separated into six groups, with each group representing the

Table 2
Histogram Correlation and Bias for Day and Night Nonfrozen Ocean Cases at 900 cm^{-1}

AIRS-bt900	Day correlation	Day bias ± stddev (K) 1,437 cases	Night correlation	Night bias ± stddev (K) 1,377 cases	Day-night bias (K)
SARTA_TwoSlab(C)	0.9502	−2.33 ± 22.1	0.9707	−0.96 ± 19.5	−1.3
SARTA_TwoSlab(P)	0.9621	+2.23 ± 22.9	0.9710	+2.80 ± 20.4	−0.6
PCRTM_ERO	0.9629	+0.53 ± 21.5	0.9792	+1.37 ± 19.5	−0.8
PCRTM_MRO	0.9591	−0.21 ± 21.1	0.9796	−0.36 ± 19.1	−0.5
PCRTM_ERO2	0.9680	+0.96 ± 22.8	0.9785	+1.37 ± 21.1	−0.5
PCRTM_MRO4	0.9715	−0.53 ± 22.36	0.9625	+0.38 ± 19.85	−0.8
HT_CMO	0.9773	+1.09 ± 22.58	0.9591	+1.12 ± 20.36	−0.0
HT_CRO	0.9695	+2.18 ± 22.26	0.9638	+2.53 ± 20.04	−0.3
HT_CMRO	0.9774	+1.15 ± 22.56	0.9613	+1.26 ± 20.29	−0.1
HT_SMRO	0.9764	+0.60 ± 22.54	0.9591	+1.12 ± 20.36	−0.5
HT_SRO	0.9692	+1.69 ± 22.22	0.9629	+2.47 ± 20.07	−0.7
HT_SMRO	0.9765	+0.67 ± 22.52	0.9590	+1.18 ± 20.34	−0.5
RTTOV_MRO	0.9666	−4.22 ± 21.42	0.9748	−3.65 ± 19.5	−0.8
RTTOV_CMSS	0.9107	+0.69 ± 21.62	0.9105	+1.04 ± 20.0	−0.4
σ-IASI	0.9261	+0.75 ± 20.9	0.9437	+2.02 ± 19.2	−1.3
CRTM_tcc	0.8816	−0.98 ± 21.1	0.8915	+1.46 ± 19.97	−0.5
CRTM_mro	0.9552	−0.72 ± 23.9	0.9819	−0.10 ± 20.8	−0.6
CRTM_2col	0.9553	+0.12 ± 23.9	0.9817	+0.71 ± 21.3	−0.6
Clear column RTM (SARTA)	0.4168	−29.57 ± 22.8	0.4631	−25.78 ± 22.1	+3.8
Corr $>$0.9		17 of 18		17 of 18	
mean bias		+0.3		+0.8	
mean stddev		22		20	

Table 3
Bias and Standard Deviation of bt900 Calculated for 1,437 Day Nonfrozen Ocean Cases Relative to CRTM_mro, HT_SMRO, PCRTM_MRO4, and RTTOV_MRO

bt900 (RTM-reference)	Reference CRTM_mro bias ± stddev (K)	Reference HT_SMRO bias ± stddev (K)	Reference PCRTM_MRO4 bias ± stddev (K)	Reference RTTOV_MRO bias ± stddev (K)
SARTA TwoSlab(C) pnewM1 pnewM1	+1.69 ± 12.10	2.99 ± 11.79	+1.79 ± 10.52	−1.90 ± 11.63
SARTA TwoSlab(P) pnew999	−2.72 ± 11.32	−1.58 ± 10.69	−2.75 ± 9.76	−6.47 ± 10.79
PCRTM_ERO	−1.28 ± 9.90	+0.12 ± 6.83	−1.00 ± 6.39	−4.78 ± 6.59
PCRTM_MRO	−0.32 ± 13.89	1.22 ± 9.60	−0.06 ± 9.80	−3.65 ± 9.47
PCRTM_ERO2	−1.28 ± 12.58	−0.06 ± 9.69	−1.27 ± 9.46	−4.94 ± 9.64
PCRTM_MRO4	−0.13 ± 11.44	+1.26 ± 7.57	0.00 ± 0.00	+3.59 ± 7.51
HT_CMO	−1.65 ± 12.54	−0.43 ± 0.39	−1.68 ± 7.69	−5.31 ± 5.72
HT_CRO	−2.75 ± 12.19	−1.40 ± 1.79	−2.74 ± 7.44	−6.41 ± 5.87
HT_CMRO	−1.72 ± 12.55	−0.48 ± 0.35	−1.75 ± 7.69	−5.38 ± 5.73
HT_SMO	−1.17 ± 12.41	+0.04 ± 0.17	−1.20 ± 7.58	−4.83 ± 5.57
HT_SRO	−2.25 ± 12.08	−0.91 ± 1.82	−2.25 ± 7.35	−5.91 ± 5.74
HT_SMRO	−1.24 ± 12.42	0.00 ± 0.00	−1.26 ± 7.57	−4.90 ± 5.57
RTTOV_MRO	+3.65 ± 12.70	+4.90 ± 5.57	+3.59 ± 7.51	0.00 ± 0.00
RTTOV_CMSS	−1.34 ± 10.35	−0.02 ± 5.62	−1.23 ± 6.93	−4.92 ± 6.45
σ-IASI-As	−1.49 ± 12.85	−0.10 ± 6.85	−1.37 ± 7.99	−5.00 ± 4.34
CRTM_tcc	+0.20 ± 14.02	+1.64 ± 14.07	+0.43 ± 11.86	−3.26 ± 10.57
CRTM_mro	0.00 ± 0.00	+1.24 ± 12.42	+0.13 ± 11.44	−3.65 ± 12.70
CRTM_2col	−0.60 ± 3.43	+0.47 ± 12.22	+0.65 ± 11.22	−4.29 ± 12.75
Five-group bias	−0.2	+1.5	+0.3	−3.4
Five-group stddev	12.3	7.6	8.7	6.5

six RTM developers. The histogram correlations with AIRS exceeded 0.95 for five of the six groups for day and night cases. The histogram correlations were slightly higher for the night cases than for the day cases. This observation may be related to a day/night dependence of the cloud structure or microphysics properties. A more in-depth study of his observation is beyond the scope of this paper. The row labeled "clear column RTM" used SARTA without clouds. The mean bias relative to AIRS for all RTMs was +0.3 K (range − 4.2 K to +2.2 K) for the day cases, and + 0.8 K (range − 3.6 K to +2.8 K) for the night cases. The number following the plus-minus symbol in Table 2 is the stddev of the differences, typically 22 K for the day and 20 K for the night cases. Using the typical stddev for nighttime, the probable error in the mean is about $22/\sqrt{1377} = 0.6$ K (assuming random sampling and uncorrelated errors). Bias differences of more than three times the probable error, 2 K, are significant.

When the RTM calculations are compared to one another, the effect of the collocation error is eliminated, since we are comparing calculations for the same cloud conditions. Results are shown in Table 3 for the 1,437 day nonfrozen ocean cases using four RTMs as references: CRTM_mro, HT_SMRO, PCRTM_MRO4, and RTTOV_MRO. For the "five-group" summary in the last row we used only the first entry from each group, excluding the RTM used as the reference. The bias between RTMs was −0.2, +1.5, +0.3, and − 3.4 K, and the stddevs were 12.3, 7.6, 8.7, and 6.5 K, respectively, for the four reference RTMs.

In order to explore the extent to which a small bias on a global scale may be the result of compensating biases, we divided the data into latitude zones. Results are summarized in Table 4 for the tropical zone ($|\text{lat}| < 30°$) with 3,644 cases; 2,662 cases for the extratropical zone ($|\text{lat}| > 30°$), limited to nonfrozen surface cases using stemp >275 K; and 1,070 cases from the polar zone ($|\text{lat}| > 60°$). Based on the last column in Table 4, which shows the difference between the mean tropical and the mean midlatitude bias, some RTMs show a latitude dependence in the bias of several degree kelvin.

Table 5 summarizes the results at 2,616 cm^{-1} for day and night nonfrozen ocean. The bottom row summarizes the results in terms of a mean bias and stddev, excluding RTMs with less than 0.9 histogram correlation with AIRS. At night 16 of the 18 RTMs had a mean bias relative to AIRS of −1.8 K with 20 K stddev and five of the six RTM teams produced results with histogram correlation with AIRS better than 0.95. During the day only two of the six RTM teams produced results with histogram correlations with AIRS better than 0.95. For these cases the mean bias was +2.4 K, and the mean stddev was 16 K.

Table 4
Bias and Standard Deviation Between AIRS bt900 and Different RTMs Separated Into the Tropical, Midlatitude, and Polar Zones (as Defined in the Text)

bt900 (AIRS observed—calculated; K)	Tropical zone 3,644 cases bias ± stddev (K)	Mid latitude 2,662 cases bias ± stddev (K)	Polar 1,070 cases bias ± stddev (K)	Tropical—midlatitude bias (K)
SARTA TwoSlab(C)	+0.41 ± 22.59	−4.66 ± 14.84	+3.19 ± 10.15	+5.0
SARTA TwoSlab(P)	+4.15 ± 23.51	−2.57 ± 15.02	+0.79 ± 10.06	+6.7
PCRTM_ERO	+2.63 ± 22.48	−2.86 ± 13.86	−0.53 ± 9.60	+5.5
PCRTM_MRO	+0.35 ± 22.01	−3.42 ± 13.93	−0.56 ± 9.63	+3.8
PCRTM_ERO2	+3.21 ± 24.33	−2.65 ± 14.84	−0.41 ± 9.79	+5.9
PCRTM_MRO4	+0.94 ± 23.19	−3.12 ± 14.36	−0.32 ± 9.81	+4.1
HT_CMO	+1.12 ± 23.41	−0.84 ± 14.99	+1.39 ± 9.65	+2.0
HT_CRO	+2.97 ± 23.08	−0.17 ± 14.68	+1.48 ± 9.58	+3.1
HT_CMRO	+1.17 ± 23.40	−0.78 ± 14.97	+1.40 ± 9.65	+2.0
HT_SMO	+0.92 ± 23.39	−1.08 ± 14.98	+1.15 ± 9.72	2.0
HT_SRO	+2.76 ± 23.06	−0.42 ± 14.68	+1.24 ± 9.65	3.2
HT_SMRO	+0.97 ± 23.38	−1.03 ± 14.96	+1.16 ± 9.72	2.0
RTTOV_MRO	−4.33 ± 22.32	−4.50 ± 14.49	−0.24 ± 9.77	0.2
RTTOV_CMSS	+2.71 ± 22.24	−2.35 ± 14.05	−0.06 ± 10.13	5.1
σ-IASI-As	+1.23 ± 22.35	+0.19 ± 14.45	+2.21 ± 9.34	1.0
CRTM_tcc	+2.60 ± 22.39	−2.76 ± 15.14	+0.73 ± 9.98	5.4
CRTM_mro	+1.95 ± 24.62	−5.60 ± 14.67	−1.68 ± 10.50	7.6
CRTM_2col	+2.94 ± 24.57	−5.24 ± 14.73	−1.69 ± 10.60	8.2

4. Discussion of the Results

Under clear conditions at night, SARTA, PCRTM, and RTTOV have previously been shown to agree with each other and with AIRS within 0.05 K bias and 0.1 K stddev (Saunders et al., 2007). The current versions of SARTA, PCRTM, and RTTOV, including CRTM, σ-IASI, and HT-FRTC under clear conditions, all have shown the same level of agreement. Under cloudy conditions the agreement is not as close and the magnitudes of the differences are wavenumber dependent.

Table 5
Histogram Correlation, Bias, and Standard Deviation at 2,616 cm^{-1} for Day and Night Nonfrozen Ocean

bt2616 (AIRS observed—calculated)	Day correlation	Day bias ± stddev (K) 1,437 cases	Night correlation	Night bias ± stddev (K) 1,377 cases
SARTA TwoSlab(C)	0.8744	+5.00 ± 14.79	0.9738	−3.06 ± 18.40
SARTA TwoSlab(P)	0.8779	+7.05 ± 15.57	0.9746	−0.37 ± 19.45
PCRTM_ERO	0.9855	+1.55 ± 15.90	0.9371	−0.29 ± 19.23
PCRTM_MRO	0.9846	+0.73 ± 15.84	0.9334	−1.88 ± 18.84
PCRTM_ERO2	0.9804	+2.52 ± 16.79	0.9563	+0.58 ± 20.56
PCRTM_MRO4	0.9766	+0.91 ± 16.22	0.9446	−1.25 ± 19.47
HT_CMO	0.6669	+15.04 ± 20.11	0.9075	−2.53 ± 20.49
HT_CRO	0.6492	+15.97 ± 19.76	0.9809	−1.43 ± 20.12
HT_CMRO	0.6653	+15.13 ± 20.10	0.9074	−2.46 ± 20.47
HT_SMO	0.9215	+3.69 ± 15.86	0.9791	−2.11 ± 20.59
HT_SRO	0.9628	+3.87 ± 15.83	0.9736	−0.83 ± 20.14
HT_SMRO	0.9245	+3.65 ± 15.88	0.9799	−2.02 ± 20.56
RTTOV_MRO	0.8948	+4.81 ± 15.86	0.9574	−6.48 ± 19.85
RTTOV_CMSS	0.8803	+8.07 ± 15.26	0.9605	−2.38 ± 19.02
σ-IASI_as	0.4809	+20.94 ± 18.94 ([a])	0.8739	+5.37 ± 19.50
CRTM_tcc	0.3991	+20.55 ± 17.60	0.6623	+6.38 ± 20.52
CRTM_mro	0.6680	+13.90 ± 18.74	0.9604	−2.16 ± 19.58
CRTM_2col	0.6410	+15.33 ± 18.59	0.9486	−1.04 ± 19.63
Corr >0.9		7 of 18		16 of 18
Summary mean (stdev)		+2.4 (16)		−1.8 (20)

[a]Solar reflected component not implemented.

4.1. The Longwave Region

We define the longwave region as portions of the spectrum with wavenumbers lower than 1,700 cm^{-1}. In this region, the differences between AIRS and RTMs are relatively day/night independent (Figure 1) and range between ±4 K. The correlation between the histogram calculated from the AIRS observations and the histograms calculated for several of the RTMs at 900 cm^{-1} (Table 2 and Figure 2) exceeds 0.97. The bias averaged over 17 of 18 RTMs at 900 cm^{-1} for the day and night nonfrozen oceans was +0.3 and + 0.8 K, respectively (Table 2). However, Table 4 shows that the low bias for the nonfrozen oceans for some RTMs was due to the compensating effects of a bias for the tropical zone balanced by a bias of the opposite signs in the midlatitude and polar zones. A high correlation between the observed and calculated histograms and a zone-independent low bias are a measure of the skill of the RTM and the statistical fidelity of the ECMWF specification of the atmospheric state, including clouds. The bias between the clear column RTM calculations and AIRS observations is more than −25 K (Table 2). The typically 20 K stddev of the difference between AIRS and the RTMs is essentially the same with and without clouds. This indicates that the high stddev of (AIRS-RTM) is dominated by the mismatch between the clouds observed by AIRS and the clouds specified by the ECMWF model.

RTTOV_MRO is biased about 4-K high relative to AIRS (Table 2). As shown in Table 3, where we compare the RTMs to reference RTMs, all RTMs are biased low relative to RTTOV_MRO. RTTOV_MRO used the OPAC cumulus cloud-type option. RTTOV_Cloud fraction Maximum Single Stream (CMSS) used the RO overlap scheme and was optimized for middle to upper tropospheric sounding channels, not for window channels. RTTOV_CMSS shows much less bias relative to AIRS than RTTOV_MRO in the global analysis (Table 2) but shows a large bias of opposite signs for the zonal bias (Table 4). These observations suggest that a combination of cloud types (derived from the cloud, temperature, or water vapor profiles) may produce a closer match to observations than choosing one cloud type. Future work will examine the impact of cloud-type assumptions on the RTMs' match to observations.

The typical stddev of the RTMs relative to AIRS, 20 K, decreases to a range of 6 to 12 K when the RTMs are compared to one another (Table 3), excluding siblings within the same RTM group. Since the RTMs used the same cloud input profile, the decrease from 20 to 12 K (or less) is dominated by the elimination of the collocation error. The stddevs of the differences are in this case related to differences in the way the ECMWF cloud description is converted to cloud microphysical parameters and then to the radiances calculated by the RTMs. When this conversion is identical, as in the case of CRTM_mro and CRTM_2col, the stddev of the difference was 3 K and was due to the difference in the overlap assumption alone.

4.2. The Shortwave Region

We define the shortwave region as portions of the spectrum with wavenumbers greater than 2,000 cm^{-1}. By inspection of Figure 1 we already noted that the spectral patterns for the different RTMs are less consistent in the shortwave region than in the longwave region, even for the night data. However, at night three of the six RTMs (Figure 1) have less than 2-K bias relative to AIRS and five of the six RTMs have histogram correlations better than 0.95 (Table 5). At night the histogram correlations at 2,616 cm^{-1} are not inconsistent with those at 900 cm^{-1}. During the day the results from only two of the six RTM teams reached histogram correlations better than 0.95, and the bias values relative to AIRS were much larger than those at night and the result at 900 cm^{-1}. If cloud scattering parameters at 2,616 cm^{-1} were too weak, it would have impacted the night calculations as well, but the night calculations (for three of the RTMs) agree reasonably well with AIRS. The degradation of the results during the day is probably related to the use of Chou scaling, which was not designed for shortwave calculations (Chou et al., 1999). This is clearly shown in the comparison of HT_CRO (with the Chou approximation) and HT_SRO (using full scattering) in Figure 3. The tail of the histogram of HT_CRO at (stemp-bt2616) extends all the way to 100 K for the coldest clouds, while the tail of the histogram of HT_SRO stops at 60 K. The PCRTM_MRO also uses full scattering. SARTA and RTTOV used Chou scaling, while CRTM used the advanced doubling adding method (Liu & Weng, 2006). Full scattering calculations usually are assumed to be costly in terms of computation time, but this need not be the case. For example, PCRTM performs full scattering calculations with multiple streams and multiple scatterings performed offline to generate lookup tables. However, even by employing full scattering, the HT_SRO histogram at 2,616 cm^{-1} (Figure 3b) showed fewer clear or low cloud cases (stemp-bt2616 < 0 K) calculated by the RTMs than were observed by AIRS. This suggests that the reflectance from the Earth's surface has a stronger angular dependence than Lambertian scattering.

In the discussion of the histograms calculated from the RTMs at 900 cm^{-1} we noted the differences between AIRS observations and the RTMs for 40 < (stemp-bt900) < 70 K cases (Figure 2). This effect is much less pronounced at 2,616 cm^{-1}, particularly at night (Figure 3a). We believe that in this region a significant portion of the scenes contains multiple cloud types. This may amplify any systematic bias that exists in the assumptions about cloud microphysics and their assumed spectral dependence. The interpretation of these differences in terms of cloud types is outside of the scope of this paper.

4.3. ECMWF Cloud Bias and RTM Cloud Bias

The bias in the RTMs relative to AIRS has two components:

1. The ECMWF cloud description is vulnerable to systematic errors.
2. The methodologies used by the RTMs to convert the cloud description into radiances are likely to contain assumptions which lead to systematic biases.

In order to quantify this bias, we assume that the results from the six RTM teams represent plausible and sufficiently independent radiometric realizations of the cloud effects. At 900 cm^{-1} the RTMs show a bias in the range from +1.5 to −3.4 K relative to one another (Table 3). Relative to AIRS the RTMs have a + 0.3 K (+0.8 K) mean bias for the day (night) nonfrozen oceans (Table 2). These results indicate that the radiative effect of a bias in the ECMWF clouds could be of the order of 1 K.

The difference between the mean tropical and mean midlatitude bias (Table 4, last column) for each RTM could reveal a cloud-type dependence in the ECMWF clouds or in the RTM cloud algorithms. Several of the six RTM groups have a zonal bias lower than 2 K. The low zonal bias seen in the results from these RTMs is consistent with the radiative effect of a zonal ECMWF cloud bias of less than 2 K. The observation that several of the RTMs achieve a low zonal bias and a high histogram correlation relative to the observations indicates that the low global bias is not the result of compensatory much larger cloud-type-dependent biases.

We interpret the zonal bias seen in the three other RTM groups, which ranges from 4 to 8 K, as a cloud-type dependence in those RTMs. The RTTOV_CMSS has a 5-K zonal bias, compared to 0.2 K for RTTOV_MRO (Table 4). On the other hand, RTTOV_CMSS shows much less bias relative to AIRS than RTTOV_MRO (Table 2). Both use a single (but different) cloud type. A combination of cloud types (derived from the cloud, temperature, or water vapor profiles) may produce a closer match to observations than choosing one cloud type. A future analysis of cloud-type effects on the RTMs could include data acquired in cloudy conditions from other instruments.

5. Summary

The objective of our paper was to evaluate the degree to which the radiative effects of clouds in NWC models agree with collocated hyperspectral observations. We selected AIRS observations and AIRS RTMs for our analysis. We selected data provided by the ECMWF (ECMWF, 2009) as representative for the definition of the atmospheric states with clouds. We used the bias and histogram correlations relative to AIRS observations for the 2,616- and 900-cm^{-1} atmospheric window channels as performance metrics. For some RTMs the histogram calculated at 900 cm^{-1} has a correlation of better than 0.95 with the histogram derived from the AIRS observations, with a bias relative to AIRS of less than 2 K for nonfrozen ocean day and night data. However, several of the six RTM groups showed between 0- and 2-K bias between the tropical zone and the midlatitude zone at 900 cm^{-1}, while others had a bias between 4 and 8 K. This observation and the high histogram correlation with AIRS show that the ECMWF cloud prescription may have a bias, but the radiative effect of the bias at 900 cm^{-1} is most likely less than 2 K, relatively insignificant compared to the bias introduced by some RTMs. The results for the 2,616-cm^{-1} window channel are consistent with day and night results at 900 cm^{-1} only when full scattering calculations were used. For these cases the correlation between the histogram deduced from the AIRS observations and the histograms calculated by the RTMs exceeds 0.95 and the bias at night is less than 2 K relative to AIRS. During the day the AIRS observations at 2616 cm^{-1} are 2 to 4 K higher than the RTM calculations with full scattering. This suggests that the reflectance of the surface has a steeper angular dependence than Lambertian.

Our study created a testable data set, baseline results, and testing methodology to support continuing RTM development, with the goal of increasing the utilization of hyperspectral observations in the forecast. As

illustrated in Figure 1, there is no need (with the current state of the art RTMs) to make these calculations for all channels, since just one or two surface channels will provide valuable insights. However, the selection of a shortwave channel requires an RTM with full scattering. The choice of the RTM and how many channels to use comes down to computer resource requirements.

Appendix A: Appendixes

A1. Model Profiles (Contributed by Alan Geer)

Model profiles were taken from the ECMWF operational global weather forecasting system on 1 March 2009. The best available estimate of the atmospheric state was taken every 3 hr, being a mixture of analysis and very short range forecast. At the time, cycle 35r1 of the ECMWF system was operational and full documentation is available from ECMWF (2009). This describes cycle 33r1, but there were no major changes going to 35r1. The model fields used 91 levels. An additional level at 0.005 hPa was added using the U.S. Standard Atmosphere to avoid ambiguity when different RTMs were using the model fields. The forecast model uses T799 (roughly 25 km) spatial binning. Each AIRS position and observing time from 1 March 2009 was associated with the nearest forecast time and interpolated across the 35r1 grid points in time and space.

Analyses and forecasts are based on clouds and precipitation models using three main schemes: convection by a mass flux scheme (Bechtold et al., 2004; Tiedtke, 1989), large-scale cloud and precipitation, including the possibility of ice supersaturation (Tiedtke, 1993; Tompkins et al., 2007), and an eddy-mass flux turbulent diffusion scheme for the boundary layer, representing stratocumulus (Köhler et al., 2011). Together these contribute to producing the vertical profile of cloud water, cloud ice, and cloud fraction at every grid point. Where necessary to assume an overlap formulation for clouds in the radiation scheme, a generalized formulation was assumed, increasing from MRO to RO with increasing cloud layer separation (Barker, 2008).

The ECMWF analysis is a combination of short-range forecast and observational information, including satellite radiances, satellite-retrieved atmospheric motion vectors, near-surface wind vectors from scatterometers, Global Navigation Satellite System radio-occultation measurements, and conventional data sources including ground stations, ships, radiosondes, and aircraft. Of particular, relevance to the current study is that AIRS and IASI radiances are assimilated but in clear-sky areas only (Collard & McNally, 2009). As a consequence, the cloud description in the ECMWF model does not contain AIRS cloud information. Further, clouds and precipitation are constrained in the analysis by the assimilation of cloud and precipitation-affected microwave imager radiances (Bauer et al., 2006).

A2. Selection of the Test Data Set (Contributed by Evan Manning)

Each day AIRS produces 3 million spectra, each with 2,378 spectral channels. The locations of the spectra are biased toward the polar areas due to the high inclination of the Earth Observing System Aqua orbit. In order to test the relative performance of cloudy RTAs, we created a data set with emphasis on cloud variability. This data set was created using stratified sampling: the clouds are roughly characterized by the difference between the surface temperature (stemp), provided by ECMWF, and the brightness temperatures measured in five sounding regions from AIRS, including the brightness temperatures at 1,231 cm^{-1} (bt1231). We traversed the spectra in time order and assigned to each spectrum a tag which combined the following elements:

1. Day versus night (the divide was solar zenith angle = 90; two bins).
2. Land/sea + latitude band. The 30° bins. Nonpolar bins were divided into land and sea. Sea was defined as any AIRS footprint containing less the 1% land (10 bins).
3. bt1231 in 10-K increments between 170 and 360 K (19 bins).
4. stemp-bt1231 in 10-K increments from −40 to +210 K (26 bins).
5. We defined five broad spectral bands at [650, 800], [800, 1200], [1200, 1700], [1700, 2400], and [2400, 2700] cm^{-1}. For each band we used the mean brightness temperature in the band minus bt1231, bt_band-bt1231, to define 20 bins in 10-K increments from −110 to +110 K (20 bins per band).

This allows for up to $2 \times 10 \times 19 \times 26 \times 20^5 = \sim 30$ billion bins, but most bins were empty. Each spectrum's tag was compared to the tags of the spectra previously collected. If the tag did not match any, then the new spectrum was added to the data set. This procedure created 7,377 uniquely tagged spectra. The latitude,

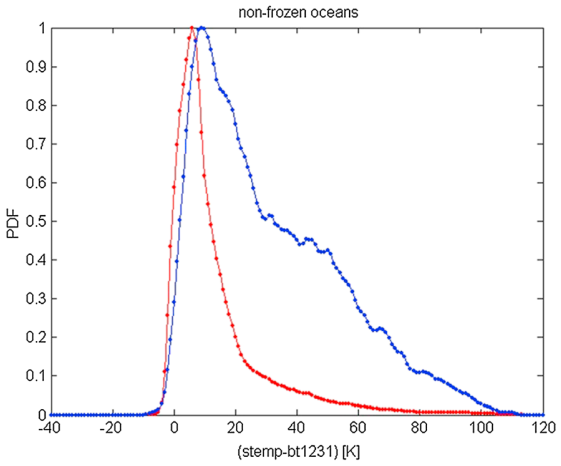

Figure A1. The red trace shows the distribution of the cloud effect (stemp-bt1231) for an area-representative random sample of the nonfrozen oceans. The blue trace is the distribution of the stratified sample.

longitude, solar zenith, and solar azimuth angles and the ECMWF definition of the state of the atmosphere associated with this set and the associated AIRS spectral radiances were posted on the anonymous FTP site at "ftp://thunder.jpl.nasa.gov/hha/Cloudy_RTA/atm.state". The rta7377readme.20160518.txt explains the details.

The distribution of the 7,377 test cases does not match the distribution of clouds in a global grid, but the set spans the natural variability of spectra, which is dominated by clouds. The emphasis on clouds is illustrated in Figure A1. The red trace in Figure A1 is the distribution of the cloud effect (stemp-bt1231) for a global area representative random sample of the nonfrozen oceans. A large fraction of the ocean is covered by relatively low or broken clouds. The peak of the random sampled distribution is at 5 K. Only 7% of the nonfrozen oceans are associated (stemp-bt1231) $>$ 50 K, (roughly corresponding to brightness temperatures colder than 250 K). The blue trace in Figure A1 is the distribution of the cloud effect in the test set. The peak of the distribution is at 8 K, and 30% of the test data are associated with (stemp-bt1231) $>$ 50 K.

A3. RTM Model Summaries

A3.1. Community RTM (Contributed by Moradi and Wilson)

The Community RTM, CRTM, (Liu et al., 2008), is a fast RTM developed by the Joint Center for Satellite Data Assimilation that is widely used in the United States (including at the National Aeronautics and Space Administration Global Modeling and Assimilation Office) to assimilate satellite radiances. The current version is 2.2.3. CRTM is capable of simulating microwave and infrared radiances using atmospheric profiles of pressure, temperature, humidity, and other species such as ozone. CRTM also includes capabilities to simulate satellite cloudy radiances. The ice cloud single scattering properties are based on Baum et al. (2011). All spectra were calculated with CRTM 2.2.3. However, within this version CRTM gives the user wide flexibility for the cloud overlap assumption and the cloud composition. Six cloud types can be defined at the same time: water, ice, rain, snow, graupel, and hail. The calculations presented in this paper used only water and ice clouds based on cloud liquid and ice water content profiles.

CRTM requires pressure values at levels, as well as layer averaged, and the layer averages of temperature, water vapor, and other absorbers as input to perform clear-sky calculations. The top pressure level is fixed at 0.005 hPa. For the calculation of cloudy radiances CRTM requires cloud liquid water content in gram per square meter and the effective radii of water and ice particles.

The same version of CRTM was used but with different assumptions. The results identified as CRTM_tcc uses equation (1) with the MO assumption and tcc, the total cloud fraction specified by ECMWF. The effective radius of the particles was calculated using equation (3) in Ou et al. (1995) for ice clouds and equation (2) in Bower et al. (1994) for water clouds. The CRTM_2col and the CRTM_mro calculations used the 2col and MRO assumption, respectively, with the identical cloud microphysics. The parameterization for ice particle effective radius used a fourth-order empirical polynomial given by Ou et al. (1995), same as CRTM_tcc. The effective water particle radius was logarithmically interpolated from 10 μm at the surface to 45 μm at the top of atmosphere, consistent with the ECMWF documentation. Following equation (1), CRTM_2col uses the maximum cloud fraction specified by each ECMWF cloud coverage profile to calculate CF. This value is close to but not exactly the same as tcc.

The CRTM results were received on 6 September 2016, revised 9 March 2017.

A3.2. Principal Component-Based RTM (Contributed by Xiuhong Chen, Xianglei Huang, Xu Liu, Qiguang Yang, and Wan Wu)

The PCRTM is a fast and accurate forward model for hyperspectral instruments with thousands of spectral channels. It uses principal components to compress spectral information and reduces computational time by performing radiative transfer calculations at just a few hundred monochromatic frequencies (Liu et al., 2006, 2016). The molecular absorption coefficients of gases are based on a lookup table calculated off-line using a line-by-line RTM based on HITRAN2008. Both ice and water clouds were parameterized into

transmittance and reflectance matrices for the isotropic thermal scattering. The ice cloud matrices were obtained using single scattering properties from Baum et al. (2011) and a 32-stream Discrete Ordinates Radiative Transfer (Stamnes et al., 1988). The water clouds were obtained the same way by using the refractive indices from Segelstein (1981). The anisotropic solar scattering is modeled according to Liu et al. (2016) and Yang et al. (2014). Transmittance and reflectance lookup tables were obtained under various conditions for parameters such as cloud optical depth, cloud effective size, wavelength, and solar and satellite zenith angles and azimuth angles (Yang et al., 2014). The non-Local Thermodynamic Equilibrium (LTE) effect was calculated according to the parameterization described by DeSouza-Machado et al. (2007).

When generating input parameters for the PCRTM from the ECMWF fields, ice cloud optical depths were calculated from ice water content as in Ebert and Curry (1992). Warm cloud optical depth based on cloud liquid water content follows Fouquart (1987). The effect of different cloud overlapping assumptions on the simulated radiance has been discussed in Chen et al. (2013). The PCRTM_MRO and PCRTM_ERO entries in Tables 2–4 represent the results obtained with a MRO assumption and an ERO assumption, respectively. The cloud fraction and cloud profiles are used to generate 50 subcolumns (Chen et al., 2013) for both overlapping assumptions. The PCRTM_ERO2 and PCRTM_MRO4 represent the simulation results using less subcolumns, namely, two subcolumns for the ERO and four subcolumns for the MRO, respectively.

The PCRTM model has been used to perform cloud and atmospheric temperature and water vapor vertical profile retrievals from hyperspectral instruments such as IASI, CrIS, and AIRS (Liu et al., 2009, 2006, 2017; Wu et al., 2017). Two validations of the PCRTM under cloudy conditions were given by Chen et al. (2013). One validation case used NOAA/GFDL data with the RO assumption, and the other one used ECMWF with MRO assumption. Validations showed satisfactory consistency between the calculated OLR and the counterparts from the GCM/analysis.

The PCRTM spectra were received 24 February 2017, revised with full scattering 14 July 2017.

A3.3. SARTA (Contributed by Sergio DeSouza-Machado and L. Strow)

SARTA RTM uses a four-column RO cloud overlap assumption. The clear column calculations use SARTA V6.0 (Strow et al., 2006). The absorption coefficients of gases are from line-by-line calculations based on HITRAN2008. The ECMWF clouds are converted into two thick slabs. Typically, this is an ice cloud between zi_top and zi_bottom and a water cloud between zw_top and zw_bottom. The Mie scattering parameters for water clouds use a modified gamma droplet size distribution of effective variance 0.1 (dimensionless) and effective radius (typically) of 20 μm. The cirrus cloud scattering parameters are based on Baum et al. (2011), and the ice effective particle size is estimated from a temperature-based parametrization by Ou et al. (1995, 2013), where the ECMWF temperature profile is used to associate the ice cloud slab top pressure with a cloud top temperature. The effective absorption due to each slab is then calculated using PCLSAM (Chou et al., 1999) scattering code and used in the SARTA TwoSlab RTM (DeSouza-Machado et al., 2018). Each pixel is then divided into four columns.

Case 1. A clear column from the surface to the Top Of the Atmosphere (TOA).
Case 2. A clear column between the surface and zw_bottom. Between zw_bottom and zw_top the precalculated water cloud absorption is added.
Case 3. A clear column between the surface and zi_bottom. Between zi_bottom and zi_top the precalculated ice cloud absorption is added.
Case 4. The transmittance calculated from case 2 up to the zi_bottom is continued with the transmittance from there to TOA using the transmittance calculated from case 3.

A cloud fraction for each case is then chosen such that all of the ice cloud and a random portion of the water cloud is seen from TOA, such that the ECMWF-specified tcc is satisfied. Details are summarized in Machado and Strow (2016) and in DeSouza-Machado et al. (2018). The difference between SARTA_TwoSlab(C) and SARTA_TwoSlab(P) is due to the difference in the way the boundaries of the thick slabs are calculated. The small differences between the results from the two SARTA versions show that the results are not very sensitive to these details.

The SARTA results were received 8 November 2016, revised to be consistent with DeSouza-Machado et al. (2018) 27 February 2017.

A3.4. Radiative Transfer for TOVS (Contributed by J. Vidot and M. Matricardi)

The fast RTM RTTOV (Saunders et al., 1999) is widely used by a number of NWCs to assimilate infrared radiance observations. In this study, we used RTTOV Version 12. The predictors of the fast atmospheric

transmittances were calculated with the line-by-line model LBLRTM 12.2 (Alvarado et al., 2013; Clough et al., 2005) that uses the AER3.2 spectroscopic database (mostly based on HITRAN 2008 but with many improvements regarding line mixing and absorption line parameters) and MTCKD 2.5.2 (Mlawer et al., 2012). The scattering by clouds is modeled using the Chou-scaling approximation (Chou et al., 1999). The liquid and ice cloud optical properties are parameterized following the work of Matricardi (2005) and Vidot et al. (2015), respectively. Within the RTTOV version the user has the option to select a limited number of cloud type and the cloud overlap assumptions. RTTOV_mro used the OPAC cumulus cloud type and the MRO assumption (Matricardi, 2005). Additionally, a much faster, experimental version of the cloud overlap method has been tested in RTTOV. This method is named CMSS. It simulates cloudy infrared radiances using equation (1) with CF set to the maximum cloud fraction in the layers above a certain pressure level (here fixed to 750 hPa). This method is optimized for middle- and upper-tropospheric sounding channels.

The RTTOV results were received 9 December 2016.

A3.5. Havemann-Taylor Fast Radiative Transfer Code (Contributed by Havemann)

For the AIRS radiance simulations presented in this paper, the HT-FRTC (Havemann, 2006) has been specifically trained for the infrared part of the electromagnetic spectrum. The HT-FRTC does only monochromatic radiative transfer calculations. The gaseous absorption of all the trace gases included in HITRAN 2008 is included in the form of lookup tables. During the code training phase monochromatic calculations are performed at a very high spectral resolution (10^{-3} cm^{-1}) for a diverse set of 1,000 atmospheric profiles and surface conditions. The training run included vertical profiles of liquid and ice cloud. The results of the radiance calculations for the training profiles at the very high spectral resolution were then used to calculate the principal components which are the eigenvectors of the covariance matrix containing the radiance spectra. The HT-FRTC works slightly different to other codes like PCRTM in that the principal components are not derived for the spectra of any particular instrument but rather at the full very high spectral resolution. This means that the spectra for any number of instruments can be calculated in a single fast code run. It requires just an offline convolution of the highly resolved principal components with the instrument response functions. For the simulations in this paper only the first 100 principal components which contain most of the variance were used. The weights of the principal components are predicted from a small number of radiance calculations at about 100 monochromatic frequencies. The optimal set of frequencies for prediction is selected by a k-means clustering algorithm which operates on all frequencies (2.5 million). A linear regression is carried out on the results on the training profiles (the dependent profiles). This regression then allows the prediction of the principal component weights for any independent profiles by calculating the radiances only at the 100 selected monochromatic frequencies.

For the simulations presented in this paper an effective radius of 10 μm was used throughout for cloud liquid droplets. The cirrus optical properties that were used in the simulations are due to Baran (Baran et al., 2014). Baran has developed an ensemble model of cirrus particles of different shapes and sizes. The optical properties are parametrized solely in terms of cirrus cloud temperature and cirrus cloud ice water content. The same parametrization is applied to all types of cirrus. The HT-FRTC allows two different treatments of scattering. Scattering can be treated approximately as a modification to the extinction by using the Chou scaling approximation (Chou et al., 1999) or the scattering phase function that can be fully accounted for (Martinet et al., 2013). In this case a monochromatic version of the Edwards-Slingo spherical harmonics radiation code is called which has been incorporated into the HT-FRTC (Edwards & Slingo, 1996; Thelen & Edwards, 2013). Calculations with Chou scaling are indicated by "C and full scattering calculations by "S".

The HT-FRTC has been run for three different cloud overlap assumptions (MRO, MO, and RO). In all cases five cloud columns were used. The columns were constructed from the horizontal cloud fraction provided for each atmospheric level, which prescribed how many of the cloud columns would be clear and how many fully overcast at each level. The different overlap assumptions then determine how the cloudy layers are stacked in the vertical. In the case of MO, all the cloudy layers are concentrated in the same columns as much as possible, in the case of RO the cloudy layers are distributed randomly across the columns, and in the case of MRO the cloudy columns are maximally overlapped in adjacent vertical layers which are both cloudy but randomly distributed if there happens to be a cloud-free layer in between. One HT-FRTC fast code run is done per cloud column. In the tables the type of scattering treatment and the kind of overlap is indicated. As an example, SMRO indicates full scattering calculations applied to the five individual cloud columns that were generated using the MRO assumption.

The HTFRTC results were received with Chou scaling 19 January 2017, revised with full scattering 17 April 2017.

A3.6. The σ-IASI-as (Contributed by Liuzzi, Masiello, and Serio)

The σ-IASI-as RTM is an advanced version of the σ-IASI model (Amato et al., 2002) with respect to cloud and aerosol treatment (Liuzzi et al., 2017). The model computes the Earth/atmosphere-emitted radiance in the spectral range 100–3,000 cm^{-1}. In its current version, the model can generate radiances in both upwelling and downwelling modes. Although initially developed for IASI, σ-IASI-as is presently a generic RTM, which is well suited for nadir viewing satellite, airplane (Grieco et al., 2007), and ground-based (Bhawar et al., 2008) infrared sensors with a sampling rate in the range 0.1–2 cm^{-1}.

The σ-IASI-as RTM calculation of gas optical depths is based on a pseudomonochromatic scheme, in which transmittances are calculated on an equally spaced wavenumber grid by means of a lookup table. For each atmospheric layer, atmospheric species, and wavenumbers, optical depths are precomputed and stored. Then, they are rescaled with air pressure and temperature. The dependence on temperature is parameterized by a second-order polynomial. This allows optical depths to be generated at any wavenumber using the version 12.2 of LBLRTM (Clough et al., 2005), equipped with the spectral library AER v_3.2 (essentially based on HITRAN 2012 spectral database—with the continuum model MT-CKD v_2.5.2; Mlawer et al., 2012).

The σ-IASI-as RTM simulates the impact of the presence of clouds and aerosols with a physically based method that comput es their extinction as a function of the effective ice or liquid water particle or droplet radii and concentrations (Liuzzi et al., 2017). The model exploits an ab-initio approach embodying Mie routines which are called iteratively within the calculation of single-layer transmittances. The results of Mie calculations are manipulated according to the scheme described in Chou et al. (1999) for calculating effective aerosol and cloud optical depths taking into account the multiple scattering effects through the so-called scaling approximation. With the scaling approximation, radiative transfer equations for a cloudy/aerosols atmosphere are identical to those for a clear atmosphere, and the difficulties in applying a multiple-scattering algorithm to a partly cloudy atmosphere (assuming homogeneous clouds) are avoided. The RTM used for the calculation of the σ-IASI spectra was identified as version 2017.as.lr. The calculations used the MO assumption and tcc specified by ECMWF.

The σ-IASI results were received on 29 November 2016, revised 17 March 2017.

Acknowledgments

The work described in this paper was carried out at the Jet Propulsion Laboratory, California Institute of Technology, under a contract with the National Aeronautics and Space Administration. Work at JPL and UMBC was funded by NASA ROSES, with the longtime support of Ramesh Kakar of NASA Headquarters. Steve Broberg helped with technical editing. The work at LARC was supported by NASA NAST-I and CLARREO projects. The work at NASA/GMAO was funded under NASA grant NNX17AE79A Goddard Space Flight Center Cooperative Agreement. The work at the University of Michigan was supported by NASA grant NNX15AC25G. The work at Meteo France was supported by the EUMETSAT NWP-SAF program. The work at the UK Met Office was supported as part of the science program theme "Improved use of Satellite Data". The 7,377 atmospheric states and associated AIRS spectra used for this paper can be found at ftp://thunder.jpl.nasa.gov/hha/Cloudy_RTA. The file readme.20160518.txt defines various parameters. The file AIRS_SRF_m140f.mat defines the AIRS SRF for each of the 2,378 channels in a MATLAB Version 7.0 format.

References

Alvarado, M. J., Payne, V. H., Mlawer, E. J., Uymin, G., Shephard, M. W., Cady-Pereira, K. E., et al. (2013). Performance of the line-by-line radiative transfer model (LBLRTM) for temperature, water vapor, and trace gas retrievals: Recent updates evaluated with IASI case studies. *Atmospheric Chemistry and Physics*, *13*(14), 6687–6711. https://doi.org/10.5194/acp-13-6687-2013

Amato, U., Masiello, G., Serio, C., & Viggiano, M. (2002). The sigma-IASI code for the calculation of infrared atmospheric radiance and its derivatives. *Environmental Modelling and Software*, *17*, 651–667. https://doi.org/10.1016/S1364-8152(02)00027-0

Aumann, H. H., Chahine, M. T., Gautier, C., Goldberg, M., Kalnay, E., McMillin, L., et al. (2003). AIRS/AMSU/HSB on the Aqua mission: Design, science objectives, data products and processing systems. *IEEE Transactions on Geoscience and Remote Sensing*, *41*(2), 253–264.

Baran, A. J., Cotton, R., Havemann, S., Furtado, K., Marenco, F., Smith, A., et al. (2014). A self-consistent scattering model for cirrus. II. The high and low frequencies. *Quarterly Journal of the Royal Meteorological Society*, *140*(680), 1039–1057. https://doi.org/10.1002/qj.2193

Barker, H. W. (2008). Representing cloud overlap with an effective decorrelation length: An assessment using CloudSat and CALIPSO data. *Journal of Geophysical Research*, *113*, D24205. https://doi.org/10.1029/2008JD010391

Bauer, P., Lopez, P., Salmond, D., Benedetti, A., Saarinen, S., & Bonazzola, M. (2006). Implementation of 1D+ 4D-Var assimilation of precipitation-affected microwave radiances at ECMWF. II: 4D-Var. *Quarterly Journal of the Royal Meteorological Society*, *132*(620), 2307–2332.

Baum, B., Yang, P., Heymsfield, A., Schmitt, C., Xie, Y., Bansemer, A., et al. (2011). Improvements to shortwave bulk scattering and absorption models for the remote sensing of ice clouds. *Journal of Applied Meteorology and Climatology*, *50*(5), 1037–1056. https://doi.org/10.1175/2010JAMC2608.1

Bechtold, P., Chaboureau, J. P., Beljaars, A., Betts, A. K., Köhler, M., Miller, M., & Redelsperger, J. L. (2004). The simulation of the diurnal cycle of convective precipitation over land in a global model. *Quarterly Journal of the Royal Meteorological Society*, *130*(604), 3119–3137.

Bennartz, R., & Greenwald, T. (2011). Current problems in scattering radiative transfer modelling for data assimilation. *Quarterly Journal of the Royal Meteorological Society*, *137*(661), 1952–1962. https://doi.org/10.1002/qj.953

Bhawar, R., Bianchini, G., Bozzo, A., Cacciani, M., Calvello, M. R., Carlotti, M., et al. (2008). Spectrally resolved observations of atmospheric emitted radiance in the H_2O rotation band. *Geophysical Research Letters*, *35*, L04812. https://doi.org/10.1029/2007GL032207

Blumstein, D., Chalon, G., Carlier, T., Buil, C., Hebert, P., Maciaszek, T., et al. (2008). IASI instrument: Technical overview and measured performances. In M. Strojnik (Ed.), *Infrared spaceborne remote sensing XII*, *Proc SPIE* (Vol. 5543, pp. 196–207).

Bower, K. N., Choularton, T. W., Latham, J., Nelson, J., Baker, M. B., & Jensen, J. (1994). A parameterization of warm clouds for use in atmospheric general circulation models. *Journal of the Atmospheric Sciences*, *51*(19), 2722–2732. https://doi.org/10.1175/1520-0469(1994)051<2722:APOWCF>2.0.CO;2

Chen, X., Huang, X., & Liu, X. (2013). Non-negligible effects of cloud vertical overlapping assumptions on longwave spectral fingerprinting studies. *Journal of Geophysical Research: Atmospheres*, *118*, 7309–7320. https://doi.org/10.1002/jgrd.50562

Chou, M.-D., Lee, K.-T., Tsay, S.-C., & Fu, Q. (1999). Parameterization for cloud longwave scattering for use in atmospheric models. *Journal of Climate*, *12*(1), 159–169. https://doi.org/10.1175/1520-0442-12.1.159

Clough, S. A., Shephard, M. W., Mlawer, E. J., Delamere, J. S., Iacono, M. J., Cady-Pereira, K., et al. (2005). Atmospheric radiative transfer modeling: A summary of the AER codes, short communication. *Journal of Quantitative Spectroscopy & Radiative Transfer*, *91*(2), 233–244. https://doi.org/10.1016/j.jqsrt.2004.05.058

Collard, A. D., & McNally, A. P. (2009). The assimilation of infrared atmospheric sounding interferometer radiances at ECMWF. *Quarterly Journal of the Royal Meteorological Society*, *135*(641), 1044–1058. https://doi.org/10.1002/qj.410

DeSouza-Machado, S., Strow, L. L., Hannon, S. E., Motteler, H. E., López-Puertas, M., Funke, B., & Edwards, D. P. (2007). Fast forward radiative transfer modeling of 4.3 μm nonlocal 965 thermodynamic equilibrium effects for infrared temperature sounders. *Geophysical Research Letters*, *34*, L01802. https://doi.org/10.1029/2006GL026684

DeSouza-Machado, S., Strow, L. L., Tangborn, A., Huang, X., Chen, X., Liu, X., et al. (2018). Single-footprint retrievals for AIRS using a fast TwoSlab cloud-representation model and the SARTA all-sky infrared radiative transfer algorithm. *Atmospheric Measurement Techniques*, *11*(1), 529–550. https://doi.org/10.5194/amt-11-529-2018

Ebert, E. E., & Curry, J. A. (1992). A parameterization of ice cloud optical properties for climate models. *Journal of Geophysical Research*, *97*(D4), 3831–3836. https://doi.org/10.1029/91JD02472

European Center for Medium-Range Weather Forecasting (ECMWF) (2009). "IFS documentation Cy33r1". Retrieved from http://www.ecmwf.int/en/forecasts/documentation-and-support

Edwards, J. M., & Slingo, A. (1996). Studies with a flexible new radiation code. I. Choosing a configuration for a large scale model. *Quarterly Journal of the Royal Meteorological Society*, *122*(531), 689–719. https://doi.org/10.1002/qj.49712253107

Errico, R. M., Bauer, P., & Mahfouf, J. F. (2007). Issues regarding the assimilation of cloud and precipitation data. *Journal of the Atmospheric Sciences*, *64*(11), 3785–3798. https://doi.org/10.1175/2006jas2044.1

Fouquart, Y. (1987). Radiative transfer in climate models. In M. E. Schlesinger (Ed.), *Physically based modelling and simulation of climate and climate changes* (pp. 223–284). Norwell, Mass: Kluwer Acad.

Geer, A. J., Baordo, F., Bormann, N., Chambon, P., English, S. J., Kazumori, M., et al. (2017). The growing impact of satellite observations sensitive to humidity, cloud and precipitation. *Quarterly Journal of the Royal Meteorological Society*, *143*(709), 3189–3206. https://doi.org/10.1002/qj.3172

Glumb, R. J., Williams, F. L., Funk, N., Chateauneuf, F., Roney, A., & Allard, R. (2003). Cross-track infrared sounder (CrIS) development status. *Proceedings of SPIE*, *5152*.

Grieco, G., Masiello, M., Matricardi, C., Serio, D. S., & Cuomo, V. (2007). Demonstration and validation of the IASI inversion scheme with NAST-I data. *Quarterly Journal of the Royal Meteorological Society*, *133*(S3), 217–232. https://doi.org/10.1002/qj.162

Guidard, V., Fourrié, N., Brousseau, P., & Rabier, F. (2011). Impact of IASI assimilation at global and convective scales and challenges for the assimilation of cloudy scenes. *Quarterly Journal of the Royal Meteorological Society*, *137*(661), 1975–1987. https://doi.org/10.1002/qj.928

Havemann, S. (2006). The development of a fast radiative transfer model based on an empirical orthogonal functions (EOF) technique. *SPIE*, *6405*, 348–358.

Hilton, F., Armante, R., August, T., Barnet, C., Bouchard, A., Camy-Peyret, C., et al. (2012). Hyperspectral Earth observation from IASI, five years of accomplishments. *Bulletin of the American Meteorological Society*, *93*(3), 347–370. https://doi.org/10.1175/BAMS-D-11-00027.1

Hogan, R. J., & Illingworth, A. J. (2000). Deriving cloud overlap statistics from radar. *Quarterly Journal of the Royal Meteorological Society*, *126*(569), 2903–2909. https://doi.org/10.1002/qj.49712656914

Kazumori, M., Geer, A. J., & English, S. J. (2016). Effects of all-sky assimilation of GCOM-W/AMSR2 radiances in the ECMWF numerical weather prediction system. *Quarterly Journal of the Royal Meteorological Society*, *142*(695), 721–737. https://doi.org/10.1002/qj.2669

Köhler, M., Ahlgrimm, M., & Beljaars, A. (2011). Unified treatment of dry convective and stratocumulus-topped boundary layers in the ECMWF model. *Quarterly Journal of the Royal Meteorological Society*, *137*(654), 43–57. https://doi.org/10.1002/qj.713

Lavanant, L., Fourrié, N., Gambacorta, A., Grieco, G., Heilliette, S., Hilton, F. I., et al. (2011). Comparison of cloud products within IASI footprints for the assimilation of cloudy radiances. *Quarterly Journal of the Royal Meteorological Society*, *137*(661), 1988–2003. https://doi.org/10.1002/qj.917

Liu, Q., Liu, X., Liu, Y., Nalli, N. R., & Tan, C. (2017). *Fast radiative transfer algorithms for real-time sounder applications*, *Capter in book reference module in Earth systems and environmental sciences*. New York: Elsevier Publishing. https://doi.org/10.1016/B978-0-12-409548-9.10391-4

Liu, Q., & Weng, F. (2006). Advanced doubling–Adding method for radiative transfer in planetary atmospheres. *Journal of the Atmospheric Sciences*, *63*(12), 3459–3465. https://doi.org/10.1175/JAS3808.1

Liu, Q., Weng, F., Han, Y., & VanDelst, P. (2008). Community Radiative Transfer Model for Scattering Transfer and Applications. Geoscience and Remote Sensing Symposium, IGARSS 2008. Retrieved from https://ieeexplore.ieee.org/document/4779942/?reload=true

Liu, X., Smith, W. L., Zhou, D. K., & Larar, A. (2006). Principal component-based radiative transfer model for hyperspectral sensors: Theoretical concept. *Applied Optics*, *45*(1), 201–209. https://doi.org/10.1364/AO.45.000201

Liu, X., Yang, Q., Li, H., Jin, Z., Wu, W., Kizer, S., et al. (2016). Development of a fast and accurate PCRTM radiative transfer model in the solar spectral region. *Applied Optics*, *55*(29), 8236–8247. https://doi.org/10.1364/AO.55.008236

Liu, X., Zhou, D. K., Larar, A. M., Smith, W. L., Schluessel, P., Newman, S. M., et al. (2009). Retrieval of atmospheric profiles and cloud properties from IASI spectra using super-channels. *Atmospheric Chemistry and Physics*, *9*(23), 9121–9142. https://doi.org/10.5194/acp-9-9121-2009

Liuzzi, G., Masiello, G., Serio, C., Meloni, D., Di Biagio, C., & Formenti, P. (2017). Consistency of dimensional distributions and refractive indices of desert dust measured over Lampedusa with IASI radiances. *Atmospheric Measurement Techniques*, *10*(2), 599–615. https://doi.org/10.5194/amt-10-599-2017

Machado, S. D., & Strow, L. L. (2016). "An accurate two-slab cloud-representation model for hyperspectral infrared radiative transfer codes", AGU2016 (A11P-01).

Martinet, P., Fourrié, N., Guidard, V., Rabier, F., Montmerle, T., & Brunel, P. (2013). Towards the use of microphysical variables for the assimilation of cloud-affected infrared radiances. *Quarterly Journal of the Royal Meteorological Society*, *139*(674), 1402–1416. https://doi.org/10.1002/qj.2046

Matricardi, M. (2005). The inclusion of aerosols and clouds in RT-IASI, the ECMWF fast radiative transfer model for the IASI, ECMWF Tech. Memo. 474 (53 pp.). Reading, UK: ECMWF

McNally, A. P. (2009). The direct assimilation of cloud-affected satellite infrared radiances in the ECMWF 4D-Var. *Quarterly Journal of the Royal Meteorological Society*, *135*(642), 1214–1229. https://doi.org/10.1002/qj.426

McNally, A. P., & Watts, P. D. (2003). A cloud detection algorithm for high-spectral-resolution infrared sounders. *Quarterly Journal of the Royal Meteorological Society*, *129*(595), 3411–3423. https://doi.org/10.1256/qj.02.208

Mlawer, E. J., Payne, V. H., Moncet, J.-L., Delamere, J. S., Alvarado, M. J., & Tobin, D. D. (2012). Development and recent evaluation of the MT_CKD model of continuum absorption. *Philosophical Transactions of the Royal Society A*, *370*, 1–37. https://doi.org/10.1098/rsta.2011.0295

Okamoto, K., McNally, A. P., & Bell, W. (2014). Progress towards the assimilation of all-sky infrared radiances: An evaluation of cloud effects. *Quarterly Journal of the Royal Meteorological Society*, *140*(682), 1603–1614. https://doi.org/10.1002/qj.2242

Ou, S. C., Liou, K. N., Takano, Y. Y., Rao, N. X., Fu, Q. Q., Heymsfield, A. J., et al. (1995). Remote sounding of cirrus cloud optical depths and ice crystal sizes from AVHRR data: Verification using FIRE II IFO measurements. *Journal of the Atmospheric Sciences*, *52*, 4143–4158. https://doi.org/10.1175/1520-0469

Ou, S. S. C., Kahn, B. H., & Liou, K.-N. (2013). Retrieval of cirrus cloud properties from the atmospheric infrared sounder: The k-coefficient approach combined with SARTA plus delta-four stream approximation. *IEEE Transactions on Geoscience and Remote Sensing*, *51*, 1010–1024.

Pavelin, E. G., English, S. J., & Eyre, J. R. (2008). The assimilation of cloud-affected infrared satellite radiances for numerical weather prediction. *Quarterly Journal of the Royal Meteorological Society*, *134*(632), 737–749. https://doi.org/10.1002/qj.243

Saunders, R., Matricardi, M., & Brunel, P. (1999). An improved fast radiative transfer model for assimilation of satellite radiance observations. *Quarterly Journal of the Royal Meteorological Society*, *125*(556), 1407–1425. https://doi.org/10.1002/qj.1999.49712555615

Saunders, R., Rayer, P., Brunel, P., von Engeln, A., Bormann, N., Strow, L., et al. (2007). A comparison of radiative transfer models for simulating Atmospheric Infrared Sounder (AIRS) radiances. *Journal of Geophysical Research*, *112*, D01S90. https://doi.org/10.1029/2006JD007088

Segelstein, D. (1981). The complex refractive index of water, (Master's thesis). University of Missouri, Kansas City.

Stamnes, K., Tsay, S. C., Wiscombe, W., & Jayaweera, K. (1988). Numerically stable algorithm for discrete-ordinate-method radiative transfer in multiple scattering and emitting layered media. *Applied Optics*, *27*, 2502–2509.

Strow, L. L., Hannon, S. E., DeSouze-Machado, S., Mottler, H. E., & Tobin, D. C. (2006). Validation of the atmospheric infrared sounder radiative transfer algorithm. *Journal of Geophysical Research*, *111*, D09S06. https://doi.org/10.1029/2005JD006146

Thelen, C., & Edwards, J. M. (2013). Short-wave radiance comparisons between SEVERI and the Unified Model. *Quarterly Journal of the Royal Meteorological Society*, *139*(675), 1665–1679. https://doi.org/10.1002/qj.2034

Tiedtke, M. (1989). A comprehensive mass flux scheme for cumulus parameterization in large-scale models. *Monthly Weather Review*, *117*(8), 1779–1800. https://doi.org/10.1175/1520-0493(1989)117<1779:ACMFSF>2.0.CO;2

Tiedtke, M. (1993). Representation of clouds in large-scale models. *Monthly Weather Review*, *121*(11), 3040–3061. https://doi.org/10.1175/1520-0493(1993)121<3040:ROCILS>2.0.CO;2

Tompkins, A. M., Gierens, K., & Rädel, G. (2007). Ice supersaturation in the ECMWF integrated forecast system. *Quarterly Journal of the Royal Meteorological Society*, *133*(622), 53–63. https://doi.org/10.1002/qj.14

Vidot, J., Baran, A. J., & Brunel, P. (2015). A new ice cloud parameterization for infrared radiative transfer simulation of cloudy radiances: Evaluation and optimization with IIR observations and ice cloud profile retrieval products. *Journal of Geophysical Research: Atmospheres*, *120*, 6937–6951. https://doi.org/10.1002/2015JD023462

Wu, W., Liu, X., Zhou, D. K., Larar, A. M., Yang, Q., Kizer, S., & Liu, Q. (2017). The application of PCRTM physical retrieval methodology for IASI cloud scene analysis. *IEEE Transactions on Geoscience and Remote Sensing*, *55*(9), 5042–5056. https://doi.org/10.1109/TGRS.2017.2702006

Yang, Q., Liu, X., Yang, P., & Wang, C. (2014). A fast radiative transfer parameterization under cloudy condition in solar spectral region, AGU2014 (A23E-3293).

Zhou, D., Larar, A., & Liu, X. (2012). Monitoring surface climate with its emissivity derived from satellite measurements, Proc. SPIE 8524, Land Surface Remote Sensing, 85240I (2012/11/21). https://doi.org/10.1117/12.974215

5.5 Patou et al. (2018)

Cet article publié en 2018 dans *Journal of Applied Meteorology and Climatology* (facteur d'impact de 2.364) présente les principaux résultats de la thèse de Maximilien Patou que j'ai co-dirigé entre 2014 et 2018 avec Jérôme Riedi (LOA). Ce travail a demandé un effort important de sélection des évènements précipitants , de retraitement des produits nuageux et de développements techniques de la méthode de suivi des cellules nuageuses. Cet article a permis de valoriser les produits nuageux développés par l'équipe nuage du CEMS et d'introduire un paramêtre morphologique des nuages dont la diminution dans le temps est corrélée avec la probabilité de formation de pluie.

Prediction of the Onset of Heavy Rain Using SEVIRI Cloud Observations

MAXIMILIEN PATOU

Université de Lille, CNRS, UMR 8518-LOA-Laboratoire d'optique Atmosphérique, F-5900 Lille, France

JÉRÔME VIDOT

Centre de Météorologie Spatiale, Météo-France, Lannion, France

JÉRÔME RIÉDI AND GUILLAUME PENIDE

Université de Lille, CNRS, UMR 8518-LOA-Laboratoire d'optique Atmosphérique, F-59000 Lille, France

TIMOTHY J. GARRETT

Department of Atmospheric Sciences, University of Utah, Salt Lake City, Utah

(Manuscript received 18 December 2017, in final form 23 July 2018)

ABSTRACT

Thunderstorms and strong precipitation events can be highly variable in space and time and therefore are challenging to forecast. Geostationary satellites are particularly well suited for studying their occurrence and development. This paper describes a methodology for tracking temporal trends in the development of these systems using a combination of a ground-based radar rainfall product and cloud fields derived from the Meteosat Second Generation's (MSG) Spinning Enhanced Visible and Infrared Imager (SEVIRI). Cloud microphysical and radiative properties and the cloud perimeter-to-area ratio are used to characterize the temporal evolution of 35 cases of isolated convective development. For synchronizing temporal trends between cases, two reference times are used: the time when precipitating clouds reach a rain intensity threshold and the time of the maximum of rain intensity during the cloud life cycle. A period of decreasing cloud perimeter-to-area ratio before heavy rainfall is observed for both synchronization techniques, suggesting this parameter could be a predictor of heavy rain occurrence. However, the choice of synchronization time does impact significantly the observed trend of cloud properties. An illustration of how this approach can be applied to cloud-resolving models is presented to evaluate their ability to simulate cloud processes.

1. Introduction

Heavy rainfall associated with hail and flash flooding can have devastating impacts on a broad range of human activities (Adachi et al. 2013). Accurate short-range forecasts of thunderstorms are necessary to provide the public with early warnings of these events (Zinner et al. 2008). Researchers looking at convective cloud systems in past decades have applied a range of approaches to track and characterize their evolution for the purpose of short-range forecasting (nowcasting) (Sieglaff et al. 2011), thunderstorm classification (Cintineo et al. 2013), mesoscale convective system (MCS) life cycle characterization (McAnelly and Cotton 1989; Roca et al. 2017), and cumulonimbus detection (Henken et al. 2011).

MCS detection using meteorological satellites (Machado et al. 1998; Carvalho and Jones 2001; Vila et al. 2008) usually relies upon identifying regions where the infrared brightness temperature passes a threshold generally below 241 K (Maddox 1980). An area overlapping technique (Mathon and Laurent 2001) has been applied recently at high temporal resolution to track the rapid evolution of convective areas (Liu et al. 2015). While such tracking techniques have mostly been applied to tropical areas, they have also been successfully extended to the midlatitudes (Morel and Senesi 2002a; Kolios and Feidas 2013). Machado and Laurent (2004) used a similar tracking technique to show a maximum in cloud-area expansion of tropical MCS close to the time of maximum precipitation.

Corresponding author: Maximilien Patou, maximilien.patou@ed.univ-lille1.fr

DOI: 10.1175/JAMC-D-17-0352.1

Such studies remain, however, limited to the MCS life cycle and to deep convection analysis.

Other studies have looked at specific stages of cloud development for nowcasting applications. Using the Spinning Enhanced Visible and Infrared Imager (SEVIRI) infrared 10.8-μm, water vapor (infrared 6.2-μm), and visible and high-resolution visible (HRV) channels, Zinner et al. (2008) focused on cumulonimbus cloud at midlatitudes to develop the so-called Cumulonimbus Tracking and Monitoring (Cb-TRAM) algorithm. In Cb-TRAM, temporal information and SEVIRI channel thresholds are used to define the stages of cloud development. This method identifies convective initiation from the temporal variation of cloud area in HRV imagery and cooling in the water vapor channel. Other convective and storm initiation nowcasting methodologies are based on relative cooling rates of developing convective cells during the early stages of development (Roberts and Rutledge 2003; Mecikalski and Bedka 2006; Mecikalski et al. 2008, 2010a,b; Sieglaff et al. 2011, 2014; Mecikalski et al. 2015). The time of convective initiation as defined by the first occurrence of a radar reflectivity greater than 35 dBZ (Roberts and Rutledge 2003; Mecikalski and Bedka 2006) is used as a reference time for cloud property temporal analyses. Mecikalski et al. (2011) studied trends in cloud effective radius (REFF), cloud optical thickness (COT), and cloud-top pressure for a 30-min period 15–45 min before convective initiation. They observed that, as cumuli deepen, COT values increase and cloud-top pressure decreases but that trends in REFF are not monotonic.

Satellite-derived cloud properties such as REFF, COT, cloud-top thermodynamic phase, and cloud-top temperature (CTT) have also been used by several authors to analyze convective cloud evolution. Lensky and Rosenfeld (2006, 2008) and Rosenfeld et al. (2008) showed a correlation between CTT and REFF as a function of aerosol content and updraft strength. Cintineo et al. (2013) studied two classes of storm (severe and nonsevere) and showed that temporal trends of these parameters can be used to extend severe-weather-warning lead times. Senf et al. (2015) compared SEVIRI COT and ice REFF retrievals with cloud anvil edge velocity and average cloud-top vertical velocities. They used the time of maximum cloud-top cooling rate for temporal synchronization to extract temporal trends from nine study cases. Their analysis of REFF retrievals showed that larger ice crystal REFF values are present for clouds tops with lower vertical velocities. This work also showed that the rate of spread of cloud anvils provides information on the strength of convective updrafts. This analysis was recently extended to more than 100 cloud anvil cases (Senf and Deneke 2017a), confirming that smaller ice crystal REFF values occur during strong rainfall periods and that high radar reflectivities occur before the time of the maximum in the cloud-top cooling rate. Moreover, cloud morphology was also studied, especially cloud perimeter P and cloud area A. Perimeter and area data have been used to estimate the fractal dimension D of regions with clouds and rain (Lovejoy 1982). On average, $P \propto A^{D/2}$, where $D \simeq 4/3$, although Batista-Tomás et al. (2016) showed that the fractal dimension changes over the course of a transition from cumulonimbus to cirrus. The A/P ratio was directly introduced by Vila and Machado (2004) and interpreted as the compactness of cloud to characterize the shape and internal structure of convective systems.

The aforementioned studies highlight that temporal analysis of cloud-top morphology, cloud-top microphysics, and radiative properties can be used to characterize the development of convective clouds. However, many of these studies have not included a combined temporal analysis of precipitation at the ground and cloud-top observations from geostationary satellites. We propose in this work an approach to analyze precipitating-cloud development from geostationary satellite–based and ground-based radar data observations. In particular, we propose a combined analysis of temporal trends in REFF, COT, CTT, cloud-top phase, the cloud perimeter-to-area ratio (CPAR), and the maximum of rainfall values at the ground. The objective is to evaluate whether the evolution of cloud parameters derived from geostationary satellites carries information that could be used to anticipate the onset of heavy precipitation. The data used in this study, the tracking methods, and the case study selection are described in section 2. We present in section 3 a temporal analysis of 35 study cases and discuss a preliminary illustration of how such analyses could be used to evaluate cloud-resolving models. Conclusions, limitations of this approach, and future prospects are provided in section 4.

2. Observational data

a. Data and products

For our analyses, we use data from SEVIRI onboard the geostationary Meteosat Second Generation (MSG) satellites (Schmetz et al. 2002). A high temporal resolution is necessary to resolve finer details in convective cloud development (Adler and Fenn 1979; Cintineo et al. 2013). For this, we use the Rapid Scan Service (RSS) of SEVIRI, which provides a 5-min temporal resolution and a spatial resolution over France of approximately 4–5 km. From these high temporal resolution observations we generate a cloud mask (CM), a cloud typing (CT), and four parameters describing

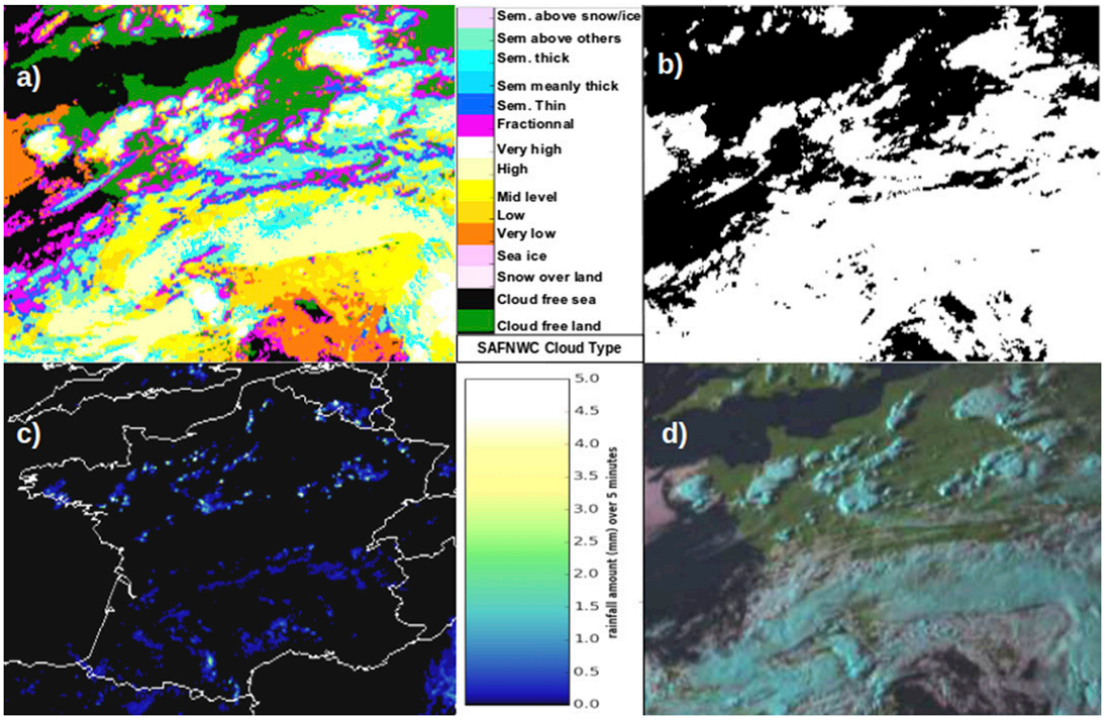

FIG. 1. (a) SAFNWC cloud-type product, (b) cloud mask generated with selection of all cloud types excluding fractional clouds, (c) PANTHERE accumulated rain over 5 min projected onto the SEVIRI RSS grid, and (d) EUMETSAT red–green–blue (RGB) natural color image following the Rosenfeld et al. (2008) method. All data are at 1630 UTC 23 Apr 2011.

cloud properties (REFF, COT, CTT, and the cloud-top phase). Cloud detection and typing are obtained using the European Organisation for the Exploitation of Meteorological Satellites (EUMETSAT) Satellite Application Facility on Support to Nowcasting and Very Short Range Forecasting (SAFNWC) cloud-mask and cloud-type product as described by Derrien and Le Gléau (2005, 2010). The algorithms use multispectral thresholding techniques to detect cloudy pixels and classify clouds. An example of the SAFNWC cloud type product over France is shown in Fig. 1a. Our cloud tracking method uses a simple binary mask (cloud cover of interest) to detect cloud shape and area. This binary mask (Fig. 1b) is a selection of all cloud types excluding the fractional clouds corresponding to partially cloudy pixels (represented in pink in Fig. 1a).

Two algorithms are used to provide REFF, COT, CTT, and cloud-top phase. The 2016 version of the SAFNWC package software (Le Gléau 2016) is used to retrieve CTT and cloud types in this study. For REFF and COT values, we used visible–infrared 1.6-μm retrievals from the SEV06-CLD cloud product distributed by ICARE/AERIS (2017). The SEV06-CLD product is an adaptation for SEVIRI of the operational Collection 6 MODIS (MOD06/MYD06) cloud optical and microphysical retrieval algorithm (Platnick et al. 2001, 2003, 2017) and the *GOES-16* cloud-top properties algorithm (Heidinger and Pavolonis 2009; Heidinger et al. 2010). The latest microphysical and optical assumptions for ice clouds assumed in the of MODIS Collection 6 algorithm are used in SEV06-CLD. For ice crystals, a gamma size distribution consisting of severely roughened compact aggregated columns is used (Platnick et al. 2017). The SEV06-CLD algorithm, similar to the MODIS algorithm, follows the approach of Nakajima and King (1990) to infer COT and REFF. This approach uses lookup table of precalculated reflectance pairs in the visible (0.6 and 0.8 μm) and near-infrared (1.6 μm) spectra for discrete values of COT and REFF. The reflectance in the visible range is mainly sensitive to the optical thickness while the reflectance at 1.6 μm is affected by water/ice particle absorption, and therefore carries information on the particle size and thermodynamic phase. Cloud-top phase information is retrieved by using an infrared bispectral method adapted for SEVIRI similar to the method described in Platnick et al. (2003). A similar method has been evaluated previously by Wolters et al. (2008) using SEVIRI observations, ground-based lidar, and cloud radar data. Because of the daytime limitation of SEV06-CLD COT and REFF retrievals, we have only used data collected when the SEVIRI solar zenith angle $\leq 70°$. Note also that because

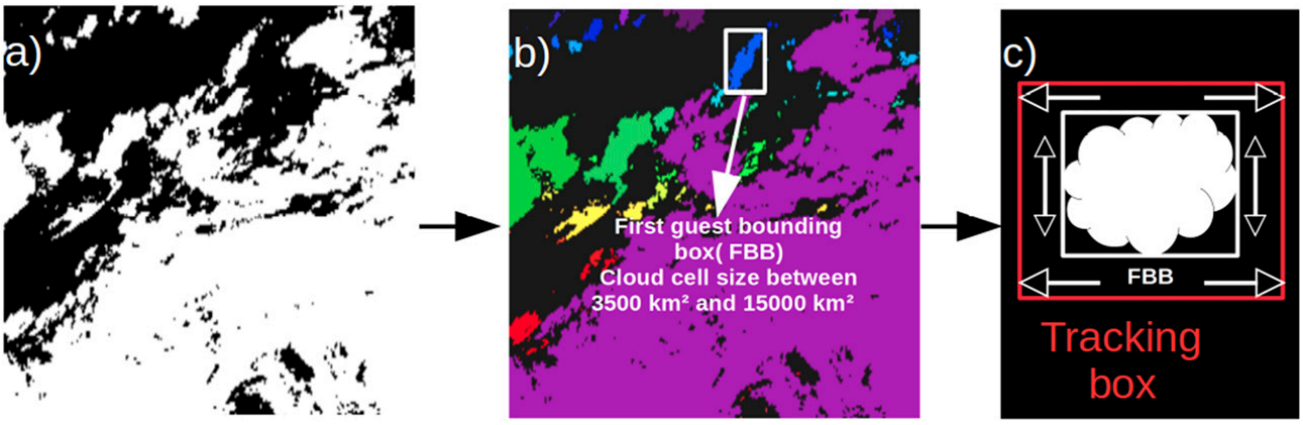

FIG. 2. Schematic view of the detection of an isolated cloud during daytime. Example at 1600 UTC 23 Apr 2011 of isolated cloud detection under fair weather conditions and the box-area determination method for tracking the cloud. (a) Cloud cover colored in white considered in the tracking procedure. (b) Labeled image to detect cloud objects and first bounding box (FBB) detection of isolated cloud. (c) Increase of the FBB to define the tracking box where the tracking is performed.

of SEVIRI's coarser spatial resolution compared to MODIS, the COT and REFF retrievals are more prone to biases in cases of heterogeneous cloud cover (Zhang and Platnick 2011; Zhang et al. 2012).

To provide an estimate of rainfall intensity during the cloud life cycle, we have used the Météo-France rain accumulation PANTHERE (Programme Aramis Nouvelles Technologies en Hydrométéorologie Extension et Renouvellement) product (Tabary 2007) that is based on the French ground-based radar network. This product has the same temporal resolution (5 min) as SEVIRI RSS and provides an accumulation of rain over the past 5 min at a spatial resolution of 1 km. The PANTHERE product is based on a conversion of reflectivity Z to rain rate R using a Z–R-like relationship corrected for partial beam blocking and other artifacts (Tabary 2007). Derivation of a 5-min rain accumulation is made by using a cross-correlation advection field to mitigate undersampling effects. Details, improvement, and validation against rain gauges can be found in Tabary (2007), Tabary et al. (2007), Renard et al. (2012), and Figueras i Ventura and Tabary (2013). Collocation of the PANTHERE product with SEVIRI cloud products is performed by simple aggregation of rain data into the nearest neighbor SEVIRI grid to obtain spatially coherent information (Fig. 1c). Here, we limit our analysis to an area over France (Figs. 1a–d) due to the PANTHERE product availability. EUMETSAT red–green–blue (RGB) false-color composite imagery (Fig. 1d) is used as a complement to manually analyze the presence of clouds and clear-sky conditions for the 35 cases studied in section 3.

b. *Cloud object tracking methodology*

We wish to establish the history leading up to a precipitation event by considering the development of the entire cloud system, without needing to specify a priori a temperature threshold. We have developed a cloud tracking method specifically designed to estimate cloud perimeter corresponding to the interface between isolated clouds and their clear-sky surroundings. In this method, we avoid the use of a specific CTT criterion as much as possible to include analysis of the preconvective environment and the period without precipitation. This method is not designed to detect convective clouds but to analyze mean cloud-top properties of the SEV06-CLD product and cloud morphology on specific periods of precipitation intensification. For this, we tried to remain as general as possible in our cloud selection and only discard the fractional cloud type of the SAFNWC product: fractional cloud type pixels represent difficult borderline cases for cloud detection and there are generally no retrievals of COT, REFF, CTT, and cloud-top phase where there is broken cloud cover.

Our cloud object tracking method is based on automatic overlap and segmentation techniques performed in three steps. The first step identifies the cloud cover considered in our tracking technique, the second step is devoted to the tracking procedure, and the last step establishes a quality index for the tracking. Starting from the cloud cover shown in Fig. 1b and reproduced in Fig. 2a, we make a distinction between each cloud cell at each time step by applying a connected-component labeling algorithm for binary mask inputs available in the Scikit-image Python library (Wu et al. 2005; van der Walt et al. 2014). This algorithm allows us to detect cloud objects. When a detected cloud cell object reaches a size range between 3500 and 15 000 km^2, a first-guess bounding box (FBB) is defined around that object. The size of this bounding

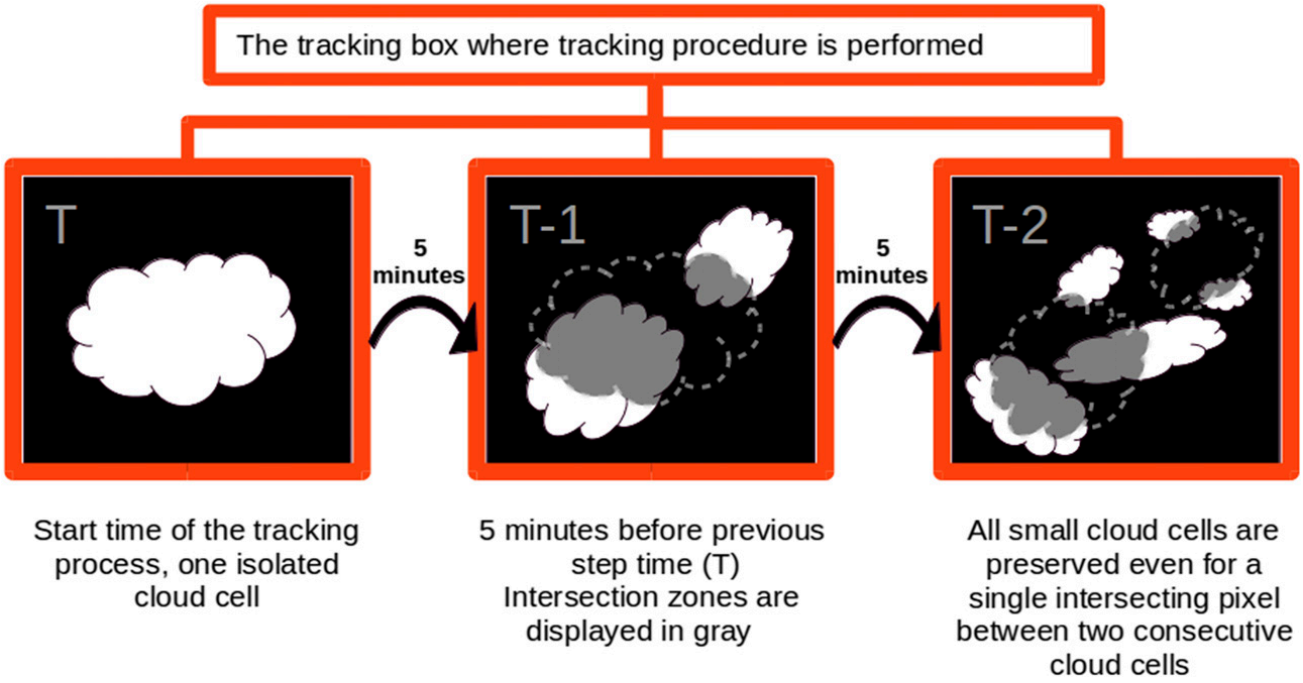

FIG. 3. Schematic view of the area-overlap-based tracking method. The tracking procedure is performed in the time-invariant tracking box. The reverse chronological order is used to determine cloud-system evolution. This tracking technique is limited to cloud systems surrounded by clear sky within the tracking box.

box is increased by 15 pixels in all directions to define a tracking box represented on Fig. 2c. The choice of a 3500–15 000-km^2-area range is inspired by Morel and Senesi, although where Morel and Senesi (2002b) used an area of 1000–10 000 km^2 to track MCS systems over France, we expanded this area to consider both the cloud system and its clear-sky surroundings.

The second step consists of temporally connecting all cloud cells. This is performed using an area-overlap-based technique for successive images similar to previous studies (Mathon and Laurent 2001; Zinner et al. 2008; Liu et al. 2015). Because SEVIRI RSS data have a short refresh period of 5 min this approach is especially efficient (Liu et al. 2015). Clouds can be tracked in successive images provided there is an intersection of their areas. However, as explained by Arnaud et al. (1992), a cloud does not generally stay as a single connected object during a tracking procedure. Using the largest intersection surface between two successive images can artificially reduce the cloud system apparent lifetime (Mathon and Laurent 2001).

To address these concerns, we have adopted a cloud tracking strategy where we first analyze cloud evolution by searching backward in time (i.e., two consecutive images correspond to an image at time T and an image at time $T - 5$ min). Second, the tracking procedure is initiated and performed only within the tracking box defined in the detection procedure (Fig. 2c). The tracking box is a time-invariant area and sets the boundaries where the cloud is tracked. A reverse chronological order is used to track a cloud object among the entire set of objects detected within the tracking box during the daytime. As shown in Fig. 3, dashed lines indicate the previous location of cloud cells, and gray areas correspond to the overlap between adjoining time steps. A cloud object is preserved even for a single intersecting pixel between two consecutive cloud cells so as to increase the duration of the tracking period.

The use of a fixed tracking box to track clouds comes from a trade-off between a need to detect cloud system development within the clear surroundings and a desire for a tracking technique that does not rely on the detection of convective clouds based on CTT criteria. The time of the tracking box corresponds to the time at which the cloud object reaches the size range between 3500 and 15 000 km^2. It is important to keep in mind that we use a reverse chronological order to track cloud systems. Therefore, this time corresponds to the beginning of the tracking procedure and the latest moment of cloud development on the period analyzed. The size range criterion is only applied at this specific time and not imposed at other time steps.

Our tracking method is designed to detect complex situations when a cloud object outside of the tracking box extends across the tracking-box border to contaminate the interior of the tracking area. To deal with these

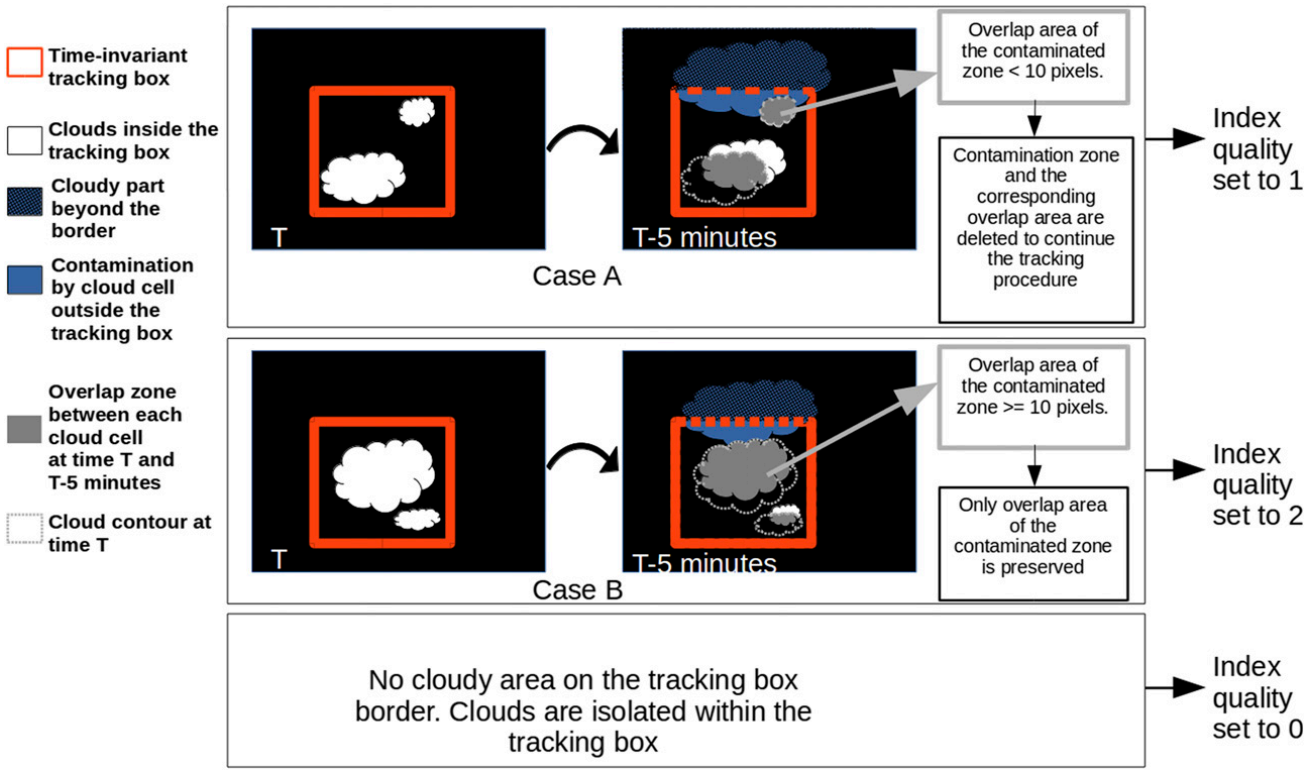

FIG. 4. Complex situations with cloud contamination on the border of the tracking box. (top) Case A: A small tracked cloud cell overlaps with another large size cloud cell outside the tracking box. (bottom) Case B: The cloud mask used as input classifies a large cloud cell within the tracked cloud set and a large cloud cell outside the tracking box as the same cloud object. A threshold of intersection area (gray) between the cloud object at time T and the cloud contamination at time $T - 5$ min on the tracking-box border (blue area) is used to continue to track the cloud cell.

situations, we consider the number of intersecting pixels between two consecutive cloud cells (Fig. 4). A threshold of 10 pixels of overlap between consecutive cloud objects categorizes these cases as either case A for an overlap area less than 10 pixels or case B for an overlap area greater than or equal to 10 pixels. Classification as either case A or B is done for each time step and for all clouds straddling the edges of the tracking box. Once these clouds are classified, they are deleted entirely for case A (Fig. 4, case A), or their corresponding overlap areas are preserved for case B (Fig. 4, case B). The occurrence of clouds near the borders of the tracking box tends to be temporary and we continue to track clouds even for these complex situations.

As a final step, an index for tracking quality is defined at each time step. It is set to zero in the absence of clouds on the edges of the tracking box, to 1 if there is at least one instance of case A and no case B, or to 2 if at least one case B is detected. A tracking quality index of zero indicates local, isolated clouds development and weak displacement in the tracking box. We want to highlight that the tracking box and quality index definitions are only designed to detect isolated cloud systems when cloud perimeter can be computed. The tracking quality index is useful to estimate the quality of perimeter, area, or CPAR estimates. A quality index greater than 1 indicates that we have poor quality of these estimates. However, the tracked box is not adapted to study cloud systems associated with the fastest horizontal displacement.

c. *Case study selection and classification*

A tracked cloud is automatically flagged as "valid" and selected if the tracking duration is greater than 2 h (Fig. 5a). Tracked clouds identified as being valid do not contribute to another cloud tracking. Cloud perimeter is then estimated in pixel number from the binary cloud mask. Perimeter estimation is converted to kilometers using a fixed pixel length of 4.5 km, which provides a reasonable estimate, especially given that it is perimeter temporal trends that are considered. The cloud perimeter-to-area ratio (CPAR) is defined as P/A, where P and A are, respectively, the total perimeter and the total area for the tracked cloud objects in the tracking box. REFF, COT, cloud phase, CTT,

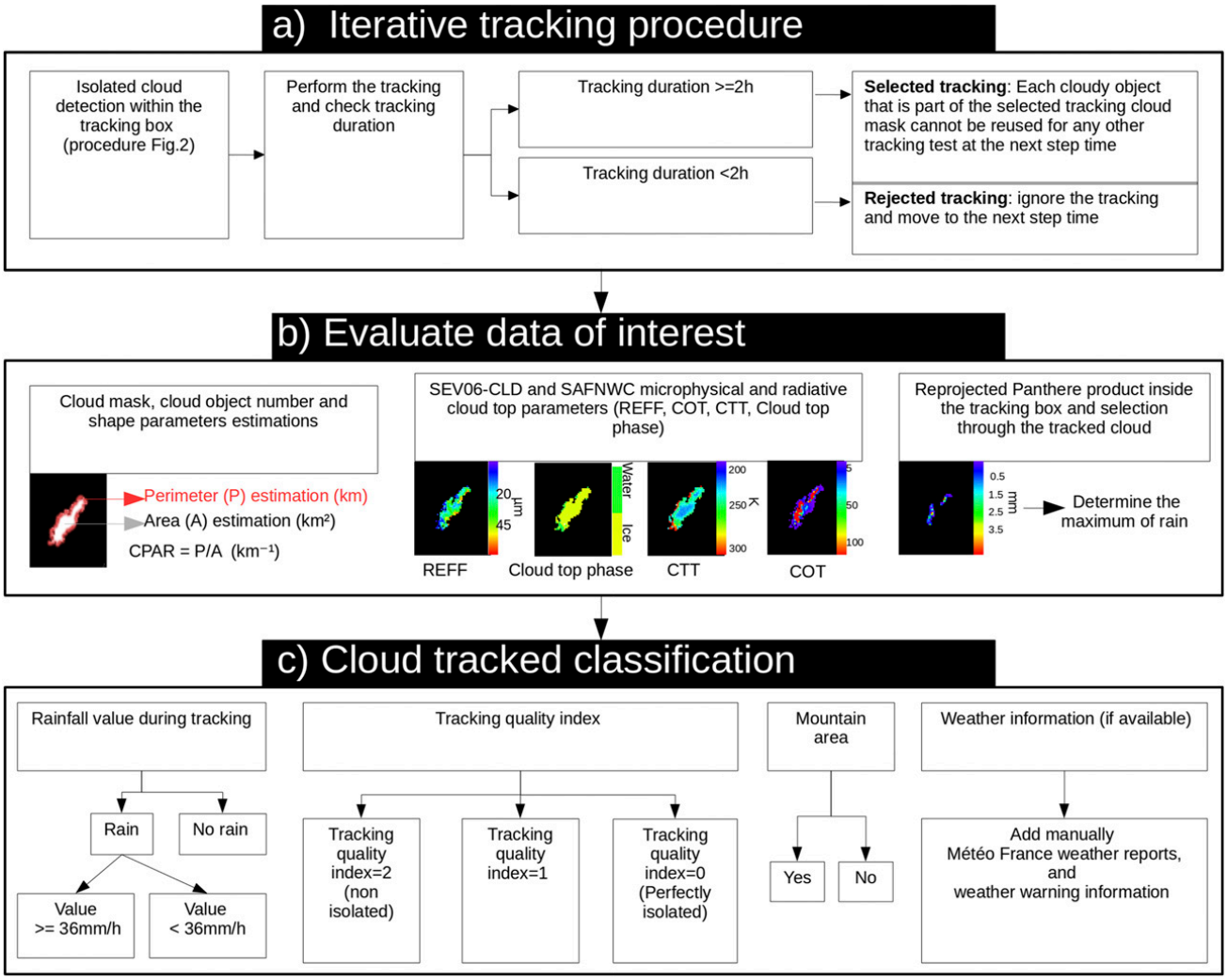

FIG. 5. Automatic cloud tracking selection and classification; only weather information is added manually.

CPAR, and the maximum of rain for each time step are evaluated for tracked clouds (Fig. 5b). The maximum of precipitation is converted for further analysis to units of millimeters per hour. Classification of tracked cloud objects is made based on the occurrence and amount of rain, the quality index, and the local orography (Fig. 5c). We identify tracked clouds with a rain accumulation >3 mm over 5 min and with quality index values of zero as ''strong isolated rainfall events'' separately from other rainy events. All tracked cloud systems with an index quality different from 0 corresponding to non-isolated cloud systems are filtered to study only cloud morphology of isolated cloud systems surrounded by clear sky. We selected 35 case studies over France using the method described in Fig. 5. Figure 6 shows the locations of the tracking boxes for the selected cases.

Daily weather reports and weather regional warnings from Météo-France were analyzed to confirm the presence of storms in tracked-cloud-system regions. (See the appendix for details.)

3. Temporal analysis of case studies over France

a. *Reference time synchronization based on the rainfall product*

Because the tracked systems we consider have different lifetimes and occur at different times of the day, it is necessary to synchronize them to an arbitrary reference time in order to obtain a statistical representation of their life cycle. The choice of this reference time is particularly important as it impacts our ability to highlight temporal behavior around specific stages of cloud development.

Two times are defined to synchronize the evolution of each of the 35 tracked clouds: the time of the maximum value of rain rates during cloud evolution T_{max} and the time of the first occurrence of a rain-rate value reaching

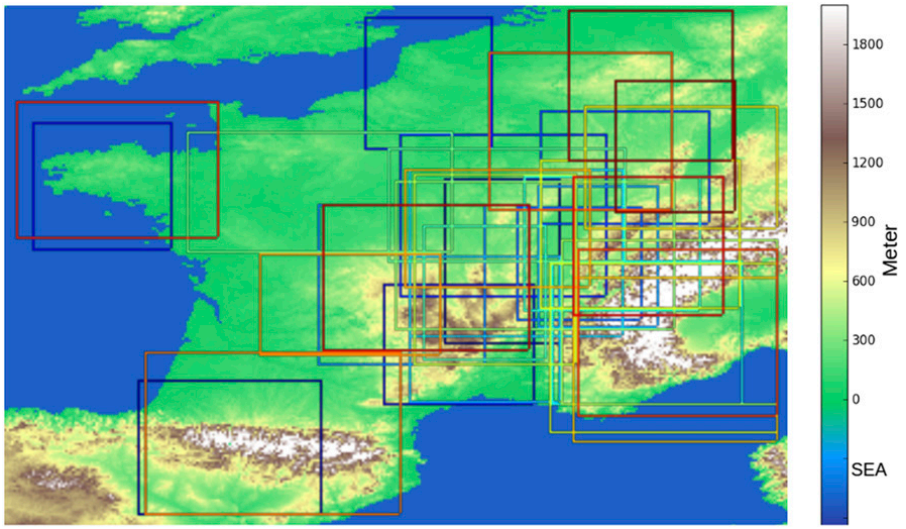

FIG. 6. Elevation map (shading) of France with tracking boxes of the 35 study cases (colored boxes).

an instantaneous threshold of 36 mm h^{-1} T_{thresh}. The synchronizations are performed on the maximum, minimum, median, first quartile (Q1), third quartile (Q3), and interquartile range (IQR) sequences by interpolating the variables onto two relative time scales: T–T_{max} and T–T_{thresh}. This is similar to the approach used by Senf and Deneke (2017a). For each time step, a tracked cloud is associated with a precipitation area at the ground composed of a set of rain-rate values. In this study, we only consider the maximum value of this set of rain rates for each time step. Figure 7 shows the temporal evolution of the statistical distribution of these maximum values derived from the PANTHERE product for the tracked ensemble. The use of T_{thresh} and T_{max} is aimed at two different purposes. Time T_{thresh} is based on a fixed threshold of rain intensity and is suited for separation of periods of weak and high rain intensity (Fig. 7b). It allows for study of cloud evolution soon after precipitation onset at a stage where rainfall invigoration processes are likely to occur. Time T_{max}, on the other hand, is defined from the maximum in the rain-rate value and therefore marks the end of a period of increasing rain intensity (Fig. 7a).

Maximum rain rates are highly heterogeneous, with instantaneous values ranging between 36 and 180 mm h^{-1} at T_{max} (Fig. 7a). There are clear differences in the IQR during the −120–0-min period shown in Fig. 7. For example, at −60 min the IQR is about 2.4 mm h^{-1} using T_{thresh} synchronization (Fig. 7b) while it is 25.2 mm h^{-1} using T_{max} synchronization (Fig. 7a). Differences can also be found in the evolution of extreme values. Maximum values reach 33.6 and 144 mm h^{-1}, respectively, for the T_{thresh} and T_{max} synchronizations. These differences are explained by the heterogeneity of the rain period, rain intensity and tracking duration between study cases.

The cases among the total of 35 that are being tracked at any given time, relative to the T_{thresh} and T_{max} synchronization, are represented in Figs. 7c and 7d. Statistical distributions in Figs. 7a and 7b are calculated from these tracked cases. For example, the distribution of maximum values of rain rate calculated at −120 min using T_{max} synchronization is derived from 33 study cases (see Fig. 7c at −120 min). Clouds are tracked over periods with or without rain and the number of tracked cases exhibiting precipitation (not shown) is dependent on whether T_{max} and T_{thresh} is chosen. For example, at −90 min, 15 tracked clouds exhibit precipitation using T_{max} synchronization versus five clouds using T_{thresh} synchronization.

b. *Analyzed mean of REFF, COT, CTT, and cloud-top phase*

To assign an equal weight to each individually tracked cloud when performing analysis of temporal behavior of REFF, COT, and CTT of the ensemble, we first compute the mean values of these cloud properties for each tracked cloud system and then perform the time synchronization. Mean-value calculations depend on selection of the cloud area of interest in the tracking procedure. We consider cloud systems without any a priori selection of convective parts by using cloud-top temperature thresholding. In principle, this approach allows for the cloud-top phase transition to be observed at earlier stages so as to not track only cloud anvils.

Cloud phase classification from SEV06-CLD identifies each cloudy pixel as being either liquid water,

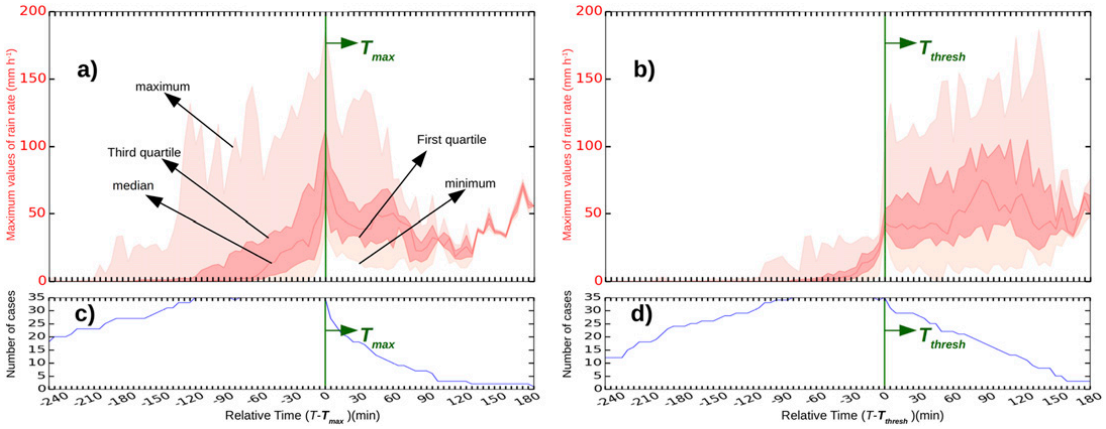

FIG. 7. Temporal behavior of maximum of rain-rate values for the 35 selected cases. Time scale is defined according to the chosen reference time. (a),(b) T_{max} and T_{thresh} time synchronization, respectively; T_{max} and T_{thresh} are represented by green vertical lines. The interquartile range and the area between the maximum and the minimum curves are colored in light red and pink, respectively. The red curve represents the median values. They are indicated by black arrows in (a). (c),(d) The evolution of the number of cases that are tracked relative to the T_{max} time synchronization and T_{thresh} time synchronization, respectively.

undetermined phase, or ice phase. Manual inspection of this classification from SEV06-CLD alongside CTT evolution reveals that areas of rainfall are located close to parts of the tracked system with the coldest CTT, and either an ice or undetermined phase. This observation is supported by the temporal decrease in mean CTT prior to heavy rainfall (Fig. 8). At 1 h before T_{thresh}, the median of CTT distributions is approximately 279 K and it is approximately 260 K at T_{thresh} (Fig. 8b). Then, 1 h after T_{thresh} at +60 min, the median value is 245 K (Fig. 8b). It appears that the onset of heavy precipitation is associated with rapid cloud-top cooling. The same conclusion is obtained using T_{max} temporal synchronization (Fig. 8a) although less clearly seen due to a higher IQR. Nonetheless, faster cloud-top cooling is associated with increasing rain intensity, consistent with previous cloud-top cooling observations (Negri and Adler 1981; Roberts and Rutledge 2003; Senf et al. 2015; Senf and Deneke 2017a).

Cloud-top phase classification is used to analyze mean ice REFF values separately. Figure 9 shows the fraction of ice REFF retrievals relative to total number of successful REFF retrievals (Figs. 9a,b), the mean ice crystal REFF (Figs. 9c,d), and mean ice cloud COT (Figs. 9e,f). From the percentage of ice REFF retrievals, there is an increase in the ice phase fractional area at cloud top concurrent with an increase in rain intensity. Median values for the fraction of ice (based on successful REFF retrievals) are greater than 50% after T_{thresh} and correspond to the occurrence of heavy rainfall at T_{max}. While not surprising, this point illustrates the potential of such analysis for studies of the lead time between cloud-top glaciation and the onset of precipitation.

The temporal rate of change in the ice cloud fraction at cloud top retrieved using geostationary satellites has previously been used in a probabilistic model to assess the potential for the development of severe weather in developing convection (Cintineo et al. 2014). Moreover, Cintineo et al. (2013) have demonstrated that this parameter skillfully discriminates between severe and nonsevere events classified using weather reports of tornadoes and hail, but this study does not include a temporal analysis of precipitation during cloud life cycle. Although our analysis is not limited to the coldest convective parts of clouds, the ice REFF percentage distribution presented here confirms the occurrence of a glaciation period observed by previous studies of cloud anvils evolution (Senf et al. 2015; Senf and Deneke 2017a). The percentage of undetermined phase REFF retrievals (not shown) is not negligible. It is between 10% and 30% when ice REFF percentage increase and precipitation areas were not observed for clouds classified as liquid water clouds.

The mean REFF of ice clouds (Figs. 9c,d) is more challenging to interpret. Using the T_{thresh} synchronization, mean ice REFF Q1 and Q3 values are, respectively, 14 and 22 μm at −30 min and 19 and 24 μm at 0 min. For T_{max} synchronization, the Q1-to-Q3 range is 18–26 μm at −30 min and 19–26 μm at 0 min. Relatively small ice crystals are observed 1 h before T_{thresh} and T_{max} for at least half of the tracked cases (Figs. 9g,h). Median values of the mean CTT distribution (not plotted) associated with these ice crystals lie generally between 240 and 260 K at 30 min before both T_{max} and T_{thresh} and between 230 and 240 K at 30 min after the two reference times.

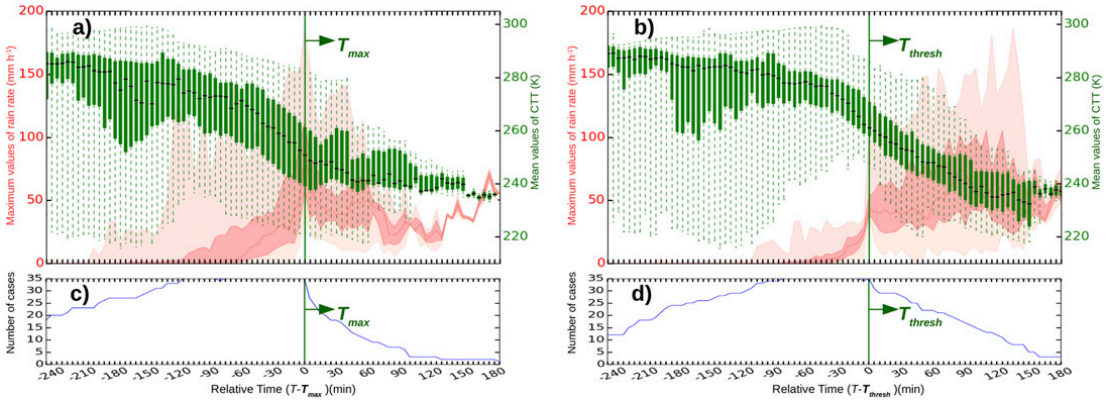

FIG. 8. Temporal evolution of box-and-whisker plot of mean of SAFNWC CTT for the 35 study cases. The interquartile range is represented by a green box where median values correspond to black lines and dotted vertical lines lie between the maximum and minimum of the distribution in the box-and-whisker plot representations. Maximum rainfall distribution of Fig. 7 is plotted in the background. (a) T_{thresh} time synchronization. (b) $T_{\max}$ time synchronization. (c),(d) As in Figs. 7c and 7d, respectively. From a statistical point of view, this is the number of cases used to construct the mean CTT distribution.

Observations of smaller ice crystals before $T_{\max}$ or T_{thresh} tend to be consistent with the hypothesis that stronger updrafts during the growth period of convective clouds lead to smaller ice crystals at cloud top (Rosenfeld et al. 2008; Senf et al. 2015; Mecikalski et al. 2016b; Senf and Deneke 2017a). An independent measure of updraft intensity would be needed to support this hypothesis even though cloud-top cooling can be used as a good proxy of updraft strength (Adler and Fenn 1979; Hamada and Takayabu 2016).

We have observed that there are increasing mean COT values over a 1-h period around T_{thresh} and $T_{\max}$ (Figs. 9e,f). Using the T_{thresh} synchronization, Q1 and Q3 values for mean ice COT are 6 and 13, respectively, at 30 min before T_{thresh} and 12 and 25 at 0 min. Using $T_{\max}$ synchronization, the Q1 and Q3 changes from 14 and 24, respectively, to 19 and 46 for the same period (Fig. 9e). Median values of the mean COT values continue to increase steadily until 40 min after T_{thresh} and 30 min after $T_{\max}$. An increase in COT values has been observed in previous studies of convective clouds using alternative synchronization techniques (Senf et al. 2015; Mecikalski et al. 2011). In this work, mean values of COT and REFF associated with liquid water cloud-top phase classification have been calculated in a similar manner as in Fig. 9 (not shown). These distributions do not show particular temporal trends in the Q1 and Q3 values or median values relative to the T_{thresh} or $T_{\max}$ reference times. Nonetheless, increases in mean values of the described parameters generally correspond to higher rain intensities and to an increasing IQR. The IQR is generally higher for $T_{\max}$ synchronization than T_{thresh} synchronization.

c. *Cloud perimeter-to-area ratio analysis*

The study of CPAR is motivated by an analysis of mixing processes for cumulus convection. For plumes and thermals, the perimeter-to-area ratio is proportional to the inverse of radius (Squires and Turner 1962) and has been used as a starting point in entrainment and detrainment parameterizations (Turner 1963; Dawe and Austin 2013; de Rooy et al. 2013).

The pioneering work of Turner (1963) proposed that entrainment is proportional to the product of the cloud updraft velocity and the perimeter of the cloud horizontal cross section, yielding the result that the fractional entrainment at a given height is inversely proportional to the cloud radius (assuming that the cloud is cylindrical). Following de Rooy and Siebesma (2010) and de Rooy et al. (2013) [Eq. (10) in this paper] the entrainment rate per unit height is given by $\varepsilon = (P/A)(u/w)$, where P and A are, respectively, the perimeter and the area at a given height of the plume or thermal, w is the updraft velocity, and u is the net entrainment velocity across the perimeter. The ratio u/w is nearly constant although with different values for plumes and thermals, according to laboratory water tank experiments (Morton et al. 1956; Turner 1963). Thus, $\varepsilon \propto$ CPAR. Low CPAR implies reduced entrainment that might mix dry stable air with the humid buoyant unstable air in clouds that is required for precipitation production. Effectively, the cores of clouds with low CPAR are more isolated per unit area from their clear-sky environment and should be expected to have a higher probability of intense precipitation production.

Clouds are neither pure plumes nor thermals, and mixing processes at cloud boundaries are complex

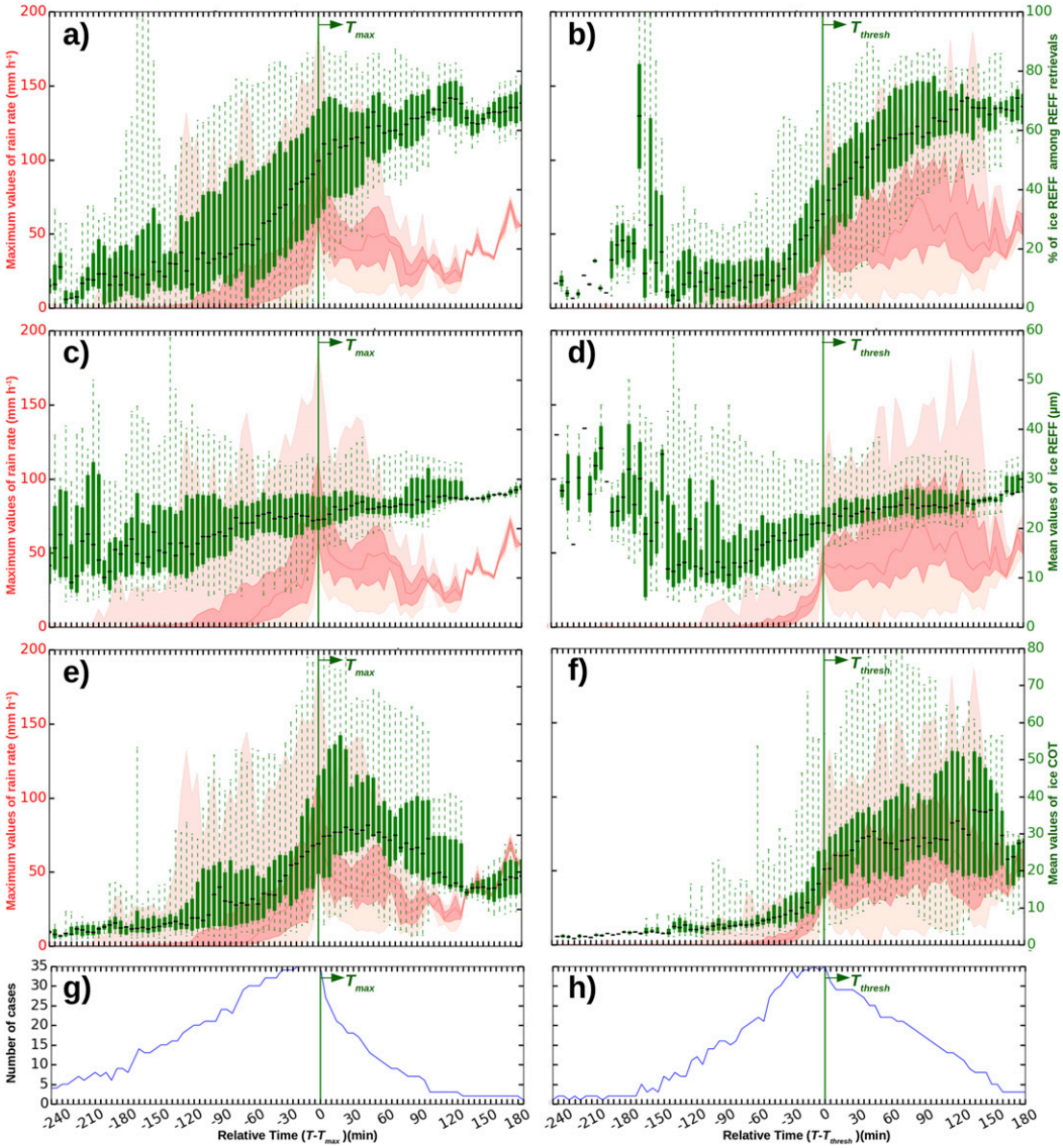

FIG. 9. As in Fig. 8, but for (a),(b) percentage values of REFF retrievals classified as ice crystals, (c),(d) mean ice REFF values, and (e),(f) mean ice COT values. (g),(h) The evolution of the number of cases presenting ice REFF and ice COT retrievals at cloud top. This is the number of cases among the 35 study cases involved in these statistical distributions. Note that these numbers are generally low during cloud life cycle because not all tracked clouds exhibit ice crystals at the same time. Synchronizations are with (left) T_{max} and (right) T_{thresh} as indicated by green arrows.

(Dawe and Austin 2013; de Rooy et al. 2013; Glenn and Krueger 2017). Despite these limitations, CPAR can be viewed as a measure of the overall magnitude of the mixing interface of a cloud system with its clear-sky surroundings. Small cumuli merge to form larger cells during thunderstorm development (Byers and Braham 1949), reducing CPAR and leading to increased probability of rain production (Sinkevich and Krauss 2014; Moseley et al. 2016).

Figure 10 shows box-and-whisker plots of CPAR for both T_{max} and T_{thresh} synchronization. For the 35 cases, tracking quality indexes are less than 2 for at least 100 min prior to the chosen reference time. The Q1 and Q3 values of the CPAR distribution decrease over a period between 60 min before T_{thresh} when the median is 0.21 km^{-1} and 50 min after T_{thresh} when the median is 0.12 km^{-1}. A similar decrease is observed for the T_{max} reference but with more variation of the median values and a larger IQR: median values decrease from 0.21 to 0.13 km^{-1} between −80 and +10 min.

Periods of decreasing CPAR correspond to rain intensification and cloud-top glaciation (Fig. 9). The

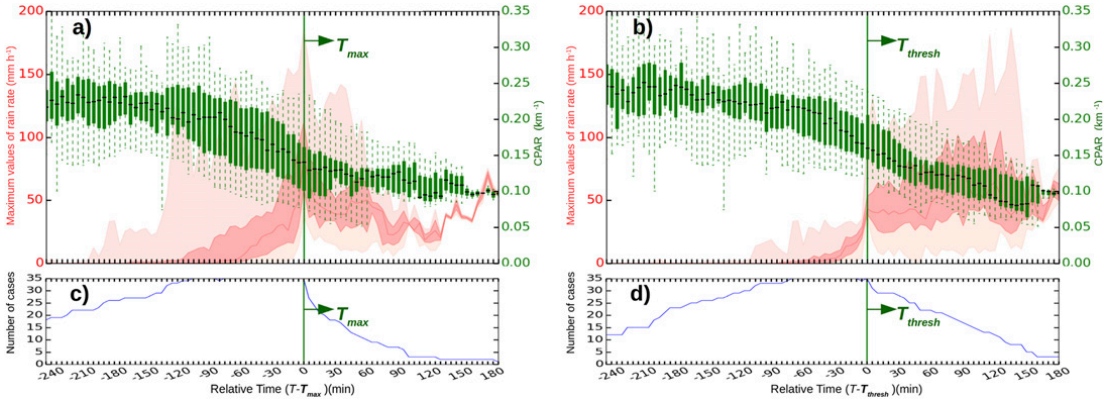

FIG. 10. As in Fig. 8, but for CPAR values: (a) T_{max} synchronization, (b) T_{thresh} synchronization, and (c),(d) the evolution of the number of cases for which the CPAR calculation is feasible.

decreases in CPAR are particularly strong during the period of anvil formation and tend to be lowest when rain rates are highest. Figure 11 represents a scatterplot of the maximum of rain-rate values at T_{max} as a function of the CPAR difference 30 min before and 30 min after T_{thresh} for 28 cases when this period is defined. This specific period of 1 h is not defined for five cases because of shorter tracking and rain periods. Figure 11 confirms that CPAR values decrease prior to intense rain for all of the 28 cases even if the maximum of rain rate at T_{max} is very heterogeneous. Thus, it appears that decreasing CPAR could be a predictor of heavy rain onset.

d. *RAMS simulations*

We apply our cloud tracking and temporal analysis methodology to cloud-resolving model simulations over France. The purpose of this work is to analyze how convection in a cloud-resolving model impacts the CPAR values, mean ICE REFF values, cloud phase classification, and mean CTT values as well as to examine the feasibility of using our tracking methodology. To achieve this, we use the Colorado State University (CSU) Regional Atmospheric Modeling System (RAMS) (Cotton et al. 2003; Saleeby and van den Heever 2013), which is a state-of-the-art 3D nonhydrostatic Eulerian numerical research model developed and maintained by the van den Heever Group at the Colorado State University Department of Atmospheric Science.

Three idealized simulations were initialized within a horizontally homogeneous midlatitude environment as described by Weisman and Klemp (1982) and Takemi (2007). Horizontal resolution is 4 km. We consider a 100 pixel × 100 pixel grid and the vertical resolution was stretched from 50 m close to the ground to 400 m in the upper troposphere on a total of 62 levels. We used cyclic boundary conditions during the 6-h simulations. CSU RAMS uses a two-moment bulk microphysical parameterization scheme (Walko et al. 1995; Meyers et al. 1997; Saleeby and Cotton 2004) with eight hydrometeors (drizzle, cloud water, rain, pristine ice, snow, aggregates, graupel, and hail) that permit the representation in detail of the various microphysical processes: nucleation, freezing, vapor deposition, collection, coalescence, riming, sedimentation, melting, and collisional breakup. Weisman and Klemp (1982) used analytical functions to initialize vertical profiles of potential temperature θ_{env} and relative humidity (RH) of a typical midlatitude environment prior to the development of strong convective storms:

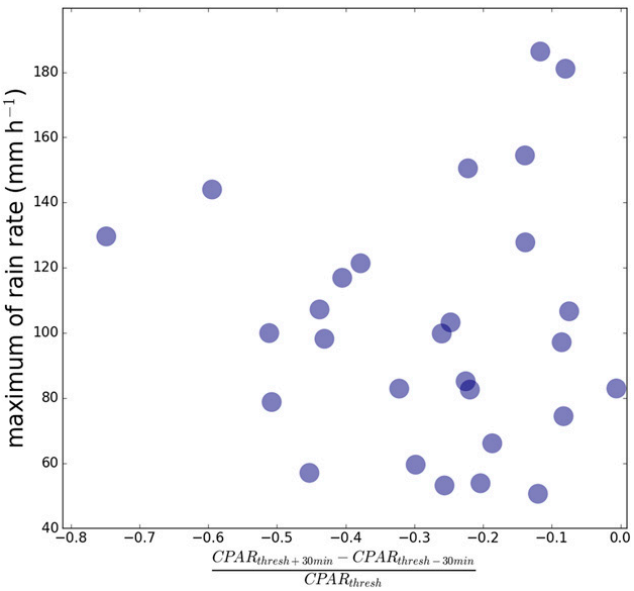

FIG. 11. Scatterplot of the maximum of rain-rate at T_{max} as a function of the difference of CPAR at T_{thresh} + 30 min and T_{thresh} − 30 min standardized by the CPAR at T_{thresh} for 28 cases when the period from 30 min before to 30 min after T_{thresh} is defined.

$$\theta_{\text{env}}(z) = \begin{cases} \theta_0 + (\theta_{\text{tr}} - \theta_0)\left(\dfrac{z}{z_{tr}}\right)^{5/4}, & \text{where} \quad z \le z_{\text{tr}} \quad (1) \\ \theta_{\text{tr}}(z)\exp\left[\dfrac{g}{c_p T_{tr}}(z - z_{tr})\right], & \text{where} \quad z > z_{\text{tr}} \quad (2) \end{cases}$$

$$\text{RH}(z) = \begin{cases} 1 - 0.75\left(\dfrac{z}{z_{\text{tr}}}\right)^{5/4}, & \text{where} \quad z \le z_{\text{tr}} \quad (3) \\ 0.25 - 2 \times 10^{-5} \times (z - z_{\text{tr}}), & \text{where} \quad z > z_{\text{tr}} \quad (4) \end{cases}$$

where z_{tr}, T_{tr}, and θ_{tr} are the altitude, temperature, and potential temperature at the tropopause, respectively; θ_0 is the surface potential temperature. Here, we fixed identical environmental conditions for the three simulations. The surface temperature is set at 300 K, and the tropopause altitude at 12 km with a temperature and potential temperature of 213 and 343 K, respectively. Following Takemi (2007), the low-level moisture (below 1.5 km) was increased to a constant value of 16 g kg^{-1} in order to represent a well-mixed boundary layer. The westerly wind profile decreased from 10 m s^{-1} at the ground to 2 m s^{-1} at 2.5 km in altitude and was constant above. Therefore, the environmental convective available potential energy (CAPE) was 3600 J kg^{-1} for each of three simulations before triggering convection allowing us to focus the study on the impact of the convection triggering mechanism only. To create the ascent necessary to trigger deep convection, we introduced (i) a warm bubble for the first simulation, (ii) low-level wind convergence for the second simulation, and (iii) idealized orographic forcing for the third simulation. Each of these mechanisms has been adjust to trigger deep convection within the same 64-km^2 geographic area and below 1.5 km in altitude. The warm bubble is represented by a perturbation of the potential temperature and moisture profiles of +2 K and +10%, respectively, up to an altitude of 1.5 km and over a surface area of 64 km^2. Low-level wind convergence (Loftus et al. 2008) is characterized by a divergence amplitude of -10^{-6} s^{-1} at the surface, linearly decreasing to zero at 1.5 km in altitude for an area of 64 km^2. Orographic forcing is represented by a witch of Agnesi curve that mimics a 64-km^2 smooth hill shape reaching a maximum height at 1500-m altitude. We examine only cloud tops in the RAMS simulations to more closely mimic SEVIRI satellite observations. In RAMS, the layer corresponding to the cloud top is defined by a threshold of 0.02 g kg^{-1} on the water mixing ratio. When this threshold is reached (from top to bottom), the model layer between this level and the next one below is considered as the cloud top in the analysis. REFF is retrieved using the parameterization of Wyser (1998). The cloud top is considered glaciated if the liquid water content of the cloud-top layer is 0 g m^{-3}.

Figure 12 shows the CPAR, the mean of the ice cloud REFF, the percentage of ice REFF retrievals at cloud top, and the mean of CTT for each of the three RAMS cloud simulations. Temporal synchronization of the simulations is based on time when the instantaneous rain rate reaches 36 mm h^{-1} similar to T_{thresh} used previously. We observed an increase in mean ice REFF. The percentage of ice crystals at cloud top increases toward 100% while mean CTT and CPAR decrease at the same time prior to the reference time (Fig. 12). This period is between 5 and 10 min, which is short compared to what is noted from satellite observations. However, RAMS simulations were not performed to establish a comparison with satellite observations, and the preconvective environment is not simulated. A direct comparison between RAMS simulations and SEVIRI observations would be very limited especially for ice REFF values. Indeed, we performed only three idealized simulations with the RAMS model and the hexagonal ice crystals habit assumption made in Wyser (1998) is different from the MODIS Collection 6 algorithm. Assumptions made for ice crystals can strongly impact the derived REFF values (Wyser 1998). How convection is triggered in the model can introduce differences in temporal evolution for the simulated parameters. A period of 10 min was found before complete glaciation occurred at the top of clouds (Fig. 12b) for the warm bubble simulation [denoted (i) in the key] and the orographic forcing simulation [denoted (iii) in the key]. The maximum of the rain rate is about 49 mm h^{-1} for the first simulation and >100 mm h^{-1} for the second simulation and is associated with larger mean ice crystals of 63 μm (Fig. 12d). These simulations show the potential of using similar cloud tracking techniques for observations and simulations especially for understanding the role of environmental conditions that trigger convection on rainfall enhancement.

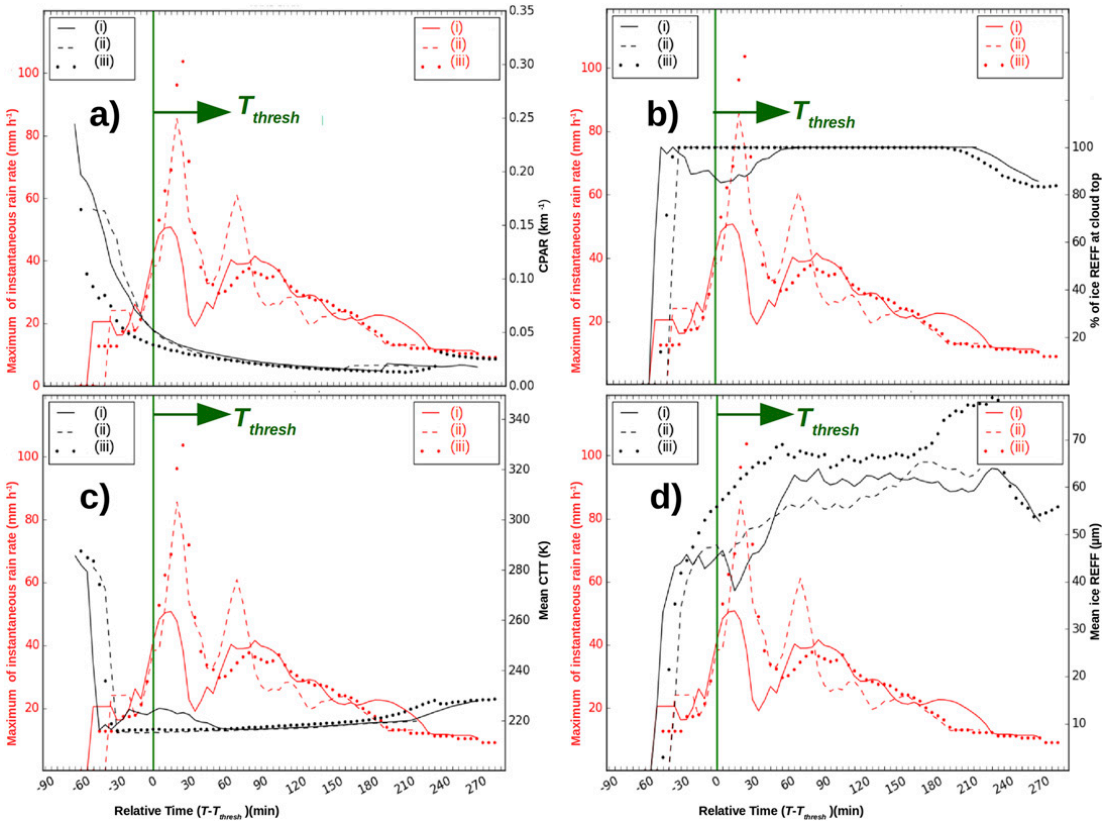

FIG. 12. Three RAMS idealized cloud simulations with different deep convection triggering. The legend indicates the triggering of convection used: (i) a warm bubble is used (solid lines), (ii) a low-level wind convergence is used (dashed lines), and (iii) an idealized orographic forcing is used (dotted lines). Red colored curves are the maximum of the instantaneous rain rate of simulated clouds. Black curves correspond to cloud-top parameters: (a) CPAR estimation, (b) percentage of ice REFF at cloud top, (c) mean of CTT, and (d) mean of ice REFF. All simulations are synchronized with T_{thresh} as indicated by green arrows.

4. Conclusions, limitations, and future prospects

In this study, we have developed a methodology to detect, track, select, and analyze the evolution of precipitating cloud systems during fair weather conditions over France. We analyzed 35 cases as a first step toward building a large database of rainfall events that includes cloud field properties observed by MSG/SEVIRI. We applied this tracking method to three RAMS simulations to illustrate how various convective triggering processes in models result in differing temporal evolution of the cloud properties that are observable by high-temporal-resolution geostationary satellites.

Our investigation has been restricted to a qualitative analysis of ice REFF, COT, CTT, cloud-top phase, and CPAR estimation for both simulations and study cases. The evolution of these parameters has been examined for convective cloud and storm characterization (Machado et al. 1998; Machado and Laurent 2004; Vila and Machado 2004; Mecikalski et al. 2011; Cintineo et al. 2013; Senf et al. 2015; Batista-Tomás et al. 2016; Bley et al. 2016). In this work, we have considered mean values of REFF, CTT, and COT for each of the 35 tracked cloud systems without using a cloud-top temperature-based tracking technique. The cloud phase classification from the SEV06-CLD product is used to analyze separately the glaciated top of cloud for COT and REFF values. First, a tracking and detection procedure was introduced to identify isolated cloud trajectories from SEVIRI. Then, precipitating clouds were identified using a ground-based radar rain product. In addition, three RAMS model simulations of clouds have been presented to illustrate an application of our method to cloud-resolving model data. The temporal evolution of CPAR, mean of ice REFF, and cloud phase at cloud tops are observed prior to the onset of precipitation in RAMS simulations by changing the way deep convection is triggered.

For analysis of cloud property evolution, we introduced two reference times determined from the observed rain rates defined by a threshold of 36 mm h^{-1} (T_{thresh}) and by the time of maximum rain-rate value

during the cloud evolution (T_{max}). The first of these times aimed at the study of the onset of precipitation at the early stages of cloud development and the second at the asymptotic behavior of cloud properties as they reach the point of a maximum rain intensity. These reference times have been defined to elucidate trends in observable cloud properties prior to heavy precipitation. Relative to the two reference times and from 35 synchronized cases, analysis of the evolution of averaged values toward T_{thresh} and T_{max} shows the following:

- a period of growth and glaciation with a decrease of CPAR and mean CTT values and an increase in ice fraction at cloud top,
- smaller mean ice REFF values between 15 and 20 μm, and
- an increase in mean COT values within the glaciated portion of the cloud top.

The choice in reference time used for synchronization of the 35 cases affects the calculated composite behavior of the cloud evolution. A smoother evolution of mean cloud properties and CPAR is observed when using for the reference time the time of first occurrence of the rain rate reaching 36 mm h^{-1}. The use of this reference time divides the tracked cloud life cycle into two distinct periods of weak rainfall and intense rainfall. It was found that CPAR decreases over a period of 2 h until the point of the maximum of rain rate during the cloud life cycle, suggesting that CPAR may be indicative of a ''phase transition'' in the cloud system from a nonprecipitating to a precipitating state. Roebeling and Holleman (2009) have shown that REFF and COT can be indirectly used to estimate instantaneous rain rates. We observe that a period of increase of these parameters together with higher variability is indeed associated with rainfall intensity enhancement. We propose that higher heterogeneity in mean COT, mean REFF, and ice fraction during periods of heavy rain may be due to the disparity of the occurrence of significant rainfall between each case.

Our analysis is limited to 35 isolated cloud systems during daytime fair-weather conditions; Météo-France meteorological information and warnings indicate large numbers of strong rainfall events occurring at night. Mecikalski et al. (2013) previously showed that cirrus anvils in a preconvective environment are very common. This presents a limitation to the study of cloud-top evolution from space prior the onset of precipitation. The cloud cover used in our tracking technique is not adapted to properly detect multilayer situations and their respective cloud evolution. However, our methodology could easily be adapted for use with methods that employ different binary cloud masks, cloud typing (Berendes et al. 2008), or overshooting top detection (Bedka et al. 2010; Bedka and Khlopenkov 2016). The data used in our paper are only available every 5 min; a higher resolution of 1 min would add significant information to study convective clouds (Mecikalski et al. 2016a).

We have also shown the feasibility of applying a satellite cloud tracking technique to the study of convective cloud top in idealized simulations. This work suggests new perspectives for comparing cloud-resolving model simulations and SEVIRI observations focusing on relating cloud dynamical processes such as strong updraft, entrainment, cloud vertical development, and to such cloud-top properties as CPAR, REFF, CTT, COT, and cloud phase. Another approach, not adopted here, could be to simulate SEVIRI radiances and derive cloud-top properties from those (Senf and Deneke 2017b). Future studies should explore a larger number of cases and simulations to evaluate the temporal evolution of cloud-top properties and CPAR as predictors of heavy rainfall periods.

Acknowledgments. This work was supported by the Programme National de Télédétection Spatiale (PNTS; http://www.insu.cnrs.fr/pnts), Grant PNTS-2016-12. SEVIRI cloud-type and cloud-top temperature data were obtained using the software from EUMETSAT's Nowcasting and Very Short Range Forecasting Satellite Applications Facility (NWCSAF). We thank the ICARE Data and Services Center for providing development support and tools. We thank two anonymous reviewers and Hartwig Deneke, whose comments helped to improve this manuscript.

APPENDIX

Météo-France Daily Weather Reports and Regional Warnings

Météo-France daily reports reanalyses (DRR) and weather regional warnings (WRW) are manually analyzed if available near the tracked cloud systems. DRR is a reanalysis of daily France weather including temperature records and rain accumulation over 6 h. We use the DRR to perform a visualization of the 35 tracked cases mainly to check occurrences of storms, hail, and strong rainfall. There are four levels of Météo-France WRW. Level 1 indicates no potentially dangerous phenomena. Level 2 indicates potentially dangerous weather but not an unusual forecast. Level 3 indicates a dangerous forecast with unusual meteorological phenomena where damage and casualties are likely to happen. The maximum level is used when exceptionally

TABLE A1. Météo France weather, tracking time, rain period, and orography information of the 35 cases.

Case	Date	Mountainous area	DDR	Level of WRW	Tracking time (UTC)	Rain period (UTC)
1	23 Apr 2011	No	Thunderstorm	2	1355–1615	1505–1615
2	23 Apr 2011	No	Thunderstorm	2	1205–1530	1320–1530
3	24 Apr 2011	No	Thunderstorm	2	0955–1305	1200–1305
4	25 Apr 2011	No	Thunderstorm	2	0850–1305	1110–1305
5	27 Apr 2011	Yes	Unstable clouds	2	0845–1105	1005–1105
6	30 Apr 2011	Yes	Convective clouds	2	0800–1220	1025–1220
7	25 May 2012	Yes	Severe thunderstorm, hail	2	0800–1340	1215–1340
8	26 May 2012	Yes	Thunderstorm, hail, strong rain	2	1025–1410	1145–1410
9	26 May 2012	Yes	Thunderstorm, hail, strong rain	2	1005–1505	1140–1505
10	26 May 2012	Yes	Thunderstorm	2	0800–1650	1135–1650
11	28 Jun 2012	Yes	Thunderstorm	2	1155–1650	1405–1650
12	19 Aug 2012	Yes	Thunderstorm, strong rain	2	0800–1505	1150–1505
13	6 Jun 2013	Yes	Thundershower	2	0940–1430	1230–1430
14	6 Jun 2013	Yes	Thundershower	2	0800–1140	1025–1140
15	6 Jun 2013	Yes	—	2	0825–1310	1035–1310
16	7 Jun 2013	No	—	2	0810–1540	1125–1540
17	7 Jun 2013	No	Instability, rain	2	0945–1440	1220–1440
18	16 Jun 2013	Yes	Thunderstorm, wind	2	1020–1630	1255–1630
19	9 Apr 2014	Yes	Thunderstorm	2	0800–1230	1105–1230
20	10 Jun 2014	Yes	Thunderstorm	2	1135–1430	1230–1430
21	11 Jun 2014	Yes	Thundershower	2	0800–1300	1125–1300
22	12 Jun 2014	Yes	Thunderstorm	2	0915–1140	1110–1140
23	12 Jun 2014	Yes	Thunderstorm	2	0800–1315	1100–1315
24	12 Jun 2014	Yes	Thunderstorm	2	0800–1305	1115–1305
25	16 Jul 2014	Yes	Thunderstorm	—	0800–1205	0945–1205
26	24 Jul 2014	No	Thunderstorm	2	0800–1140	1005–1140
27	24 Jul 2014	Yes	Thunderstorm	2	0905–1245	1040–1245
28	5 Jun 2015	No	Local thunderstorm	2	1150–1655	1350–1655
29	5 Jun 2015	Yes	Thunderstorm	2	0800–1445	1200–1445
30	7 Aug 2015	Yes	Heat wave	2	0800–1640	1155–1640
31	23 Aug 2015	Yes	Moderate rain, wind	2	0800–1030	0800–1030
32	22 Jun 2016	Yes	Thunderstorm	1	0800–1635	1400–1635
33	15 Aug 2016	Yes	Thundershower	2	0905–1520	1205–1520
34	27 Aug 2016	No	—	—	0800–1345	1135–1345
35	27 Aug 2016	Yes	Thunderstorm	3	0925–1605	1240–1605

intense meteorological phenomena are confirmed. The Météo-France WRW does not only concern heavy rainfall. In addition, the warning scale is also issued in the event of such dangerous weather phenomena as strong winds, flooding, storms, or heatwaves. Classification of dangerous events is mainly based on weather forecaster analysis and seasonal average temperatures. Therefore, in WRW data, winds are considered dangerous if the mean intensity is more than $90\,\mathrm{km\,h^{-1}}$. Hence, we have chosen to use the DRR and WRW only as a complement to rainfall product to check the occurrence of storm inside the tracking box. Temperature records of DRR indicate summer days for these 35 cases with maximum surface temperature exceeding 24°C in all cases. DRR data confirm the presence of thunderstorm, heavy rainfall, or hail near the tracked cloud objects. The majority of the 35 tracked cases are classified as level 2 of WRW. Case study tracking periods, rain periods, and information from DDR and WRW are available in Table A1.

REFERENCES

Adachi, A., T. Kobayashi, H. Yamauchi, and S. Onogi, 2013: Detection of potentially hazardous convective clouds with a dual-polarized C-band radar. *Atmos. Meas. Tech.*, **6**, 2741–2760, https://doi.org/10.5194/amt-6-2741-2013.

Adler, R. F., and D. D. Fenn, 1979: Thunderstorm vertical velocities estimated from satellite data. *J. Atmos. Sci.*, **36**, 1747–1754, https://doi.org/10.1175/1520-0469(1979)036<1747:TVVEFS>2.0.CO;2.

Arnaud, Y., M. Desbois, and J. Maizi, 1992: Automatic tracking and characterization of African convective systems on Meteosat pictures. *J. Appl. Meteor.*, **31**, 443–453, https://doi.org/10.1175/1520-0450(1992)031<0443:ATACOA>2.0.CO;2.

Batista-Tomás, A. R., O. Díaz, A. J. Batista-Leyva, and E. Altshuler, 2016: Classification and dynamics of tropical clouds by their fractal dimension. *Quart. J. Roy. Meteor. Soc.*, **142**, 983–988, https://doi.org/10.1002/qj.2699.

Bedka, K. M., and K. Khlopenkov, 2016: A probabilistic multispectral pattern recognition method for detection of overshooting cloud tops using passive satellite imager observations. *J. Appl. Meteor. Climatol.*, **55**, 1983–2005, https://doi.org/10.1175/JAMC-D-15-0249.1.

——, J. Brunner, R. Dworak, W. Feltz, J. Otkin, and T. Greenwald, 2010: Objective satellite-based detection of overshooting tops using infrared window channel brightness temperature gradients. *J. Appl. Meteor. Climatol.*, **49**, 181–202, https://doi.org/10.1175/2009JAMC2286.1.

Berendes, T. A., J. R. Mecikalski, W. M. MacKenzie, K. M. Bedka, and U. S. Nair, 2008: Convective cloud identification and classification in daytime satellite imagery using standard deviation limited adaptive clustering. *J. Geophys. Res.*, **113**, D20207, https://doi.org/10.1029/2008JD010287.

Bley, S., H. Deneke, and F. Senf, 2016: Meteosat-based characterization of the spatiotemporal evolution of warm convective cloud fields over central Europe. *J. Appl. Meteor. Climatol.*, **55**, 2181–2195, https://doi.org/10.1175/JAMC-D-15-0335.1.

Byers, H. R., and R. R. Braham, 1949: *The Thunderstorm: Report of the Thunderstorm Project.* U.S. Government Printing Office, 287 pp.

Carvalho, L. M. V., and C. Jones, 2001: A satellite method to identify structural properties of mesoscale convective systems based on the maximum spatial correlation tracking technique (MASCOTTE). *J. Appl. Meteor.*, **40**, 1683–1701, https://doi.org/10.1175/1520-0450(2001)040<1683:ASMTIS>2.0.CO;2.

Cintineo, J. L., M. J. Pavolonis, J. M. Sieglaff, and A. K. Heidinger, 2013: Evolution of severe and nonsevere convection inferred from GOES-derived cloud properties. *J. Appl. Meteor. Climatol.*, **52**, 2009–2023, https://doi.org/10.1175/JAMC-D-12-0330.1.

——, ——, ——, and D. T. Lindsey, 2014: An empirical model for assessing the severe weather potential of developing convection. *Wea. Forecasting*, **29**, 639–653, https://doi.org/10.1175/WAF-D-13-00113.1.

Cotton, W. R., and Coauthors, 2003: RAMS 2001: Current status and future directions. *Meteor. Atmos. Phys.*, **82**, 5–29, https://doi.org/10.1007/s00703-001-0584-9.

Dawe, J. T., and P. H. Austin, 2013: Direct entrainment and detrainment rate distributions of individual shallow cumulus clouds in an LES. *Atmos. Chem. Phys.*, **13**, 7795–7811, https://doi.org/10.5194/acp-13-7795-2013.

de Rooy, W. C., and P. A. Siebesma, 2010: Analytical expressions for entrainment and detrainment in cumulus convection. *Quart. J. Roy. Meteor. Soc.*, **136**, 1216–1227, https://doi.org/10.1002/qj.640.

——, and Coauthors, 2013: Entrainment and detrainment in cumulus convection: An overview. *Quart. J. Roy. Meteor. Soc.*, **139**, 1–19, https://doi.org/10.1002/qj.1959.

Derrien, M., and H. Le Gléau, 2005: MSG/SEVIRI cloud mask and type from SAFNWC. *Int. J. Remote Sens.*, **26**, 4707–4732, https://doi.org/10.1080/01431160500166128.

——, and ——, 2010: Improvement of cloud detection near sunrise and sunset by temporal-differencing and region-growing techniques with real-time SEVIRI. *Int. J. Remote Sens.*, **31**, 1765–1780, https://doi.org/10.1080/01431160902926632.

Figueras i Ventura, J., and P. Tabary, 2013: The new French operational polarimetric radar rainfall rate product. *J. Appl. Meteor. Climatol.*, **52**, 1817–1835, https://doi.org/10.1175/JAMC-D-12-0179.1.

Glenn, I. B., and S. K. Krueger, 2017: Connections matter: Updraft merging in organized tropical deep convection. *Geophys. Res. Lett.*, **44**, 7087–7094, https://doi.org/10.1002/2017GL074162.

Hamada, A., and Y. N. Takayabu, 2016: Convective cloud top vertical velocity estimated from geostationary satellite rapid-scan measurements. *Geophys. Res. Lett.*, **43**, 5435–5441, https://doi.org/10.1002/2016GL068962.

Heidinger, A. K., and M. J. Pavolonis, 2009: Gazing at cirrus clouds for 25 years through a split window. Part I: Methodology. *J. Appl. Meteor. Climatol.*, **48**, 1100–1116, https://doi.org/10.1175/2008JAMC1882.1.

——, ——, R. E. Holz, B. A. Baum, and S. Berthier, 2010: Using CALIPSO to explore the sensitivity to cirrus height in the infrared observations from NPOESS/VIIRS and GOES-R/ABI. *J. Geophys. Res.*, **115**, D00H20, https://doi.org/10.1029/2009JD012152.

Henken, C. C., M. J. Schmeits, H. Deneke, and R. A. Roebeling, 2011: Using MSG-SEVIRI cloud physical properties and weather radar observations for the detection of Cb/TCu Clouds. *J. Appl. Meteor. Climatol.*, **50**, 1587–1600, https://doi.org/10.1175/2011JAMC2601.1.

ICARE/AERIS, 2017: Algorithm details: SEV06-CLD project. ICARE Data and Services Center, https://dx.doi.org/10.25326/1.

Kolios, S., and H. Feidas, 2013: An automated nowcasting system of mesoscale convective systems for the Mediterranean basin using Meteosat imagery. Part I: System description. *Meteor. Appl.*, **20**, 287–295, https://doi.org/10.1002/met.1282.

Le Gléau, H., 2016: Algorithm theoretical basis document for the cloud product processors of the NWC/GEO. Tech. Rep., EUMETSAT/SAFNWC/Météo France, 114 pp., http://www.nwcsaf.org/web/guest/scientific-documentation.

Lensky, I. M., and D. Rosenfeld, 2006: The time–space exchangeability of satellite retrieved relations between cloud top temperature and particle effective radius. *Atmos. Chem. Phys.*, **6**, 2887–2894, https://doi.org/10.5194/acp-6-2887-2006.

——, and ——, 2008: Clouds-Aerosols-Precipitation Satellite Analysis Tool (CAPSAT). *Atmos. Chem. Phys.*, **8**, 6739–6753, https://doi.org/10.5194/acp-8-6739-2008.

Liu, J., C. Liu, X. Gu, and D. Qin, 2015: Detection of rapidly developing convection using rapid scan data from a geostationary satellite. *Remote Sens. Lett.*, **6**, 604–612, https://doi.org/10.1080/2150704X.2015.1062160.

Loftus, A. M., D. B. Weber, and C. A. Doswell III, 2008: Parameterized mesoscale forcing mechanisms for initiating numerically simulated isolated multicellular convection. *Mon. Wea. Rev.*, **136**, 2408–2421, https://doi.org/10.1175/2007MWR2133.1.

Lovejoy, S., 1982: Area–perimeter relation for rain and cloud areas. *Science*, **216**, 185–187, https://doi.org/10.1126/science.216.4542.185.

Machado, L. A. T., and H. Laurent, 2004: The convective system area expansion over Amazonia and its relationships with convective system life duration and high-level wind divergence. *Mon. Wea. Rev.*, **132**, 714–725, https://doi.org/10.1175/1520-0493(2004)132<0714:TCSAEO>2.0.CO;2.

——, W. B. Rossow, R. L. Guedes, and A. W. Walker, 1998: Life cycle variations of mesoscale convective systems over the Americas. *Mon. Wea. Rev.*, **126**, 1630–1654, https://doi.org/10.1175/1520-0493(1998)126<1630:LCVOMC>2.0.CO;2.

Maddox, R. A., 1980: Mesoscale convective complexes. *Bull. Amer. Meteor. Soc.*, **61**, 1374–1387, https://doi.org/10.1175/1520-0477(1980)061<1374:MCC>2.0.CO;2.

Mathon, V., and H. Laurent, 2001: Life cycle of Sahelian mesoscale convective cloud systems. *Quart. J. Roy. Meteor. Soc.*, **127**, 377–406, https://doi.org/10.1002/qj.49712757208.

McAnelly, R. L., and W. R. Cotton, 1989: The precipitation life cycle of mesoscale convective complexes over the central United States. *Mon. Wea. Rev.*, **117**, 784–808, https://doi.org/10.1175/1520-0493(1989)117<0784:TPLCOM>2.0.CO;2.

Mecikalski, J. R., and K. M. Bedka, 2006: Forecasting convective initiation by monitoring the evolution of moving cumulus in daytime GOES imagery. *Mon. Wea. Rev.*, **134**, 49–78, https://doi.org/10.1175/MWR3062.1.

——, ——, S. J. Paech, and L. A. Litten, 2008: A statistical evaluation of GOES cloud-top properties for nowcasting convective initiation. *Mon. Wea. Rev.*, **136**, 4899–4914, https://doi.org/10.1175/2008MWR2352.1.

——, W. M. MacKenzie Jr., M. Koenig, and S. Muller, 2010a: Cloud-top properties of growing cumulus prior to convective initiation as measured by Meteosat Second Generation. Part I: Infrared fields. *J. Appl. Meteor. Climatol.*, **49**, 521–534, https://doi.org/10.1175/2009JAMC2344.1.

——, ——, ——, and ——, 2010b: Cloud-top properties of growing cumulus prior to convective initiation as measured by Meteosat Second Generation. Part II: Use of visible reflectance. *J. Appl. Meteor. Climatol.*, **49**, 2544–2558, https://doi.org/10.1175/2010JAMC2480.1.

——, P. D. Watts, and M. Koenig, 2011: Use of Meteosat Second Generation optimal cloud analysis fields for understanding physical attributes of growing cumulus clouds. *Atmos. Res.*, **102**, 175–190, https://doi.org/10.1016/j.atmosres.2011.06.023.

——, P. Minnis, and R. Palikonda, 2013: Use of satellite derived cloud properties to quantify growing cumulus beneath cirrus clouds. *Atmos. Res.*, **120–121**, 192–201, https://doi.org/10.1016/j.atmosres.2012.08.017.

——, J. K. Williams, C. P. Jewett, D. Ahijevych, A. LeRoy, and J. R. Walker, 2015: Probabilistic 1-h convective initiation nowcasts that combine geostationary satellite observations and numerical weather prediction model data. *J. Appl. Meteor. Climatol.*, **54**, 1039–1059, https://doi.org/10.1175/JAMC-D-14-0129.1.

——, C. P. Jewett, J. M. Apke, and L. D. Carey, 2016a: Analysis of cumulus cloud updrafts as observed with 1-min resolution super rapid scan GOES imagery. *Mon. Wea. Rev.*, **144**, 811–830, https://doi.org/10.1175/MWR-D-14-00399.1.

——, D. Rosenfeld, and A. Manzato, 2016b: Evaluation of geostationary satellite observations and the development of a 1–2 h prediction model for future storm intensity. *J. Geophys. Res.*, **121**, 6374–6392, https://doi.org/10.1002/2016JD024768.

Meyers, M. P., R. L. Walko, J. Y. Harrington, and W. R. Cotton, 1997: New RAMS cloud microphysics parameterization. Part II: The two-moment scheme. *Atmos. Res.*, **45**, 3–39, https://doi.org/10.1016/S0169-8095(97)00018-5.

Morel, C., and S. Senesi, 2002a: A climatology of mesoscale convective systems over Europe using satellite infrared imagery. I: Methodology. *Quart. J. Roy. Meteor. Soc.*, **128**, 1953–1971, https://doi.org/10.1256/003590002320603485.

——, and ——, 2002b: A climatology of mesoscale convective systems over Europe using satellite infrared imagery. II: Characteristics of European mesoscale convective systems. *Quart. J. Roy. Meteor. Soc.*, **128**, 1973–1995, https://doi.org/10.1256/003590002320603494.

Morton, B. R., F. R. S. Sir Geoffrey Taylor, and J. S. Turner, 1956: Turbulent gravitational convection from maintained and instantaneous sources. *Proc. Roy. Soc. London*, **234A**, 1–23, https://doi.org/10.1098/rspa.1956.0011.

Moseley, C., C. Hohenegger, P. Berg, and J. O. Haerter, 2016: Intensification of convective extremes driven by cloud–cloud interaction. *Nat. Geosci.*, **9**, 748–752, https://doi.org/10.1038/ngeo2789.

Nakajima, T., and M. D. King, 1990: Determination of the optical thickness and effective particle radius of clouds from reflected solar radiation measurements. Part I: Theory. *J. Atmos. Sci.*, **47**, 1878–1893, https://doi.org/10.1175/1520-0469(1990)047<1878:DOTOTA>2.0.CO;2.

Negri, A. J., and R. F. Adler, 1981: Relation of satellite-based thunderstorm intensity to radar-estimated rainfall. *J. Appl. Meteor.*, **20**, 288–300, https://doi.org/10.1175/1520-0450(1981)020<0288:ROSBTI>2.0.CO;2.

Platnick, S., J. Y. Li, M. D. King, H. Gerber, and P. V. Hobbs, 2001: A solar reflectance method for retrieving the optical thickness and droplet size of liquid water clouds over snow and ice surfaces. *J. Geophys. Res.*, **106**, 15 185–15 199, https://doi.org/10.1029/2000JD900441.

——, M. D. King, S. A. Ackerman, W. P. Menzel, B. A. Baum, J. C. Riedi, and R. A. Frey, 2003: The MODIS cloud products: Algorithms and examples from Terra. *IEEE Trans. Geosci. Remote Sens.*, **41**, 459–473, https://doi.org/10.1109/TGRS.2002.808301.

——, and Coauthors, 2017: The MODIS cloud optical and microphysical products: Collection 6 updates and examples from Terra and Aqua. *IEEE Trans. Geosci. Remote Sens.*, **55**, 502–525, https://doi.org/10.1109/TGRS.2016.2610522.

Renard, F., P.-M. Chapon, and J. Comby, 2012: Assessing the accuracy of weather radar to track intense rain cells in the Greater Lyon area, France. *Atmos. Res.*, **103**, 4–19, https://doi.org/10.1016/j.atmosres.2011.08.008.

Roberts, R. D., and S. Rutledge, 2003: Nowcasting storm initiation and growth using *GOES-8* and WSR-88D data. *Wea. Forecasting*, **18**, 562–584, https://doi.org/10.1175/1520-0434(2003)018<0562:NSIAGU>2.0.CO;2.

Roca, R., T. Fiolleau, and D. Bouniol, 2017: A simple model of the life cycle of mesoscale convective systems cloud shield in the tropics. *J. Climate*, **30**, 4283–4298, https://doi.org/10.1175/JCLI-D-16-0556.1.

Roebeling, R. A., and I. Holleman, 2009: SEVIRI rainfall retrieval and validation using weather radar observations. *J. Geophys. Res.*, **114**, D21202, https://doi.org/10.1029/2009JD012102.

Rosenfeld, D., W. L. Woodley, A. Lerner, G. Kelman, and D. T. Lindsey, 2008: Satellite detection of severe convective storms by their retrieved vertical profiles of cloud particle effective radius and thermodynamic phase. *J. Geophys. Res.*, **113**, D04208, https://doi.org/10.1029/2007JD008600.

Saleeby, S. M., and W. R. Cotton, 2004: A large-droplet mode and prognostic number concentration of cloud droplets in the Colorado State University Regional Atmospheric Modeling System (RAMS). Part I: Module descriptions and supercell test simulations. *J. Appl. Meteor.*, **43**, 182–195, https://doi.org/10.1175/1520-0450(2004)043<0182:ALMAPN>2.0.CO;2.

——, and S. C. van den Heever, 2013: Developments in the CSU-RAMS aerosol model: Emissions, nucleation, regeneration, deposition, and radiation. *J. Appl. Meteor. Climatol.*, **52**, 2601–2622, https://doi.org/10.1175/JAMC-D-12-0312.1.

Schmetz, J., P. Pili, S. Tjemkes, D. Just, J. Kerkmann, S. Rota, and A. Ratier, 2002: An introduction to Meteosat Second Generation (MSG). *Bull. Amer. Meteor. Soc.*, **83**, 977–992, https://doi.org/10.1175/1520-0477(2002)083<0977:AITMSG>2.3.CO;2.

Senf, F., and H. Deneke, 2017a: Satellite-based characterization of convective growth and glaciation and its relationship to precipitation formation over central Europe. *J. Appl. Meteor. Climatol.*, **56**, 1827–1845, https://doi.org/10.1175/JAMC-D-16-0293.1.

——, and ——, 2017b: Uncertainties in synthetic Meteosat SEVIRI infrared brightness temperatures in the presence

of cirrus clouds and implications for evaluation of cloud microphysics. *Atmos. Res.*, **183**, 113–129, https://doi.org/10.1016/j.atmosres.2016.08.012.

——, F. Dietzsch, A. Hünerbein, and H. Deneke, 2015: Characterization of initiation and growth of selected severe convective storms over central Europe with MSG-SEVIRI. *J. Appl. Meteor. Climatol.*, **54**, 207–224, https://doi.org/10.1175/JAMC-D-14-0144.1.

Sieglaff, J. M., L. M. Cronce, W. F. Feltz, K. M. Bedka, M. J. Pavolonis, and A. K. Heidinger, 2011: Nowcasting convective storm initiation using satellite-based box-averaged cloud-top cooling and cloud-type trends. *J. Appl. Meteor. Climatol.*, **50**, 110–126, https://doi.org/10.1175/2010JAMC2496.1.

——, ——, and ——, 2014: Improving satellite-based convective cloud growth monitoring with visible optical depth retrievals. *J. Appl. Meteor. Climatol.*, **53**, 506–520, https://doi.org/10.1175/JAMC-D-13-0139.1.

Sinkevich, A. A., and T. W. Krauss, 2014: Changes in thunderstorm characteristics due to feeder cloud merging. *Atmos. Res.*, **142**, 124–132, https://doi.org/10.1016/j.atmosres.2013.06.007.

Squires, P., and J. S. Turner, 1962: An entraining jet model for cumulo-nimbus updraughts. *Tellus*, **14**, 422–434, https://doi.org/10.3402/tellusa.v14i4.9569.

Tabary, P., 2007: The new French operational radar rainfall product. Part I: Methodology. *Wea. Forecasting*, **22**, 393–408, https://doi.org/10.1175/WAF1004.1.

——, J. Desplats, K. D. Khac, F. Eideliman, C. Gueguen, and J.-C. Heinrich, 2007: The new French operational radar rainfall product. Part II: Validation. *Wea. Forecasting*, **22**, 409–427, https://doi.org/10.1175/WAF1005.1.

Takemi, T., 2007: Environmental stability control of the intensity of squall lines under low-level shear conditions. *J. Geophys. Res.*, **112**, D24110, https://doi.org/10.1029/2007JD008793.

Turner, J. S., 1963: The motion of buoyant elements in turbulent surroundings. *J. Fluid Mech.*, **16**, 1–16, https://doi.org/10.1017/S0022112063000549.

van der Walt, S., and Coauthors, 2014: scikit-image: Image processing in Python. 19 pp., http://arxiv.org/abs/1407.6245.

Vila, D., and L. Machado, 2004: Shape and radiative properties of convective systems observed from infrared satellite images. *Int. J. Remote Sens.*, **25**, 4441–4456, https://doi.org/10.1080/01431160410001726085.

——, ——, H. Laurent, and I. Velasco, 2008: Forecast and Tracking the Evolution of Cloud Clusters (ForTraCC) using satellite infrared imagery: Methodology and validation. *Wea. Forecasting*, **23**, 233–245, https://doi.org/10.1175/2007WAF2006121.1.

Walko, R., W. Cotton, M. Meyers, and J. Harrington, 1995: New RAMS cloud microphysics parameterization. Part I: The single-moment scheme. *Atmos. Res.*, **38**, 29–62, https://doi.org/10.1016/0169-8095(94)00087-T.

Weisman, M. L., and J. B. Klemp, 1982: The dependence of numerically simulated convective storms on vertical wind shear and buoyancy. *Mon. Wea. Rev.*, **110**, 504–520, https://doi.org/10.1175/1520-0493(1982)110<0504:TDONSC>2.0.CO;2.

Wolters, E. L. A., R. A. Roebeling, and A. J. Feijt, 2008: Evaluation of cloud-phase retrieval methods for SEVIRI on *Meteosat-8* using ground-based lidar and cloud radar data. *J. Appl. Meteor. Climatol.*, **47**, 1723–1738, https://doi.org/10.1175/2007JAMC1591.1.

Wu, K., E. Otoo, and A. Shoshani, 2005: Optimizing connected component labeling algorithms. Lawrence Berkeley National Laboratory, 13 pp., http://www.escholarship.org/uc/item/7jg5d1zn.

Wyser, K., 1998: The effective radius in ice clouds. *J. Climate*, **11**, 1793–1802, https://doi.org/10.1175/1520-0442(1998)011<1793:TERIIC>2.0.CO;2.

Zhang, Z., and S. Platnick, 2011: An assessment of differences between cloud effective particle radius retrievals for marine water clouds from three MODIS spectral bands. *J. Geophys. Res.*, **116**, D20215, https://doi.org/10.1029/2011JD016216.

——, A. S. Ackerman, G. Feingold, S. Platnick, R. Pincus, and H. Xue, 2012: Effects of cloud horizontal inhomogeneity and drizzle on remote sensing of cloud droplet effective radius: Case studies based on large-eddy simulations. *J. Geophys. Res.*, **117**, D19208, https://doi.org/10.1029/2012JD017655.

Zinner, T., H. Mannstein, and A. Tafferner, 2008: Cb-TRAM: Tracking and monitoring severe convection from onset over rapid development to mature phase using multi-channel Meteosat-8 SEVIRI data. *Meteor. Atmos. Phys.*, **101**, 191–210, https://doi.org/10.1007/s00703-008-0290-y.

Chapitre 6

Bibliographie

Bibliographie

Andrey-Andrés, J., Fourrié, N., Guidard, V., Armante, R., Brunel, P., Crevoisier, C., and Tournier, B. (2018). A simulated observation database to assess the impact of the IASI-NG hyperspectral infrared sounder. *Atmospheric Measurement Techniques*, 11(2) :803–818. (Cité en page 63.)

Aumann, H. H., Chen, X., Fishbein, E., Geer, A., Havemann, S., Huang, X., Liu, X., Liuzzi, G., DeSouza-Machado, S., Manning, E. M., Masiello, G., Matricardi, M., Moradi, I., Natraj, V., Serio, C., Strow, L., Vidot, J., Wilson, R. C., Wu, W., Yang, Q., and Yung, Y. L. (2018). Evaluation of radiative transfer models with clouds. *Journal of Geophysical Research : Atmospheres*, 123(11) :6142–6157. (Cité en pages 26 et 57.)

Baran, A. J., Francis, P. N., Labonnote, L.-C., and Doutriaux-Boucher, M. (2001). A scattering phase function for ice cloud : Tests of applicability using aircraft and satellite multi-angle multi-wavelength radiance measurements of cirrus. *Quarterly Journal of the Royal Meteorological Society*, 127(577) :2395–2416. (Cité en page 47.)

Baran, A. J., Hill, P., Furtado, K., Field, P., and Manners, J. (2014). A coupled cloud physics radiation parameterization of the bulk optical properties of cirrus and its impact on the Met Office Unified Model Global Atmosphere 5.0 configuration. *Journal of Climate*, 27(20) :7725–7752. (Cité en page 47.)

Baran, A. J. and Labonnote, L.-C. (2007). A self-consistent scattering model for cirrus. I : The solar region. *Quarterly Journal of the Royal Meteorological Society*, 133(629) :1899–1912. (Cité en page 47.)

Barret, B., Le Flochmoen, E., Sauvage, B., Pavelin, E., Matricardi, M., and Cammas, J. P. (2011). The detection of post-monsoon tropospheric ozone variability over south Asia using IASI data. *Atmospheric Chemistry and Physics*, 11(18) :9533–9548. (Cité en page 35.)

Bauer, P., Kelly, G., and Andersson, E. (2003). SSM/I radiance assimilation at ECMWF. In *Proc. GEWEX/ECMWF Workshop on Humidity Analysis*, page 167âĂŞ175. (Cité en page 19.)

Bauer, P., Moreau, E., Chevallier, F., and O'keeffe, U. (2006). Multiple-scattering microwave radiative transfer for data assimilation applications. *Quarterly Journal of the Royal Meteorological Society*, 132(617) :1259–1281. (Cité en page 20.)

Blackmore, T., Saunders, R., and Keogh, S. (2014). Verifying NWP model analyses and forecasts using simulated satellite imagery. In *Proceedings of the 2014 EUMETSAT Meteorological Satellite Conference*. (Cité en pages 39 et 41.)

Borbas, E. and Ruston, B. (2010). The RTTOV UWiremis IR land surface emissivity module. NWPSAF Associate Scientist mission report NWPSAF-MO-VS-042, NWP-SAF. (Cité en page 39.)

Boudala, F. S., Isaac, G. A., Fu, Q., and Cober, S. G. (2002). Parameterization of effective ice particle size for high-latitude clouds. *International Journal of Climatology*, 22(10) :1267–1284. (Cité en page 45.)

Carmagnola, C. M., Domine, F., Dumont, M., Wright, P., Strellis, B., Bergin, M., Dibb, J., Picard, G., Libois, Q., Arnaud, L., and Morin, S. (2013). Snow spectral albedo at Summit, Greenland : measurements and numerical simulations based on physical and chemical properties of the snowpack. *The Cryosphere*, 7(4) :1139–1160. (Cité en page 41.)

Chahine, M. T. (1974). Remote sounding of cloudy atmospheres. I. the single cloud layer. *Journal of the Atmospheric Sciences*, 31(1) :233–243. (Cité en page 37.)

Chen, Y., Han, Y., Van Delst, P., and Weng, F. (2010). On water vapor Jacobian in fast radiative transfer model. *Journal of Geophysical Research : Atmospheres*, 115(D12). (Cité en page 35.)

Chevallier, F., Michele, S. D., and McNally, A. (2006). Diverse profile datasets from the ECMWF 91 level short range forecast. NWPSAF report NWPSAF-EC-TR-010, NWP-SAF. (Cité en page 33.)

Chou, M.-D., Lee, K.-T., Tsay, S.-C., and Fu, Q. (1999). Parameterization for cloud longwave scattering for use in atmospheric models. *Journal of Climate*, 12(1) :159–169. (Cité en pages 37 et 70.)

Clough, S., Shephard, M., Mlawer, E., Delamere, J., Iacono, M., Cady-Pereira, K., Boukabara, S., and Brown, P. (2005). Atmospheric radiative transfer modeling : a summary of the AER codes. *Journal of Quantitative Spectroscopy and Radiative Transfer*, 91(2) :233 – 244. (Cité en page 52.)

Collard, A. D. (2007). Selection of IASI channels for use in numerical weather prediction. *Quarterly Journal of the Royal Meteorological Society*, 133(629) :1977–1991. (Cité en page 38.)

Crevoisier, C., Clerbaux, C., Guidard, V., Phulpin, T., Armante, R., Barret, B., Camy-Peyret, C., Chaboureau, J.-P., Coheur, P.-F., Crépeau, L., Dufour, G., Labonnote, L., Lavanant, L., Hadji-Lazaro, J., Herbin, H., Jacquinet-Husson, N., Payan, S., Péquignot, E., Pierangelo, C., Sellitto, P., and Stubenrauch, C. (2014). Towards IASI-New Generation (IASI-NG) : impact of improved spectral resolution and radiometric noise on the retrieval of thermodynamic, chemistry and climate variables. *Atmospheric Measurement Techniques*, 7(12) :4367–4385. (Cité en page 35.)

de Brux, J., Mevel, A., Ni, J., and Quinet, E. (2018). évaluation socioéconomique de Météo-France. Technical report, France Stratégie. (Cité en page 17.)

De Wachter, E., Barret, B., Le Flochmoën, E., Pavelin, E., Matricardi, M., Clerbaux, C., Hadji-Lazaro, J., George, M., Hurtmans, D., Coheur, P.-F., Nedelec, P., and Cammas, J. P. (2012). Retrieval of Metop-A/IASI CO profiles and validation with MOZAIC data. *Atmospheric Measurement Techniques*, 5(11) :2843–2857. (Cité en page 35.)

Delanoe, J. and Hogan, R. J. (2010). Combined Cloudsat-CALIPSO-MODIS retrievals of the properties of ice clouds. *Journal of Geophysical Research : Atmospheres*, 115(D4). (Cité en page 48.)

Deng, M., Mace, G. G., Wang, Z., and Okamoto, H. (2010). Tropical composition, cloud and climate coupling experiment validation for cirrus cloud profiling retrieval using Cloudsat radar and CALIPSO lidar. *Journal of Geophysical Research : Atmospheres*, 115(D10). (Cité en page 48.)

Derrien, M. and Gléau, H. L. (2005). MSG/SEVIRI cloud mask and type from SAFNWC. *International Journal of Remote Sensing*, 26(21) :4707–4732. (Cité en page 39.)

Descheemaecker, M., Plu, M., Marécal, V., Claeyman, M., Olivier, F., Aoun, Y., Blanc, P., Wald, L., Guth, J., Sič, B., Vidot, J., Piacentini, A., and Josse, B. (2019). Monitoring aerosols over europe : an assessment of the potential benefit of assimilating the VIS04 measurements from the future MTG/FCI geostationary imager. *Atmospheric Measurement Techniques*, 12(2) :1251–1275. (Cité en page 41.)

Deuzé, J., Herman, M., and Santer, R. (1989). Fourier series expansion of the transfer equation in the atmosphere-ocean system. *Journal of Quantitative Spectroscopy and Radiative Transfer*, 41(6) :483 – 494. (Cité en page 25.)

Emde, C., Buras-Schnell, R., Kylling, A., Mayer, B., Gasteiger, J., Hamann, U., Kylling, J., Richter, B., Pause, C., Dowling, T., and Bugliaro, L. (2016). The libRadtran software package for radiative transfer calculations (version 2.0.1). *Geoscientific Model Development*, 9(5) :1647–1672. (Cité en page 45.)

Eresma, R. and McNally, A. (2014). Diverse profile datasets from the ECMWF 137-level short-range forecasts. NWPSAF report NWPSAF-EC-TR-17, ECMWF. (Cité en page 55.)

Errico, R. M. (1997). What is an adjoint model ? *Bulletin of the American Meteorological Society*, 78(11) :2577–2592. (Cité en page 20.)

Errico, R. M., Bauer, P., and Mahfouf, J.-F. (2007). Issues regarding the assimilation of cloud and precipitation data. *Journal of the Atmospheric Sciences*, 64(11) :3785–3798. (Cité en page 19.)

Eyre, J. (1991). A fast radiative transfer model for satellite sounding systems. Technical Memoranda 176, ECMWF. (Cité en pages 28, 32, 33 et 36.)

Eyre, J. R., English, S. J., and Forsythe, M. (2019). Assimilation of satellite data in numerical weather prediction. part I : the early years. *Quarterly Journal of the Royal Meteorological Society*, n/a(n/a). (Cité en page 19.)

Eyre, J. R., Kelly, G. A., McNally, A. P., Andersson, E., and Persson, A. (1993). Assimilation of TOVS radiance information through one-dimensional variational analysis. *Quarterly Journal of the Royal Meteorological Society*, 119(514) :1427–1463. (Cité en page 19.)

Eyre, J. R. and Menzel, W. P. (1989). Retrieval of cloud parameters from satellite sounder data : A simulation study. *Journal of Applied Meteorology*, 28(4) :267–275. (Cité en page 37.)

Eyre, J. R. and Woolf, H. M. (1988). Transmittance of atmospheric gases in the microwave region : a fast model. *Applied Optics*, 27(15) :3244–3249. (Cité en page 32.)

Faijan, F., Lavanant, L., and Rabier, F. (2012). Towards the use of cloud microphysical properties to simulate IASI spectra in an operational context. *Journal of Geophysical Research : Atmospheres*, 117(D22). (Cité en page 44.)

Farouk, I., Fourrié, N., and Guidard, V. (2019). Homogeneity criteria from AVHRR information within IASI pixels in a numerical weather prediction context. *Atmospheric Measurement Techniques*, 12(6) :3001–3017. (Cité en page 44.)

Field, P. R., Heymsfield, A. J., and Bansemer, A. (2007). Snow size distribution parameterization for midlatitude and tropical ice clouds. *Journal of the Atmospheric Sciences*, 64(12) :4346–4365. (Cité en pages 47 et 68.)

Fourrié, N. and Rabier, F. (2004). Cloud characteristics and channel selection for IASI radiances in meteorologically sensitive areas. *Quarterly Journal of the Royal Meteorological Society*, 130(600) :1839–1856. (Cité en page 44.)

Garand, L., Turner, D., Larocque, M., Bates, J., Boukabara, S., Brunel, P., Chevallier, F., Deblonde, G., Engelen, R., Hollingshead, M., et al. (2001). Radiance and Jacobian intercomparison of radiative transfer models applied to HIRS and AMSU channels. *Journal of Geophysical Research : Atmospheres*, 106(D20) :24017–24031. (Cité en pages 52 et 54.)

Geer, A. J. and Baordo, F. (2014). Improved scattering radiative transfer for frozen hydrometeors at microwave frequencies. *Atmospheric Measurement Techniques*, 7(6) :1839–1860. (Cité en page 68.)

Geer, A. J., Bauer, P., and ODell, C. W. (2009). A revised cloud overlap scheme for fast microwave radiative transfer in rain and cloud. *Journal of Applied Meteorology and Climatology*, 48(11) :2257–2270. (Cité en page 68.)

Geer, A. J., Lonitz, K., Weston, P., Kazumori, M., Okamoto, K., Zhu, Y., Liu, E. H., Collard, A., Bell, W., Migliorini, S., Chambon, P., Fourrié, N., Kim, M.-J., Kopken-Watts, C., and Schraff, C. (2018). All-sky satellite data assimilation at operational weather forecasting centres. *Quarterly Journal of the Royal Meteorological Society*, 144(713) :1191–1217. (Cité en pages 19 et 67.)

Geer, A. J., Migliorini, S., and Matricardi, M. (2019). All-sky assimilation of infrared radiances sensitive to mid- and upper-tropospheric moisture and cloud. *Atmospheric Measurement Techniques*, 12(9) :4903–4929. (Cité en pages 38, 49, 58, 59, 67 et 68.)

Getzewich, B. J., Vaughan, M. A., Hunt, W. H., Avery, M. A., Powell, K. A., Tackett, J. L., Winker, D. M., Kar, J., Lee, K.-P., and Toth, T. D. (2018). Calipso lidar calibration at 532 nm : version 4 daytime algorithm. *Atmospheric Measurement Techniques*, 11(11) :6309–6326. (Cité en page 72.)

Gordon, I., Rothman, L., Hill, C., Kochanov, R., Tan, Y., Bernath, P., Birk, M., Boudon, V., Campargue, A., Chance, K., Drouin, B., Flaud, J.-M., Gamache, R., Hodges, J., Jacquemart, D., Perevalov, V., Perrin, A., Shine, K., Smith, M.-A., Tennyson, J., Toon, G., Tran, H., Tyuterev, V., Barbe, A., Csaszar, A., Devi, V., Furtenbacher, T., Harrison, J., Hartmann, J.-M., Jolly, A., Johnson, T., Karman, T., Kleiner, I., Kyuberis, A., Loos, J., Lyulin, O., Massie, S., Mikhailenko, S., Moazzen-Ahmadi, N., Muller, H., Naumenko, O., Nikitin, A., Polyansky, O., Rey, M., Rotger, M., Sharpe, S., Sung, K., Starikova, E., Tashkun, S., Auwera, J. V., Wagner, G., Wilzewski, J., Wcislo, P., Yu, S., and Zak, E. (2017). The HITRAN2016 molecular spectroscopic database. *Journal of Quantitative Spectroscopy and Radiative Transfer*, 203 :3 – 69. HITRAN2016 Special Issue. (Cité en page 31.)

Guedj, S., Guidard, V., Menetrier, B., Mahfouf, J.-F., and Rabier, F. (2014). Future benefits of high-density radiance data from MTG-IRS in the AROME fine-scale forecast model. Eumetsat research report, CNRM/CNRS, Meteo-France. (Cité en page 63.)

Heidinger, A. K., ODell, C., Bennartz, R., and Greenwald, T. (2006). The Successive-Order-of-Interaction radiative transfer model. part I : Model development. *Journal of Applied Meteorology and Climatology*, 45(10) :1388–1402. (Cité en page 25.)

Heinemann, T., Latanzio, A., and Roveda, F. (2002). The EUMETSAT multi-sensor precipitation estimate (MPE). Eumetsat report, EUMETSAT. (Cité en page 60.)

Hersbach, H. and Dee, D. (2016). ERA5 reanalysis is in production. *ECMWF Newsletter*, (147). (Cité en page 34.)

Hess, M., Koepke, P., and Schult, I. (1998). Optical properties of aerosols and clouds : The software package OPAC. *Bulletin of the American Meteorological Society*, 79(5) :831–844. (Cité en pages 44 et 72.)

Hilton, F., Armante, R., August, T., Barnet, C., Bouchard, A., Camy-Peyret, C., Capelle, V., Clarisse, L., Clerbaux, C., Coheur, P.-F., Collard, A., Crevoisier, C., Dufour, G., Edwards, D., Faijan, F., FourriÃľ, N., Gambacorta, A., Goldberg, M., Guidard, V., Hurtmans, D., Illingworth, S., Jacquinet-Husson, N., Kerzenmacher, T., Klaes, D., Lavanant, L., Masiello, G., Matricardi, M., McNally, A., Newman, S., Pavelin, E., Payan, S., PÃľquignot, E., Peyridieu, S., Phulpin, T., Remedios, J., SchlÃijssel, P., Serio, C., Strow, L., Stubenrauch, C., Taylor, J., Tobin, D., Wolf, W., and Zhou, D. (2012). Hyperspectral earth observation from IASI : Five years of accomplishments. *Bulletin of the American Meteorological Society*, 93(3) :347–370. (Cité en page 52.)

Hocking, J. (2015). A visible/infrared multiple-scattering model for RTTOV. NWP SAF report MO-TR-031, UK Metoffice. (Cité en page 39.)

Hocking, J., Rayer, P., Rundle, D., Saunders, R., Matricardi, M., Geer, A., Brunel,

P., and Vidot, J. (2017). RTTOV v12 users guide. NWP-SAF report NWPSAF-MO-UD-037, NWP-SAF. (Cité en page 33.)

Jacquinet-Husson, N., Armante, R., Scott, N., Chédin, A., Crépeau, L., Boutammine, C., Bouhdaoui, A., Crevoisier, C., Capelle, V., Boonne, C., Poulet-Crovisier, N., Barbe, A., Benner, D. C., Boudon, V., Brown, L., Buldyreva, J., Campargue, A., Coudert, L., Devi, V., Down, M., Drouin, B., Fayt, A., Fittschen, C., Flaud, J.-M., Gamache, R., Harrison, J., Hill, C., Hodnebrog, Ã., Hu, S.-M., Jacquemart, D., Jolly, A., Jimenez, E., Lavrentieva, N., Liu, A.-W., Lodi, L., Lyulin, O., Massie, S., Mikhailenko, S., Muller, H., Naumenko, O., Nikitin, A., Nielsen, C., Orphal, J., Perevalov, V., Perrin, A., Polovtseva, E., Predoi-Cross, A., Rotger, M., Ruth, A., Yu, S., Sung, K., Tashkun, S., Tennyson, J., Tyuterev, V., Auwera, J. V., Voronin, B., and Makie, A. (2016). The 2015 edition of the GEISA spectroscopic database. *Journal of Molecular Spectroscopy*, 327 :31 – 72. New Visions of Spectroscopic Databases, Volume II. (Cité en page 31.)

Lavanant, L., Fourrié, N., Gambacorta, A., Grieco, G., Heilliette, S., Hilton, F. I., Kim, M.-J., McNally, A. P., Nishihata, H., Pavelin, E. G., and Rabier, F. (2011). Comparison of cloud products within IASI footprints for the assimilation of cloudy radiances. *Quarterly Journal of the Royal Meteorological Society*, 137(661) :1988–2003. (Cité en page 24.)

Liu, X., Yang, Q., Li, H., Jin, Z., Wu, W., Kizer, S., Zhou, D. K., and Yang, P. (2016). Development of a fast and accurate PCRTM radiative transfer model in the solar spectral region. *Appl. Opt.*, 55(29) :8236–8247. (Cité en page 57.)

Lucht, W., Schaaf, C. B., and Strahler, A. H. (2000). An algorithm for the retrieval of albedo from space using semiempirical BRDF models. *IEEE Transactions on Geoscience and Remote Sensing*, 38(2) :977–998. (Cité en page 40.)

Manna, A. J. (1985). 25 years of TIROS satellites. *Bulletin of the American Meteorological Society*, 66(4) :421–423. (Cité en page 27.)

Martinet, P., Fourrié, N., Bouteloup, Y., Bazile, E., and Rabier, F. (2014a). Toward the improvement of short-range forecasts by the analysis of cloud variables from IASI radiances. *Atmospheric Science Letters*, 15(4) :342–347. (Cité en page 67.)

Martinet, P., Fourrié, N., Guidard, V., Rabier, F., Montmerle, T., and Brunel, P. (2013). Towards the use of microphysical variables for the assimilation of cloud-affected infrared radiances. *Quarterly Journal of the Royal Meteorological Society*, 139(674) :1402–1416. (Cité en pages 38 et 44.)

Martinet, P., Lavanant, L., Fourrié, N., Rabier, F., and Gambacorta, A. (2014b). Evaluation of a revised IASI channel selection for cloudy retrievals with a focus on the Mediterranean basin. *Quarterly Journal of the Royal Meteorological Society*, 140(682) :1563–1577. (Cité en pages 38 et 44.)

Matricardi, M. (2005). The inclusion of aerosols and clouds in RTIASI, the ECMWF fast radiative transfer model for the infrared atmospheric sounding interfero-

meter. Technical Memoranda 474, ECMWF. (Cité en pages 37, 38, 44, 45, 57, 68 et 72.)

Matricardi, M. (2009). Technical Note : An assessment of the accuracy of the RTTOV fast radiative transfer model using IASI data. *Atmospheric Chemistry and Physics*, 9(18) :6899–6913. (Cité en page 54.)

Matricardi, M., Chevallier, F., Kelly, G., and Thépaut, J.-N. (2004). An improved general fast radiative transfer model for the assimilation of radiance observations. *Quarterly Journal of the Royal Meteorological Society*, 130(596) :153–173. (Cité en pages 32 et 35.)

McFarquhar, G. M., Iacobellis, S., and Somerville, R. C. J. (2003). SCM simulations of tropical ice clouds using observationally based parameterizations of microphysics. *Journal of Climate*, 16(11) :1643–1664. (Cité en page 45.)

McMillin, L. M., Crone, L. J., and Kleespies, T. J. (1995). Atmospheric transmittance of an absorbing gas. 5. improvements to the OPTRAN approach. *Appl. Opt.*, 34(36) :8396–8399. (Cité en page 35.)

McMillin, L. M. and Fleming, H. E. (1976). Atmospheric transmittance of an absorbing gas : a computationally fast and accurate transmittance model for absorbing gases with constant mixing ratios in inhomogeneous atmospheres. *Appl. Opt.*, 15(2) :358–363. (Cité en pages 25 et 32.)

McMillin, L. M., Fleming, H. E., and Hill, M. L. (1979). Atmospheric transmittance of an absorbing gas. 3 : A computationally fast and accurate transmittance model for absorbing gases with variable mixing ratios. *Appl. Opt.*, 18(10) :1600–1606. (Cité en page 32.)

McMillin, L. M., Xiong, X., Han, Y., Kleespies, T. J., and Delst, P. V. (2006). Atmospheric transmittance of an absorbing gas. 7. further improvements to the OPTRAN 6 approach. *Appl. Opt.*, 45(9) :2028–2034. (Cité en page 35.)

McNally, A. P. (2002). A note on the occurrence of cloud in meteorologically sensitive areas and the implications for advanced infrared sounders. *Quarterly Journal of the Royal Meteorological Society*, 128(585) :2551–2556. (Cité en page 44.)

McNally, A. P. (2009). The direct assimilation of cloud-affected satellite infrared radiances in the ECMWF 4D-Var. *Quarterly Journal of the Royal Meteorological Society*, 135(642) :1214–1229. (Cité en pages 20 et 37.)

McNally, A. P., Andersson, E., Kelly, G., and Saunders, R. W. (1999). The use of raw TOVS/ATOVS radiances in the ECMWF 4D-Var assimilation system. ECMWF Newsletter 83, ECMWF. (Cité en page 19.)

Menzel, W. P., Smith, W. L., and Stewart, T. R. (1983). Improved cloud motion wind vector and altitude assignment using VAS. *Journal of Climate and Applied Meteorology*, 22(3) :377–384. (Cité en page 37.)

Merchant, C., Embury, O., Borgne, P. L., and Bellec, B. (2006). Saharan dust in nighttime thermal imagery : Detection and reduction of related biases in retrieved sea surface temperature. *Remote Sensing of Environment*, 104(1) :15 – 30. (Cité en page 72.)

Mlawer, E. J., Payne, V. H., Moncet, J.-L., Delamere, J. S., Alvarado, M. J., and Tobin, D. C. (2012). Development and recent evaluation of the MT_CKD model of continuum absorption. *Philosophical Transactions of the Royal Society A : Mathematical, Physical and Engineering Sciences*, 370(1968) :2520–2556. (Cité en page 32.)

Morcrette, J.-J. and Jakob, C. (2000). The response of the ECMWF model to changes in the cloud overlap assumption. *Monthly Weather Review*, 128(6) :1707–1732. (Cité en page 38.)

Niro, F., Jucks, K., and Hartmann, J.-M. (2005). Spectra calculations in central and wing regions of CO2 IR bands. IV : software and database for the computation of atmospheric spectra. *Journal of Quantitative Spectroscopy and Radiative Transfer*, 95(4) :469 – 481. (Cité en page 53.)

ODell, C. W., Bauer, P., and Bennartz, R. (2007). A fast cloud overlap parameterization for microwave radiance assimilation. *Journal of the Atmospheric Sciences*, 64(11) :3896–3909. (Cité en page 68.)

ODell, C. W., Heidinger, A. K., Greenwald, T., Bauer, P., and Bennartz, R. (2006). The Successive-Order-of-Interaction radiative transfer model. part II : Model performance and applications. *Journal of Applied Meteorology and Climatology*, 45(10) :1403–1413. (Cité en page 25.)

Okamoto, K. (2017). Evaluation of IR radiance simulation for all-sky assimilation of Himawari-8/AHI in a mesoscale NWP system. *Quarterly Journal of the Royal Meteorological Society*, 143(704) :1517–1527. (Cité en pages 49 et 67.)

Okamoto, K., McNally, A. P., and Bell, W. (2014). Progress towards the assimilation of all-sky infrared radiances : an evaluation of cloud effects. *Quarterly Journal of the Royal Meteorological Society*, 140(682) :1603–1614. (Cité en page 38.)

Okamoto, K., Sawada, Y., and Kunii, M. (2019). Comparison of assimilating all-sky and clear-sky infrared radiances from himawari-8 in a mesoscale system. *Quarterly Journal of the Royal Meteorological Society*, 145(719) :745–766. (Cité en page 49.)

Ou, S. and Liou, K.-N. (1995). Ice microphysics and climatic temperature feedback. *Atmospheric Research*, 35(2) :127 – 138. (Cité en page 45.)

Pangaud, T., Fourrie, N., Guidard, V., Dahoui, M., and Rabier, F. (2009). Assimilation of airs radiances affected by mid- to low-level clouds. *Monthly Weather Review*, 137(12) :4276–4292. (Cité en pages 20 et 37.)

Patou, M., Vidot, J., Riédi, J., Penide, G., and Garrett, T. J. (2018). Prediction of the onset of heavy rain using SEVIRI cloud observations. *Journal of Applied Meteorology and Climatology*, 57(10) :2343–2361. (Cité en pages 26 et 61.)

Pavelin, E. G., English, S. J., and Eyre, J. R. (2008). The assimilation of cloud-affected infrared satellite radiances for numerical weather prediction. *Quarterly Journal of the Royal Meteorological Society*, 134(632) :737–749. (Cité en page 37.)

Petty, G. (2006). *A First Course in Atmospheric Radiation*. Sundog Publishing, Madison, Wisconsin. (Cité en pages 29 et 30.)

Poli, P. and Brunel, P. (2018). Assessing reanalysis quality with early sounders nimbus-4 iris (1970) and nimbus-6 hirs (1975). *Advances in Space Research*, 62(2) :245 – 264. (Cité en page 34.)

Rothman, L., Gordon, I., Babikov, Y., Barbe, A., Benner, D. C., Bernath, P., Birk, M., Bizzocchi, L., Boudon, V., Brown, L., Campargue, A., Chance, K., Cohen, E., Coudert, L., Devi, V., Drouin, B., Fayt, A., Flaud, J.-M., Gamache, R., Harrison, J., Hartmann, J.-M., Hill, C., Hodges, J., Jacquemart, D., Jolly, A., Lamouroux, J., Roy, R. L., Li, G., Long, D., Lyulin, O., Mackie, C., Massie, S., Mikhailenko, S., MÃijller, H., Naumenko, O., Nikitin, A., Orphal, J., Perevalov, V., Perrin, A., Polovtseva, E., Richard, C., Smith, M., Starikova, E., Sung, K., Tashkun, S., Tennyson, J., Toon, G., Tyuterev, V., and Wagner, G. (2013). The HITRAN2012 molecular spectroscopic database. *Journal of Quantitative Spectroscopy and Radiative Transfer*, 130 :4 – 50. HITRAN2012 special issue. (Cité en page 65.)

Rothman, L., Gordon, I., Barbe, A., Benner, D., Bernath, P., Birk, M., Boudon, V., Brown, L., Campargue, A., Champion, J.-P., Chance, K., Coudert, L., Dana, V., Devi, V., Fally, S., Flaud, J.-M., Gamache, R., Goldman, A., Jacquemart, D., Kleiner, I., Lacome, N., Lafferty, W., Mandin, J.-Y., Massie, S., Mikhailenko, S., Miller, C., Moazzen-Ahmadi, N., Naumenko, O., Nikitin, A., Orphal, J., Perevalov, V., Perrin, A., Predoi-Cross, A., Rinsland, C., Rotger, M., Åăimeckova, M., Smith, M., Sung, K., Tashkun, S., Tennyson, J., Toth, R., Vandaele, A., and Auwera, J. V. (2009). The HITRAN2008 molecular spectroscopic database. *Journal of Quantitative Spectroscopy and Radiative Transfer*, 110(9) :533 – 572. HITRAN. (Cité en pages 53 et 65.)

Rothman, L., Jacquemart, D., Barbe, A., Benner, D. C., Birk, M., Brown, L., Carleer, M., Chackerian, C., Chance, K., Coudert, L., Dana, V., Devi, V., Flaud, J.-M., Gamache, R., Goldman, A., Hartmann, J.-M., Jucks, K., Maki, A., Mandin, J.-Y., Massie, S., Orphal, J., Perrin, A., Rinsland, C., Smith, M., Tennyson, J., Tolchenov, R., Toth, R., Auwera, J. V., Varanasi, P., and Wagner, G. (2005). The HITRAN 2004 molecular spectroscopic database. *Journal of Quantitative Spectroscopy and Radiative Transfer*, 96(2) :139 – 204. (Cité en page 65.)

Rozanov, V., Rozanov, A., Kokhanovsky, A., and Burrows, J. (2014). Radiative transfer through terrestrial atmosphere and ocean : Software package SCIATRAN. *Journal of Quantitative Spectroscopy and Radiative Transfer*, 133 :13 – 71. (Cité en page 25.)

Saunders, R., Hocking, J., Rundle, D., Rayer, P., Havemann, S., Matricardi, M., Geer, A., Lupu, C., Brunel, P., and Vidot, J. (2017). RTTOV-12 science and validation report. NWP-SAF report NWPSAF-MO-TV-41, NWP-SAF. (Cité en page 33.)

Saunders, R., Hocking, J., Turner, E., Rayer, P., Rundle, D., Brunel, P., Vidot, J., Roquet, P., Matricardi, M., Geer, A., Bormann, N., and Lupu, C. (2018). An

update on the RTTOV fast radiative transfer model (currently at version 12). *Geoscientific Model Development*, 11(7) :2717–2737. (Cité en pages 19, 26, 28, 39 et 72.)

Saunders, R., Matricardi, M., and Brunel, P. (1999). An improved fast radiative transfer model for assimilation of satellite radiance observations. *Quarterly Journal of the Royal Meteorological Society*, 125(556) :1407–1425. (Cité en pages 28 et 32.)

Saunders, R., Rayer, P., Brunel, P., von Engeln, A., Bormann, N., Strow, L., Hannon, S., Heilliette, S., Liu, X., Miskolczi, F., Han, Y., Masiello, G., Moncet, J.-L., Uymin, G., Sherlock, V., and Turner, D. S. (2007). A comparison of radiative transfer models for simulating atmospheric infrared sounder (AIRS) radiances. *Journal of Geophysical Research : Atmospheres*, 112(D1). (Cité en pages 52 et 54.)

Schaaf, C. B., Gao, F., Strahler, A. H., Lucht, W., Li, X., Tsang, T., Strugnell, N. C., Zhang, X., Jin, Y., Muller, J.-P., Lewis, P., Barnsley, M., Hobson, P., Disney, M., Roberts, G., Dunderdale, M., Doll, C., d'Entremont, R. P., Hu, B., Liang, S., Privette, J. L., and Roy, D. (2002). First operational BRDF, albedo nadir reflectance products from MODIS. *Remote Sensing of Environment*, 83(1) :135 – 148. The Moderate Resolution Imaging Spectroradiometer (MODIS) : a new generation of Land Surface Monitoring. (Cité en page 40.)

Schaepman-Strub, G., Schaepman, M., Painter, T., Dangel, S., and Martonchik, J. (2006). Reflectance quantities in optical remote sensingâĂŤdefinitions and case studies. *Remote Sensing of Environment*, 103(1) :27 – 42. (Cité en page 39.)

Schepers, D., aan de Brugh, J., Hahne, P., Butz, A., Hasekamp, O., and Landgraf, J. (2014). LINTRAN v2.0 : A linearised vector radiative transfer model for efficient simulation of satellite-born nadir-viewing reflection measurements of cloudy atmospheres. *Journal of Quantitative Spectroscopy and Radiative Transfer*, 149 :347 – 359. (Cité en page 25.)

Scott, N. A. and Chedin, A. (1981). A fast line-by-line method for atmospheric absorption computations : The Automatized Atmospheric Absorption Atlas. *Journal of Applied Meteorology*, 20(7) :802–812. (Cité en page 53.)

Spurr, R. and Christi, M. (2014). On the generation of atmospheric property jacobians from the (V)LIDORT linearized radiative transfer models. *Journal of Quantitative Spectroscopy and Radiative Transfer*, 142 :109 – 115. (Cité en page 55.)

Stamnes, K., Tsay, S., Wiscombe, W., and Jayaweera, K. (1988). Numerically stable algorithm for discrete-ordinate-method radiative transfer in multiple scattering and emitting layered media. *Appl. Opt.*, 27(12) :2502–2509. (Cité en pages 39 et 41.)

Strow, L. L., Hannon, S. E., De Souza-Machado, S., Motteler, H. E., and Tobin, D. (2003). An overview of the AIRS radiative transfer model. *IEEE Transactions on Geoscience and Remote Sensing*, 41(2) :303–313. (Cité en page 57.)

Tabary, P. (2007). The new french operational radar rainfall product. part I : Methodology. *Weather and Forecasting*, 22(3) :393–408. (Cité en page 60.)

Tang, G., Yang, P., Kattawar, G. W., Huang, X., Mlawer, E. J., Baum, B. A., and King, M. D. (2018). Improvement of the simulation of cloud longwave scattering in broadband radiative transfer models. *Journal of the Atmospheric Sciences*, 75(7) :2217–2233. (Cité en pages 70 et 73.)

Tran, H., Flaud, P.-M., Gabard, T., Hase, F., von Clarmann, T., Camy-Peyret, C., Payan, S., and Hartmann, J.-M. (2006). Model, software and database for line-mixing effects in the v3 and v4 bands of CH4 and tests using laboratory and planetary measurements I : N2 (and air) broadenings and the earth atmosphere. *Journal of Quantitative Spectroscopy and Radiative Transfer*, 101(2) :284 – 305. (Cité en page 53.)

Vidot, J., Baran, A. J., and Brunel, P. (2015). A new ice cloud parameterization for infrared radiative transfer simulation of cloudy radiances : Evaluation and optimization with IIR observations and ice cloud profile retrieval products. *Journal of Geophysical Research : Atmospheres*, 120(14) :6937–6951. (Cité en pages 26, 46, 47 et 68.)

Vidot, J., Bennartz, R., ODell, C. W., Preusker, R., Lindstrot, R., and Heidinger, A. K. (2009). CO2 retrieval over clouds from the OCO mission : Model simulations and error analysis. *Journal of Atmospheric and Oceanic Technology*, 26(6) :1090–1104. (Cité en page 25.)

Vidot, J. and Borbas, E. (2014). Land surface VIS/NIR BRDF atlas for RTTOV-11 : model and validation against SEVIRI land SAF albedo product. *Quarterly Journal of the Royal Meteorological Society*, 140(684) :2186–2196. (Cité en pages 26 et 40.)

Vidot, J., Brunel, P., Dumont, M., Carmagnola, C., and Hocking, J. (2018). The VIS/NIR land and snow BRDF atlas for RTTOV : Comparison between MODIS MCD43C1 C5 and C6. *Remote Sensing*, 10(2) :21. (Cité en page 43.)

Vidot, J., Jourdan, O., Kokhanosvky, A. A., Szczap, F., Giraud, V., and Rozanov, V. V. (2010). Retrieval of tropospheric NO2 columns from satellite measurements in presence of cirrus : A theoretical sensitivity study using SCIATRAN and prospect application for the A-train. *Journal of Quantitative Spectroscopy and Radiative Transfer*, 111(4) :586 – 601. (Cité en page 25.)

Vidot, J., Landgraf, J., Hasekamp, O., Butz, A., Galli, A., Tol, P., and Aben, I. (2012). Carbon monoxide from shortwave infrared reflectance measurements : A new retrieval approach for clear sky and partially cloudy atmospheres. *Remote Sensing of Environment*, 120 :255 – 266. The Sentinel Missions - New Opportunities for Science. (Cité en page 25.)

Vidot, J., Santer, R., and Aznay, O. (2008). Evaluation of the MERIS aerosol product over land with AERONET. *Atmospheric Chemistry and Physics*, 8(24) :7603–7617. (Cité en page 25.)

Weng, F., Han, Y., van Delst, P., Liu, Q., Kleespies, T., Yan, B., and Marshall, J. L. (2005). JCSDA community radiative transfer model (CRTM). In *ITSC-XIV : Beijing, China, 25-31 May 2005*. (Cité en page 25.)

Wexler, H. and Fritz, S. (1960). TIROS reveals cloud formations. *Science*, 131(3415) :1708–1710. (Cité en page 27.)

Wyser, K. (1998). The effective radius in ice clouds. *Journal of Climate*, 11(7) :1793–1802. (Cité en page 45.)

Yang, P., Mlynczak, M. G., Wei, H., Kratz, D. P., Baum, B. A., Hu, Y. X., Wiscombe, W. J., Heidinger, A., and Mishchenko, M. I. (2003). Spectral signature of ice clouds in the far-infrared region : Single-scattering calculations and radiative sensitivity study. *Journal of Geophysical Research : Atmospheres*, 108(D18). (Cité en page 50.)

Zoogman, P., Liu, X., Chance, K., Sun, Q., Schaaf, C., Mahr, T., and Wagner, T. (2016). A climatology of visible surface reflectance spectra. *Journal of Quantitative Spectroscopy and Radiative Transfer*, 180 :39 – 46. (Cité en page 71.)